UNIVERSITY OF SOUTHAMPTON

ROLLOVER AND INTERFACIAL STUDIES IN LNG MIXTURES

by

T. Agbabi

Submitted for the degree of Doctor of Philosophy

INSTITUTE OF CRYOGENICS,

SOUTHAMPTON,

ENGLAND, U.K.

OCTOBER 1987

UNIVERSITY OF SOUTHAMPTON

ABSTRACT

FACULTY OF ENGINEERING

INSTITUTE OF CRYOGENICS

Doctor of Philosophy

ROLLOVER AND INTERFACIAL STUDIES IN LNG MIXTURES

by Tom Agbabi

An experimental investigation into LNG rollover has been performed, using cryogenic liquids to simulate a two-layered LNG system.

A vacuum insulated glass vessel was designed and constructed for rollover simulation experiments. Thin metal oxide coatings on the inner jacket of the vessel enabled the simultaneous heating and visualisation of the liquid in the vessel. Mixtures of liquid nitrogen and liquid oxygen were successfully used to form two differing density layers. An oxygen analysing system with an accuracy of 0.01% by volume oxygen, and a fifteen junction copper-constantan thermocouple array were used for primary measurements of mass concentration and temperature.

For a number of initial density differences between layers, various liquid layer heating configurations were used to obtain the variations in evaporation flowrate, and detailed temperature and concentration profiles during experiments. Convective flow patterns in single and two-component liquid mixtures were obtained, using the Schlieren method.

Results show that the mixing of layers is primarily due to entrainment of fluid from the intermediate layer separating the two convective layers. The intermediate layer can be described by Double-Diffusive convection theory, and controls the transport of heat and mass between layers. The measured peak flowrate is a function of the initial density difference between layers. The peak to equilibrium flowrate values are much lower than those reported in rollover incidents, due to the enhanced mixing processes occurring in the simulation mixture. A correlation between the evaporative mass flux and bulk fluid superheat fails during transient heating conditions, and cannot predict very high flowrates. Schlieren flow - visualisation studies clearly show various surface patterns for increasing surface evaporation mass fluxes.

CONTENTS

NOMENCLATURE

a,	Horizontal wavenumber corresponding to convective rolls.
A,	Cross-sectional area, m^2
C,	Constant
c_p,	Specific heat capacity, $J\,kg^{-1}K^{-1}$
d,	Depth of fluid, m
D_{AB},	Mass diffusivity of A diffusing through liquid solvent B, $m^2\,s^{-1}$
D_m,	Mass diffusivity, $m^2\,s^{-1}$
D_s.	Mass diffusivity of salt, $m^2\,s^{-1}$
f_i,	Fugacity of component i, $N\,m^{-2}$
F_s,	Flux of salt through interface, $kg\,m^{-2}\,s^{-1}$
g,	Acceleration due to gravity, $m\,s^{-2}$
$(H-H_o)$,	Excess enthalpy, J
J_{Az},	Mass flux of component A diffusing in Z direction, $kg\,m^{-2}\,s^{-1}$
K_T	Thermal conductivity, $W\,m^{-1}\,K^{-1}$
L	Latent heat of vaporisation $J\,kg^{-1}$
LAr,	Liquid Argon
LIN,	Liquid Nitrogen
LOX,	Liquid Oxygen
LCH_4,	Liquid Methane
LNG,	Liquid Natural Gas
m_b,	Total mass of lower layer, kg
m_T,	Total mass of top layer, kg
m_{o_2b},	Mass of LOX in lower layer, kg
m_{o_2T},	Mass of LOX in top layer, kg
$\dot{m}$	Vapour mass flux, $kg\,m^{-2}\,s^{-1}$
$\dot{m}_*$,	Modified vapour mass flux, $K^{4/3}$
$\dot{m}_v$,	Vapour mass flowrate, $kg\,s^{-1}$
m_L,	Mass of layer, kg
M_{Az},	Measured mass flux through intermediate layer, $kg\,m^{-2}s^{-1}$
p,	Solution of characteristic equation
P,	Pressure, $N\,m^{-2}$
p_i,	Partial pressure of i^{th} component in multi-component mixture, $N\,m^{-2}$
$\dot{Q}_i$,	Measured heat flux through intermediate layer, $W\,m^{-2}$
$\dot{Q}_s$,	Solid conduction heat flux, $W\,m^{-2}$
$\dot{Q}_b$,	Heat leak into bottom layer, J
ΔS,	Concentration difference between layers, % LOX in mixture.
t,	Time, s
T,	Temperature, K
T_b,	Bulk fluid temperature, K
T_m,	Liquid mixture temperature, K
T_W,	Wall temperature, K
ΔT,	Temperature difference between layers, K
ΔT_b,	Temperature rise of fluid during time interval Δt, K
ΔT_s,	Bulk fluid temperature above corresponding saturation temperature, K
(TO),	Thermal overfill, J
u,	Velocity of flow, $m\,s^{-1}$
$\underline{v}$,	Vector velocity $= \underline{i}\,u_x + \underline{k}\,u_z$, $m\,s^{-1}$
V_B, V_A,	Molecular volumes of constituents B and A, $cm^3\,mol^{-1}$
x_i	Mole fraction of component i in liquid phase
x_{o_2g}	Gaseous oxygen volume fraction
x_{o_2L}	LOX volume fraction
z	Vertical distance, m

z_i Mole fraction of component i in vapour phase.
α Thermal diffusivity, $m^2 s^{-1}$
β_T Fractional change in density per unit temperature change, K^{-1}
β_s Fractional change in density per unit concentration change (% LOX)
θ Temperature field parameter
λ Eigenvalue solution
μ_B Viscosity of solution B, centipoises
ν Kinematic viscosity, $m^2 s^{-1}$
π_i Partial pressure of pure component i in vapour phase.
ρ Density of fluid, $Kg\,m^{-3}$
ρ_m Density of liquid mixture, $Kg m^{-3}$
ρ_{O_2} Density of LOX, $kg\,m^{-3}$
ρ_{N_2} Density of LIN, $Kg\,m^{-3}$
σ Salinity field parameter
ω Velocity of flow in Z - direction, $m\,s^{-1}$
ψ Stream function.

Dimensionless parameters

Gr, Grashof number, $(\beta_T \Delta T d^3 g)/\nu^2$
Le, Lewis number, $K_T/(\rho C_p D_{AB})$
Nu, Nusselt number, $(\dot{Q}_s d)/(K_T \Delta T)$
Pr, Prandtl number, $\nu/\alpha = \mu C_p/K_T$
R, Stability parameter, $(\beta_s \Delta S)/(\beta_T \Delta T)$
Ri, Richardson number, $(\Delta\rho g d)/(\rho u^2)$
Ra, Thermal Rayleigh number, $(g\beta_T \Delta T d^3)/(\alpha\nu)$
Rs, Solute Rayleigh number, $(g\beta_s \Delta S d^3)/(\alpha\nu)$
τ, Diffusivity ratio, D_m/α

Mathematical operations

D/Dt, Substantial derivitive = $\frac{\partial}{\partial t} + v_x\frac{\partial}{\partial x} + v_y\frac{\partial}{\partial y} + v_z\frac{\partial}{\partial z}$

$\exp(x)$, or e^x, exponential function of x

$\nabla = \underline{i}\frac{\partial}{\partial x} + \underline{j}\frac{\partial}{\partial y} + z\frac{\partial}{\partial z}$

1.0 INTRODUCTION

For greater storage volume capacity, natural gas is stored in its liquid form (termed LNG). The low boiling point of LNG (~ 112 K) requires that it be stored in thermally well insulated storage tanks. The inevitable heat leak through the side walls and base of the storage tank leads to evaporation of the liquid in the tank. Very high unexpected evaporation rates can sometimes occur at the liquid-vapour interface. The mixing of liquid layers that produce high vapour flowrates is commonly known as "Rollover".

Evaporation flowrate variations at the surface of cryogenic liquids can also be attributed to superheating and vapour explosions. The mechanisms which create instabilities in cryogenic liquids are not yet completely understood. However, superheating, vapour explosions and rollover are all associated with thermal overfill, where the heat absorbed by vaporisation is less than the total heat flux into the stored cryogenic liquid.

Rollover may occur when LNG of a different density is added to a partially filled tank. If the two sets of liquid are not adequately mixed, stratified layers may form. Fig. 1 shows a typical LNG storage tank with two layers of LNG. The difference in density between the two layers is due to temperature and composition differences. Because LNG is a mixture of methane, heavier hydrocarbons, nitrogen and some lighter gases, the liquid composition can vary considerably. For example, pipeline gas in the North-East of the U.S.A. may be 95% methane, compared with Libyan LNG which might be 65% methane, 25% ethane and 10% propane or higher hydrocarbons.

As well as the natural gas source, the time spent in transportation and time in the final storage tank affect the LNG composition and temperature. The presence of nitrogen increases the mixture density and decreases the mixture temperature. The nitrogen concentrations, however, are generally less than 3%.

The stored superheat energy of a submerged layer in a typical tank may be exceedingly large. Using the tank in

Fig.1 for example, and assuming the liquid to be 100% methane, a lower layer of 3 metres depth superheated 1 K above saturation contains an excess energy of 3×10^9 J. The rapid uncontrollable release of this energy would be hazardous.

Prevention of rollover is necessary in terms of the danger of overpressurisation, and the loss of vast quantities of gas released through venting. A number of preventative measures have been suggested, such as;

1) Efficient mixing by either top or bottom filling, depending on whether the cargo is denser or lighter than the existing fluid.
2) Using mechanical mixing devices to mix all incoming LNG with all liquid in the tank.
3) The overdesigning of storage tanks and vapour handling systems to accomodate the maximum rate of vapour generation that can be created during rollover.
4) Limiting the range of LNG composition added to the tank.

The choice of particular preventative measures depends on the type of installations and liquid processes involved. If the convective boundary layer in the lower layer cannot penetrate the interface between layers, two separate convective systems will exist. The mass and heat transfer processes by diffusion and thermal conduction between layers, will govern the time and intensity of the mixing process.

If rollover does take place, the tank vent valves must be able to release the vapour generated in an emergency to avoid overpressurisation. The sizing of the vent valves is determined by the peak evaporation flowrate as well as the rate of rise of the flowrate during rollover.

The aim of the work described in this report was to promote further understanding of the rollover phenomenon using cryogenic liquids as test fluids. Experiments involving the measurement of the two diffusing elements (heat and mass) were considered, to see their effect on the mixing processes in a multicomponent cryogenic liquid system. These investigations were considered necessary, because heat and mass transfer processes control the release of stored superheat energy, and therefore relate to the

Fig. 1. Typical LNG storage tank containing liquid layers of different density.

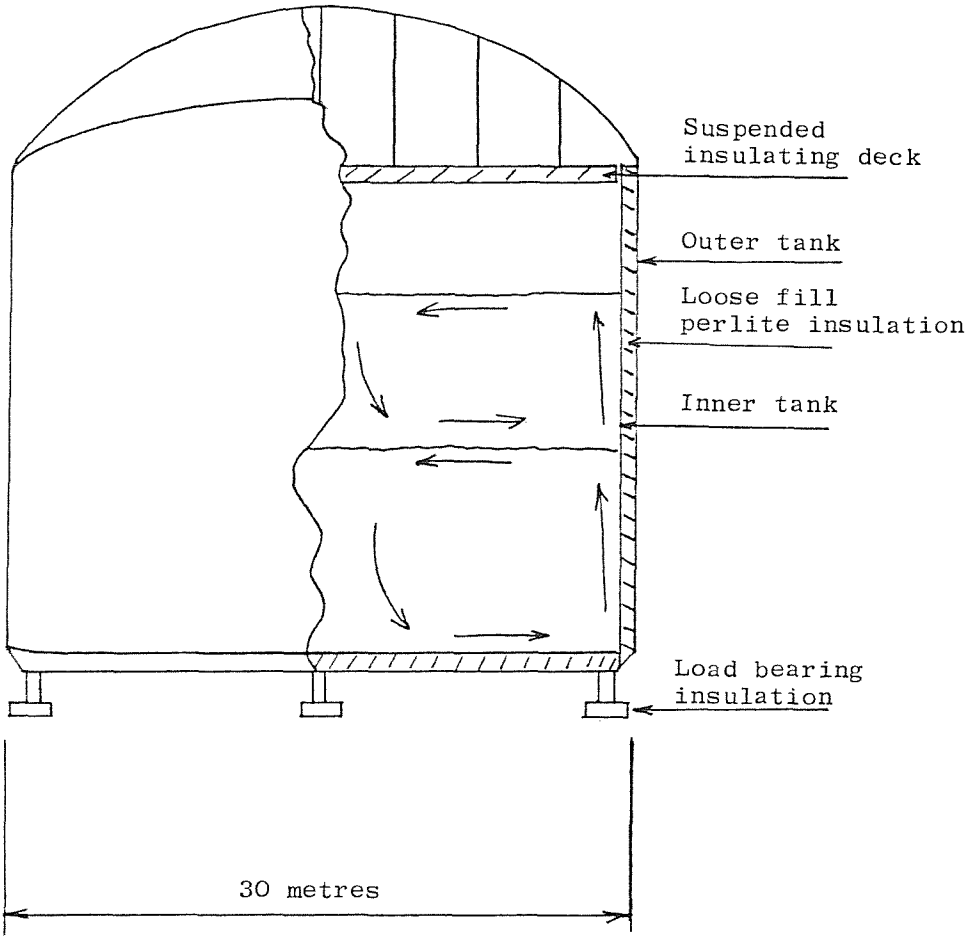

final peak flowrate produced and the time constant associated with the rollover event.

Following a chapter on the theory of mixing of layers, this thesis describes how mixtures of liquid nitrogen and liquid oxygen have been developed to simulate LNG rollover. This technique has allowed a large number of rollover events to be studied and recorded. The results are discussed, and some firm conclusions are reached about Double-Diffusive convection in the lead up to rollover, and the final peak flowrate recorded in rollover events.

1.1 Previous Investigations

Rollover Incidents

Sarsten (1) gives an account of the rollover in an LNG tank at the SNAM LNG terminal in La Spezia, Italy. The incident occurred in August 1971, after one of the storage tanks was bottom filled over an eleven hour period by the LNG ship Esso Brega. Eighteen hours after filling, LNG tank 51 experienced a sudden increase in pressure. The nominal tank design pressure of 500 mm of water was exceeded by 210 mm of water. The safety valves discharged vapour for one hour and fifteen minutes, and the vent released vapour at high rates for about three hours. Fortunately, no damage was done to the tank.

Table 1 shows the compositions of the initial tank liquid and the Esso Brega cargo. The Esso Brega had been in harbour for more than a month. During this time, the cargo got hotter and heavier than it was when loaded in Masso El Brega, Libya, as a result of the evaporation of light components in the LNG.

Another recorded rollover event (2) occurred at the Fos-Sur-Mer LNG terminal in 1978. During vapour flowrate tests, the evaporation rate increased to twenty times the normal rate. From the flowrate time plot of the event, the total loss of vapour from the 36 m diameter tank was 160,000 cubic metres of gas.

1.2 Mathematical Models

Chaterjee and Geist (3) developed a model to describe the fluid behaviour in stratified LNG tanks. The model assumes a tank with n homogenous layers heated from the sidewalls and the base of the tank. The interface heat and mass transfer equations are based on the following assumptions;

a) All layers have different densities and are separated by sharp interfaces.

b) The LNG density ρ is a function of methane mole fraction S, and temperature T only. Also, β_S and β_T are constant.

where $\beta_S = \frac{1}{\rho}\left(\frac{\partial \rho}{\partial S}\right)$ and $\beta_T = \frac{1}{\rho}\left(\frac{\partial \rho}{\partial T}\right)$

Table 1.1

Initial conditions of storage tank and ship liquid before La Spezia rollover.

Components	Initial Tank Mol %	Esso Brega Cargo Mol %
Methane	63.62	62.26
Ethane	24.16	21.85
Propane	9.36	12.66
n -Butane	1.45	1.94
Iso-Butane	0.90	1.20
n -Pentane	0.05	0.01
Iso -Pentane	0.11	0.06
Nitrogen	0.35	0.02
Temperature K	114.36	118.99
Liquid depth m	5.03	17.83
Density Kgm^{-3}	541.74	545.59
Vapour pressure Nm^{-2}	3923.0	1628 0

c) Interfacial mass transfer is by counter diffusion.

d) The heat transfer coefficient of the sidewall is not the same as that for the base of the tank.

Three rollover events were used to test the model. The predicted times to reach peak flowrates agree well with the real cases. The time and place of the cases used to test the model are not, however, given.

A model for LNG tank rollover proposed by Germeles (4) is similar to the Chattergee Geist model, except for the following differences;

a) The number of moles per layer can change, i.e. equimolar counter diffusion is not assumed.

b) The Hashemi-Wesson model (5) is used to calculate the evaporation flowrate.

c) Layers are assumed mixed when their densities are equal.

The LNG mixture is represented by a two component mixture of methane (the solvent), and a solute equivalent to all impurities of a given LNG mixture. The interface mass and heat transfer processes are based on the transport coefficients for a double-diffusive convection system (6). The computation uses data from the La Spezia incident. The computed rollover time of 34 hours is in good agreement with the observed time of 31 hours. Because of the uncertainty of the interface transport coefficients, this good agreement is considered fortunate.

A second model by Chattergee and Geist (7), takes into account the influence of nitrogen in the LNG mixture. The LNG is considered as a mixture of methane, ethane and nitrogen. The mass transfer rates for each component are derived from Turner's salt-water experiments (6). In the first model the evaporation vapour from the top layer is assumed to be methane. The three component model assumes the vapour to be a mixture of each liquid component. Like the first model, the evaporation flowrate is obtained from a flash calculation. The differential equations involving

heat and mass transfer are solved as an initial value problem using the LEANS III computer programme (8).

The model results are compared with a case where a tank lost 1% of its contents in a 24 hour period. This represented an evaporation rate 16 times the normal value. In a six month period, the nitrogen content decreased considerably, making the fresh bottom filled LNG about 10 $kg\,m^{-3}$ denser, than the original weathered LNG. The computer simulation shows that the rollover intensity increases with increased initial density differences of the layers.

The time to rollover (18 hours) agrees well with the real case (21 hours). The peak calculated flowrate is not compared with the actual event.

A rollover model proposed by Takao and Suzuki (9) is similar to that of Germeles (4), in that adjacent layers are assumed mixed when densities are equal, and the Hashemi-Wesson equation (5) is used to compute the vapour flowrate. The difference in the model, is that mass and heat transfer processes are modelled on the experimental results obtained by Takao and Narusawa (10). The calculated peak flowrate for the initial tank conditions is seven times the normal vapour flowrate.

Heastand, Shipman and Meader (11) put forward a predictive model for rollover, in which the LNG is considered to be a mixture of methane, ethane, propane, n-butane and nitrogen. The time for density equalisation in the La Spezia incident suggests appreciable mass transfer occurred at an early stage in the mixing process. The salt-water transport correlations of Turner (6) are considered inappropriate to the LNG system. Fully turbulent heat and mass transfer processes are assumed between convective cells. The vapour flowrate is described by a modified Hashemi-Wesson equation (5) which takes into account the influence of composition as well as temperature variations in the bulk fluid. Using the La Spezia incident for initial conditions, the predicted time of rollover (30.5 hours), agrees very well with the reported time of 31 hours.

1.3 Experimental Studies

Few rollover experiments have been performed using LNG as the test fluid. Sugawara, Kubota and Muraki (12) carried out an LNG rollover test in a 500 mm diameter tank. A two-layered liquid system was formed, using LNG from two different sources. The results showed that the interface between the upper and lower layers changed due to changes in the convective flows within each layer. The interface level fell rapidly just before the layers were completely mixed. An intermediate region between the two layers was seen to decrease interfacial heat and mass transfer.

Muro, Yoshiwa, Yasuda, and Miyata, Iwata and Yarmazaki (13), performed experiments using a 1 metre high 580 mm ⌀ stainless steel vacuum insulated tank. Liquid mixtures of methane, ethane and propane were used to form two stratified layers in the tank. Experiments obtained heat and mass transfer correlations based on those used by Turner (14). A correlation between the LNG surface evaporation rate and bulk fluid superheat, agreed well with results made by Beduz, Rebiai and Scurlock (15) on liquid oxygen and liquid nitrogen.

Nakano, Sugawara, Yamagata and Nakumara (16) studied the mixing of stratified layers using liquid Freon. Mixtures of Freon 11 and Freon 13 were used to simulate LNG in a storage tank. Tests were performed using a rectangular tank with two side walls made of glass. The mixing processes between the two layers depended on the source of heating. For base heating, the interface level moved little, until waves formed at the interface. The lower fluid boundary layer then penetrated up to the surface of the top layer and the top layer mixed completely with the lower layer. With side wall heating to the tank, the interface level eventually fell, but at a slower rate than that with base heating, side and base heating produced a mixture of the two processes described above.

Griffis and Smith (17), used a water-sugar system to similate the formation of layers in an LNG tank due to

side-wall heating. The main conclusion of the study was that the layer thickness due to heating will be small in an LNG tank. A calculation using hypothetical properties for an LNG mixture in its tank gives a layer spacing of $\sim$20cm, which is small compared with the height of an LNG container.

1.4 La Spezia Peak Flowrate

Rollover models using the La Spezia incident initial data, all predict the time to rollover very accurately. The models and experimental studies, however, do not explain the very high flowrate created at La Spezia.

Maher and Van Gelder (18), discussed the effect of the temperature gradient that exists at the liquid-vapour interface of an unagitated fluid. This temperature gradient can be large (15) and acts as a resistance to heat transfer very near the surface. Studies (19) have also shown that the vapour flowrate can be decreased due to the presence of impurities in the bulk liquid. These non-volatile impurities come out of solution at the surface during normal evaporation. The very large flowrate in the La Spezia incident may possibly be attributed to the sudden destruction of the thin surface layer.

2.0 THEORETICAL CONSIDERATIONS

An important thermodynamic property of a stored cryogenic liquid is its Thermal Overfill, TO (15). This is the sum of the excess enthalpy ($H - H_o$) of the stored liquid above or below the value H_o , defined as the saturation enthalpy at To and Po. When ($H - H_o$) is positive, a volume of liquid may be termed "superheated". With ($H - H_o$) negative, the term "subcooled" may be used.

The average Thermal Overfill value is the sum of the excess enthalpies of all elements in the stored liquid, i.e;

$$(TO)_{av} = \sum (H - H_o) \qquad (2.1)$$

As ($H - H_o$) is dependent on temperature, density, hydrostatic pressure, composition and thermal history, it can be positive or negative for different elements in the same tank. $(TO)_{av}$ may therefore be expressed as;

$$(TO)_{av} = (TO)_+ - (TO)_- \qquad (2.2)$$

where $(TO)_+$ = sum of positive contributions

and $(TO)_-$ = sum of all negative contributions.

When there is poor mixing in a container, the positive and negative contributions may be independent of each other. Any excess evaporation at the liquid surface will be due to $(TO)_+$, so it is more realistic to consider $(TO)_+$ as the relevant Thermal Overfill.

Thermal Overfill is also time dependant. If the total heat flux $\dot{Q}$ into the stored liquid exceeds the heat absorbed by the evaporation vapour mass flowrate $\dot{m}$ through the latent heat of vaporisation L, then;

$$\frac{\partial (TO)_{av}}{\partial t} = \dot{Q} - \dot{m} L \qquad (2.3)$$

A dangerous storage situation may therefore be predicted if it is known that $\partial/\partial t (TO)_{av}$ is positive over a period of time. This is a general method of assessing the overall stability of a stored liquid. The form of liquid instabilities that may arise due to a temperature and concentration field in a liquid, can be predicted using Double-Diffusive convection theory.

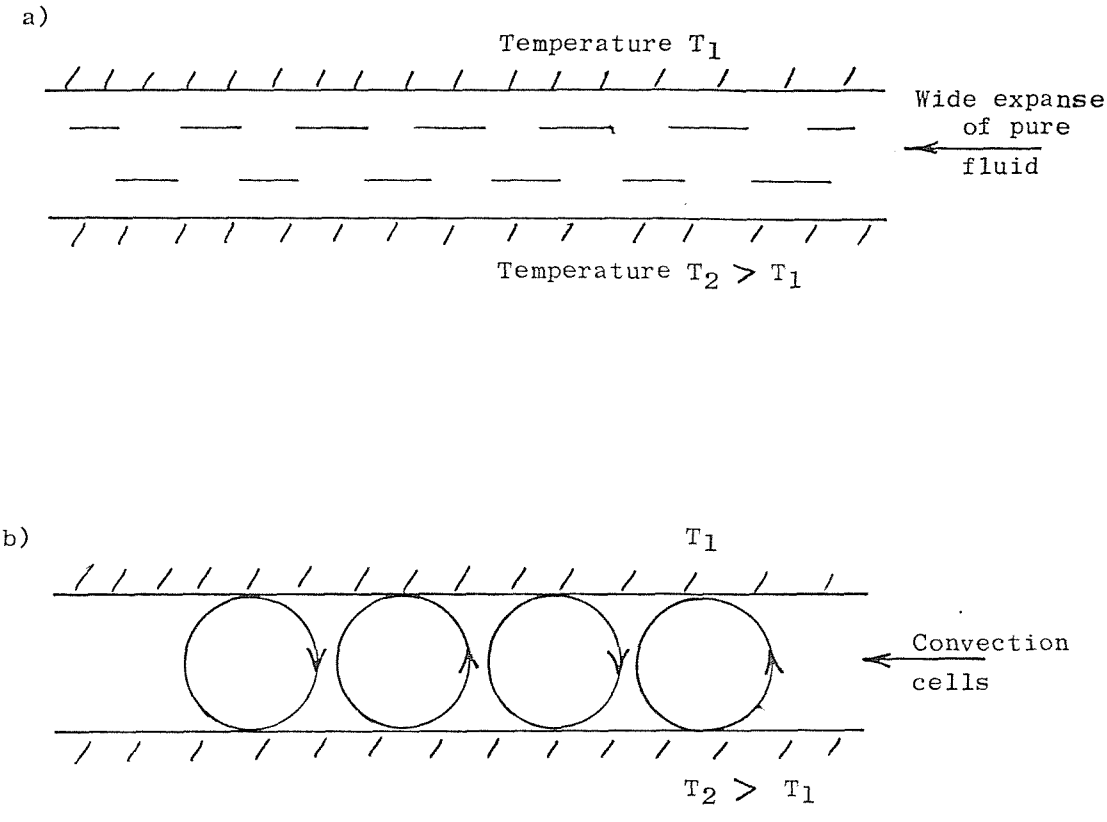

Fig. 2.1 Bénard free convection configuration

a) Ra < 1700 b) Ra > 1700

2.1 Convection Theory

As an introduction to Double-Diffusive convection, some relevant natural convection parameters will be discussed.

The Richardson number Ri, gives a measure of the importance of buoyancy effects in a fluid. Ri can be written as;

$$Ri = \frac{\Delta\rho}{\rho} \frac{g d}{u^2} \qquad (2.4)$$

Where $\Delta\rho$ is the density difference that occurs over a typical length scale L in a flow of velocity u. Equation (2.4) implies that significant buoyancy effects can occur either if $\Delta\rho/\rho$ is important, as in small-scale plumes, or if gd/u^2 is significant, as in large-scale geophysical flows. In free or natural convection, motion is due entirely to buoyancy forces in the liquid.

Two non-dimensional parameters characterising free convective flow, are the Grashof and Prandtl numbers, which are given by;

$$Gr = \frac{\beta_T (T_w - T_b) d^3 g}{\nu^2} \qquad (2.5)$$

and

$$Pr = \frac{\mu c_p}{K_T} \qquad (2.6)$$

The product (Gr.Pr) is commonly known as the Rayleigh number Ra. In the Bénard configuration (Fig.2.1), convection begins when Ra reaches a value of about 1700. Motion occurs when the destabilising effect of the temperature can overcome the action of viscosity and thermal conductivity. The density of the fluid at all positions is a function of the fluid temperature.

2.2 Double-Diffusive Convection

Double-Diffusive convection refers to motion in a fluid in which there are gradients of two or more properties with different molecular diffusivities. Each of the diffusing properties contribute to the fluid density, so motion can arise even when the density increases with depth of fluid. The form of motion depends on whether the driving

energy for motion comes from the component of higher or lower diffusivity. Detailed mathematical models of Double-Diffusive effects were first studied by Oceanographers. Two possible kinds of motion are suggested by the writers, i.e. fingers and oscillations, and these are in qualitative agreement with experimental observations.

Stommel,Aarons and Blanchard (20), considered a long narrow heat conducting pipe placed vertically in a region of the ocean. In this model, warm salty water rests over colder, denser, less salty water as shown in Fig. 2.2a. Water pumped up the pipe will quickly reach the temperature of its surroundings, due to the good heat conduction of the pipe. As the water will be less salty than the fluid surrounding the pipe, it is less dense, and therefore due to buoyancy, continues to flow up the pipe.

In the second example, explained by Stern (21), warm salty water lies underneath colder, less salty, lighter water. The motion of a small parcel of fluid isolated from its surroundings by a thin conducting shell is considered (Fig.2.2b). If the element is displaced upward, it will lose heat but not salt, and therefore fall back to its original position. Due to the finite value of the thermal diffusivity, the temperature of the element lags that of its surroundings. The element therefore returns to its initial position heavier than it was originally, and overshoots its original position. Oscillations therefore result, which are resisted only by viscous forces.

The forms of motion described above illustrate how our understanding of simple thermal convection can be misleading when dealing with two or more diffusive properties in a liquid.

2.3 Stability Theory

The linear stability of a layer of fluid maintained between horizontal boundaries has been discussed by many authors, such as Stern (21), Veronis (22), (23), Nield (24) and Baines and Gill (25). The general procedure for solving

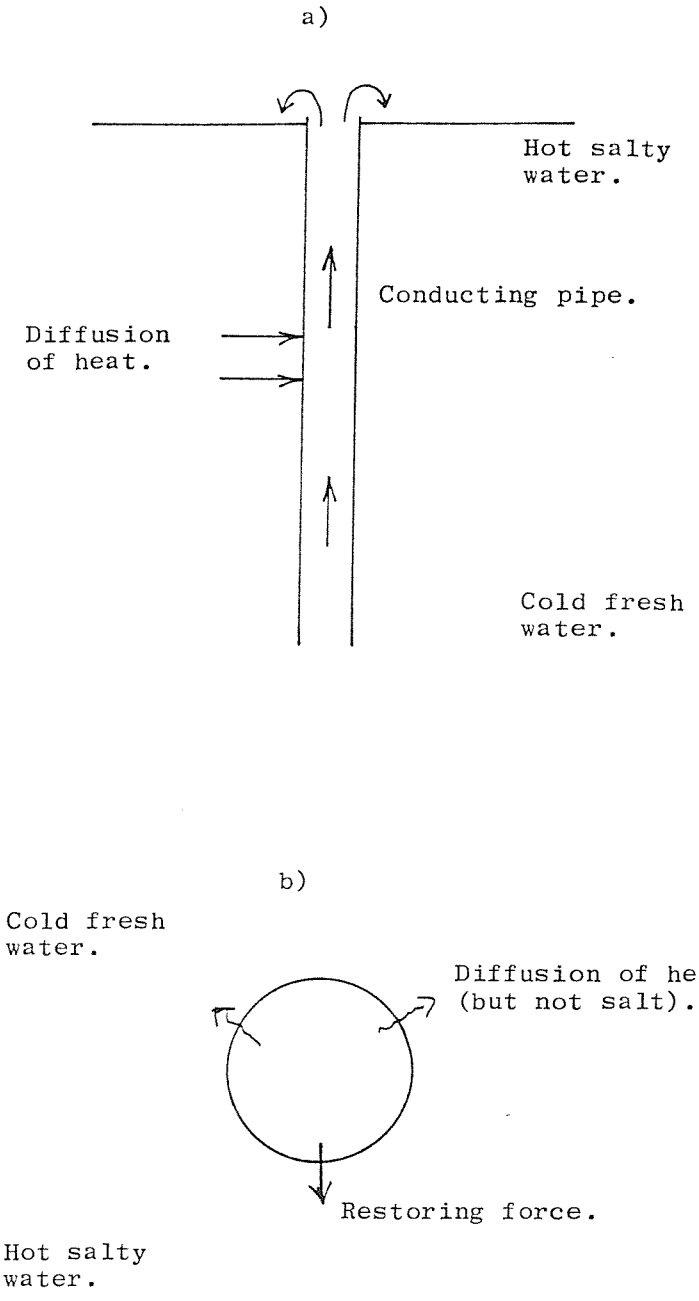

Fig. 2.2 Two possible kinds of motion in a Double-diffusive convecting fluid:

a) Salt fountain.

b) Oscillating element.

small-disturbance stability problems is as follows: Suppose X_o represents the basic flow solution. A small disturbance variable x_o is added to X_o, and $X_o + x_o$ is substituted into the flow equations. The basic terms which X_o satisfies identically are subtracted, leaving a disturbance equation for x_o. We must then show whether x_o grows with time (X_o is unstable), or damps out (X_o is stable). If x_o is assumed to be very small, the higher powers of x_o can be ignored, resulting in a linear disturbance equation which is easier to solve.

The model of the fluid containing vertical solute and temperature gradients assumes a layer of fluid of depth d, heated from below, and cooled from above. The fluid boundaries are assumed stress-free, and are perfect conductors of heat and solute. Temperature variations in convective flow create variations in fluid properties, such as density, viscosity and thermal conductivity for example. To simplify the equations describing convective flow, the Boussinesq approximation is used. This approximation assumes all fluid properties are assumed constant except for the density term that produces the buoyancy force.

The boundary temperatures are given by $T = Tm$ at $z = o$ and $T = Tm - \Delta T$ at $z = d$. The values of the solute are $S = Sm$ at $z = o$ and $S = Sm - \Delta S$ at $z = d$. The net temperature and solute values T_T and S_T are given by:

$$T_T = Tm - \Delta T\left(\frac{z}{d}\right) + T(x, y, z, t) \tag{2.7}$$

and

$$S_T = Sm - \Delta S\left(\frac{z}{d}\right) + S(x, y, z, t) \tag{2.8}$$

Where T and S are the disturbance temperature and solute. Two-dimensional motions are considered, so quantities are assumed independent of the Y co-ordinate.

The Boussinesq equations of motion used in the analysis consist of the equations of momentum;

$$\frac{D\underline{V}}{Dt} = -\frac{1}{\rho}\nabla P - g\underline{k} + \nu\nabla^2\underline{V} \tag{2.9}$$

the conservation of mass;

$$\frac{\partial u}{\partial x} + \frac{\partial \omega}{\partial z} = 0 \tag{2.10}$$

conservation of heat;

$$\frac{D}{Dt}T - \omega\frac{\Delta T}{d} = \alpha\nabla^2 T \qquad (2.11)$$

and conservation of solute;

$$\frac{D}{Dt}S - \omega\frac{\Delta S}{d} = D_m\nabla^2 S \qquad (2.12)$$

The density expression used in the buoyancy force term is:

$$\rho = \rho_b(1 - \beta_T T + \beta_s S) \qquad (2.13)$$

$\underline{K}$ is a unit vertical vector, α and D_m are the thermal and mass diffusivities. ρ_b is the bulk fluid density. ν is the kinematic viscosity, and $\underline{V} = (u, \omega)$ is the velocity. The Boussinesq equations can be reduced to dimensionless form using $\underline{V} = \underline{V}'\alpha/d$, $t = t'd^2/\alpha$, $(x, z) = d(x'z')$, $T = T'\Delta T$, $S = S'\Delta S$ and $P' = Pd^2/\rho_b\nu\alpha$

Introducing the stream function Ψ defined by:

$$u = \frac{\partial\Psi}{\partial z}, \quad \omega = \frac{\partial\Psi}{\partial x} \qquad (2.14)$$

and eliminating P using $\nabla P = -\rho_b g$, gives the linearised vorticity equation:

$$\left(\frac{1}{Pr}\frac{\partial}{\partial t} - \nabla^2\right)\nabla^2\Psi = -Ra\frac{\partial T}{\partial x} + Rs\frac{\partial S}{\partial x} \qquad (2.15)$$

The equations for T and S become:

$$\left(\frac{\partial}{\partial t} - \nabla^2\right)T + \frac{\partial\Psi}{\partial x} = 0 \qquad (2.16)$$

$$\left(\frac{\partial}{\partial t} - \tau\nabla^2\right)S + \frac{\partial\Psi}{\partial x} = 0 \qquad (2.17)$$

The primes have been dropped, so that all variables are dimensionless. As well as the Prandtl number Pr., the following dimensionless parameters appear:

ratio of molecular diffusivities: $\tau = \frac{D_m}{\alpha}$ (2.18)

Thermal Rayleigh number: $Ra = \frac{g\beta_T\Delta T d^3}{\alpha\nu}$ (2.19)

Solute Rayleigh number: $Rs = \frac{g\beta_s\Delta S d^3}{\alpha\nu}$ (2.20)

The boundary conditions at Z = 0, 1 are:

$$\Psi = 0, \qquad \frac{\partial^2}{\partial z^2}\Psi = 0, \qquad T = S = 0 \tag{2.21}$$

Using solution forms:

$$\Psi \sim e^{pt} \sin \pi a x \sin \pi z \tag{2.22}$$

and

$$T, S \sim e^{pt} \cos \pi a x \sin \pi z \tag{2.23}$$

The stability problem now involves solving for P. by substituting (2.22) and (2.23) into (2.15) to (2.17), we can obtain a cubic characteristic equation in p, which is:

$$p^3 + (P_r + \tau + 1)K^2 p^2 + \left[(\tau + P_r\tau + P_r)K^4 - (Ra - Rs)\frac{P_r \pi^2 a^2}{K^2}\right] p + P_r \tau K^2 + (Rs - \tau Ra) P_r \pi^2 a^2 = 0 \tag{2.24}$$

where $K^2 = \pi^2(a^2 + 1)$. In (2.24), $p = p_r + i\, p_i$,

is a complex number, whose real part p_r represents the growth rate, and whose imaginery part $i p_i$ allows for an oscillatory behaviour. a is the horizontal wave-number corresponding to two-dimensional convective rolls, and takes the value $2^{-1/2}$ according to linear stability theory.

For fixed values of P_r and τ, the stability boundaries (minimum Ra with Pr = 0) correspond to two straight lines in the Ra, Rs plane, whose equations are:

$$XZ: \qquad Ra = \frac{Rs}{\tau} + \frac{27\pi^4}{4} \tag{2.25}$$

and

$$XW: \qquad Ra = \left(\frac{P_r + \tau}{P_r + 1}\right) Rs + (1 + \tau)\left(1 + \frac{\tau}{P_r}\right)\frac{27\pi^4}{4} \tag{2.26}$$

These two lines are shown schematically in Fig.2.3 In the quadrant where Ra is negative (Top boundary hotter than bottom boundary), and Rs positive (bottom boundary solute concentration greater than that of top boundary), the gradients are stabilising and no growth to a disturbance is possible. In the upper left hand quadrant, all points are unstable above XZ, so that Ra_e which represents $Ra - Rs/\tau = 27\pi^4/4$ is an effective Rayleigh number with the same role as the critical Rayleigh number Ra_c in ordinary convection. With Rs = 0, the thermal Rayleigh

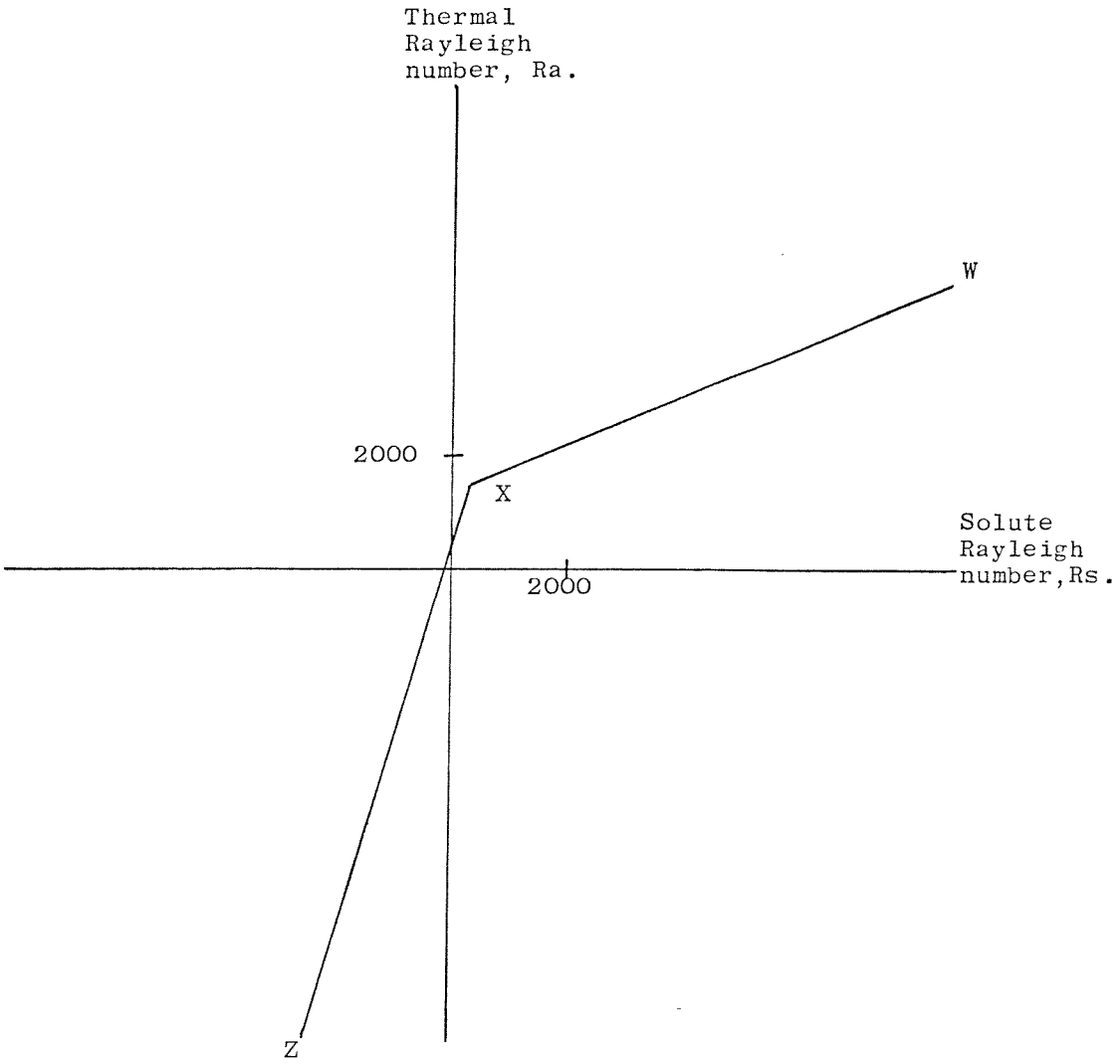

Fig. 2.3. Stability diagram for Double-Diffusive system. Regions to the right of Z X W are stable. Areas left of Z X W correspond to an unstable density gradient.

number Ra according to (2.25) is less than that for normal Bénard convection. This is due to the value of the wavenumber a. An analysis of the convective modes (22) shows that finite-amplitude steady motions occur at values of Ra considerably lower than those values predicted by linear theory. It is shown that Ra achieves a minimum at $a^2 = 1/2$ for:

$$Ra = \left[(\tau Rs)^{1/2} + \left\{ (1-\tau^2) \frac{27}{4} \pi^4 \right\}^{1/2} \right]^2 \qquad (2.27)$$

With a value of a approaching unity, the convection cells are about as high as they are wide, and a value of Ra similar to the "Bénard" Rayleigh number is achieved. When Ra and Rs are both negative, the line XZ determines the start of salt-finger type convection. For Ra and Rs positive, the region above XW indicates the onset of the diffusive or oscillatory instability.

Referring to the positive quadrant in Fig.2.3, raising the value of Ra with Rs constant (say 2000), means oscillations will occur when the destabilising effect of temperature is greater than the stabilising solute gradient effect. If Rs is increased with Ra constant, at low Rs, instability occurs, but as Rs is increased, the stabilising solute field eventually renders the system stable.

2.4 Fluxes across a diffusive interface.

Turner (14) considered how the heat transfer across a liquid-liquid interface depended on the nature of the interface. The heat transfer across the interface is compared with that possible by solid conduction. In the solid conduction model, a thin rigid sheet of perfect conductor is inserted in the interface between the layers. Diffusion of salt and wavy motion at the interface are therefore excluded. The conduction sheet is maintained at the mean temperature of the layers. The turbulent heat flux into the bulk fluid on either side of the solid plane can be described by:

$$Nu = C \; Ra^{1/3} \qquad (2.28)$$

Where Nu is the Nusselt number and Ra the thermal Rayleigh number, Nu is defined as:

$$Nu = \frac{\dot{Q}_s \, d}{K_T \, \Delta T} \tag{2.29}$$

From the definition of Nu and Ra, (2.28) may be written in the form:

$$\frac{\dot{Q}_s \, d}{K_T \, \Delta T} = C \left\{ \frac{\beta_T \, \Delta T \, d^3 \, g}{\alpha \, \nu} \right\}^{1/3} \tag{2.30}$$

Equation (2.28) implies that the heat flux Q_S is independent of the layer depth. This applies to turbulent well-mixed convective flow where the fluid in each layer is at an even temperature. (2.30) may be rewritten as:

$$\dot{Q}_s = A \, (\Delta T)^{4/3} \tag{2.31}$$

where $$A = C \, K_T \left(\frac{\beta_T \, g}{\alpha \, \nu} \right)$$

The best value for the constant C appears to be 0.085, found by Chandrasekhar(26).

If the interface is able to move, and mass is transferred, the interfacial heat transfer is dependent on the mass diffusivity, and density difference between layers, as well as the Rayleigh number. Assuming $\tau_s = D_s / \alpha$ constant, the Nusselt number can be expressed as:

$$Nu = f_1 \left(\frac{\beta_s \, \Delta S}{\beta_T \, \Delta T} \right) Ra^{1/3} \tag{2.32}$$

The mass flux across the interface is mainly due to the temperature difference existing across the interface. Hence, using the same reasoning that led to (2.32), the dimensionless mass flux will be of the form:

$$\frac{d \, F_s}{D_s \, \Delta S} = f_2 \left(\frac{\beta_s \, \Delta S}{\beta_T \, \Delta T} \right) Ra^{1/3} \tag{2.33}$$

Equation (2.33) gives the mass flux behaviour in a form that is independent of layer depth.

2.5 Mixing of Double-Diffusive Layers.

Section 2.3 discussed the possible forms of convective motion in a Double-Diffusive liquid confined between horizontal boundaries. Huppert (27), studied the stability of an intermediate layer situated between two semi-infinite constant property convective layers. An analytic expression is obtained, fitting Turner's (14) experimental results on the flux through a diffusive interface in a heat/salt system. The expression relating the ratio of interfacial heat flux Qi to that across a solid plane Q_s, with $\beta_s \Delta S / \beta_T \Delta T$ is given by:

$$\dot{Q}_i / Q_s = 3.8 \left(\beta_s \Delta S / \beta_T \Delta T \right)^{-2} \qquad (2.34)$$

combining (2.30) and (2.34), Huppert obtains a non-dimensional time τ, defined as:

$$\tau = 3.8\, c \propto T^{7/3} S^{-2} h^{-1} \left(\frac{\beta_T}{\beta_S} \right)^2 \left(\frac{\beta_T g}{\alpha \nu} \right)^{1/3} t \qquad (2.35)$$

The temperature and salinity field are expressed as $T = \tfrac{1}{2} \Delta T (1 + \theta)$ and $S = \tfrac{1}{2} \Delta S (1 + \sigma)$ respectively. θ and σ vary between - 1 and + 1. The intermediate layer thickness = h. (2.35) is used to obtain:

$$\frac{d\theta}{d\tau} = (1-\theta)^{10/3} (1-\sigma)^{-2} - (1+\theta)^{10/3} (1-\sigma)^{-2} \qquad (2.36)$$

Restricting (2.36) to the situation where the nondimensional ratio of salt to heat flux behaviour with $(\beta_s \Delta S / \beta_T \Delta T) = R$, corresponds to $R > 2$, gives:

$$\frac{d\sigma}{d\tau} = \gamma \frac{d\theta}{d\tau} \qquad (2.37)$$

where $\gamma = 0.15 \quad \beta_T \Delta T / \beta_s \Delta S$

Equilibrium positions are specified by:

$$\sigma = \frac{(1+\theta)^{5/3} - (1-\theta)^{5/3}}{(1+\theta)^{5/3} + (1-\theta)^{5/3}} = f(\theta) \qquad (2.38)$$

$$\sigma \sim 5/3\, \theta \text{ as } \theta \to 0 \text{ and } \sim \pm 1 \mp 2^{-2/3} (1 \mp \theta)^{5/3}$$

as $\theta \to \pm 1$. The points $[\theta, f(\theta)]$ represent equilibrium configurations in which there are equal fluxes through the two interfaces, but not necessarily equal temperature and salinity differences. Fig. 2.4 shows

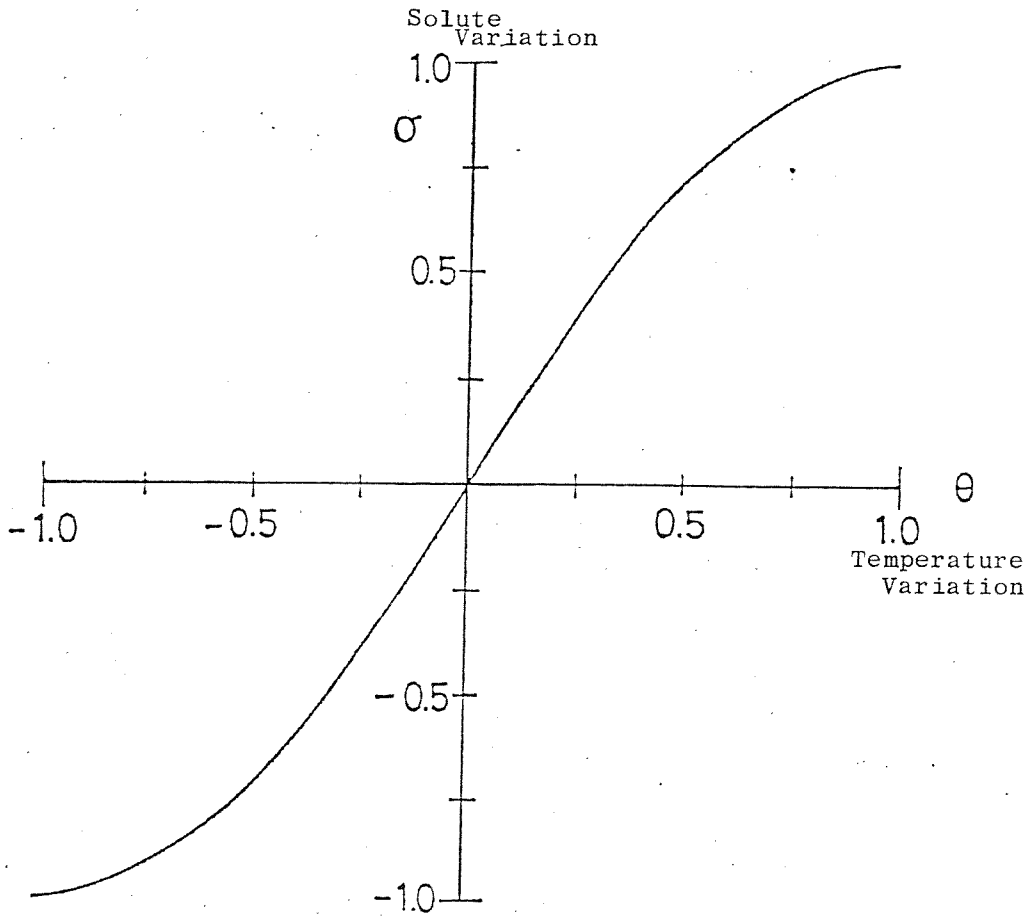

Fig. 2.4. Equilibrium positions for $\sigma = f(\theta)$ as defined by (2.38).

the function $\sigma = f(\theta)$.

Expanding the right-hand side of (2.36) using (2.38), linearising, and expressing the coefficient of θ variation by $\delta_\theta(d\theta/dt)$ and using similar notation for the σ variation gives:

$$\delta_\theta\left(\frac{d\theta}{dt}\right) = -\frac{5}{3}\left[(1+\theta)^{5/3}+(1-\theta)^{5/3}\right]^2(1-\theta^2)^{-1} = \gamma^{-1}\delta_\theta\left(\frac{d\sigma}{d\tau}\right) \qquad (2.39)$$

and $$\delta_\sigma\left(\frac{d\theta}{d\tau}\right) = \frac{1}{4}\left[(1+\theta)^{5/3}+(1-\theta)^{5/3}\right]^4(1-\theta^2)^{-5/3} = \gamma^{-1}\delta_\sigma\left(\frac{d\sigma}{d\tau}\right) \qquad (2.40)$$

The disturbance solutions of (2.36) and (2.37) are expressed in the form $\exp(\lambda\tau)$ where λ is an eigenvalue of:

$$M = \begin{bmatrix} \delta_\theta\left(\frac{d\theta}{d\tau}\right) & \delta_\sigma\left(\frac{d\theta}{d\tau}\right) \\ \delta_\theta\left(\frac{d\sigma}{d\tau}\right) & \delta_\sigma\left(\frac{d\sigma}{d\tau}\right) \end{bmatrix} \qquad (2.41)$$

substituting (2.39) and (2.40) into (2.41) gives eigenvalues: 0,

and $$\gamma\,\delta_\sigma\left(\frac{d\theta}{d\tau}\right) + \delta_\theta\left(\frac{d\theta}{d\tau}\right)$$

Therefore (θ, σ) represent equilibrium positions if:

$$\gamma \leq -\delta_\theta\left(\frac{d\theta}{d\tau}\right) \Big/ \delta_\sigma\left(\frac{d\theta}{d\tau}\right) \qquad (2.42)$$

As one of the eigenvalues of M is 0, the equilibrium is neutrally stable. An example of neutral stability is a ball on a flat surface that is pushed from one position to another on the horizontal surface. The system (ball) returns to equilibrium, but not to the position from which it was originally disturbed.

In the region where $R > 2$, the salt-flux relationship

$$\beta_s F_s / \beta_T \dot{Q}_i = 1.85 - 0.85\,R \qquad (2.43)$$

is used. (2.37) is replaced by:

$$\frac{d\sigma}{d\tau} = (1-\theta)^{10/3}(1-\sigma)^{-2}[\Omega - 0.85(1-\sigma)(1-\theta)^{-1}]$$
$$-(1+\theta)^{10/3}(1+\sigma)^{-2}[\Omega - 0.85(1+\sigma)(1+\theta)^{-1}] \qquad (2.44)$$

Where $\Omega = 1.85\ \beta_T\ T\ /\ \beta_S\ S$. The only equilibrium point of (2.36) and (2.44) is $\theta = \sigma = 0$. Testing for stability about this point, gives the characteristic quadratic equation.

$$3\lambda^2 + (25.1 - 12\Omega)\lambda - 13.6 = 0 \qquad (2.45)$$

The roots of the equation are positive and negative, which implies the equilibrium is unstable. The density of the intermediate layer and one of the adjacent layers equalise, the common interface breaks down, and two deep layers remain.

Now consider two deep convecting layers of differing composition and temperature separated by an intermediate layer of thickness dZ. This configuration may be considered unstable when the density gradient of the intermediate layer $d\rho/dZ$ tends to zero. As $\rho = f(T, S)$, we can write:

$$d\rho = \left(\frac{\partial\rho}{\partial S}\right) dS + \left(\frac{\partial\rho}{\partial T}\right) dT \qquad (2.46)$$

dividing each side by ρ gives:

$$\frac{d\rho}{\rho} = \frac{1}{\rho}\left(\frac{\partial\rho}{\partial S}\right) dS + \frac{1}{\rho}\left(\frac{\partial\rho}{\partial T}\right) dT \qquad (2.47)$$

but $\frac{1}{\rho}\left(\frac{\partial\rho}{\partial S}\right) = \beta_S$ and $\frac{-1}{\rho}\left(\frac{\partial\rho}{\partial T}\right) = \beta_T$,

$$\therefore \quad \frac{d\rho}{\rho} = \beta_S\, dS - \beta_T\, dT$$

Hence $$\frac{1}{\rho}\frac{d\rho}{dz} = \beta_S \frac{dS}{dz} - \beta_T \frac{dT}{dz} \qquad (2.48)$$

Mixing occurs when the layer densities equalise,

i.e. $d\rho/dZ = 0$. Using this condition in (2.48) gives:

$$\beta_S \frac{dS}{dZ} = \beta_T \frac{dT}{dZ} \qquad (2.49)$$

The stability or density ratio R is defined as:

$$R = \left(\frac{\beta_s \, \Delta S}{\beta_T \, \Delta T} \right) \tag{2.50}$$

Using this definition in (2.49) gives R = 1 for completely mixed layers.

3.0 EXPERIMENTAL INVESTIGATION

Experimental studies were primarily aimed at investigating the properties of a double-diffusive interface in cryogenic liquid mixtures. A two layered liquid system was considered, in order to simulate the mixing stages in an initially poorly mixed LNG tank. The necessary measurements proposed for the investigation were:

a) Heat and mass fluxes between layers

b) Interface level change and shape

c) Surface evaporation flowrate affected by a) and b)

The following sections describe the fluids and apparatus used in order to measure a), b) and c) above.

3.1 Test Liquids

Ideally, mixtures of liquid hydrocarbons should have been used in the experiments. The proximity of the LNG and its vapour to electrical equipment, however, would have posed a fire hazard. Safer and more convenient cryogens were considered. Liquid nitrogen, air, argon and oxygen were considered good alternatives.

A previous study (28) used liquid Nitrogen (LIN) and liquid argon (LIA) mixtures for LNG simulations. In this case, a pure LIN layer was positioned above a 1% v/v (by volume) LIA in LIN lower layer. LIA was chosen as the solute in LIN because of its relatively higher density: the ratio of densities of LIA to LIN at their respective normal boiling points is about 7/4. Another rather fortunate advantage of using LIA was that very small reflecting particles were observed in the Argon - nitrogen lower layer. These particles, believed to be ice or solid carbon dioxide (CO_2), enabled good flow visualisation. It was assumed that the water vapour and CO_2 originated from the argon gas cylinder used, because no particles were observed in the top LIN layer.

For mass transfer measurements, an accurate method of measuring concentrations of LIA in LIN was required. An initial concentration variation of 0.5 to 1.5% υ/υ Argon in Nitrogen lower layer was envisaged.

A number of methods for measuring the concentration were considered, such as:

a) Chromatography

b) Light absorption method

c) Magnetic suspension densimeter

d) Gravimetric method

e) Mass Spectrometer

f) Liquid dielectric properties

g) Liquid thermal conductivity.

The factors governing the choice of method used were that it should not disturb the liquid, and be sensitive enough to measure 1% concentrations with at least 10% accuracy. The instrument should also allow continuous measurement.

Methods f) and g) were first considered because of their apparent simplicity. The difference in thermal conductivity for LIN and LIA is small. For example, at 80 K, the thermal conductivity K_T for LIN is 1320 $mW\ m^{-1}\ K^{-1}$, and that of LIA 1315 $mW\ m^{-1}\ K^{-1}$. The dielectric properties of the two liquid are also quite similar. The dielectric constant for Argon at - 191°C and Nitrogen at - 203°C are 1.53 and 1.454 respectively. Also, the stray capacity of leads can greatly affect results and could be difficult to eliminate.

Chromatography appeared to be the best of the methods mentioned, because of the wide range of detectors available.

In chromatography, a complex mixture is separated, and the amounts of constituents are measured. The separation process is based upon the distribution of a sample between two phases. One of the phases is a stationary bed of large surface area, and the other phase is a gas which percolates through the stationary bed. The sample constituents are attracted to the stationary phase. Those substances with a greater affinity to the stationary phase take longer to get through than those with less attraction.

Argon is considered to be a very inert gas.

The choice of the stationary phase and phase holder (column) to separate an argon - nitrogen - helium (carrier gas) mixture posed a problem. An alternative solute that came to be considered was Liquid oxygen (LOX).

Oxygen is chemically more active than argon, so any analytical method involving a chemical reaction could be used. Another advantage of LOX is that its density is less than that of LIA, but greater than that of LIN. More LOX would be needed to provide a sufficiently dense bottom layer of liquid. Higher concentrations of solute would therefore be easier to measure.

Oxygen Analysis.

There are a number of methods of oxygen detection, some of these are: gas chromatography, electrical conductivity, electrochemical cells, gas chromatography, heat of reaction, paramagnetic and thermomagnetic analysis. The method used mainly depends on whether the oxygen is in the gas or dissolved state, and on the detection limit required. For this investigation, the LOX and LIN would be evaporated into the gas phase for analysis.

The thermomagnetic and electrochemical type analysers seemed most promising. A schematic diagram of a thermomagnetic analyser is shown in Fig.3.1a). The two heated filaments form part of a wheatstone bridge, one of which is in the region of a magnetic field.

With no oxygen in the sample stream, the gas diffuses equally into each of the filament cavities and the bridge is balanced. Any oxygen in the stream is attracted towards the magnetic field because oxygen is paramagnetic.

However, as the oxygen warms up on approaching the filament, its paramagnetism decreases. This oxygen is then replaced by cooler more magnetic oxygen, and the process is repeated. A convective flow therefore develops which cools the measuring filament and unbalances the bridge. The measurement unit should be encased in a vacuum cell to eliminate outside temperature disturbances. This type of analyser would typically be used in a high sample flowrate application. The flowrate of gas passing through the analyser would have to be small, because only a small amount of the liquid to be analysed could be used.

The construction of a miniature paramagnetic analyser was considered. Fig.3.1b) shows one possible design. With no oxygen in the flow, there is no net flow around the stainless steel tube. Sensors T1 and T2 therefore record the same temperature. When oxygen is present, it is diverted down the magnet-surrounded arm of the stainless steel tube and causes flow around this circuit. T2 therefore exceeds T1 , and the measure of this difference depends on the amount of oxygen present in the flow.

Most commercial gas phase analysers are of the electrochemical type. Because of the wide variety of electrochemical oxygen analysers, ranging from simple hand held devices to microprocessor controlled devices, it was decided to purchase an electrochemical analyser, rather than construct a device. An example of a commercial instrument is shown in Fig.3.2. The oxygen to be measured diffuses through a metallised elastic membrane (which forms the cathode), and dissolves in the electrolyte (in this case Na CL). By applying a voltage between the anode and cathode, an electrochemical process takes place. At the cathode for example, the following reaction takes place;

$$O_2 + 2\,H_2O + 4\,e^- \longrightarrow 4OH^- \qquad (3.1)$$

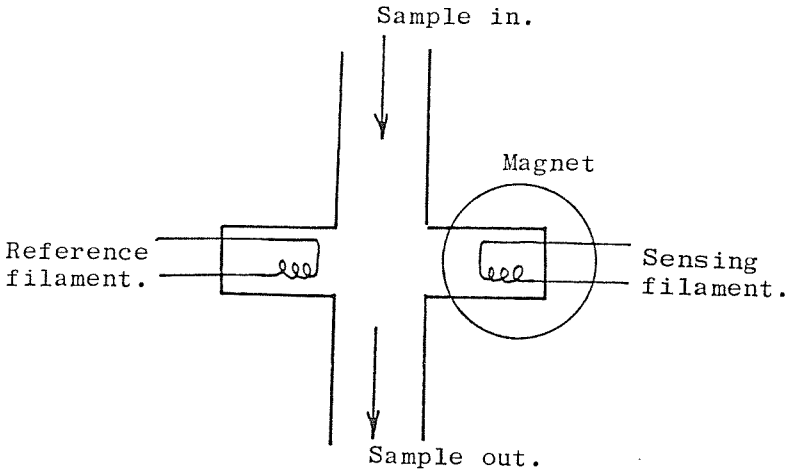

Fig.3.1a). Thermomagnetic oxygen analyser.

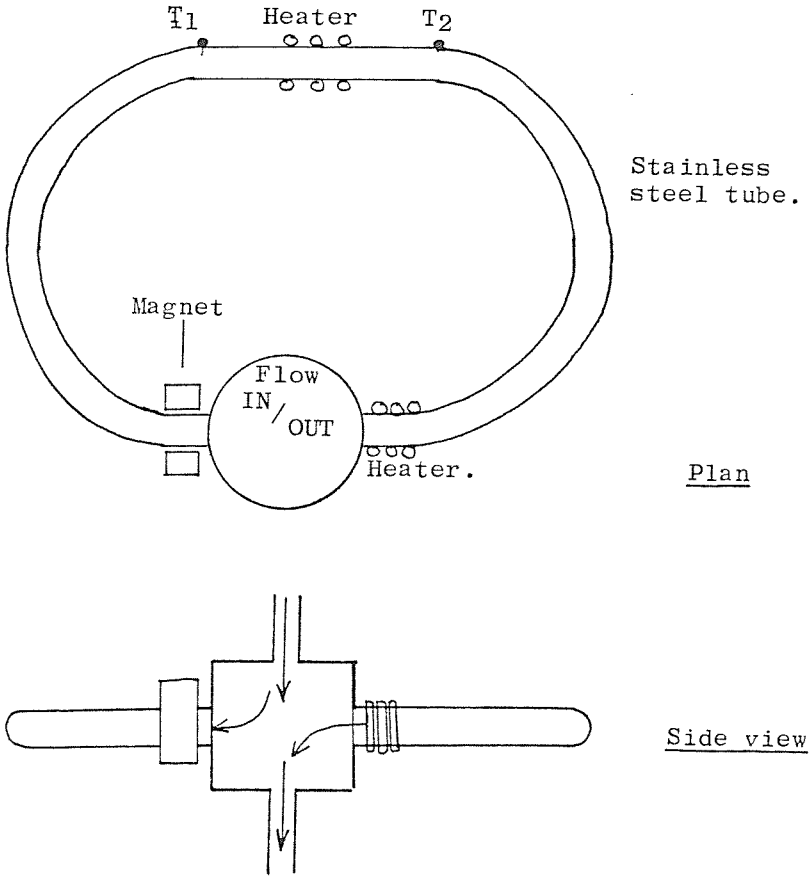

Fig.3.1b). Proposed design of paramagnetic oxygen analyser.

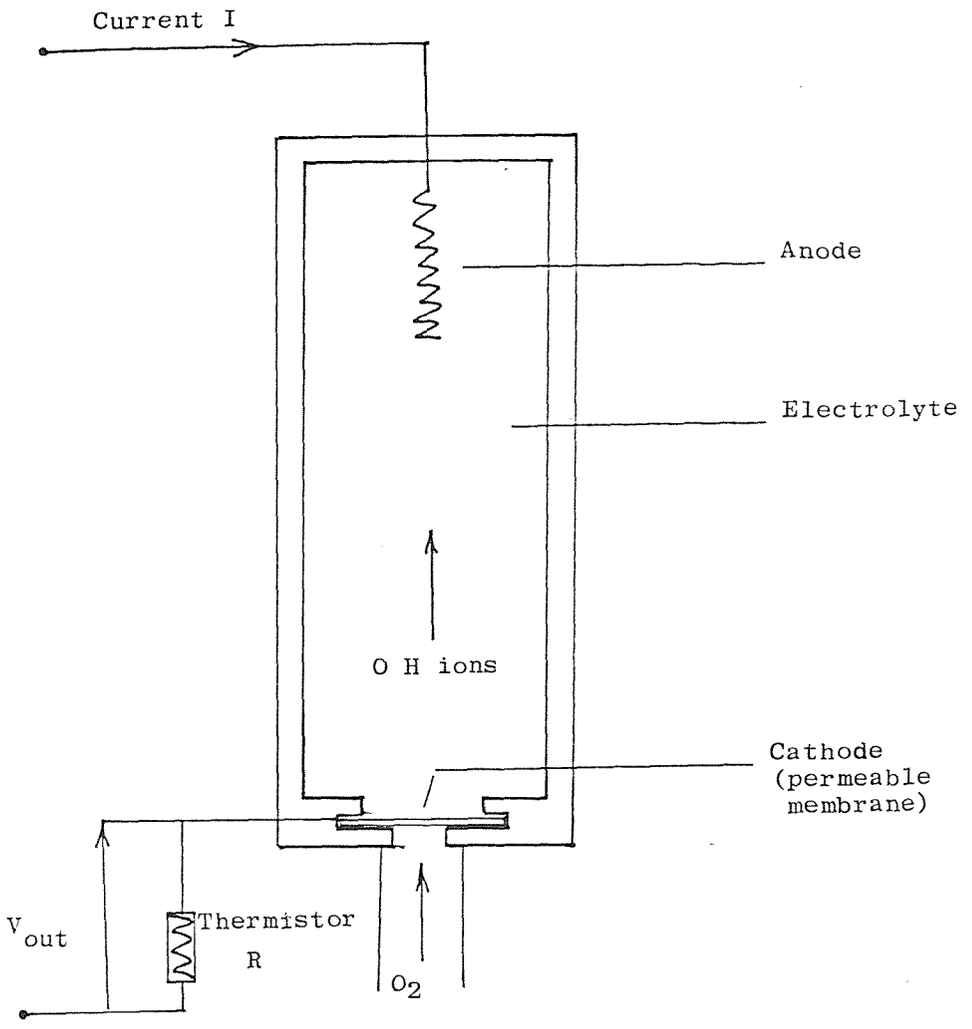

Fig.3.2. Electrochemical oxygen analyser.

The result is a low current between the anode and cathode which is directly proportioned to the oxgygen partial pressure. This therefore gives the oxygen molar concentration under constant pressure conditions.

Because the rate of diffusion of oxygen through the membrane varies by about 3% per ^{o}C, a thermistor is used to automatically adjust the output signal to compensate for temperature changes.

Liquid Mixtures.

Equations for the density and saturation temperature of the LOX - LIN mixtures were required. If the oxygen - nitrogen liquid mixture can be shown to approximate an ideal solution, simple formulae can be used. It can be shown that the partial pressure Pi of the i^{th} component in a multi-component mixture is related to the vapour pressure of the pure component π_i and its liquid concentration x_i by the relationship:

$$P_i = \pi_i \, x_i \qquad (3.2)$$

This is known as Raoult's law, which is valid for all solutions at sufficiently low concentrations. An ideal solution is one in which Raoult's law applies for all concentrations. If the vapour phase is not a perfect gas, a solution can be defined as ideal if the fugacity of component i, f_i, in the vapour mixture is given by:

$$f_i = f_i^{\circ} \, x_i \qquad (3.3)$$

Where Z_i is the liquid concentration of component i, and f_i° is the fugacity of the pure i^{th} component in the same phase and at the same temperature and pressure as the mixture. Lewis and Randall (29) found that:

$$f_i = f_i^{\circ} \, Z_i \qquad (3.4)$$

Where Z_i is the vapour concentration.

Krichevsky and Torocheshnikov (30) showed that mixtures of oxygen and nitrogen and nitrogen and carbon monoxide satisfy (3.3) up to pressures close to the critical point.

Fig. 3.4 shows the fugacity of nitrogen in oxygen-nitrogen mixtures as a function of concentration according to the calculations of Krichevsky and Torocheshnikov.

In an ideal solution, all properties can be calculated from the pure component data. There is no volume change on mixing. The mixture volume Vm is given by:

$$Vm = x_1 V_1 + x_2 V_2 + \ldots\ldots\ldots x_n V_n \qquad (3.5)$$

Where x_n and V_n are the concentration and volume of each component. The excess values of enthalpy, entropy and Gibb's free energy of an ideal solution are also zero.

The density, ρ_m, of an oxygen - nitrogen - mixture can therefore be expressed as:

$$\rho_m = x_{O_2} \rho_{O_2} + x_{N_2} \rho_{N_2} \qquad (3.6)$$

Or simply in terms of the oxygen volume fraction x_{O_2}, and the oxygen and nitrogen density ρ_{O_2} and ρ_{N_2} at a particular temperature:

$$\rho_m = (\rho_{O_2} - \rho_{N_2}) x_{O_2} + \rho_{N_2} \qquad (3.7)$$

Using Raoult's law and assuming an ideal solution, the mole fraction of component 1 in the liquid phase x_1, is given by:

$$x_1 = \frac{P - \pi_2}{\pi_1 - \pi_2} \qquad (3.8)$$

Where P = total pressure of vapour phase

π_1 = Partial pressure of component 1 vapour phase.

π_2 = Partial pressure of component 2 vapour phase.

The mole fraction of component 1 in the vapour phase Z_1, is:

$$Z_1 = \frac{\pi_1 x_1}{P} \qquad (3.9)$$

Using (3.8) and (3.9), the temperature - composition plot for a Nitrogen - oxygen mixture can be obtained. In this investigation, P = 1 atmosphere. Table 3.1 gives the

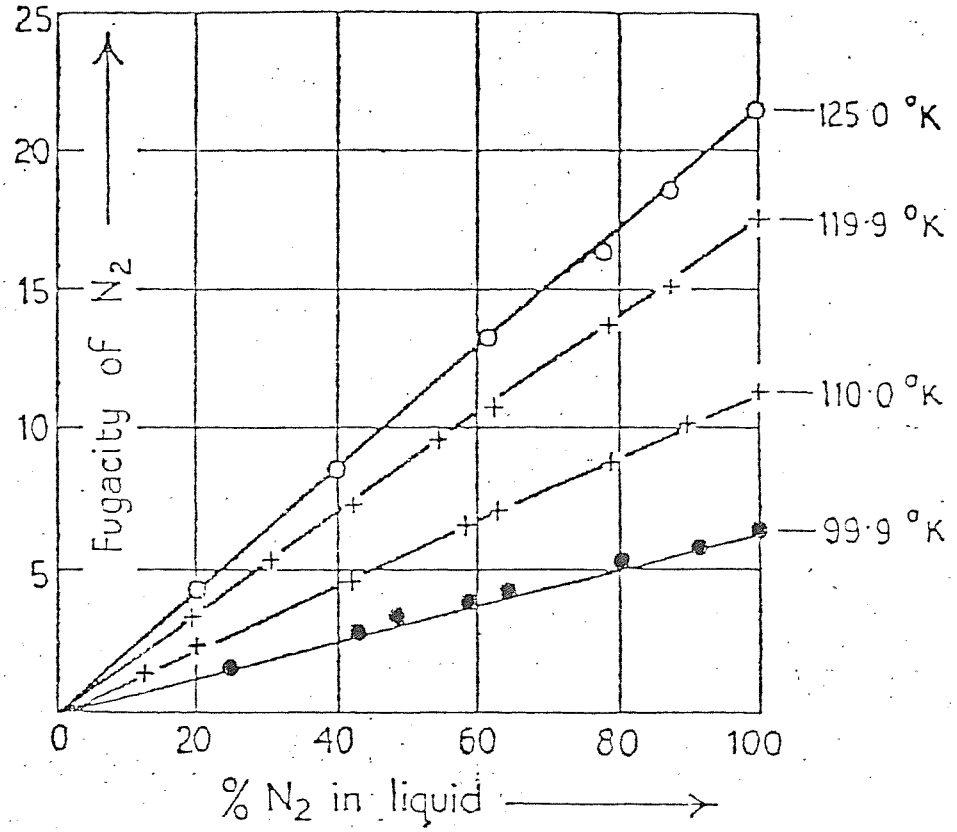

Fig.3.4. Fugacity of nitrogen in oxygen - nitrogen mixtures.

Table 3.1. Oxygen and Nitrogen Partial Pressures.

Temperature K	Oxygen Pressure (atm)	Nitrogen Pressure (atm)
76	0.16685	0.84901
77	0.19387	0.95784
78	0.22431	1.0770
79	0.25848	1.2072
80	0.29671	1.3489
81	0.33933	1.5029

Table 3.2. Liquid and Vapour Compositions derived from Table 3.1.

Temperature K	X_1	Z_1
77.36	0	0
78	0.090	0.020
79	0.218	0.056
80	0.332	0.099
81	0.432	0.147

partial pressures of Oxygen and Nitrogen at various temperatures. From this data, values of α_1, and Z_1, are obtained for a suitable temperature range (Table 3.2). These values are shown plotted in Fig.3.5. The mixture saturation temperatures were not expected to exceed 78.0.K. A linear temperature - composition behaviour was assumed between 77.36 and 78 K. The mixture temperature T_m in Kelvin was therefore taken as:

$$T_m = 7.111\ \alpha_{O_2 L} + 77.36 \qquad (3.10)$$

So for a 2% v/v LOX in LIN mixture, the mixture saturation temperature would be 77.50 K.

3.2 Instrumentation.

The apparatus used in the experiments were all new constructions, except a Schlieren flow visualisation dewar, which was a modification of an earlier design.

Variable Heat Input Glass Dewar.

To allow flow observation during an experimental run, a vacuum insulated glass vessel was constructed. Two semi-transparent metal oxide coatings were formed on the outside of the inner jacket of the dewar, to serve as electrical heaters. The thin metallic coatings were applied by heating the glass to 600°C and then a metal solution was sprayed onto the hot glass surface. The toxic solution used was made up as follows:

First mixture:	86 gm. Antimony Tetrachloride + 10 ml alcohol.
Second mixture:	13 ml Stannic Chloride + 30 ml alcohol.

2.5 ml of the first mixture was added to the second mixture. This mixture was then topped up with alcohol to bring the total volume up to 50 ml. The dewar was prepared by Hampshire (R + D) Glassware ltd.

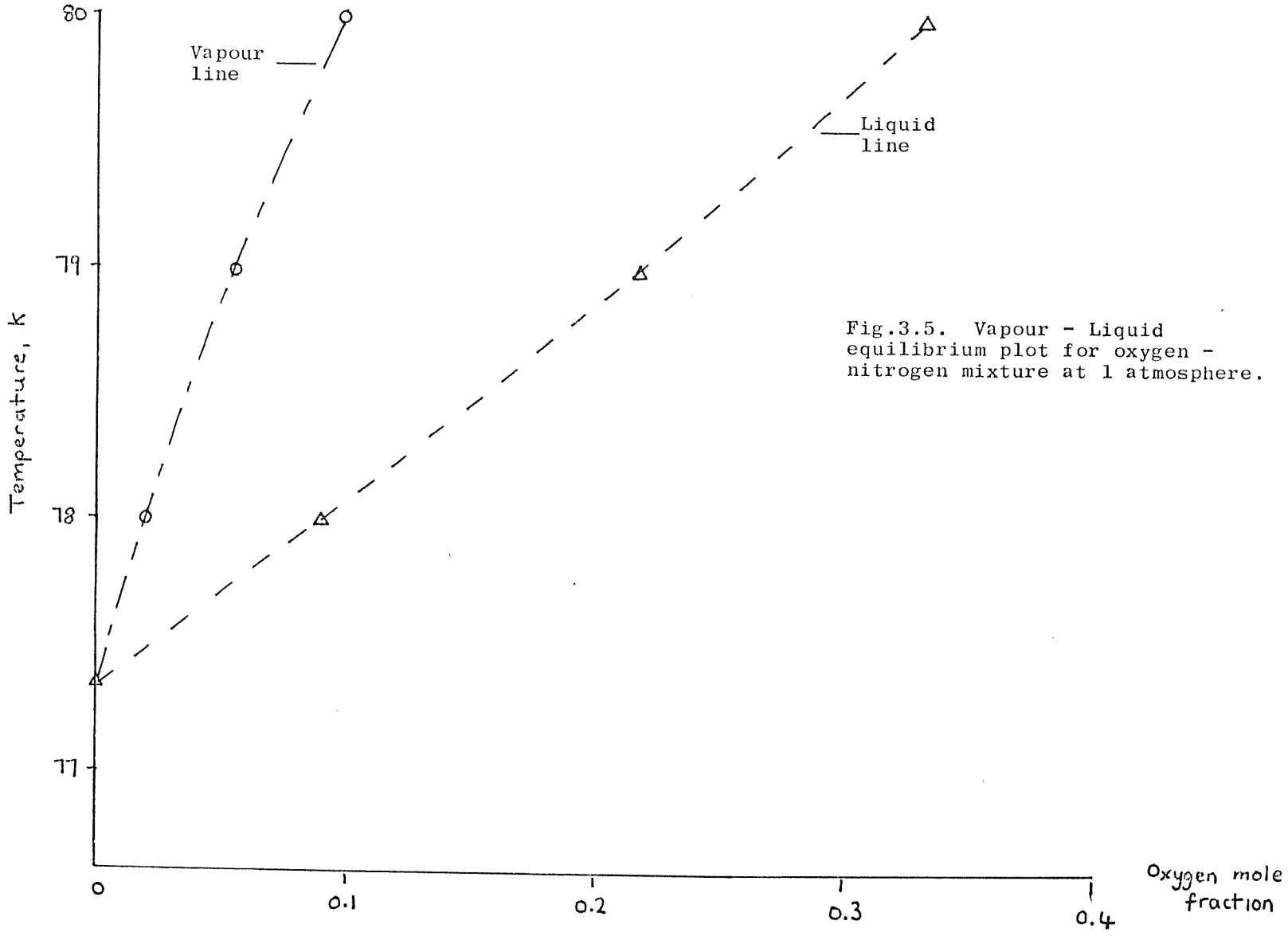

Fig.3.5. Vapour - Liquid equilibrium plot for oxygen - nitrogen mixture at 1 atmosphere.

On the first jacket sprayed, the surface resistance of the coating was found to be uneven: local hot spots existed. The solution was to increase the resistance of low resistance areas by decreasing the thickness of the oxide film. This was achieved by rubbing the surface with a diamond compound abrasive grease. The coating, having been fused into the glass surface, was difficult to remove.

An even resistance profile could not be achieved. A second inner jacket was sprayed, but this too had an uneven resistance profile on each heater. After modifying the coating spraying procedure, a third inner jacket was produced, with a fairly even resistance on each heater. Fig. 3.6. shows the circumferential heat distribution of each heater for the given voltage inputs. Both heaters show vertical gradients in temperature. The horizontal distribution is more even, so all fluid at a particular level receives the same amount of heat. In dynamic terms, the gain in fluid momentum is the same for all sections of each heater.

Providing a suitable connection between the oxide coating and the heater supply wires proved to be a problem. For heating purposes, two thin conducting strips, diametrically opposed, and running down the length of each heater, were required. A silver-based electrically conductive paint was tested. Thin strips were painted onto a glass sample and baked at 150^{o}C for 30 minutes to improve the electrical and mechanical properties of the paint. The paint withstood several immersions in LIN without peeling off.

A reliable connection between the supply wires and conducting strips was also required. Various test configurations of thin copper strips were attached to the oxide coating by the conductive paint. The bonds were, however, too weak at LIN temperatures. A more reliable method was a pressure contact between the strip and a metal spring (phospher - bronze). Thermal contraction could therefore be accommodated. The spring contact was initially secured to the glass with silicone rubber. With four of

Fig.3.6 Transparent heater temperature profiles in degrees centigrade.

Top heater - H 1 Voltage 28 Volts
Resistance 67 Ω

Ambient temperature 27°C.

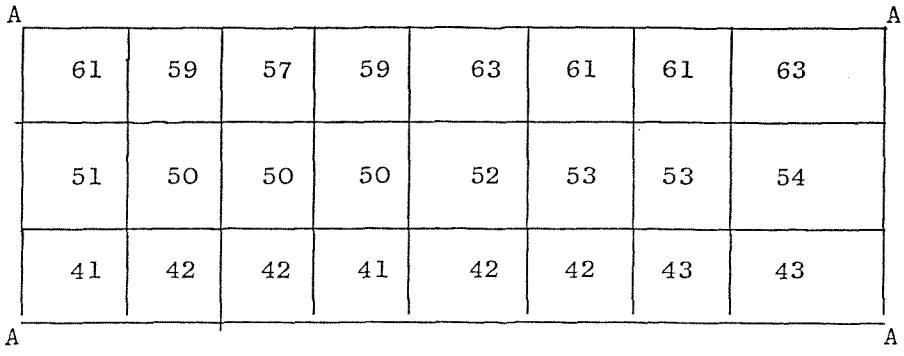

Bottom heater - H 2 Voltage 30 Volts
Resistance 81 Ω

Ambient temperature 26°C.

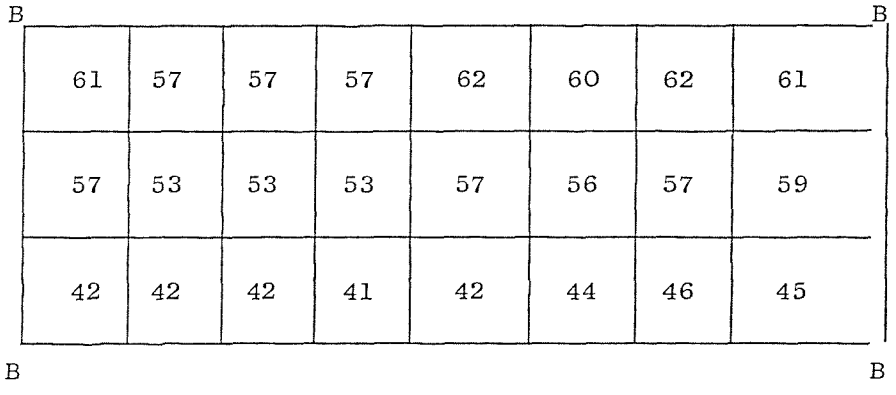

these spring contacts attached to the dewar, a test at LIN temperatures was carried out. Three of the pressure contacts broke off due to the cracking of the silicon rubber restraint which was under tension.

Finally, glass bridges were used to hold down the pressure contacts. Fig.3.7 shows a photograph of the heating section of the experimental dewar. The conductive strips are bright - platinum coatings, painted on, and baked at 500°C. The heating sections are 90 mm long. Spaced 70 mm apart. The dewar inner diameter is 65 mm.

Temperature and Concentration Measurements.

The temperature profiles of the fluid mixtures were measured using copper - constantan thermocouples. Fourteen copper junctions were attached at intervals along a constantan wire held vertical by the weight of a small stainless steel ballbearing. The wires used were 0.122 mm. diameter approved thermocouple wires (BSS 1844). The copper-constantan reference junction was maintained at 0°C by a constant temperature reference instrument (Zeref). The emf's of the thermocouples were measured using a Solartron Digital Volt Meter (DVM) and a data logging system. Fig.3.8 shows the thermocouple arrangement with the mixture concentration analysis apparatus. The surrounding LIN both reduced the heat inleak into the experimental dewar.

All the pipework and tubing to the oxygen analyser sensor head was made as small as possible. This reduced the effect of mixtures extracted at different times mixing together, and also improved the time response of the system. Tests on the vapourising unit showed that a steady vapour pumping rate of 60 cm^{-3} min^{-1} could be maintained by careful manipulation of the needle valve. This vapour flowrate corresponds to the extraction of 5 mm depth of liquid in three hours. The oxygen analysing system used was an Orbisphere Model 27153 Oxygen Detector. The instrument is of the electrochemical type described earlier, with a gold plated cathode in contact with the membrane via a thin film of the electrolyte (potassium hydroxide) used in

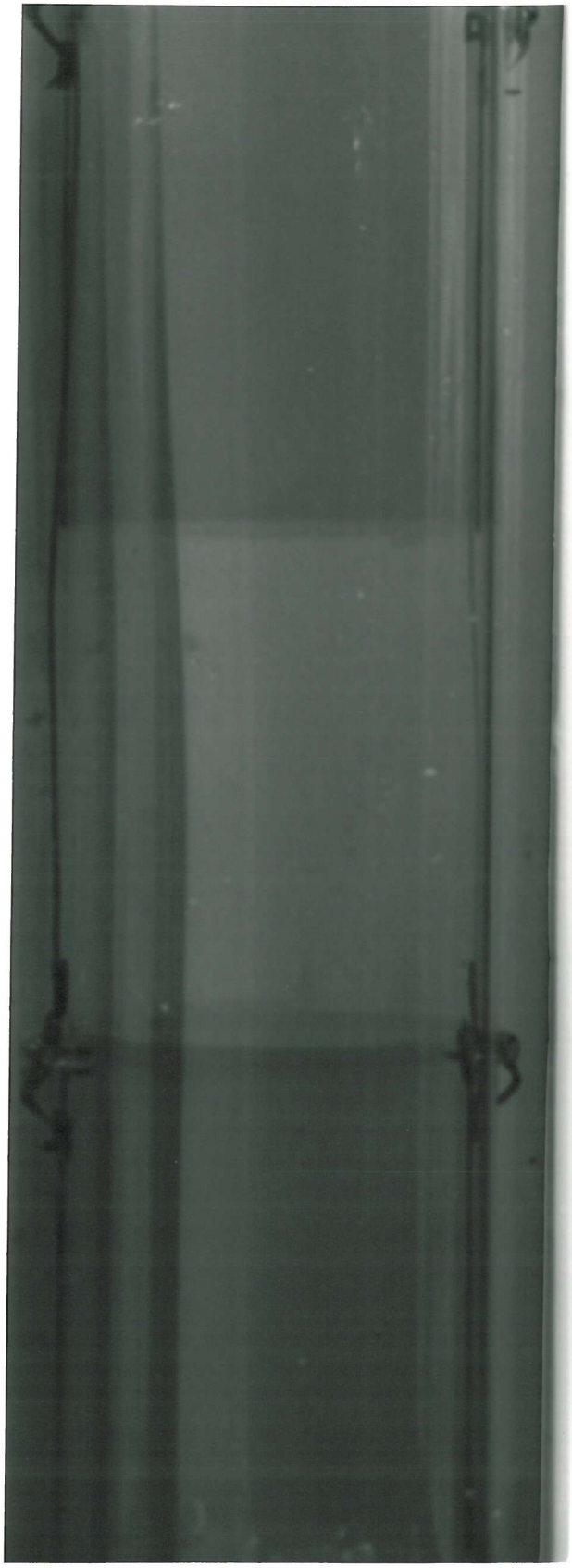

Fig. 3.7 Photograph showing metal oxide heating sections of visualisation dewar.

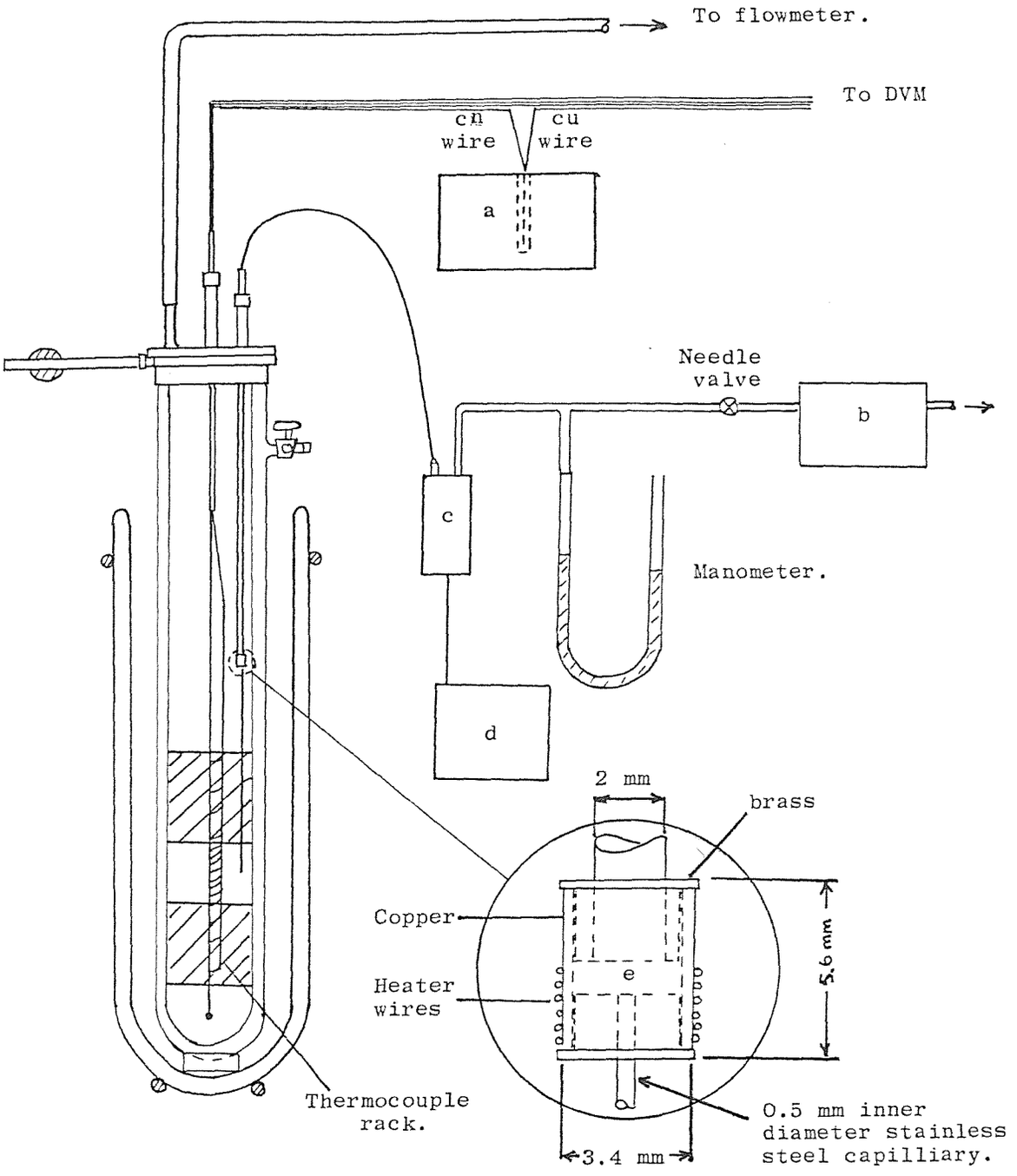

Fig.3.8. Temperature and oxygen concentration measurement apparatus: a: constant temperature source, b: rotary pump, c: oxygen analyser sensor head, d: oxygen analyser meter display, e: mixture vapourising chamber.

the sensor. The instrument has three measuring ranges, 0 - 1.999, 0 - 19.99 and 0 - 199.9 KPa partial pressure of oxygen. Calibration of the sensor was performed by exposing the sensor head to air saturated with water vapour. By adjusting the meter indication via the gain control, the instrument was calibrated to a known oxygen partial pressure (0.2 atmospheres).

Concentration profiles of the liquid mixtures were obtained by moving the mixture extraction line. Moving the stainless steel line caused the vapour flowrate to sometimes change dramatically, but it would steady after about twenty seconds. The flowrates were measured with a Schell MKS model 259 flowmeter, with a range of 0 to 500 standard cubic centimetres (SCCM). After zeroing, the meter provides a 0 - 5 V d.c. output corresponding to 0 - 100% of the meter range, the calibration factor for oxygen and nitrogen is one, so voltages read were multiplied by a hundred to give direct readings in SCCM.

Schlieren Flow Visualisation Dewar.

The Schlieren method was used to observe the flow at the liquid - liquid, and liquid - vapour interface of two and single layer liquid mixtures. This optical method makes use of the refractive index variations in the fluid. These variations are caused by density changes which occur as a result of temperature or concentration gradients across the liquid surface. A diagram of a dewar used for this purpose is shown in Fig. 3.9. Parallel white light passing down through the fluid is reflected back up the vessel by the stainless steel mirror. Fig.3.10 shows the optical arrangement. The light reflected through the liquid is focused on a knife edge, so that any light deflected by the fluid doesn't go through the knife edge slot, and therefore creates a dark region in the final image.

To reduce the heat leak down the stainless steel neck, the Schlieren dewar was modified as shown in Fig.3.11. The copper flange was hard soldered to the stainless steel tube. A leak-tight seal between the copper vacuum can and

Fig. 3.9. Dewar used for Schlieren visualisation.

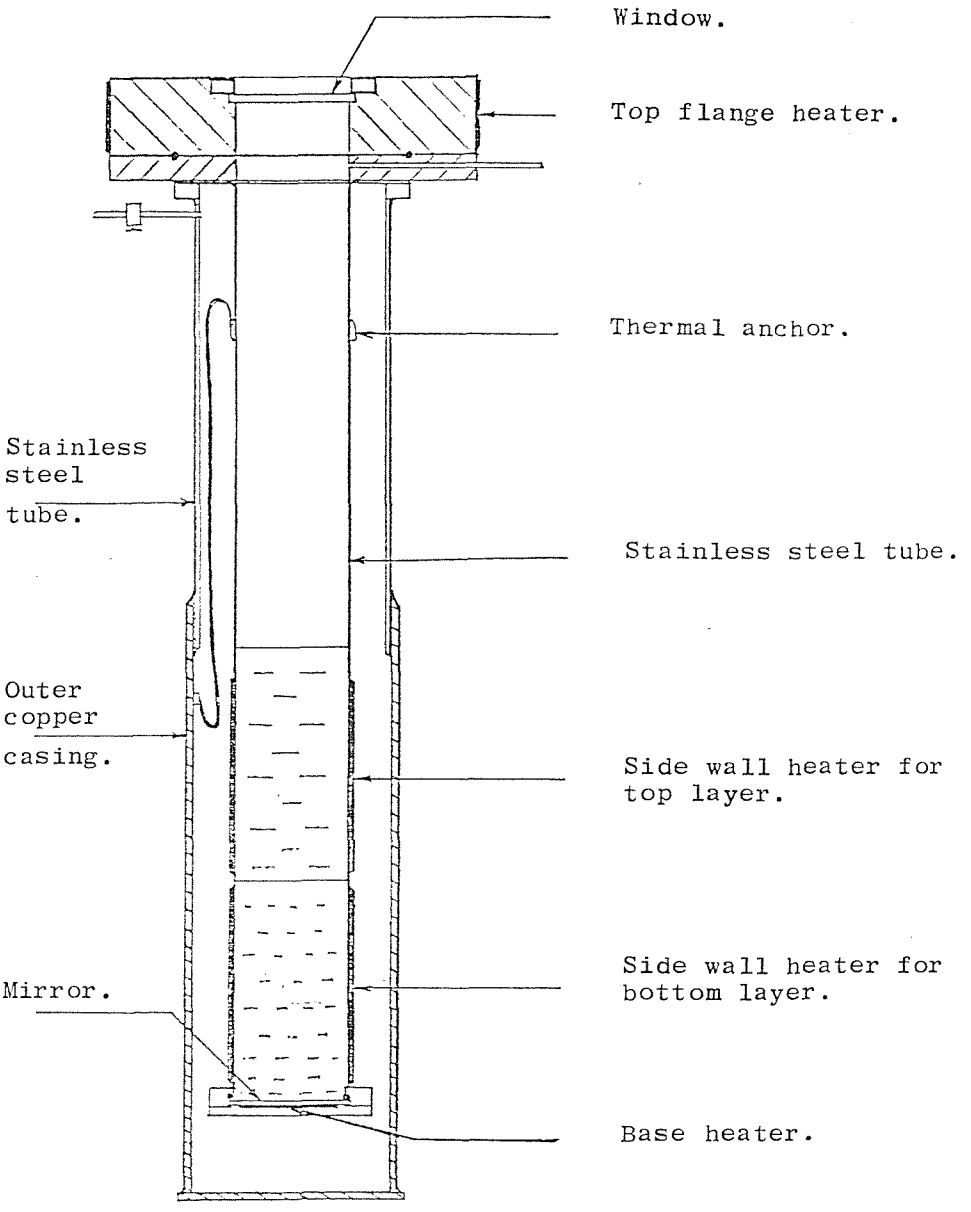

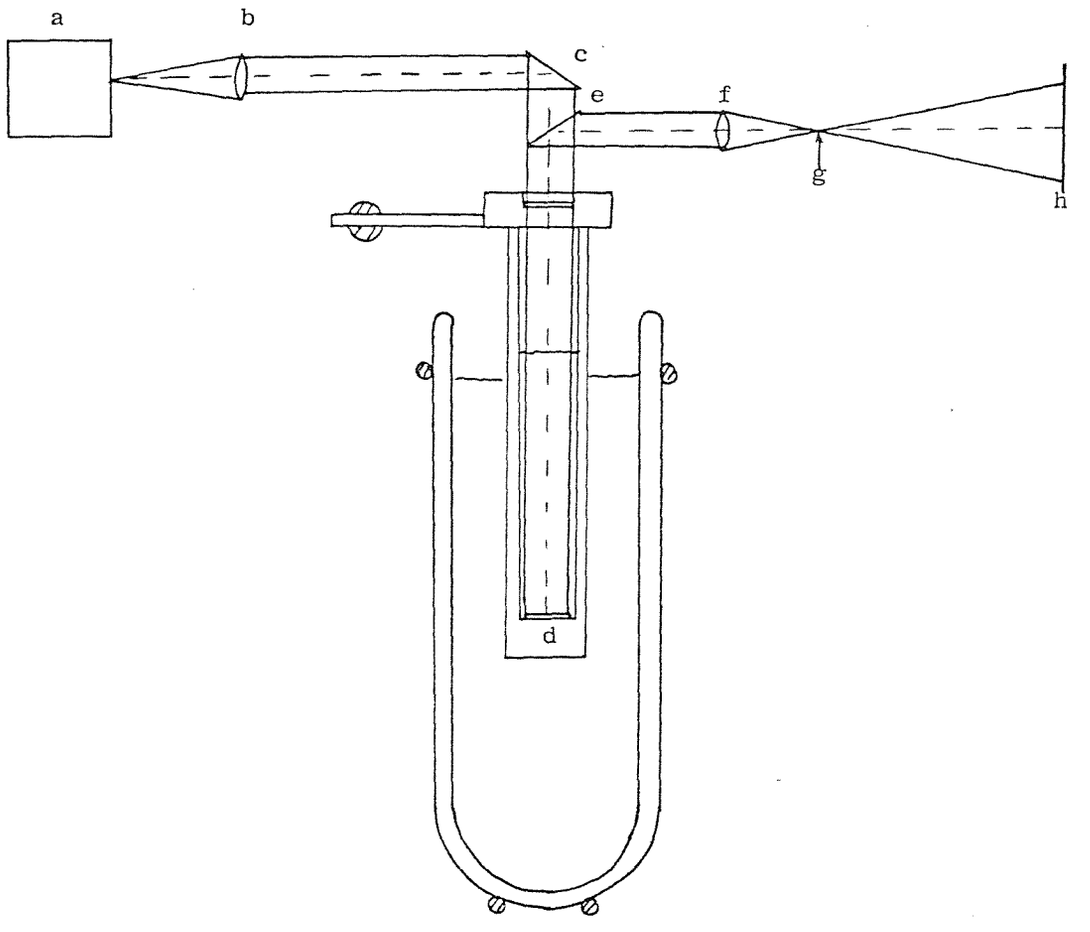

Fig.3.10. Schlieren visualisation optics.
a: light source, b: lens, c: reflecting mirror, d: mirror,
e: semi-reflecting mirror, f: lens, g: knife edge,
h: screen or camera.

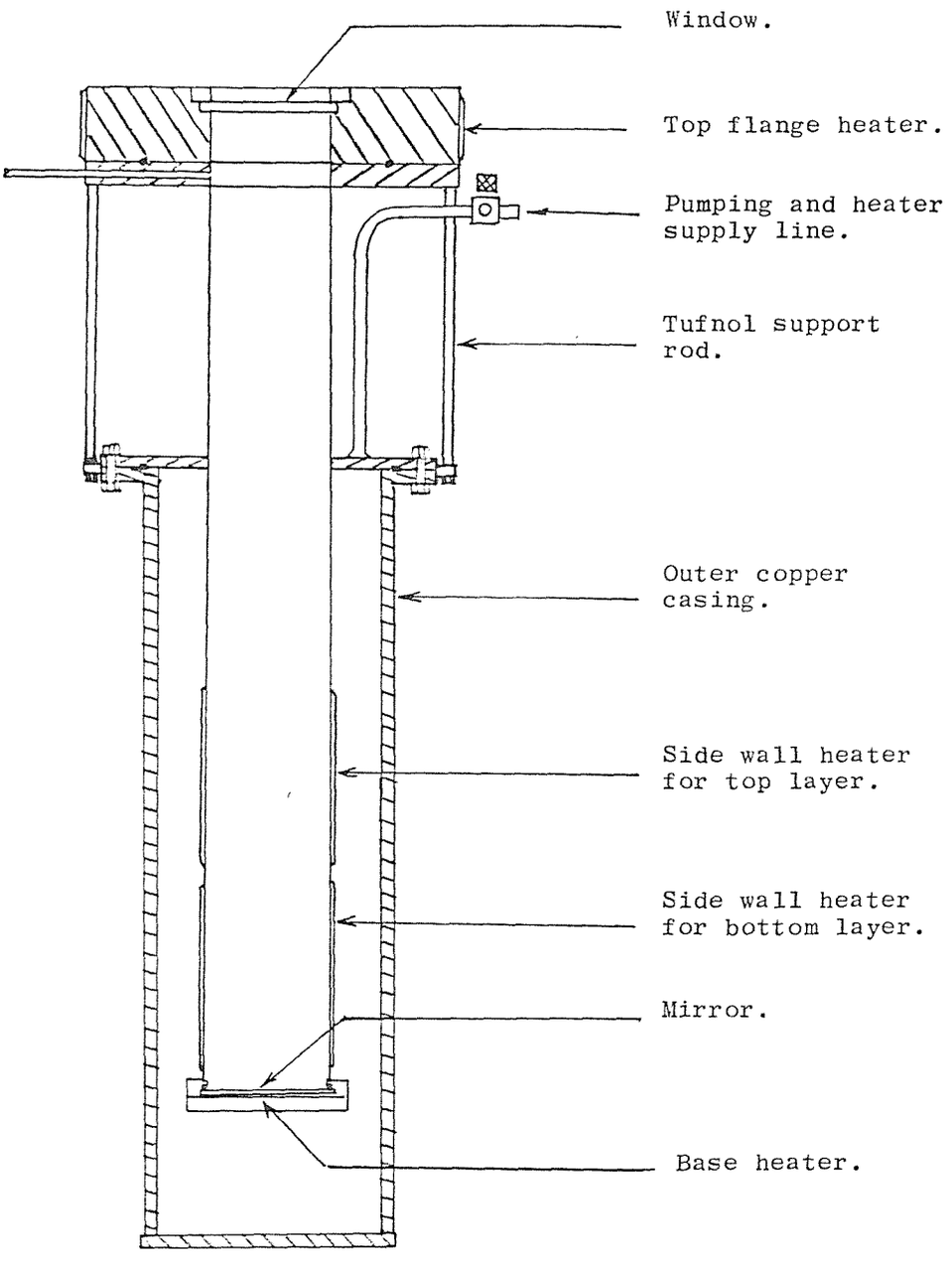

Fig.3.11. Modified Schlieren Dewar.

Fig. 3.12.

Formation of liquid layers.

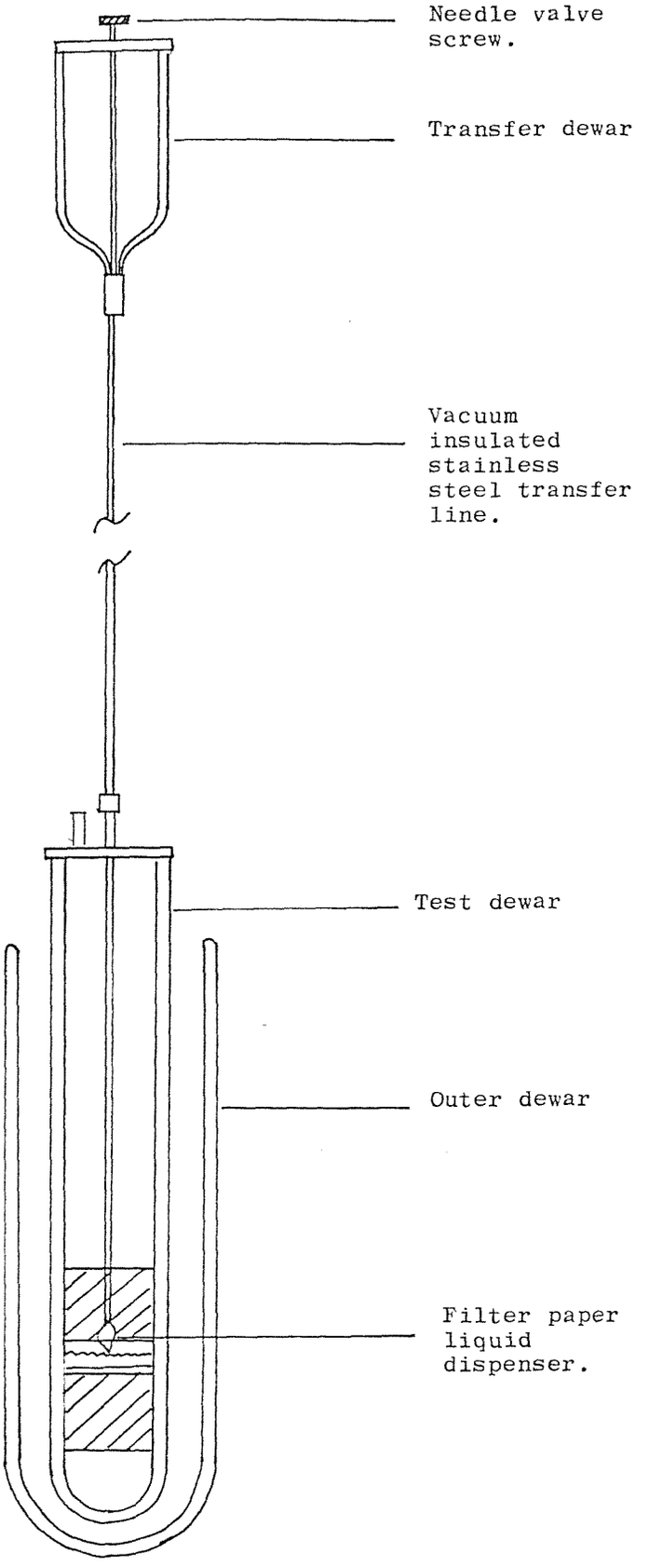

the flange was made using an indium o-ring seal. Most of the heat travelling down the neck enters the copper flange and vacuum can, which is in contact with a surrounding LIN bath.

3.3 Experimental Procedure.

A two layered column of liquid was formed in the experimental dewar using the liquid dispensing system shown in Fig. 3.12. The bottom layer fluid was initially filtered into the transfer dewar. The inner volume of the experimental dewar was then pumped, and the needle valve in the transfer dewar opened to allow flow of liquid into the test dewar. The outer dewar was then filled with LIN.

When the correct liquid level had been met, the needle valve was closed and the pumping stopped. The pumping of the dewar space served two purposes. Firstly, pumping the vapour space subcooled the bottom layer liquid, thereby reducing the chances of it mixing in the top layer. Secondly, the pumping produced a faster flow of fluid down the transfer line. A rubber bladder was inserted between the pump and the pumping line to indicate the pressure in the dewar. When a very clear particle-free bottom layer was required, time was allowed for the bladder to reach atmospheric pressure.

The top layer fluid was now filtered into the transfer dewar. With the test dewar open to the atmosphere, the top layer was slowly trickled onto the bottom layer.

The LIN used in the experiments was obtained from laboratory dewars. The oxygen concentration of the LIN in a dewar was measured. In a dewar filled one hour before from the liquefier, the concentration amounted to 0.6% oxygen in nitrogen. The LOX was produced by liquefying oxygen from a gas cylinder. The oxygen purity of the gas cylinders was 99.5%. This purity of gas is known to contain at least 0.3% argon.

Having formed the layers, the bottom layer was then heated to bring its temperature up to that of the top layer. When the temperatures of each layer were equal, heating was stopped. After 30 minutes, a stable concentration profile was obtained. For a selected heat input to the top and bottom layers, the temperature concentration and flowrate data were recorded at 2 minute intervals. After the layers had mixed, and the flowrate had settled, the superheat in the now mixed liquid was removed by placing a metal rod in the liquid. The metal rod was then inserted again to boil the liquid. The temperature and concentration of the liquid were measured. For this particular oxygen concentration, equation (3.10) was used to calculate the corresponding saturation temperature. This temperature, together with the measured thermocouple emfs of the rapidly boiling liquid, served as a temperature reference for the thermocouple emfs recorded in the experiment.

4.0 EXPERIMENTAL RESULTS

Rollover simulations were performed using LIN (Liquid nitrogen) and LOX (Liquid oxygen) mixtures in the experimental vessel described in Section 3.2. The two variables changed were the initial concentration difference between layers, and the heat input to each layer. Schlieren flow visualisation experiments were performed to observe the convective processes occurring at the liquid-vapour interface of a LIN pool. The uncertainty of the measurements and derived results are discussed in Section 4.6.

4.1 Rollover Experiment Results.

The top layer initial oxygen concentration in all tests was approximately 1% v/v (by volume). Table 4.1 shows the initial layer concentration and density differences for the set of rollover experiments shown in Figs. 4.1 to 4.13. The temperature and composition plots shown correspond to the mean values recorded in each layer. These were obtained from detailed vertical temperature and composition profiles, that are shown in Appendix B. Only five or six profile histories for each experiment are shown for clarity of presentation. The displays, however, show the general behaviour from the start of heating (0 minutes), to when both layers are mixed. The rollover summaries also show the mean evaporation flowrate produced during experiments, and the equilibrium flowrate, $\dot{V}_e$ calculated using the total heat input to the liquid. All the composition plots refer to oxygen vapour concentrations measured at the oxygen analyser sensor head. The heating conditions are shown in the small vessel diagrams beside each plot.

Liquid temperatures were calculated from the emf of the copper-constantan thermocouples, assuming a thermocouple sensitivity of 16 μ Volts per degree temperature change between 75 K and 80 K (BS 4937: Part 5: 1974).

After obtaining an even temperature distribution throughout the two layers, a static (i.e. no heating) concentration profile was obtained to assess the depth of

Table 4.1 Rollover Experiment Initial Conditions.

Experiment	Initial layer concentration difference, % LOX ω/ω	Initial layer density difference $Kg\,m^{-3}$
a 1	0.53	2.1
a 2	0.52	2.0
a 3	0.61	2.4
a 4	0.70	2.8
a 5	0.67	2.6
a 6	0.59	2.3
b 1	2.37	8.4
b 2	2.53	9.6
b 3	2.92	11.5
b 4	2.23	7.9
c 1	5.97	23
c 2	4.89	19
d 1	7.89	31

Fig.4.1. Rollover Summary. Run a 1.

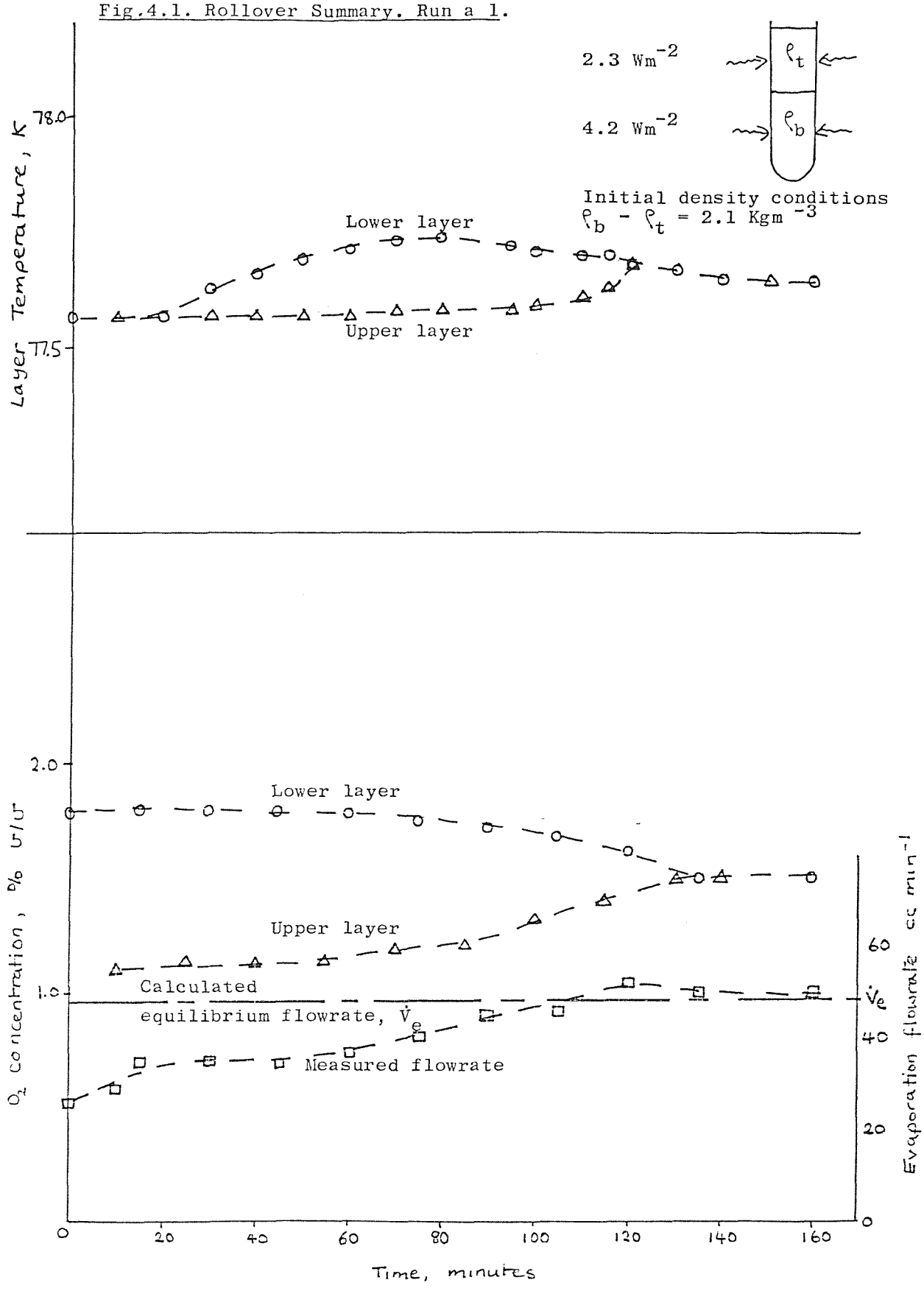

Fig.4.2. Run a 2

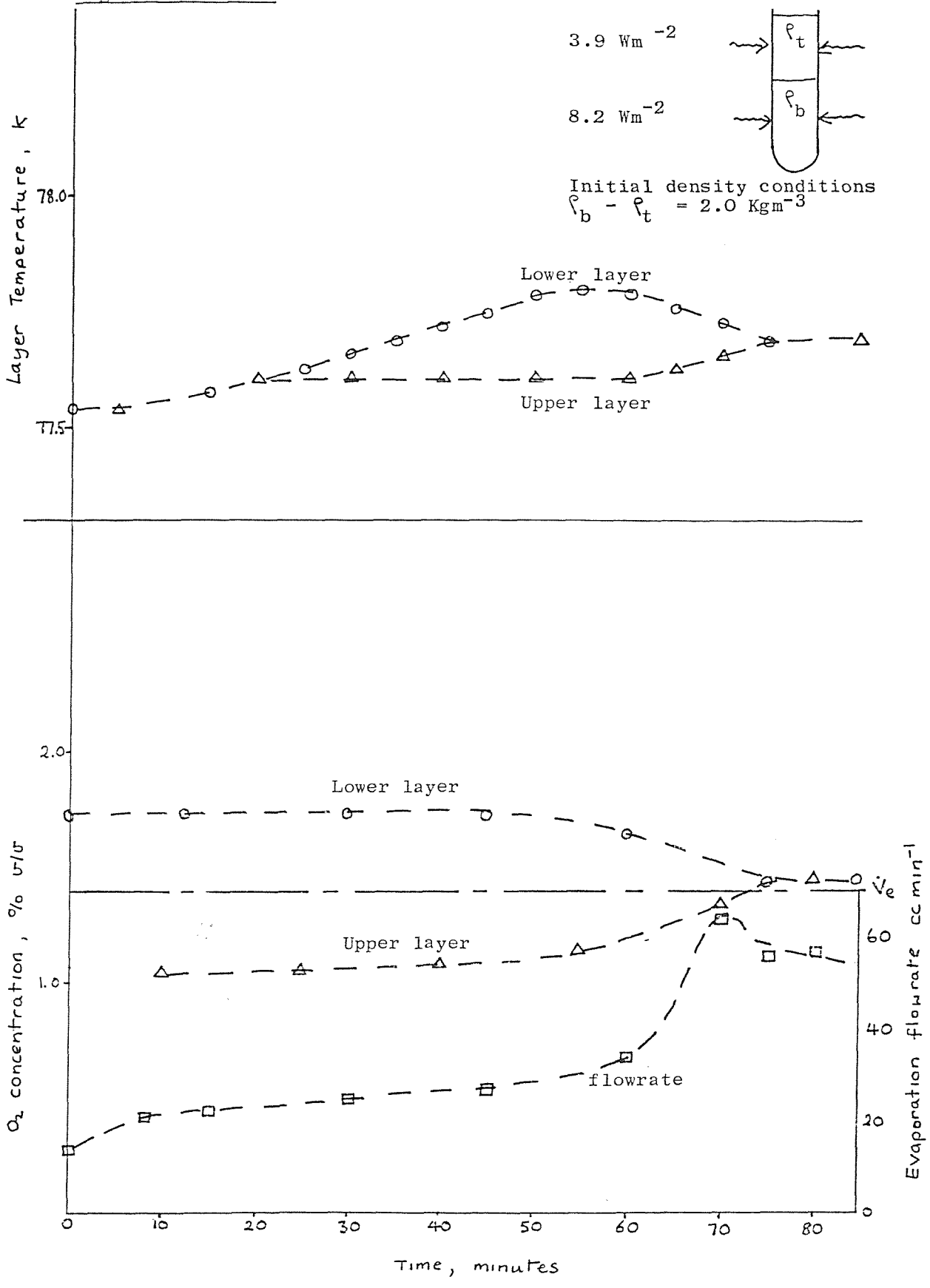
3.9 Wm -2
8.2 Wm-2
ρt
ρb
Initial density conditions
ρb - ρt = 2.0 Kgm-3
Layer Temperature, K
78.0
77.5
Lower layer
Upper layer
2.0
1.0
O2 concentration, % v/v
Lower layer
Upper layer
flowrate
V̇e
60
40
20
0
Evaporation flowrate cc min-1
0
10
20
30
40
50
60
70
80
Time, minutes

Fig.4.3. Run a 3

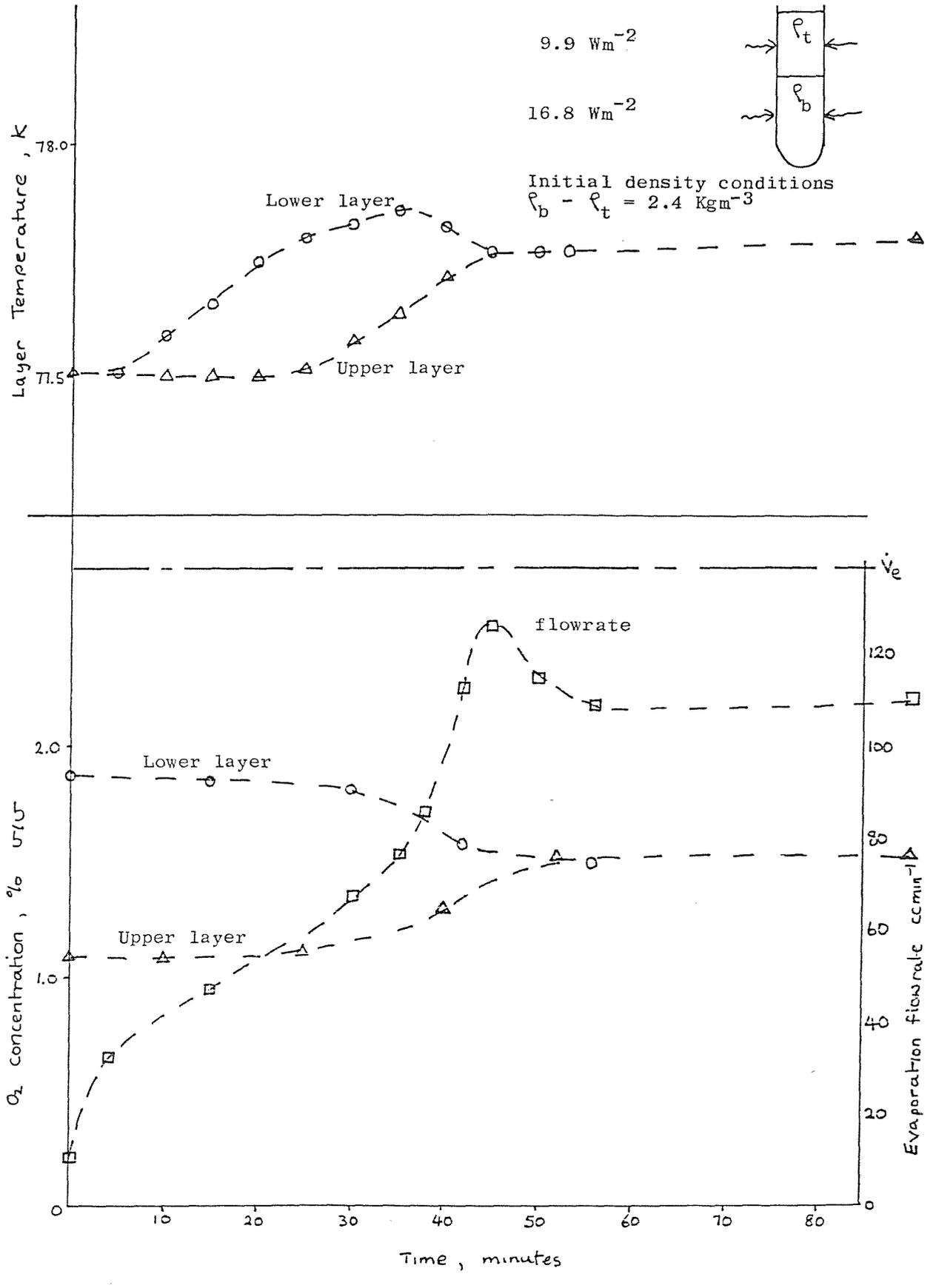
9.9 Wm^{-2}
16.8 Wm^{-2}
ρ_t
ρ_b
Initial density conditions
$\rho_b - \rho_t$ = 2.4 Kgm^{-3}
Layer Temperature, K
78.0
77.5
Lower layer
Upper layer
$\dot{V}_e$
flowrate
120
100
80
60
40
20
0
2.0
1.0
0
Lower layer
Upper layer
O_2 concentration, % v/v
Evaporation flowrate ccmin^{-1}
10
20
30
40
50
60
70
80
Time, minutes

Fig.4.4. Run a 4.

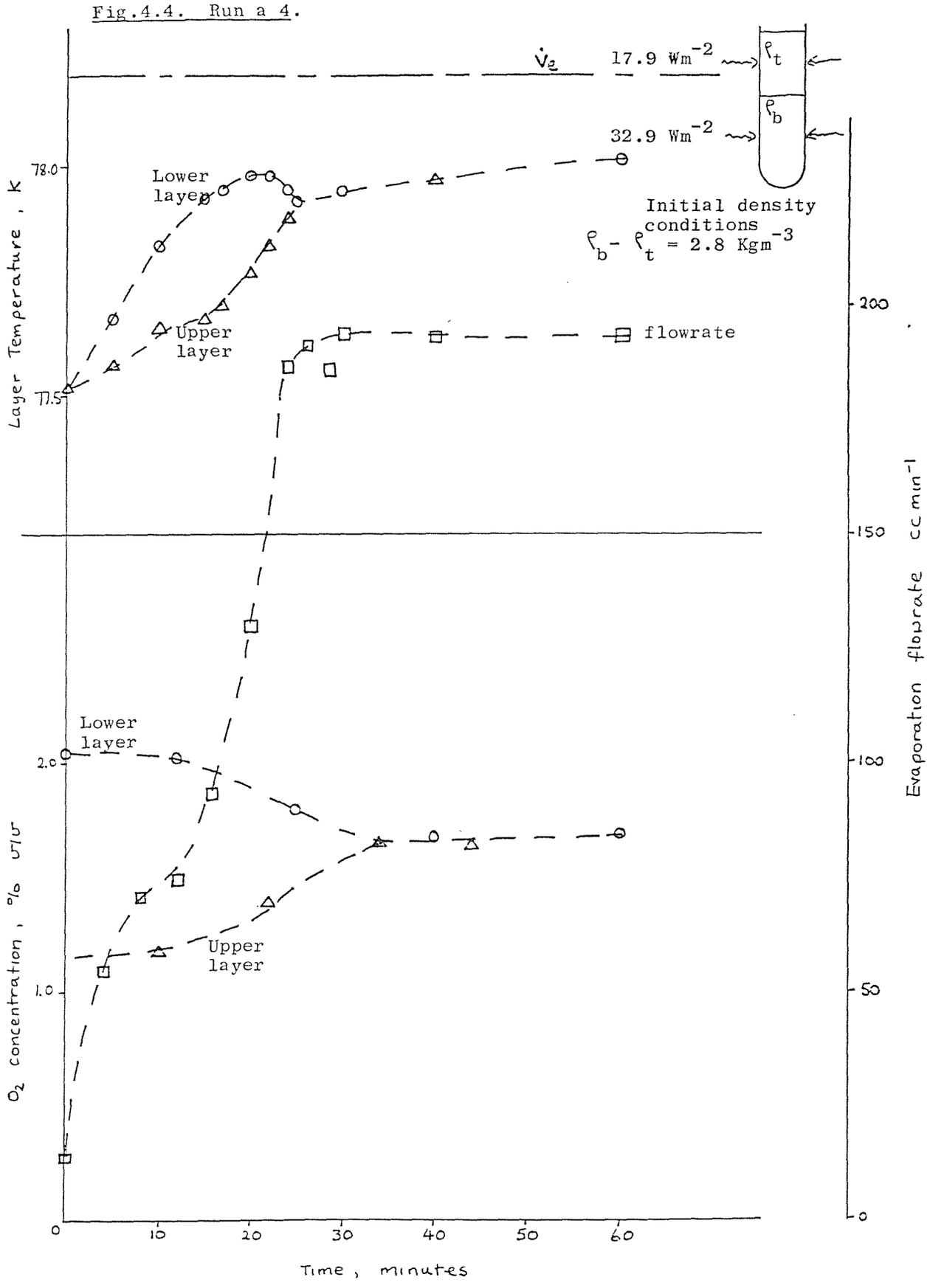
$\dot{V}_2$
17.9 Wm^{-2}
32.9 Wm^{-2}
ρ_t
ρ_b
Initial density conditions
$\rho_b - \rho_t$ = 2.8 Kgm^{-3}
Lower layer
Upper layer
flowrate
Layer Temperature, K
78.0
77.5
200
150
100
50
0
Evaporation flowrate cc min^{-1}
Lower layer
Upper layer
O_2 concentration, % v/v
2.0
1.0
0
10
20
30
40
50
60
Time, minutes

Fig.4.5. Run a 5.

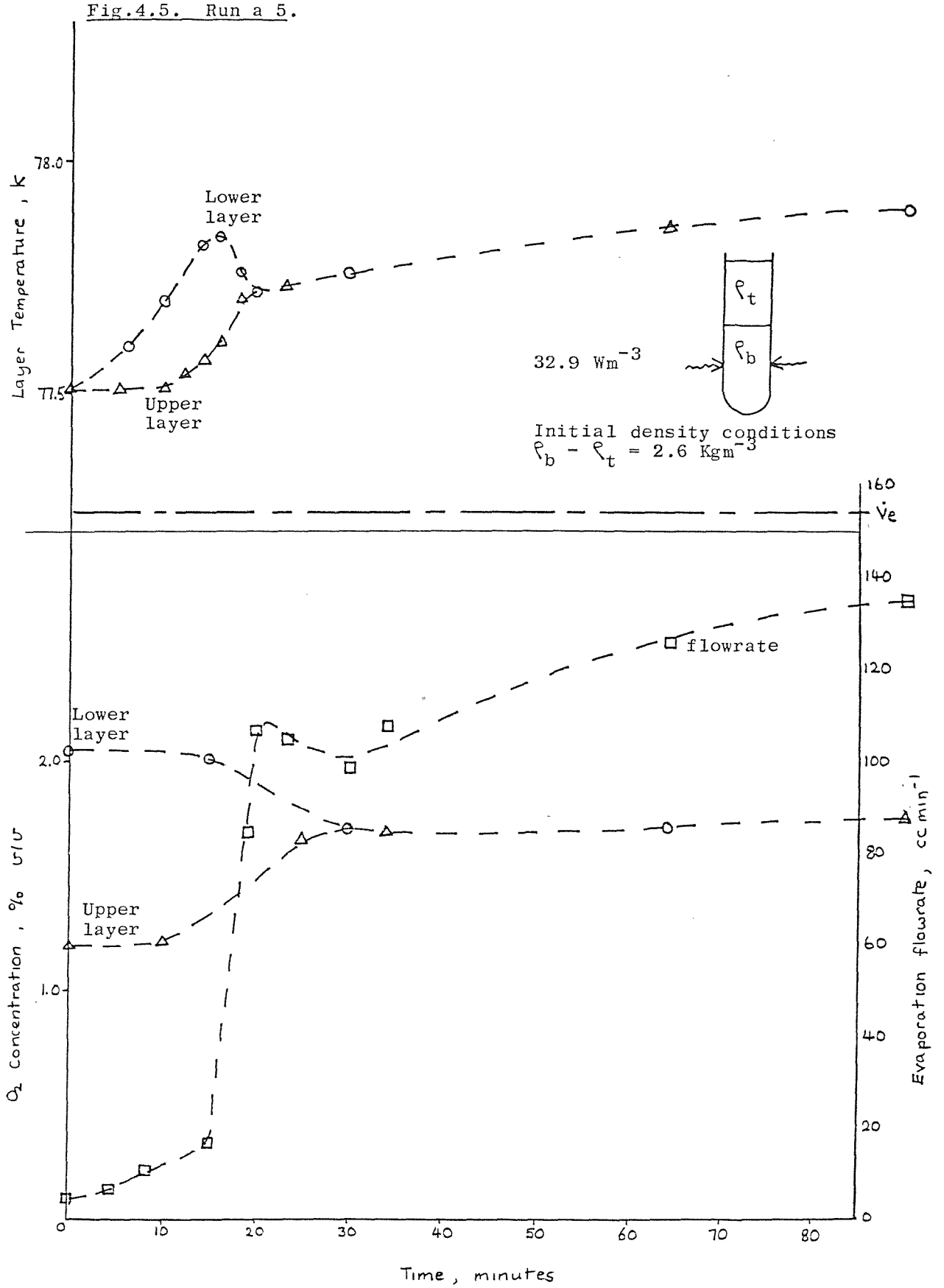
Layer Temperature , K
78.0
77.5
Lower layer
Upper layer
32.9 Wm^{-3}
ρ_t
ρ_b
Initial density conditions
$\rho_b - \rho_t$ = 2.6 Kgm^{-3}
160
$\dot{V}_e$
140
120
100
80
60
40
20
0
flowrate
Lower layer
Upper layer
2.0
1.0
O_2 Concentration , % v/v
Evaporation flowrate, cc min^{-1}
0
10
20
30
40
50
60
70
80
Time , minutes

Fig. 4.6. Run a 6.

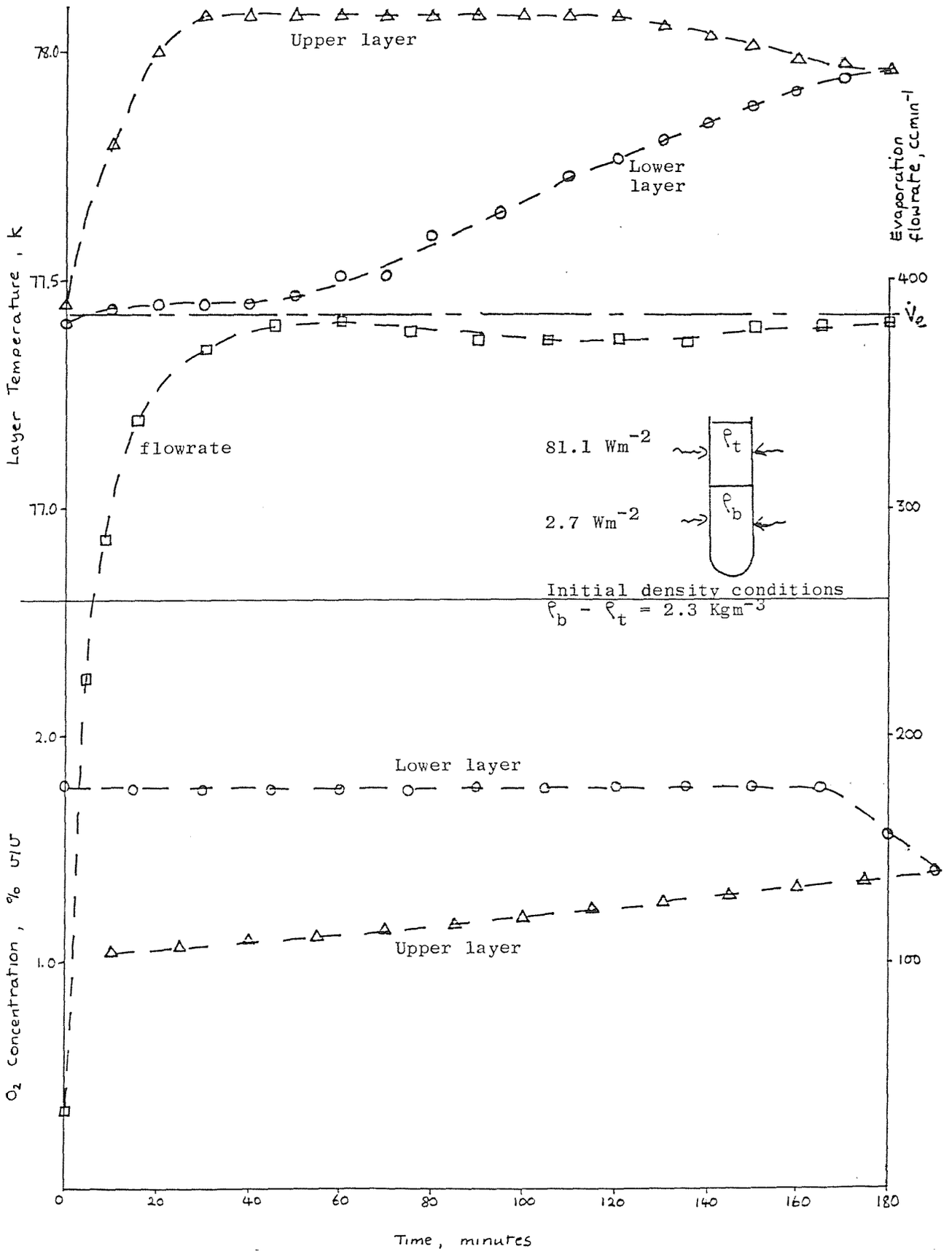
Upper layer
Lower layer
flowrate
Layer Temperature, K
78.0
77.5
77.0
Evaporation flowrate, ccmin⁻¹
400
300
200
100
$\dot{V}_e$
81.1 Wm⁻²
2.7 Wm⁻²
ρ_t
ρ_b
Initial density conditions
$\rho_b - \rho_t = 2.3$ Kgm⁻³
Lower layer
Upper layer
O₂ Concentration, % v/v
2.0
1.0
0
20
40
60
80
100
120
140
160
180
Time, minutes

Fig. 4.7. Run b 1.

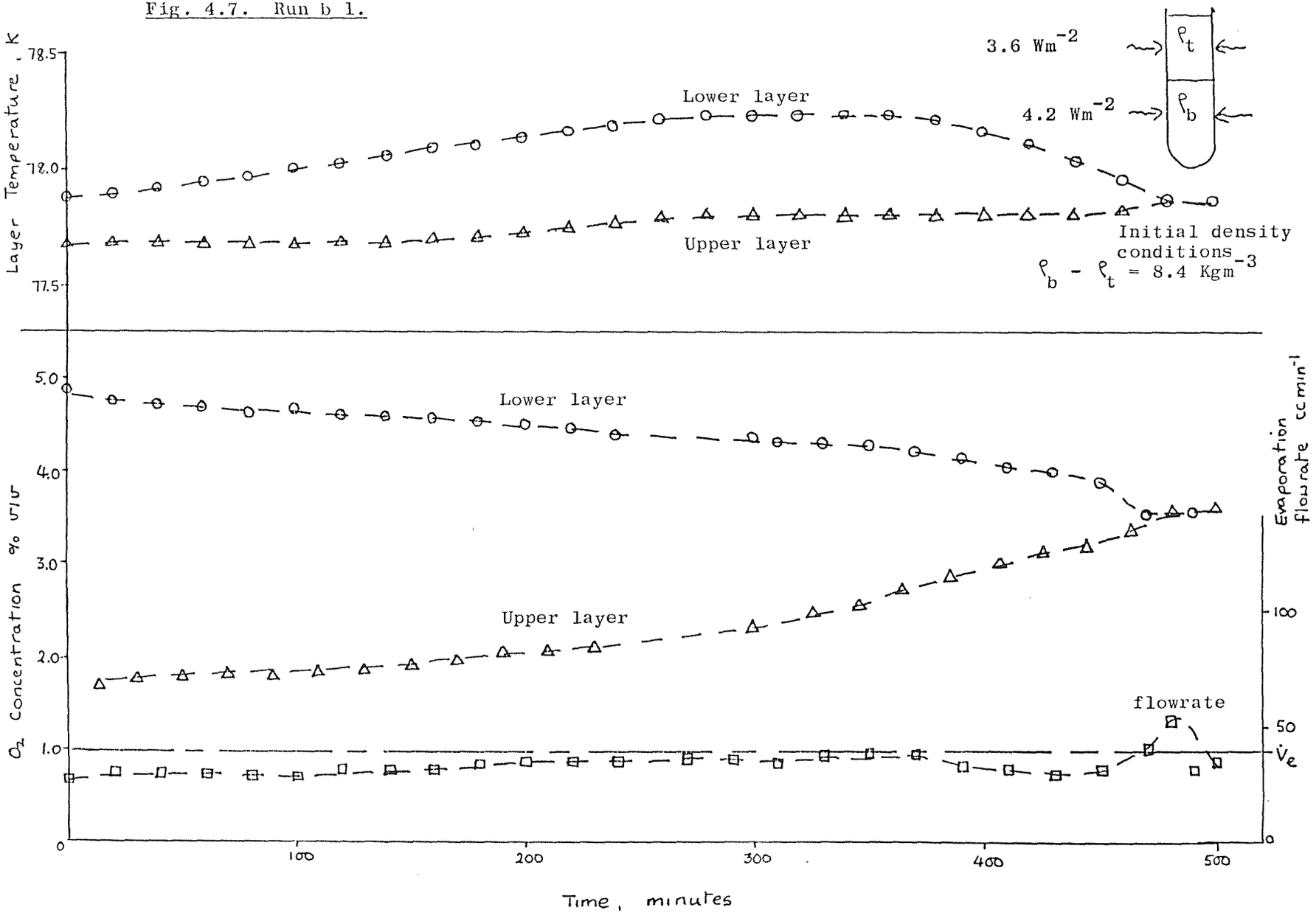
Layer Temperature, K
78.5
78.0
77.5
Lower layer
Upper layer
3.6 Wm^{-2}
4.2 Wm^{-2}
ρ_t
ρ_b
Initial density conditions
$\rho_b - \rho_t$ = 8.4 Kgm^{-3}
O_2 Concentration % v/v
5.0
4.0
3.0
2.0
1.0
0
Lower layer
Upper layer
flowrate
$\dot{V}_e$
Evaporation flowrate cc min^{-1}
100
50
0
100
200
300
400
500
Time, minutes

Fig. 4.8. Run b 2.

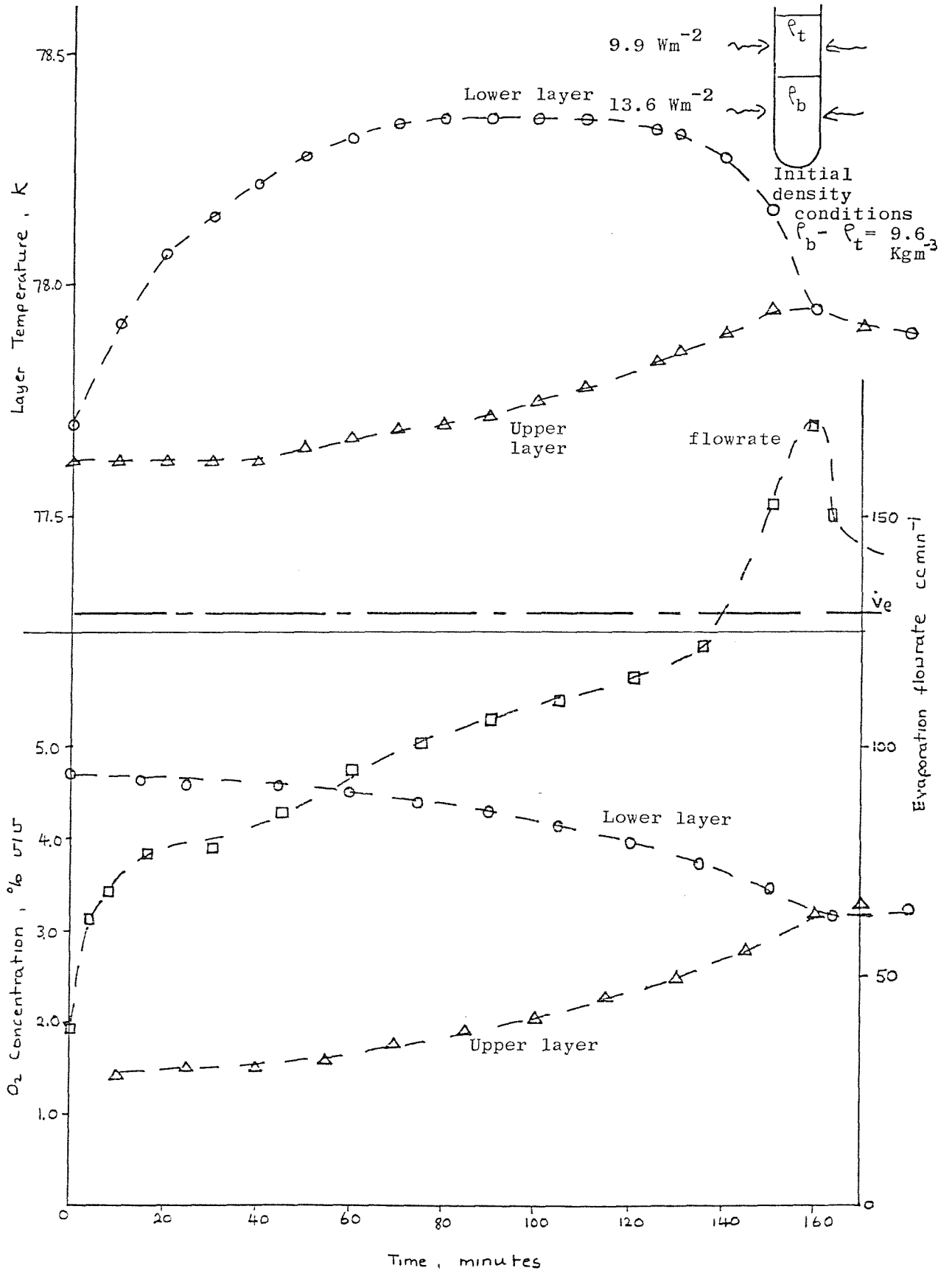
9.9 Wm^{-2}
13.6 Wm^{-2}
ρ_t
ρ_b
Initial density conditions
$\rho_b - \rho_t = 9.6$ Kgm^{-3}
Lower layer
Upper layer
flowrate
$\dot{V}_e$
Layer Temperature, K
78.5
78.0
77.5
O_2 Concentration, % v/v
5.0
4.0
3.0
2.0
1.0
Evaporation flowrate cc min^{-1}
150
100
50
0
Lower layer
Upper layer
0
20
40
60
80
100
120
140
160
Time, minutes

Fig.4.9. Run b 3.

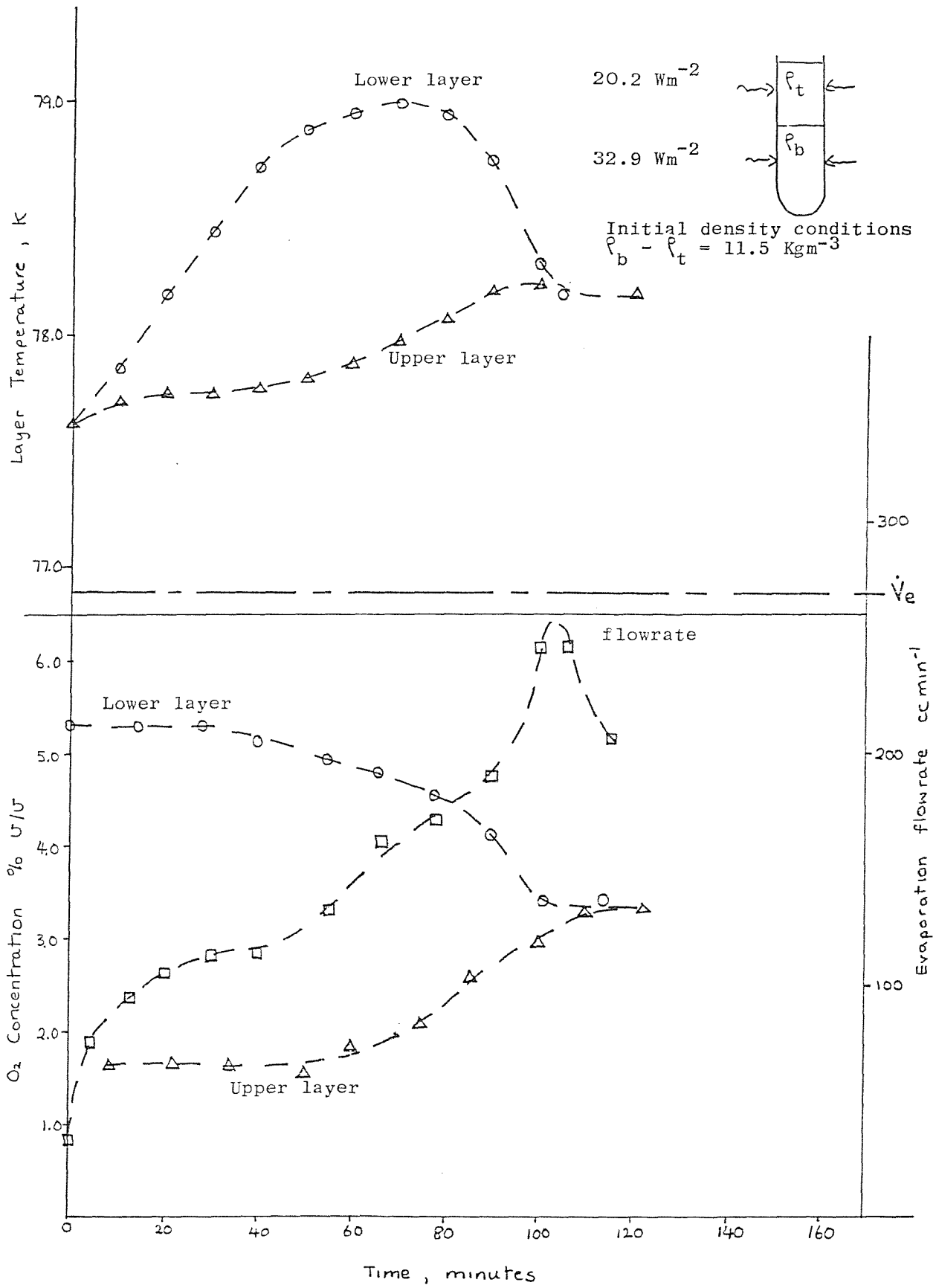
Lower layer
20.2 Wm^{-2}
32.9 Wm^{-2}
ρ_t
ρ_b
Initial density conditions
$\rho_b - \rho_t$ = 11.5 Kgm^{-3}
Layer Temperature , K
79.0
78.0
77.0
Upper layer
300
200
100
$\dot{V}_e$
flowrate
Lower layer
Upper layer
O_2 Concentration % U/U
6.0
5.0
4.0
3.0
2.0
1.0
Evaporation flowrate cc min^{-1}
0
20
40
60
80
100
120
140
160
Time , minutes

Fig.4.10. Run b 4.

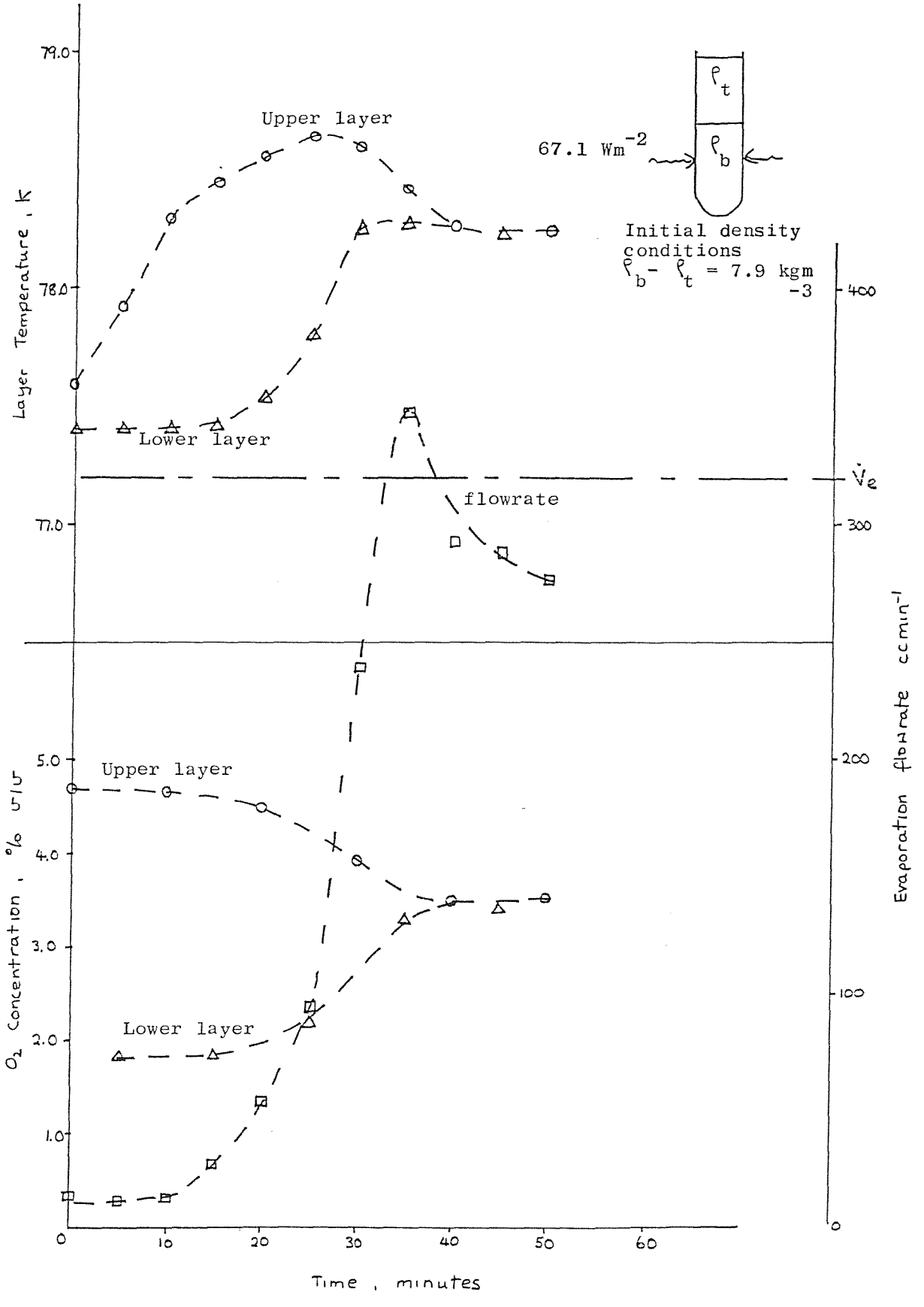

Fig. 4.11. Run c 1.

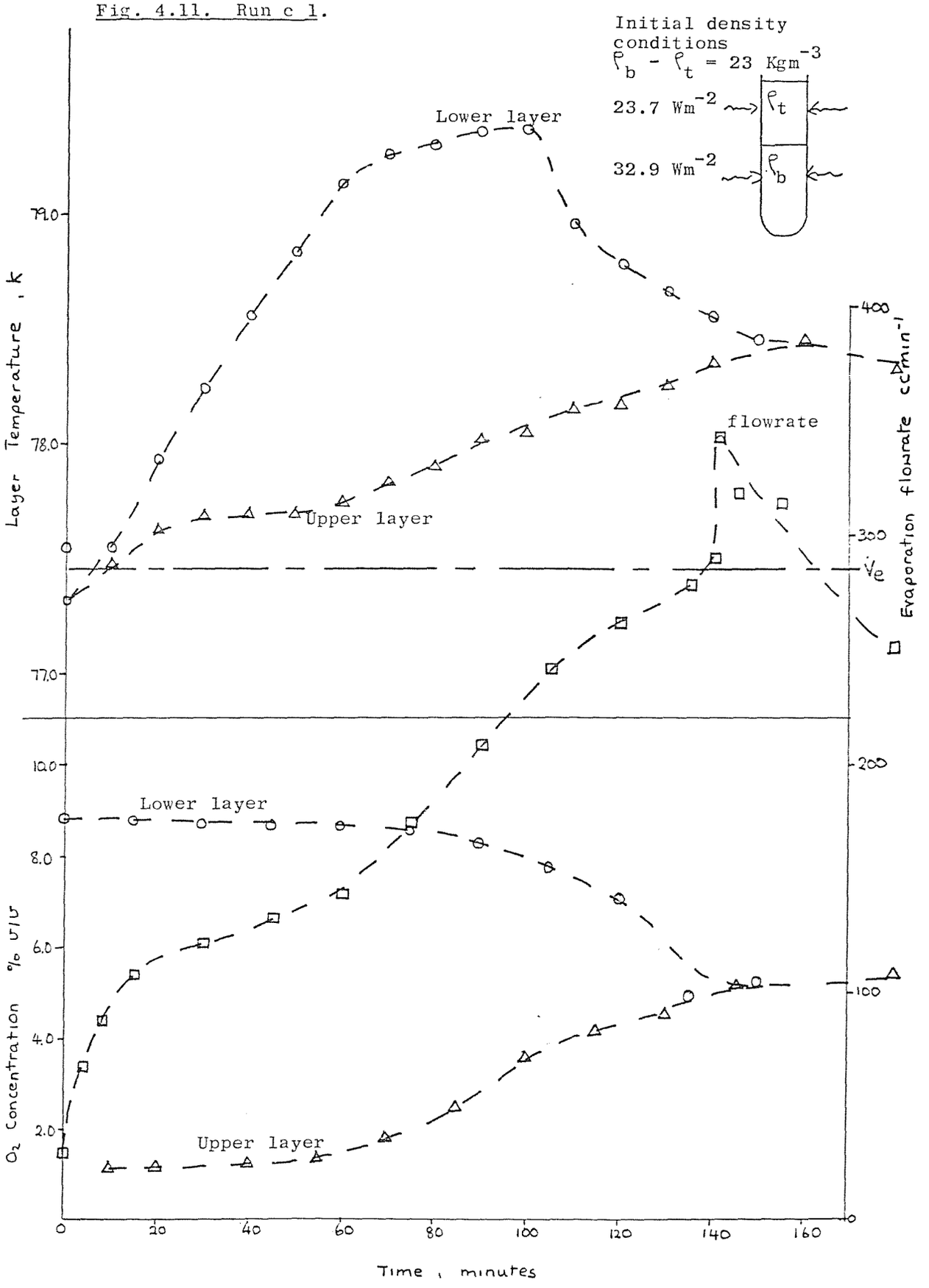

Fig. 4.12. Run c 2.

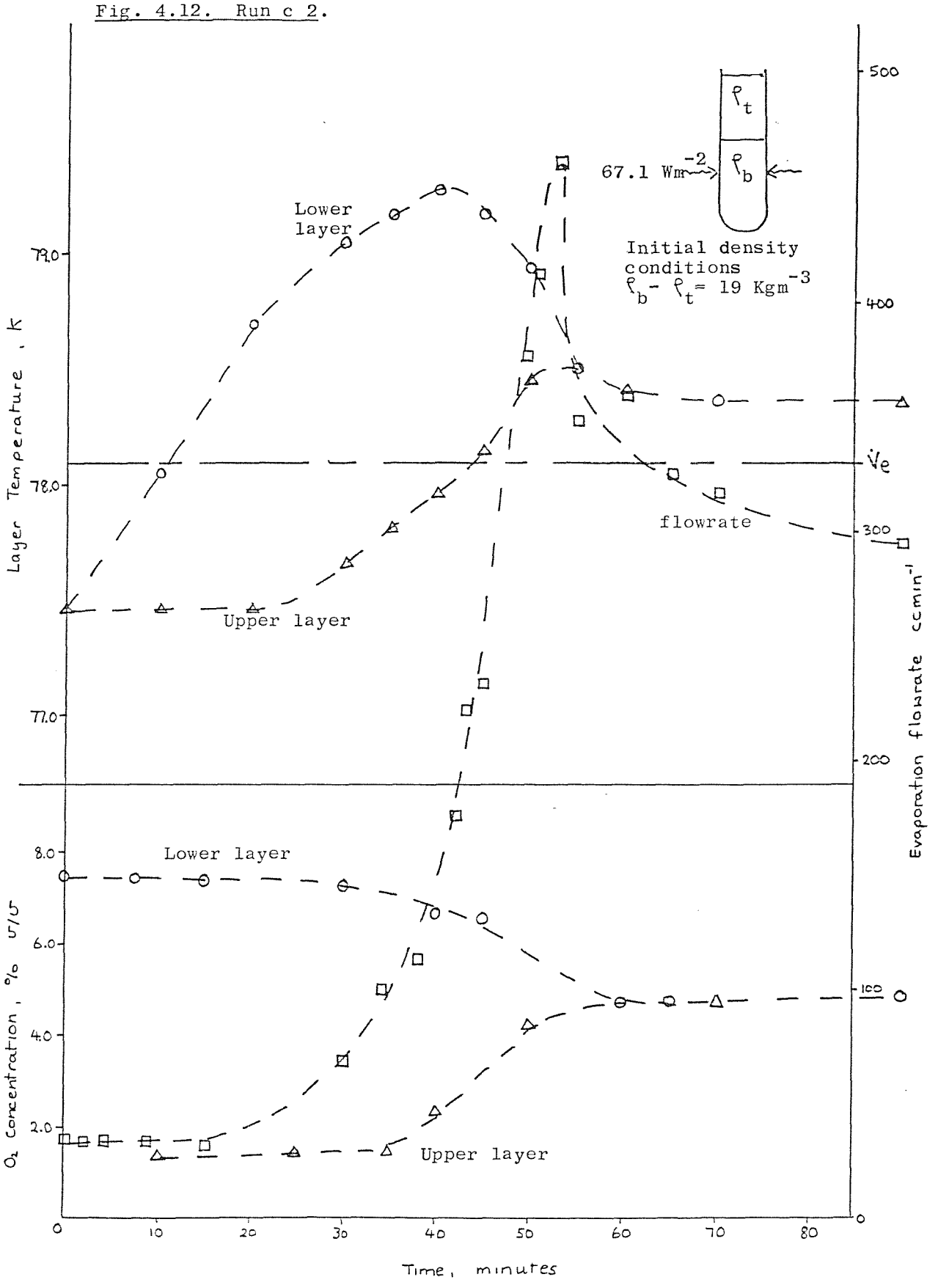

Fig. 4.13. Run d 1.

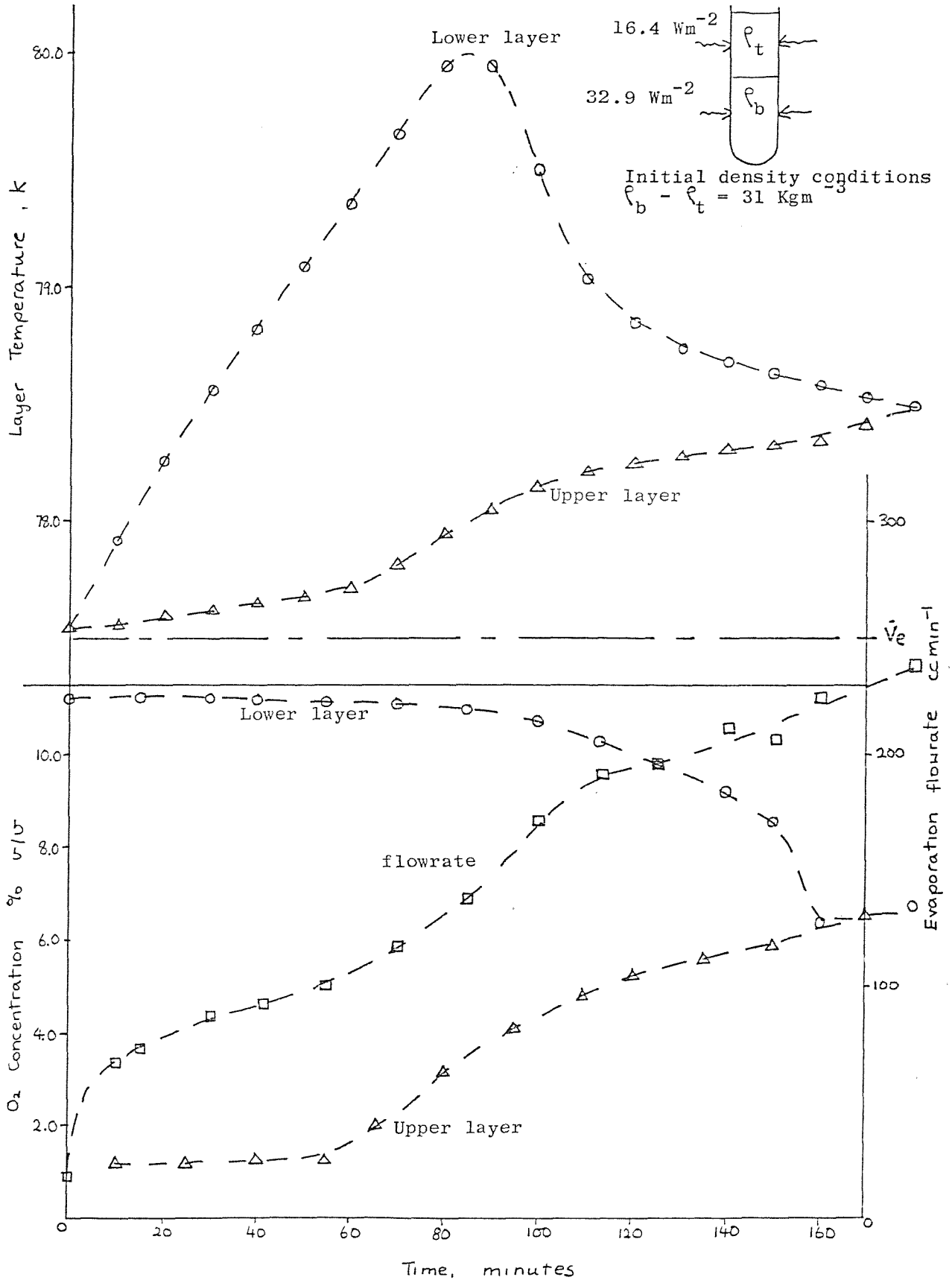

each layer prior to heating for an experimental run. The heating conditions for each layer in top and bottom layer heated experiments, were determined on an equal heating per unit volume basis.

The heating values shown beside each plot correspond to the power per unit circumferential area supplied by each heater. The power input to the liquid layer could also have been specified by the power per unit periphery, or even the total power for each layer. The heating per unit area specification, however, allows direct comparison with large scale containers.

Two factors were not considered in the layer heating calculations. The first factor is that not all the heat supplied by the heater went into the liquid. The fact that an outer bath of LIN was maintained around the well pumped experimental dewar, however, meant that any heat losses due to radiation or conduction were considered negligible.

The second assumption made was that the heat entering the vessel via the transparent heaters eventually diffused to all sections of liquid. Observations of the fluid flow during experimental runs showed that a small layer of liquid at the base of the dewar never mixed, even when the top and bottom layers had mixed completely. This section of fluid lying below the bottom section of the lower heater, typically amounted to 100 cm^3 volume of liquid. The lower layer heating per unit wall area was therefore higher than the calculated heat flux of the top layer.

In full size LNG containers, the largest heat inleak to the liquid is through the base of the container, due to heat transmission through the tank supports (see Table 4.2). The lower section of liquid in a two-layer system would therefore receive a higher portion of the total heat inleak.

Table 4.2. Heat inleak to Canvey Island 800 m^3 tank filled to operational maximum level. (British Gas).

Location	Heat flux (Wm^{-2})	Heat flow (Kw)
Base	15.3	10
Sidewall(liquid)	6.7	7.4
Sidewall(Vapour)	5.2	1.0
Top dome	3.3	2.3

4.2 Liquid-Liquid Intermediate Layer Behaviour.

The movement of the intermediate region between the convective layers during a number of experiments are shown in Figs. 4.14 to 4.18. The time variation of the intermediate layers shown were obtained from the concentration profiles for each experiment. Some intermediate points were obtained from temperature profile plots because the layer positions recorded from the temperature and concentration data agreed well (within $\pm$ 2.5 mm).

The temperature and concentration profile plots shown in Appendix B include the initial depths of each layer just after the layers were formed. During the process of heating the sub-cooled bottom layer to bring its temperature up to that of the top layer, the interface level moved upwards. For 2.5 Kgm^{-3} initial density conditions (runs a1 to a6), the interface often rose at least 20 mm.

The initial lower layer boundary position shown in Figs. 4.14 to 4.18 were referred to a level of 0 mm. The plots show that the intermediate layer falls abruptly during the final stages of mixing. Table 4.3 gives the speed of the mean depth of the intermediate layer during these final stages.

In some preliminary experiments, a simple two-junction thermocouple arrangement was used, to measure the mean temperatures in each layer. The temperatures from the thermocouples were obtained using a thermocouple temperature indicator. Oxygen concentrations were measured at a position 3 cm. above and below the observed bottom layer interface boundary. Video recordings of the liquid-liquid interface boundary movement were made during some of these trial experimental runs. Figs. 4.19 and 4.20 show the liquid mixture behaviour during two typical experiments, including layer flow visualisation. The bottom layer interface boundary behaviour for the experiments are summarised in the vessel diagrams shown beside the temperature, concentration and flowrate data. The diagrams show the convective loops operating in each layer. In the bottom layer heated

Fig.4.14. Intermediate layer movement.

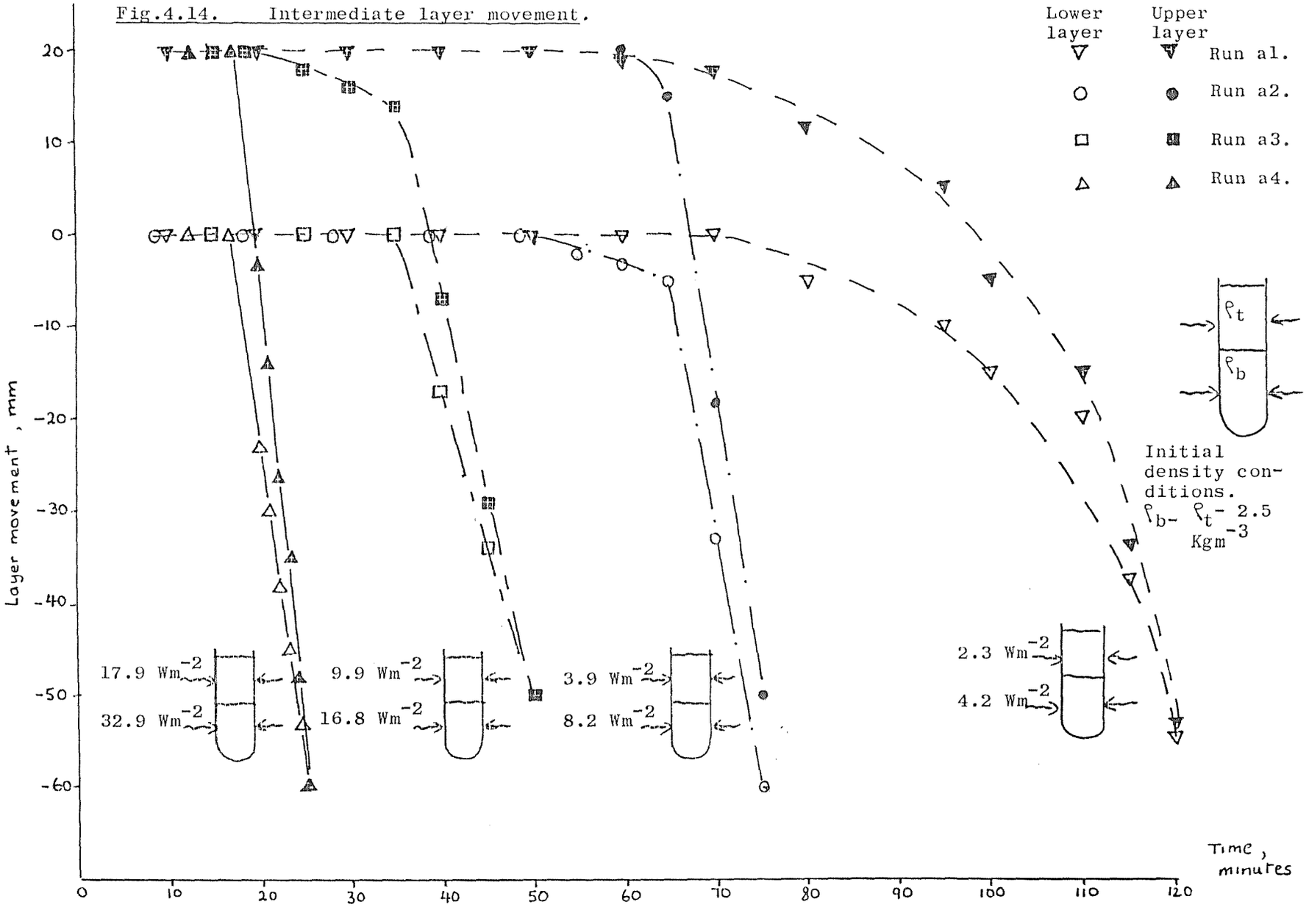

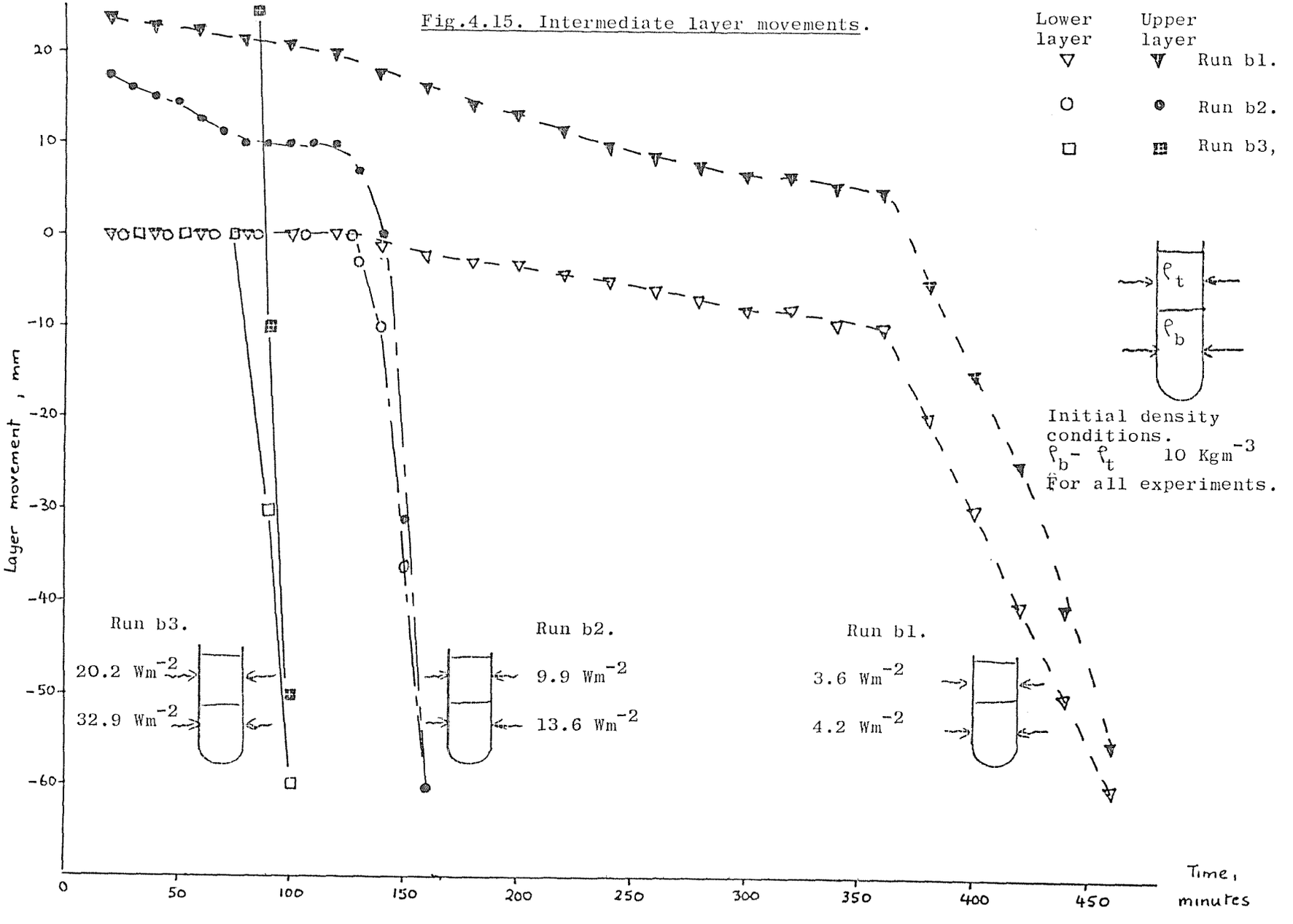
Fig.4.15. Intermediate layer movements.
Lower layer
Upper layer
Run b1.
Run b2.
Run b3,
Layer movement , mm
Time, minutes
20
10
0
-10
-20
-30
-40
-50
-60
0
50
100
150
200
250
300
350
400
450
Initial density conditions.
$\rho_b - \rho_t$ 10 Kgm^{-3}
For all experiments.
Run b3.
20.2 Wm^{-2}
32.9 Wm^{-2}
Run b2.
9.9 Wm^{-2}
13.6 Wm^{-2}
Run b1.
3.6 Wm^{-2}
4.2 Wm^{-2}

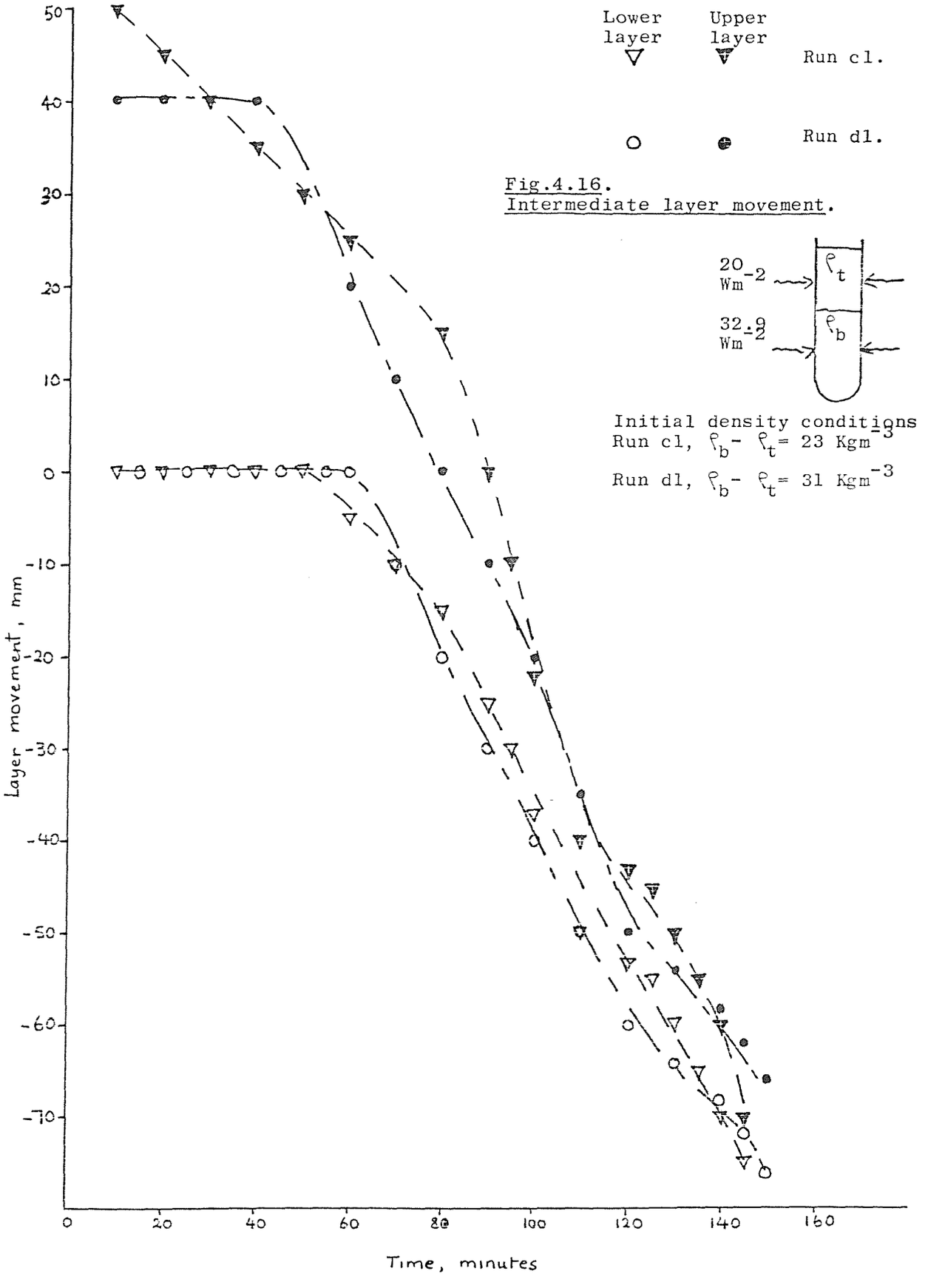

Fig.4.16.
Intermediate layer movement.

Fig.4.17. Intermediate Layer Movement.

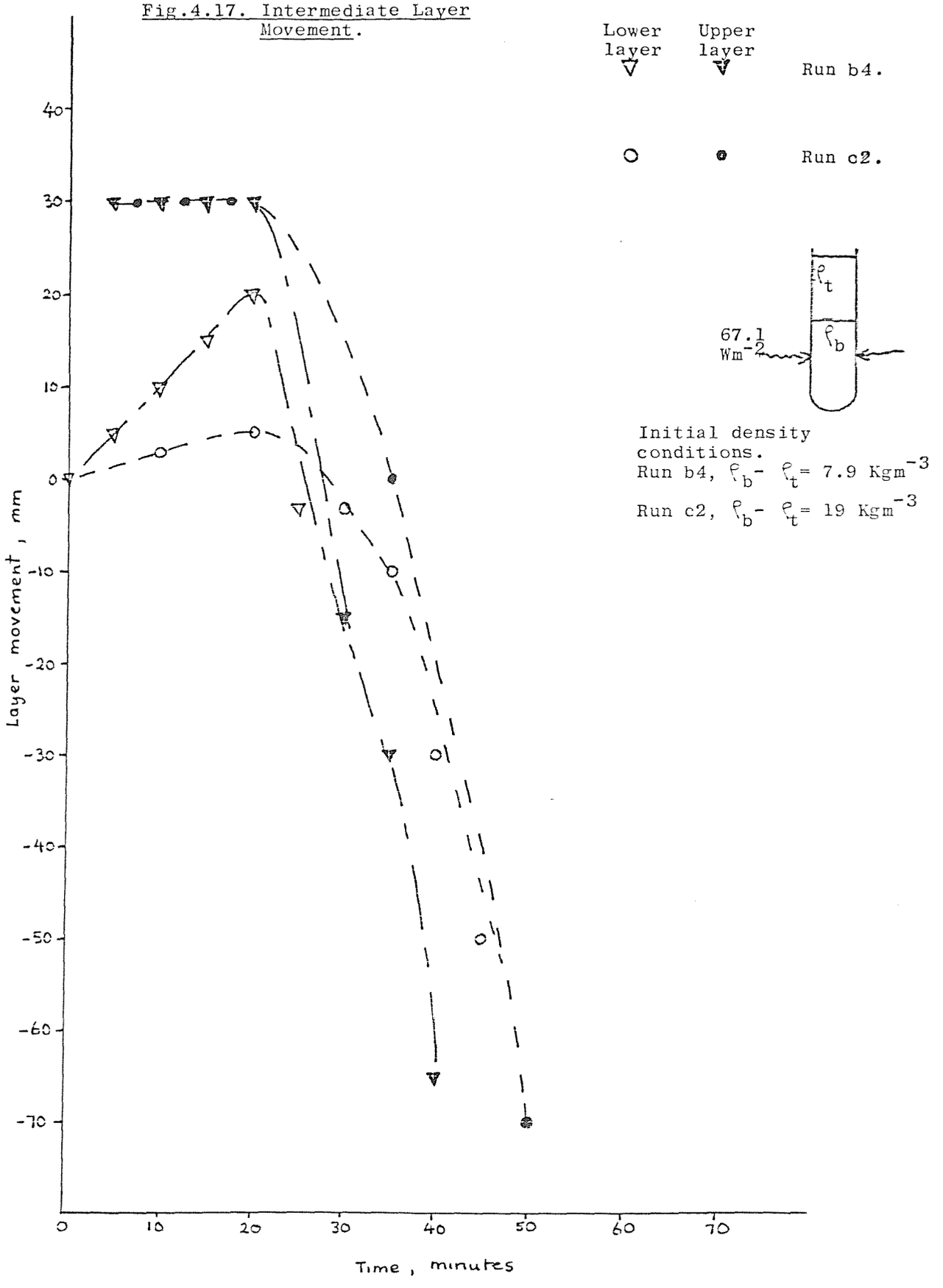

Fig.418. Intermediate Layer Movement.

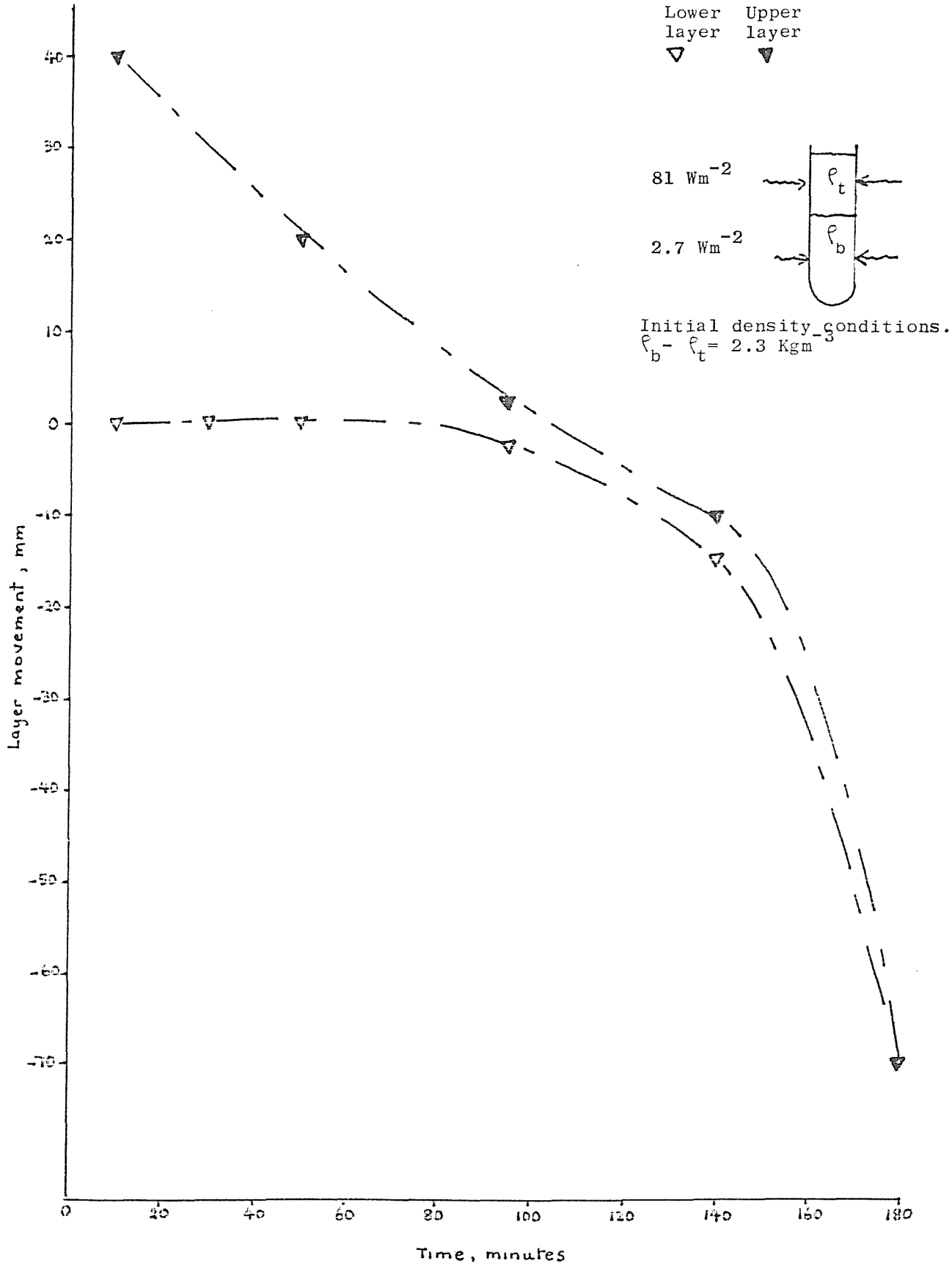

Table 4.3. Intermediate layer descending speed.

Experiment	Interface drop mm	Time interval minutes	Interface speed $mm\ min^{-1}$	Initial layer density difference Kgm^{-3}
Run a 4	60	7	8.6	2.8
Run a 3	50	13	3.8	2.4
Run a 2	50	8	6.3	2.0
Run a 1	18	Last 5 mins	3.6	2.1
Run b 3	55	16	3.4	11.5
Run b 2	60	25	2.4	9.6
Run b 1.	48	84	0.6	8.4
Run c 1.	73	75	1.0	23
Run d 1	71	80	0.9	31
Run b 4	65	13	5.0	7.9
Run c 2	70	18	3.9	19
Run a 6	52	30	1.7	2.3

Fig. 4.19. Bottom layer heated experiment including flow visualisation.

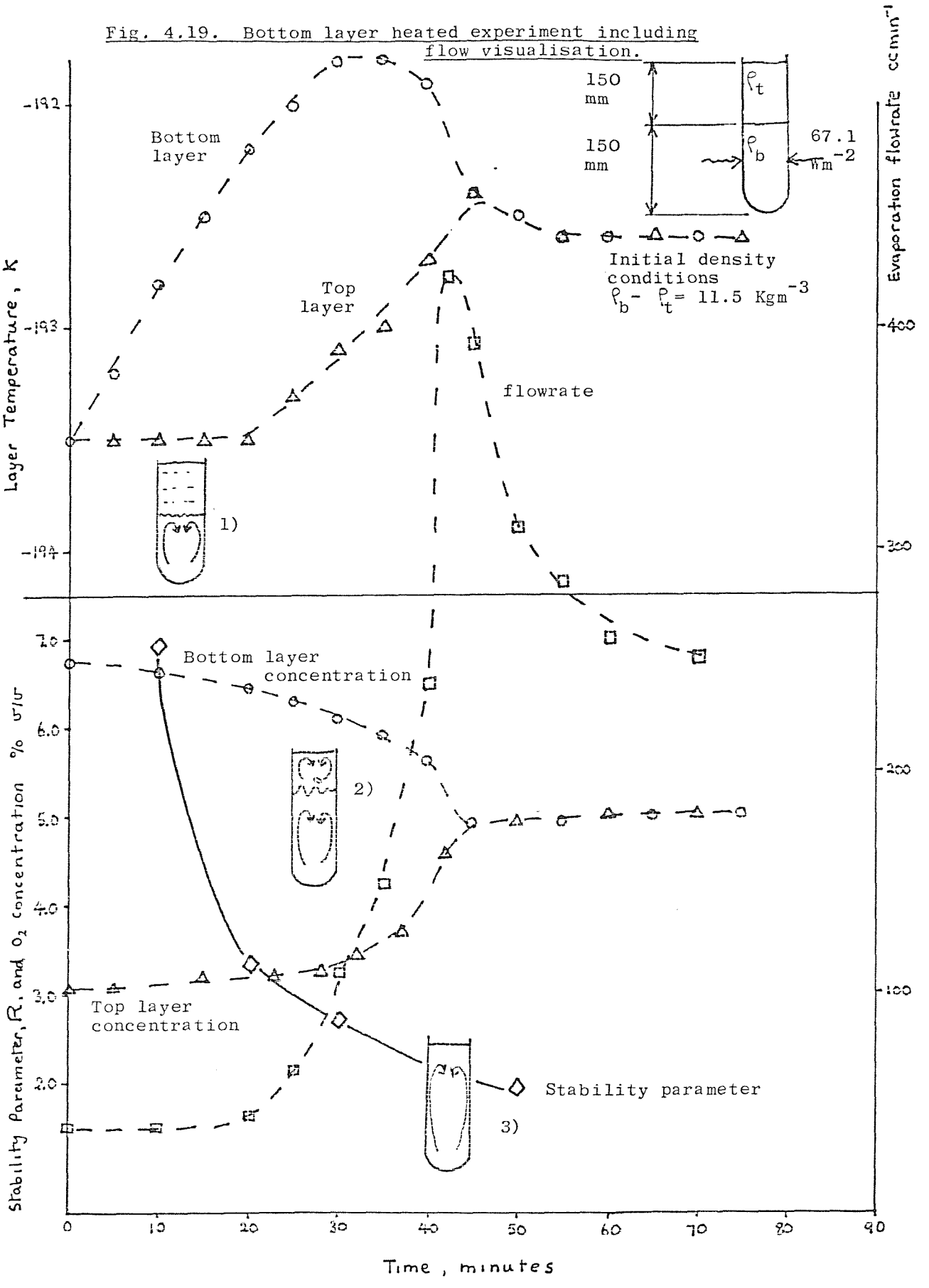

Fig. 4.20. Top and bottom layer heated experiment including flow visualisation.

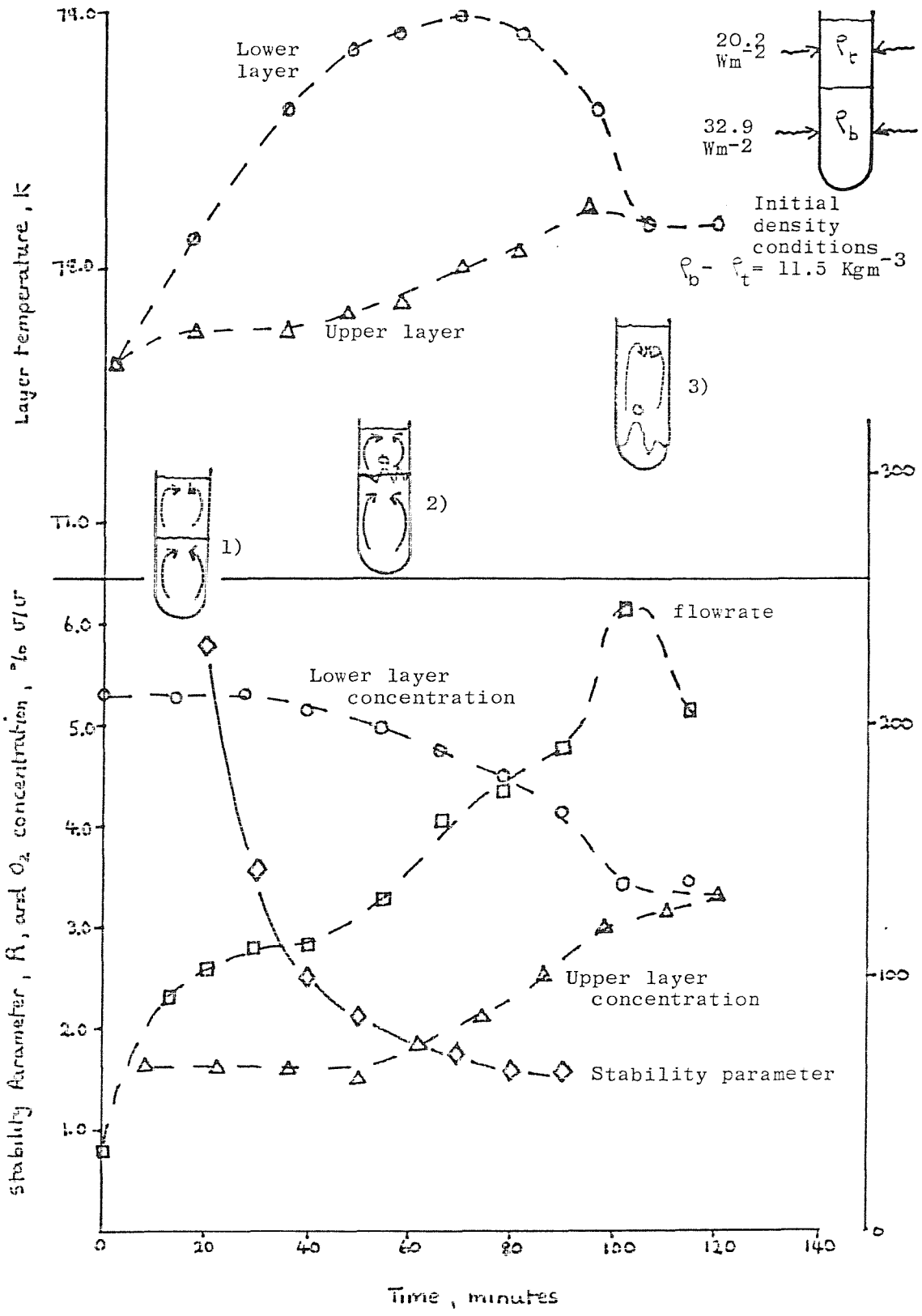

experiment (Fig 4.19), no convective motion was observed in the top layer for the first 20 minutes. After 20 minutes, the top layer received sufficient heat from the bottom layer to start a convective loop.

Flow visualisation was achieved by shining a high intensity light source through the mid-section of the experimental dewar. Fig. 4.21. shows the optical arrangement used. Small light-scattering particles were introduced into the liquid via a stainless steel tube after layer formation. Video recordings were made using a Sony VO-5800 PS U-matic video cassette recorder.

4.3. Liquid-Liquid interface heat and mass transfer.

A simple energy balance on the bottom layer mixture was used to calculate the heat transfer through the liquid-liquid interface. Assuming that all heat entering the liquid $\dot{Q}_b$, was supplied by the heater, and that $\dot{Q}_{ab}$ was absorbed, with $\dot{Q}_i$ transferred through the interface, $\dot{Q}_i$ is given by:

$$\dot{Q}_i = \dot{Q}_b - \dot{Q}_{ab} \qquad (4.1)$$

As $\dot{Q}_{ab} = m_b c_p \frac{\Delta T_b}{\Delta t}$,

$$\dot{Q}_i = \dot{Q}_b - m_b c_p \frac{\Delta T_b}{\Delta t} \qquad (4.2)$$

$\dot{Q}_b$ was calculated from the heater power supplied, the LIN saturation value for $c_p = 2.051\ kJ\ kg^{-1}K^{-1}$ was used, and $\Delta T_b/\Delta t$ was obtained from the summarised plots. m_2, the mass of the lower layer, was calculated using the lower layer boundary changes for volume calculations, and the layer temperature and LOX concentrations for density calculations. Temperature - density values of LOX and LIN used, were obtained by fitting a fifth order polynomial to published data (31), (32), to obtain density data for 0.1 K increments in temperature.

Fig. 4.21. Lighting arrangement used for observing interface motion.

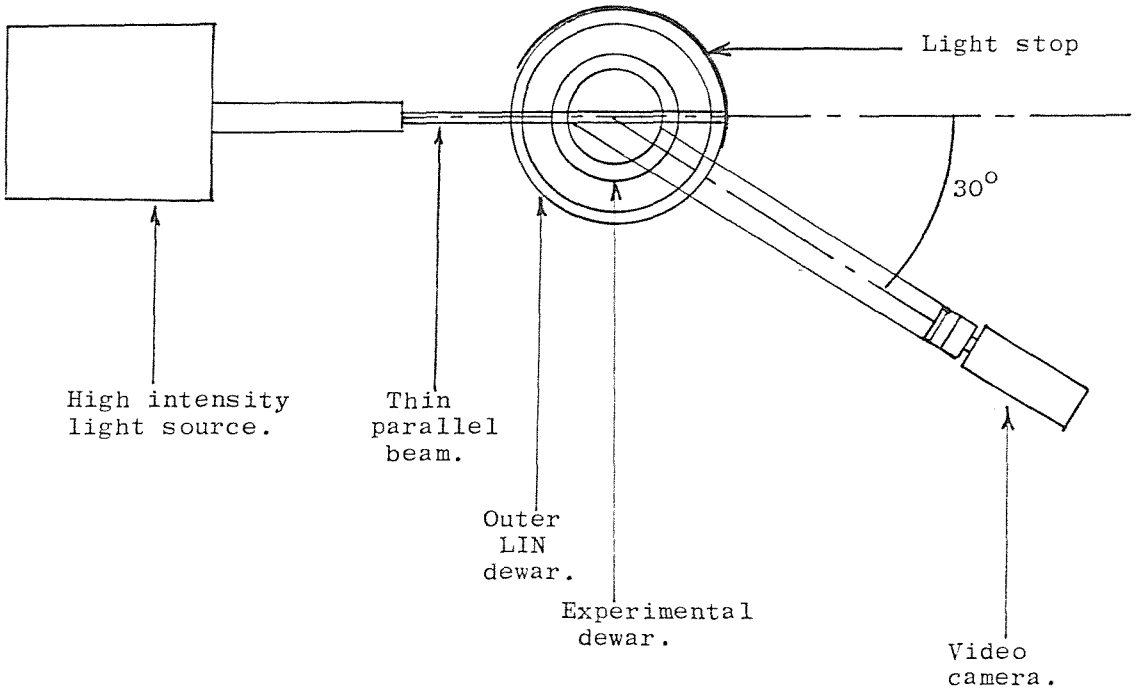

As mentioned earlier in Section 4.1, all the concentration plots refer to oxygen vapour concentrations. For the same reference temperatures, the liquid to gas expansion ratio of oxygen is greater than that of nitrogen. One would therefore expect the gaseous oxygen concentration x_{O_2g} to read higher than the LOX concentration υ_g/υ_L, x_{O_2L}. An expression for x_{O_2L} in terms of x_{O_2g} is given by:

$$x_{O_2L} = \frac{679\, x_{O_2g}}{886 - 207 x_{O_2g}} \qquad (4.3)$$

The reasoning leading to (4.1) is given in Appendix A. For liquid mixture density and saturation temperature calculations, where x_{O_2L} was required, a computer programme was written, giving values of x_{O_2L} for 0.01% increments of x_{O_2g}, for x_{O_2g} ranging from 0 to 12%.

Ratios of the interface heat transfer $\dot{Q}_i$ to the solid conduction heat transfer $\dot{Q}_s$, were obtained for various values of the stability parameter R. The constant A in the expression for $\dot{Q}_s$ (equation 2.31) was calculated using LIN saturation values for the various parameters. The following fluid properties were used (33):

$k_T = 0.1396$ $\quad Wm^{-1}\,K^{-1}$

$\beta_T = 5.63$ $\quad \times 10^{-3}\,K^{-1}$

$\nu = 1.943$ $\quad \times 10^{-7}\,m^2\,S^{-1}$

$\alpha = 8.43$ $\quad \times 10^{-8}\,m^2\,S^{-1}$

$g = 9.81$ $\quad m\,S^{-2}$

$$A = 0.085 \times 0.1396 \left(\frac{9.81 \times 5.63 \times 10^{-3}}{8.43 \times 10^{-8} \times 1.934 \times 10^{-7}}\right)$$
$$= 178.21 \text{ units}$$
$$= 178.21\ \Delta T^{4/3} \quad Wm^{-2} \qquad (4.4)$$
$$\text{or } 0.0178\ \Delta T^{4/3} \quad W\,cm^{-2}$$

The stability parameter or density ratio R, defined as:

$$R = \left(\frac{\beta_s \Delta S}{\beta_T \Delta T} \right) \tag{2.50}$$

Was expressed as:

$$R = 0.85 \frac{\Delta S}{\Delta T} \tag{4.5}$$

Where ΔS is the Layer LOX composition difference in %, and ΔT is the temperature difference between the layers. A plot showing the variation of $\dot{Q}_i / \dot{Q}_s$, with R for a variety of experiments is shown in Fig. 4.22.

The LOX mass flux through the interface was compared with the theoretical molecular mass flux, driven by the concentration gradient existing between the layers. A mass flux equation proposed by de Groot (34) is given by:

$$J_{AZ} = - \rho_o D_{AB} \frac{d\omega_A}{dz} \tag{4.6}$$

Where J_{AZ}= mass flux of component A diffusing in Z direction relative to the mass average velocity,

ρ_o = overall fluid density

$\frac{d\omega_A}{dz}$ = mass fraction concentration gradient.

and D_{AB} = mass diffusivity of A diffusing through liquid solvent B.

There are a number of empirical equations that can be used to calculate the liquid mass diffusivity D_{AB}. Wilke and Chang (35) proposed the following correlation for nonelectrolytes in an infinitely dilute solution:

$$\frac{D_{AB} M_B}{T} = \left\{ 7.5 \times 10^{-8} (\Phi M_B)^{\frac{1}{2}} \right\} / V_A^{0.6} \tag{4.7}$$

Scheibel (36) suggested that the Wilke-Chang equation be modified to eliminate the association parameter Φ , giving:

$$\frac{D_{AB} M_B}{T} = \frac{K}{V_A^{1/3}} \tag{4.8}$$

Fig.4.22. Interface heat flux behaviour.
Broken-line curve represents salt-water experimental results of Turner (14).

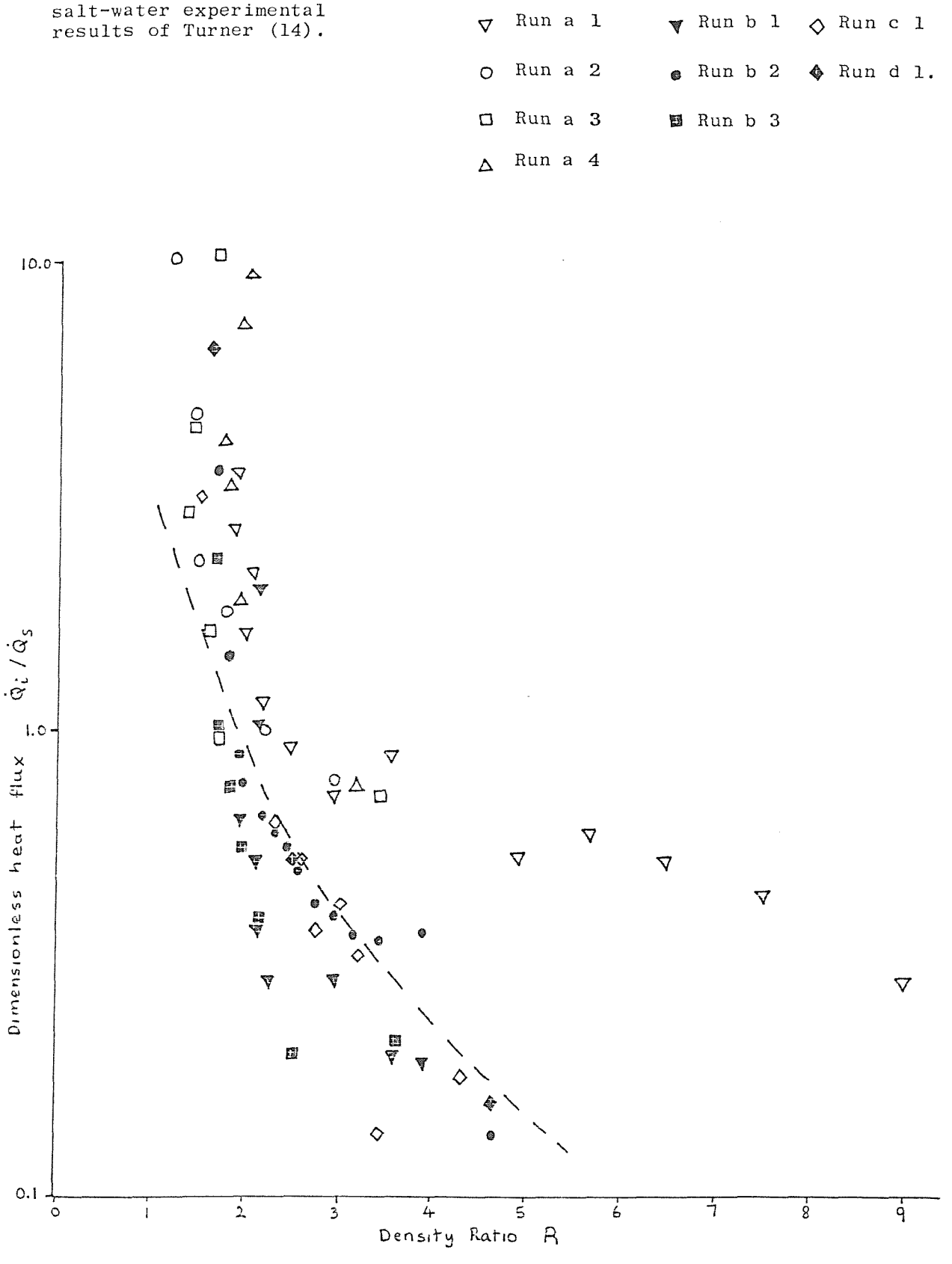

Where K is given by:

$$K = (8.2 \times 10^{-8}) \left[1 + \left(\frac{3 V_B}{V_A} \right)^{2/3} \right]$$

V_B and V_A are the molecular volumes of constituent B and A at their normal boiling points, in $cm^3\ mol^{-1}$, μ_B is the viscosity of the solution in centipoises, and T is the absolute temperature in K. In this investigation A represents LOX, and B represents LIN. The fluid properties necessary to calculate D_{AB} for LOX diffusing through LIN (33), (37), are:

$$V_A = 25.6 \quad cm^3\ mol^{-1}$$

$$V_B = 31.2 \quad cm^3\ mol^{-1}$$

$$\mu_B = 158 \times 10^{-3} \text{ centipoise (LIN)}$$

$$T = 77.36 \text{ K.}$$

$$\therefore D_{AB} = 4.60 \times 10^{-5}\ cm^2\ S^{-1} \text{ using (4.8)}$$

It should be noted that equation (4.8) may have an error of up to 20% for the calculated value of D_{AB}.

Referring back to equation 4.7, the overall fluid density ρ_o, was taken as the mean value of the layer densities. The mass fraction concentration gradient was calculated using the expression:

$$\frac{\Delta \omega_A}{Z} = \frac{\left(\frac{m_{O_2 b}}{m_b}\right) - \left(\frac{m_{O_2 t}}{m_t}\right)}{Z} \qquad (4.9)$$

where:

$m_{O_2 b}$ = mass of LOX in lower layer
$m_{O_2 t}$ = mass of LOX in top layer
m_b = total mass of lower layer
m_t = total mass of top layer
Z = intermediate layer thickness

The measured mass flux through the interface, M_{AZ}, was obtained from:

$$M_{AZ} = \frac{m_{O_2 b}(\text{at } t_1) - m_{O_2 b}(\text{at } t_2)}{\text{Area} \times \Delta t} \qquad (4.10)$$

A plot of M_{Az}/J_{Az} against R for several experiments is shown in Fig. 4.23.

To compare the LOX/LIN system mass and heat transfer processes with an LNG mixture, a number of fluid properties of a hypothetical liquid Ethane (LC_2H_6)/liquid Methane (LCH_4) mixture, were calculated. A high concentration (i.e. 95%) LCH_4 solution was assumed, so that pure methane data could be used for calculations. Table 4.4 summarises some LC_2H_6/LCH_4 mixture properties with those of a LIN/LOX mixture. The Lewis number Le, defined as the ratio of thermal to mass diffusivity is expressed as:

$$Le = \frac{K_T}{\rho\, C_p\, D_{AB}} \qquad (4.11)$$

4.4. Evaporation Flowrate Behaviour.

Table 4.5 shows particular flowrate values for a number of experiments. The peak flowrate dependence on initial density difference between layers is shown in Fig. 4.24. The initial masses of each layer, however varied, as shown in Table 4.6. The rollover summary of the only experiment to achieve a V peak/Vm approaching 10, is shown in Fig. 4.25.

The layer superheat energies (thermal overfill) existing during representative experiments are shown in Figs. 4.26 to 4.29. The excess enthalpy (H-Ho) was calculated using:

$$(H-Ho) = M_L\, Cp\, \Delta T_s \qquad (4.12)$$

where M_L = Mass of layer.

Cp = Specific heat of LIN at saturation.

ΔT_s = Bulk temperature of layer minus the saturation temperature corresponding to the layer composition.

Fig. 4.23. Interface Mass Flux Behaviour.

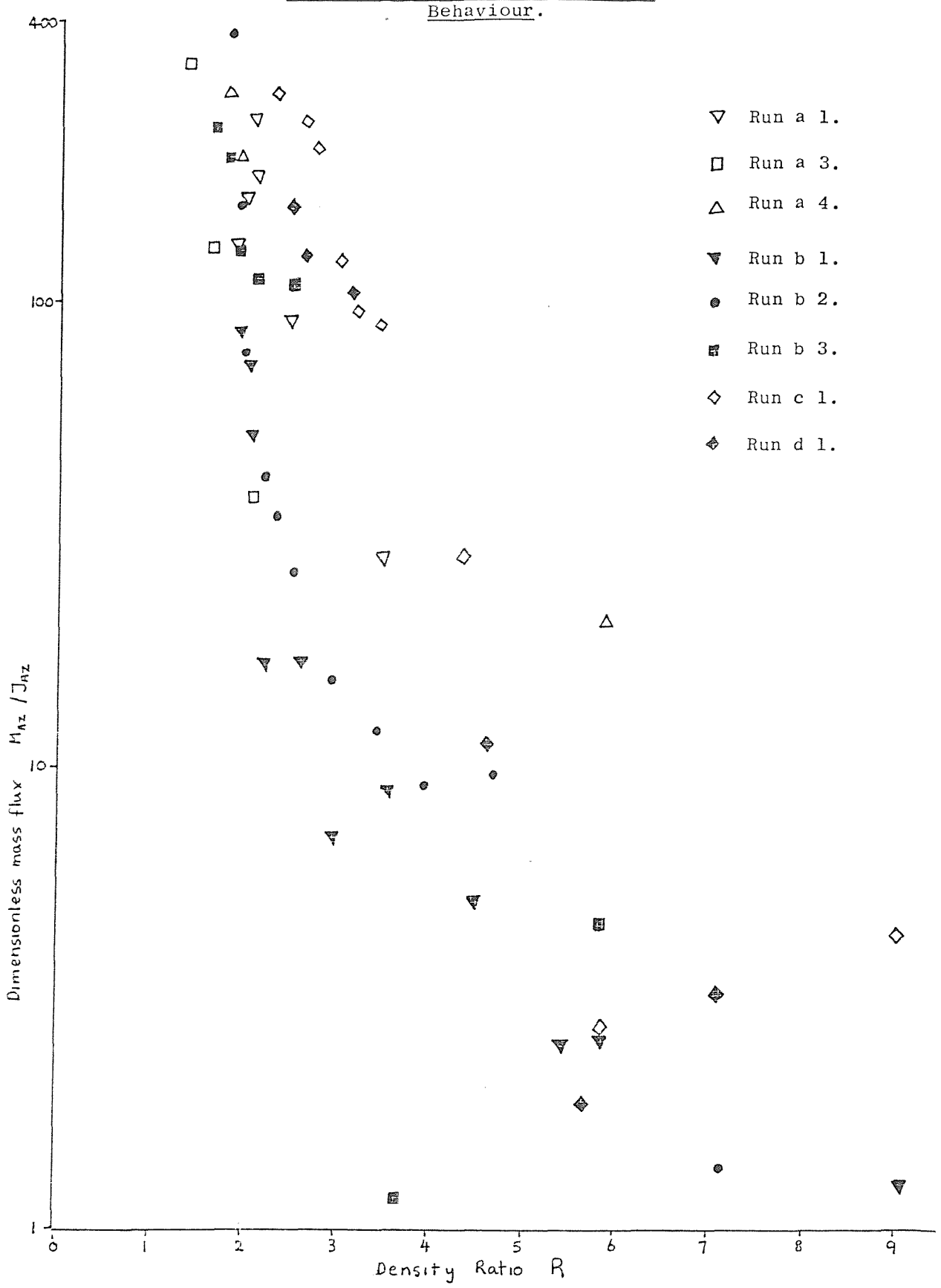

Table 4.4. Comparison of LIN/LOX Mixture Properties, with Hypothetical LNG Mixture.

Mixture	Temperature K	Pr	α $cm^2 s^{-1}$	D_{AB} $cm^2 s^{-1}$	Le
LIN/LOX	77.36	2.32 (LIN)	8.43×10^{-4} (LIN)	4.60×10^{-5}	18
LCH_4/LC_2H_6	111.7	2.11 (LCH_4)	13.2×10^{-4} (LCH_4)	5.06×10^{-5}	26

Table 4.5. Evaporation Flowrate Behaviour.

Experiment	$\Delta\rho_i$ Kgm^{-3}	$\dot{V}e$ $cc\ min^{-1}$	$\dot{V}m$ $cc\ min^{-1}$	$\dot{V}peak$ $cc\ min^{-1}$	$\frac{\dot{V}peak}{\dot{V}m}$	$\dot{Q}_T$ mW
Run a 1	2.1	47	50	52	1.04	180
Run a 2	2.0	73	51	64	1.25	283
Run a 3	2.4	143	111	126	1.14	551
Run a 4	2.8	257	190	193	1.02	995
Run b 1	8.4	39	30	42	1.40	151
Run b 2	9.6	128	115	170	1.48	493
Run b 3	11.5	268	180	232	1.29	1038
Run b 4	7.9	326	270	350	1.30	1260
Run b 7	11.0	361	-	363	-	1396
Run b 8	11.0	39	40	380	9.5	151
Run c 1	23	285	250	322	1.29	1100
Run c 2	19	326	296	462	1.56	1250
Run c 3	19	250	-	240	-	967
Run d 1	31	250	-	-	-	967

Where: $\Delta\rho_i$ = Initial liquid density difference between layers.

$\dot{Q}_T$ = Total heat input to liquid including heat-inleak.

$\dot{V}e$ = Calculated equilibrium flow using $\dot{Q}_T$.

$\dot{V}peak$ = Peak flowrate measured during experiment.

$\dot{V}m$ = Flowrate measured 30 minutes after peak flowrate.

Fig. 4.24. Rollover intensity relation to initial density difference between liquid layers.

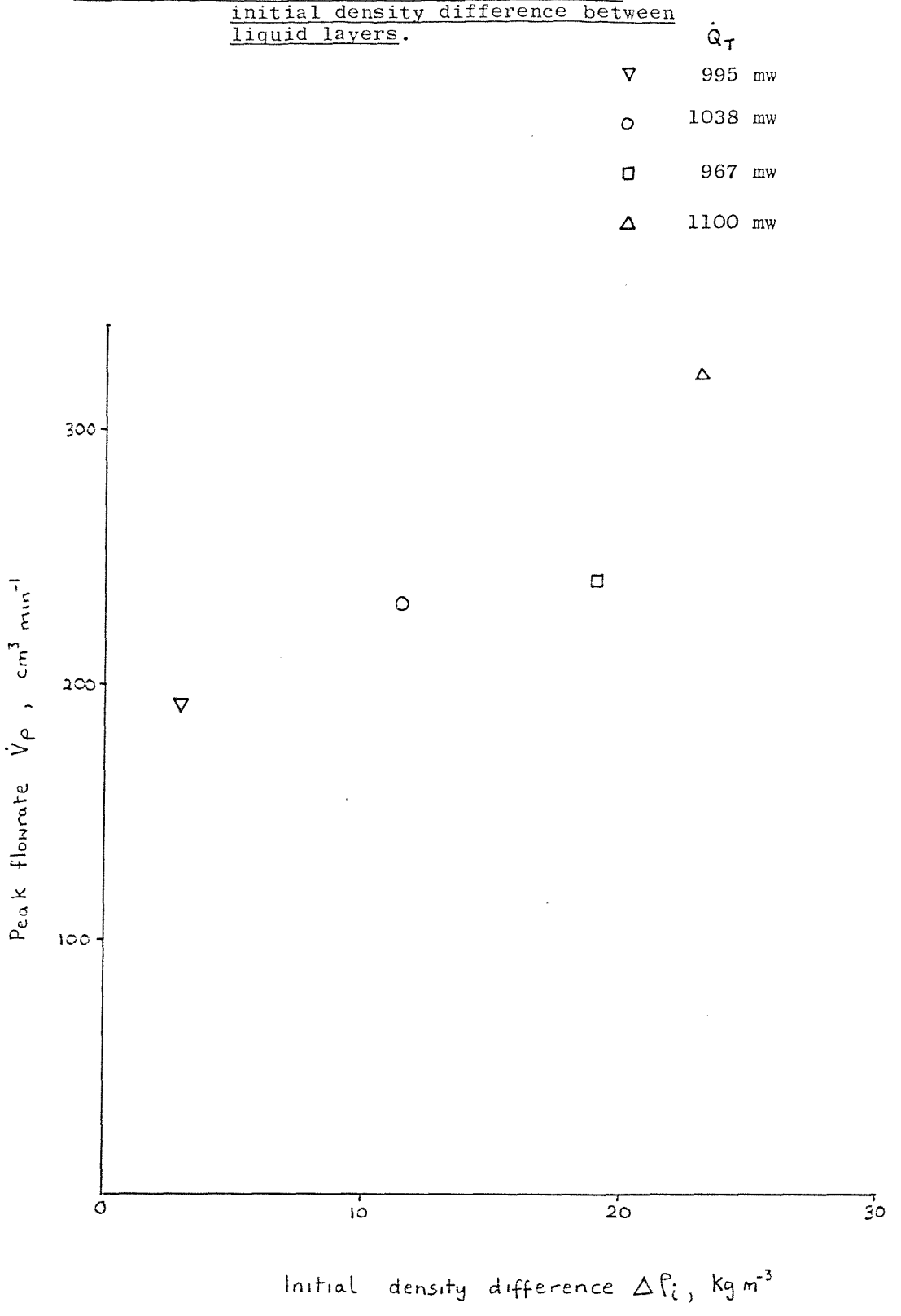

Table 4.6. Layer mass initial conditions.

Experiment	Bottom Layer Mass M_b Kg.	Top Layer Mass M_t Kg.	Total Mass $M_b + M_t$ Kg.	Initial Mass Ratio M_b/M_t
Run a 4	0.51	0.27	0.78	1.9
Run b 3	0.48	0.33	0.81	1.5
Run c 1	0.47	0.22	0.69	2.1
Run c 3	0.51	0.31	0.82	1.7

Fig.4.25. Run b 8: Unexpected flowrate behaviour.

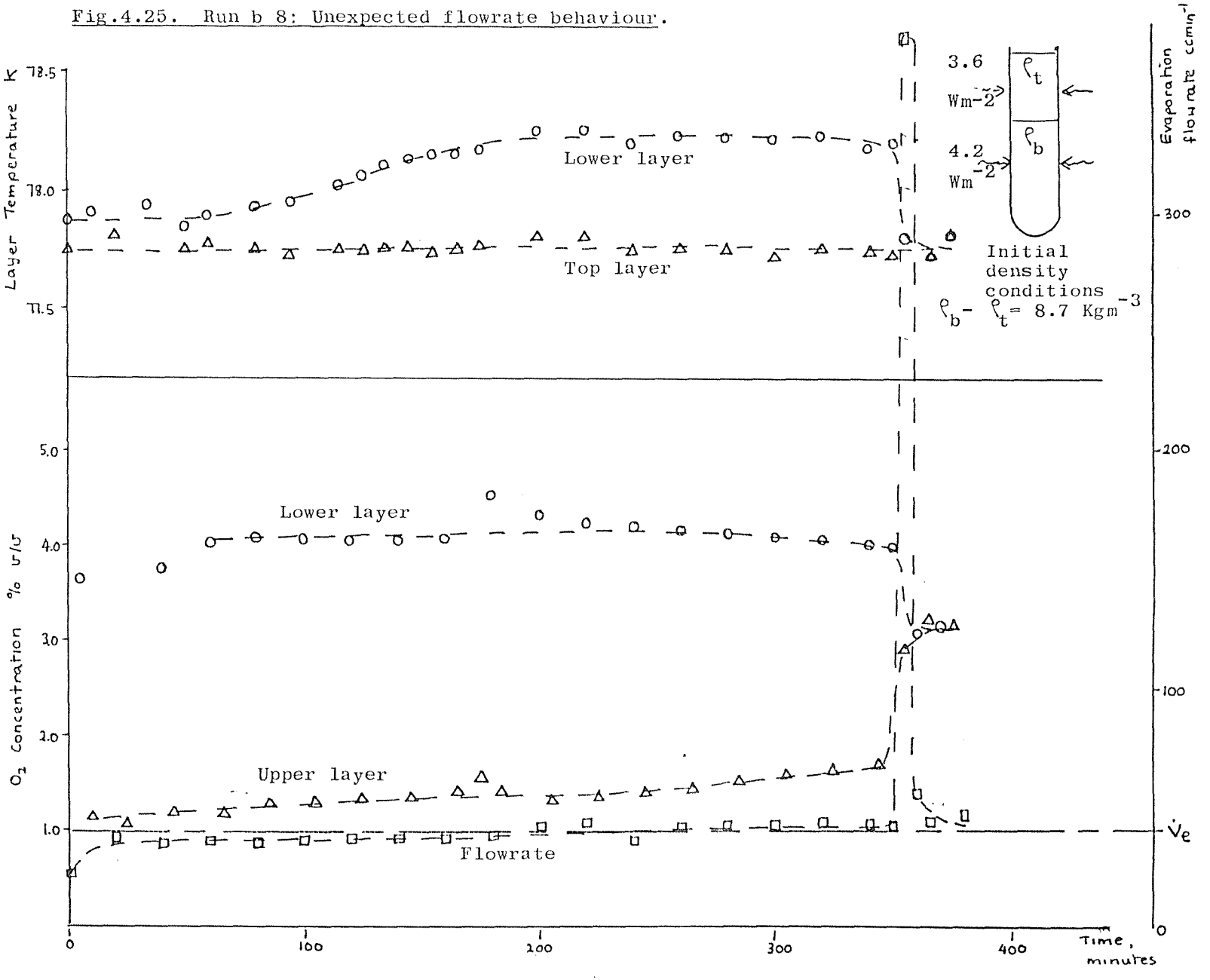

Fig. 4.26. Run a 2. Layer energy accumulation.

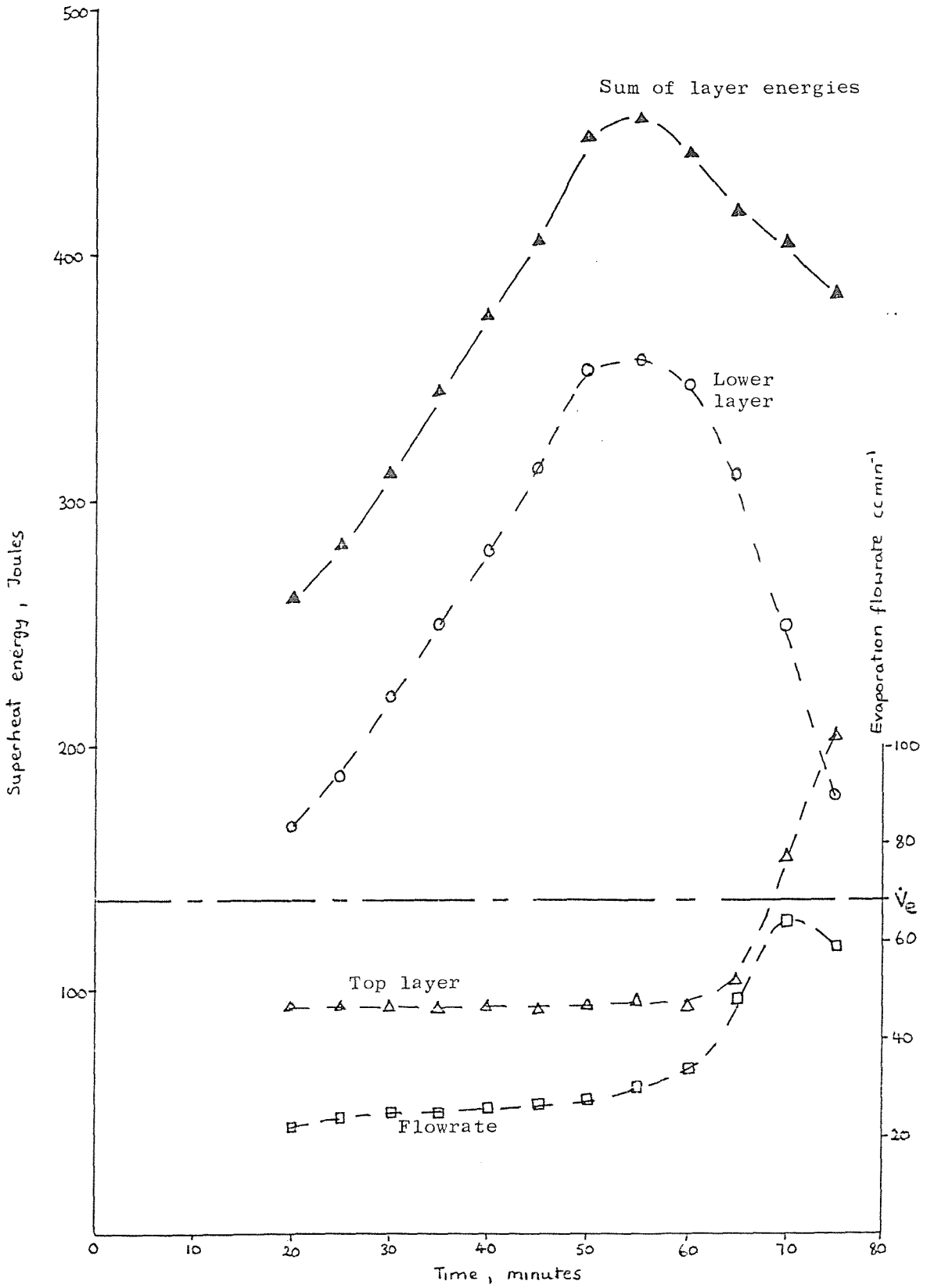

Fig. 4.27. Run b 2. Layer energy accumulation.

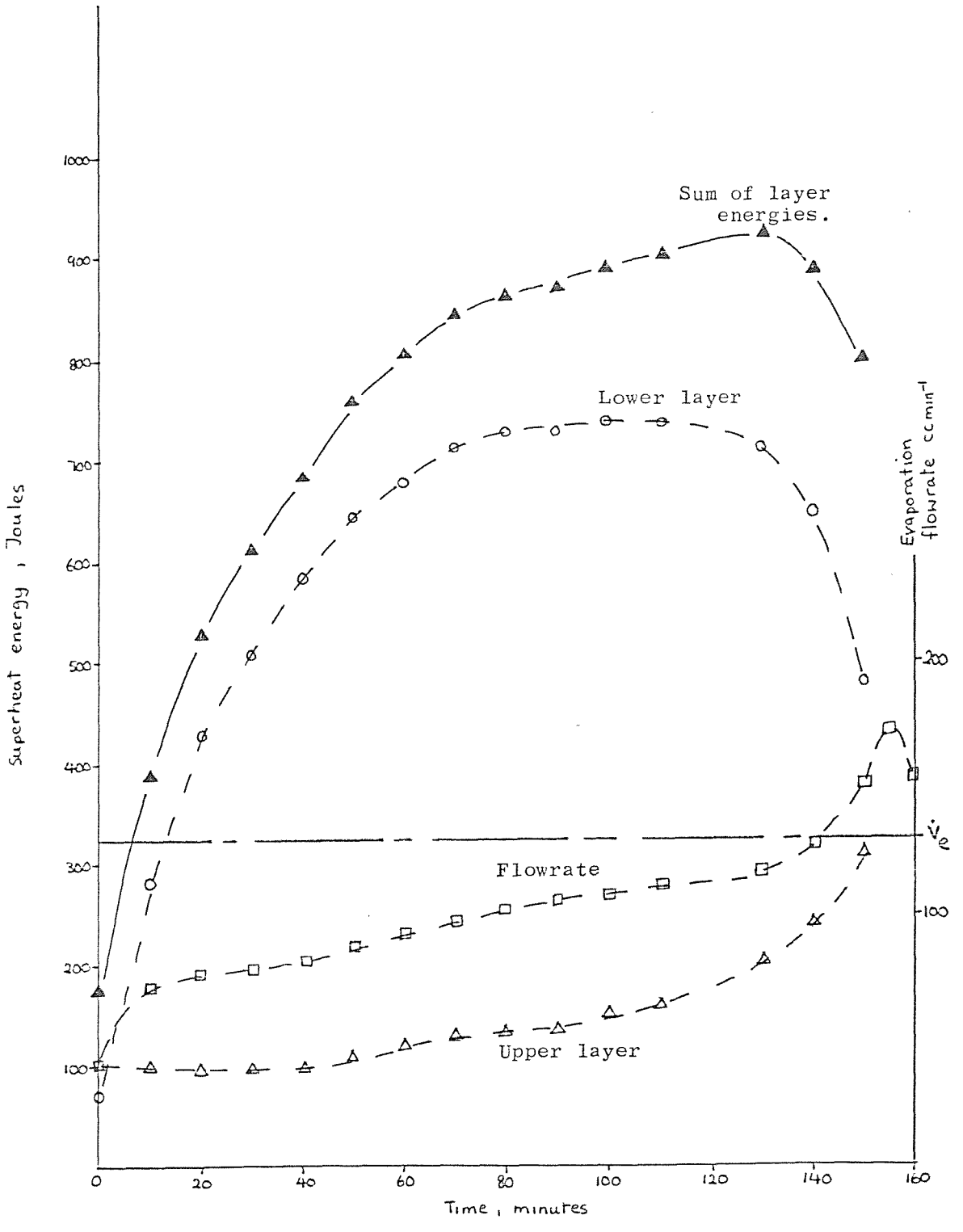

Fig. 4.28. Run c 1. Layer energy accumulation.

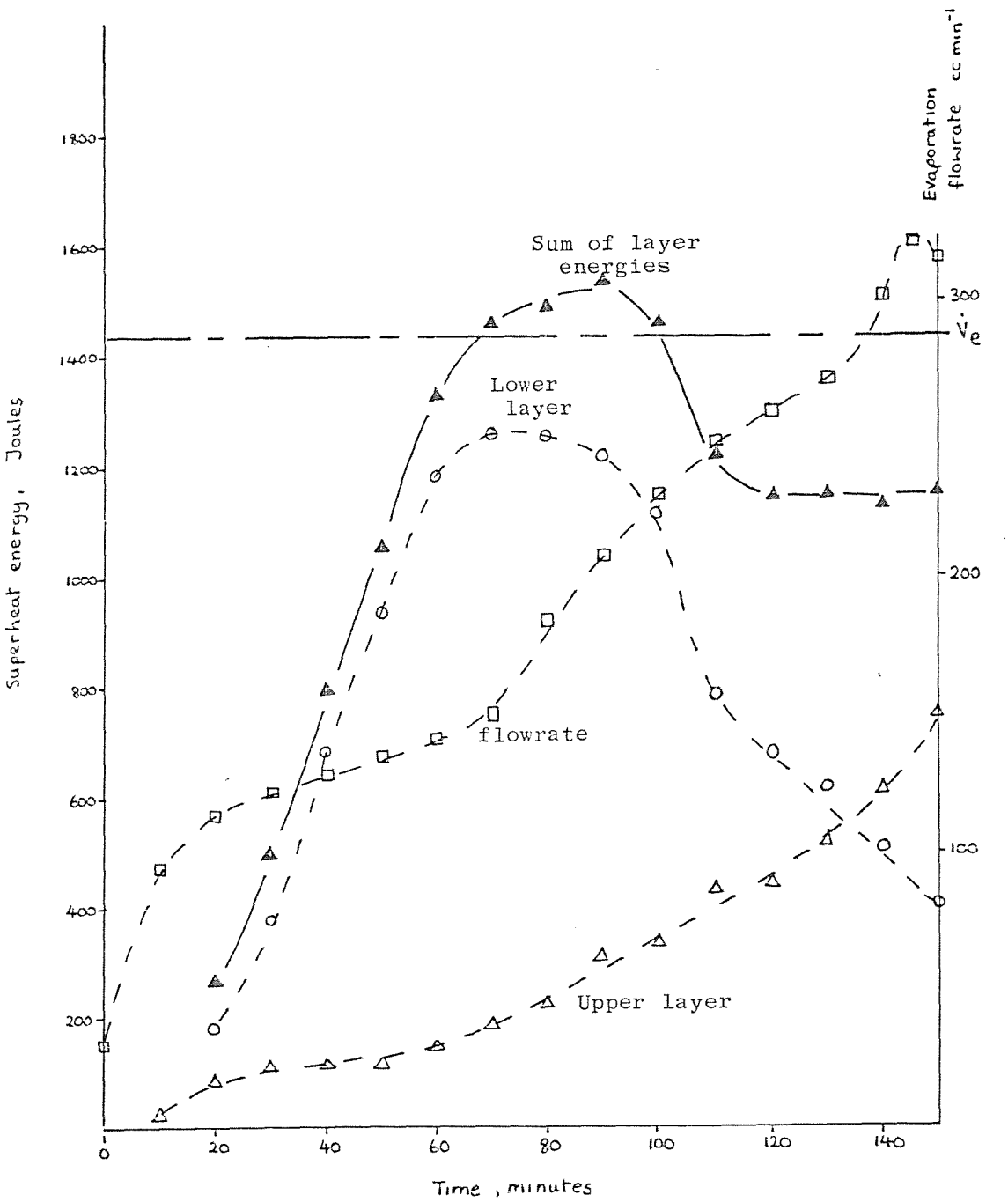

Fig. 4.29. Run c 2. Layer energy accumulation.

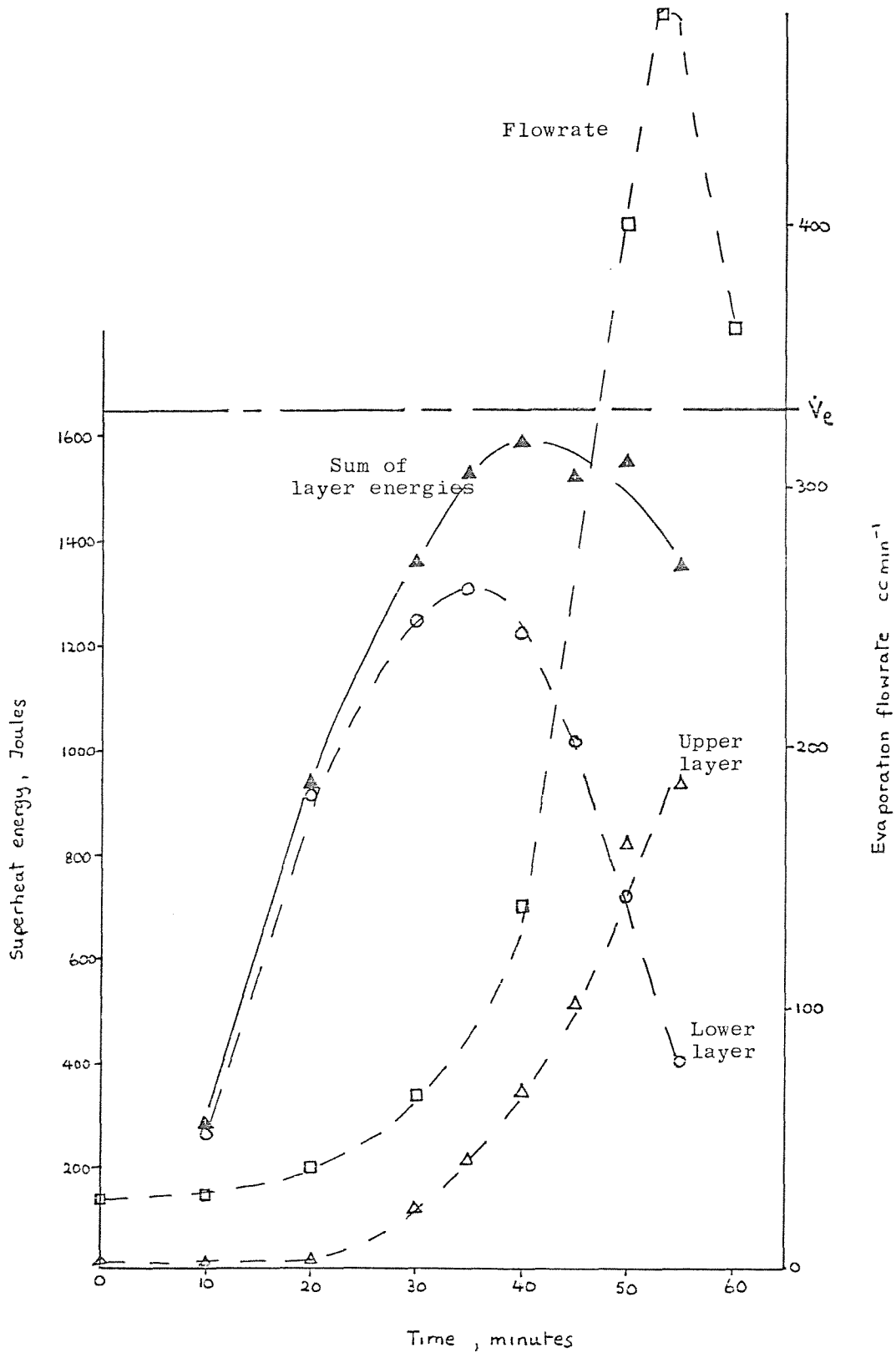

Rebiai (38) obtained a correlation between ΔT_s and the evaporation mass flux $\dot{m}$ for LIN, LOX, LCH_4, LNG and Liquid Argon (LAr). To account for differences in liquid properties, a modified mass flux $\dot{m}_*$ can be used. This is given by:

$$\dot{m}_* = \dot{m} L \left\{ \frac{\nu}{\alpha^2 g \beta_T \rho^3 C_p^3} \right\}^{1/3} \qquad (4.13)$$

Table 4.7 gives the ΔT - mass flux data from some of the experiments in this investigation. The results correspond to equilibrium conditions after the layers in an experiment had mixed. Mixture values of ρ, Cp and α were used, with pure LIN values of β_T, ν and L, in order to calculate $\dot{m}_*$. Fig. 4.30. shows a plot of the $\dot{m}_*$ data from Table 4.7. with data obtained by Rebiai for other cryogenic liquids at low ΔT_s values.

A least squares fit of the $\dot{m}$ data given in Table 4.7 gives:

$$\dot{m} = 2.88 \ \Delta T_s^{1.60} \times 10^{-3} \ Kgm^{-2} \ s^{-1} \qquad (4.14)$$

(4.14) is a useful equation for estimating the variations in flowrate based on the bulk fluid superheat (ΔT_s). Could equation (4.14) predict a sudden very high flowrate?. An experiment was performed to see how well equation (4.14) predicted the flowrate after a stop change in liquid heating conditions. Table 4.8. shows the calculated and measured results. The experiment involved heating a single 340 mm. high column of LIN in the observation dewar, with an initial heat input of 0.44 W. After the evaporation mass flux reached a steady value, the heat input was stepped up to 3.93 Watts. Fig. 4.31. shows the measured mass flux results with $\dot{m}$ calculated using equation (4.14).

4.5. Schlieren Flow-Visualisation Experiments.

The Schlieren flow-visualisation method was used to reveal the convective patterns occuring in columns of evaporating cryogenic liquids. These experiments were

Table 4.7. Equilibrium Evaporative Mass Flux Data.

Experiment	ΔT K	$\dot{m}$ x 10^{-3} $Kgm^{-2}s^{-1}$	$\dot{m}_k$ x 10^{-3} $K^{4/3}$
Run a 2	0.26	0.302	28.97
Run b 2	0.36	0.682	65.23
Run a 3	0.38	0.658	63.12
Run a 4	0.57	1.126	108.19
Run c 1	0.68	1.482	141.73
Run c 2	0.74	1.754	167.95
Run b 5	1.32	4.18	401.53

Table 4.8. Mass Flux Data for Step Change in Heat Input.

Time Minutes	Measured $\dot{m}$ x 10^{-3} Kgm^{-2}s^{-1}	ΔTs K	Calculated $\dot{m}$ x 10^{-3} Kgm^{-2}s^{-1}
0	0.60	0.44	0.77
1	1.27	0.50	0.95
2	1.76	0.59	1.24
3	2.01	0.66	1.48
4	2.31	0.73	1.74
5	2.58	0.78	1.94
6	2.76	0.84	2.18
7	2.78	0.91	2.48
8	2.86	0.97	2.74
9	2.98	1.03	3.02
10	3.15	1.06	3.16
12	3.22	1.13	3.50
15	3.76	1.25	4.12
20	4.16	1.38	4.82
25	4.27	1.44	5.16
30	4.59	1.50	5.51
35	4.92	1.52	5.63
40	4.90	1.54	5.75
45	5.10	1.57	5.93
50	5.32	1.57	5.93
55	5.22	1.61	6.17
60	5.16	1.61	6.17

Fig. 4.30. Measured Equilibrium Mass Flux Results.

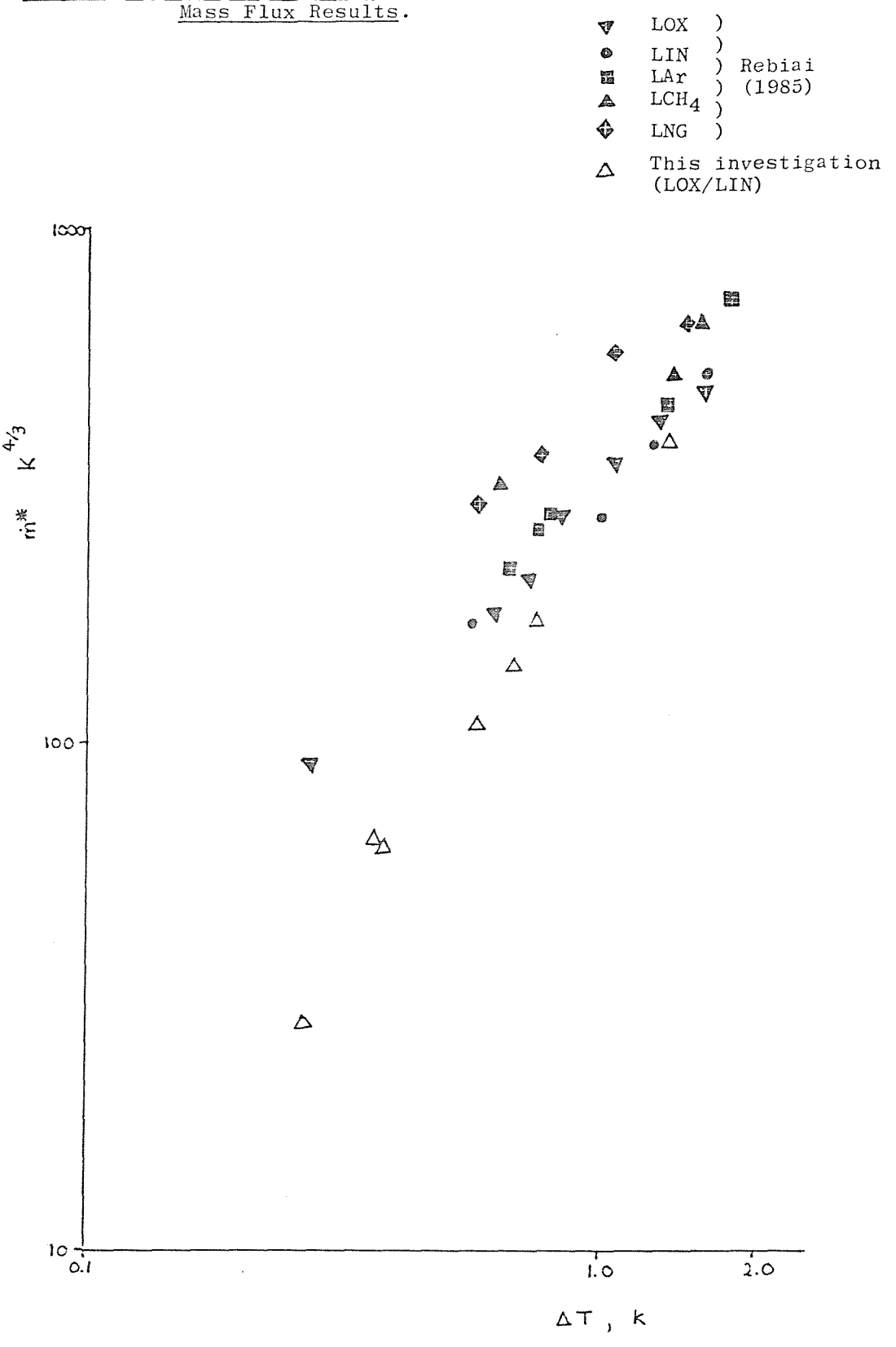

Fig. 4.31. Transient Flowrate Behaviour.

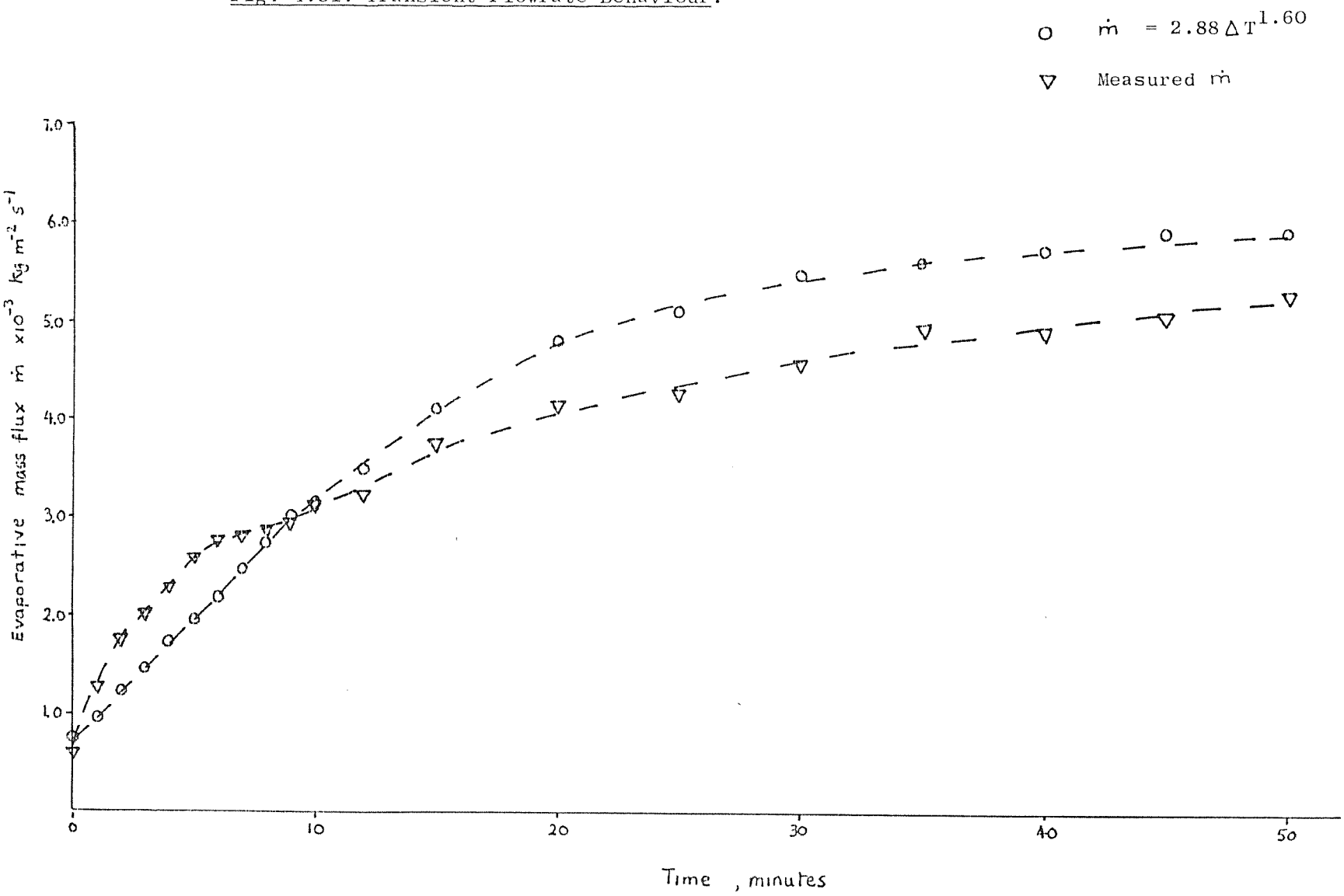

performed in order to relate the flow patterns with the surface evaporation flowrate. The surface flow pattern corresponding to very high vapour flowrates might help to explain the surface evaporation mechanism operating during rollover events.

The Schlieren method is an optical technique that makes refractive index changes visible on a screen. In a layer with no concentration differences, extremes of temperature (i.e. hot or cold regions) appear on the Schlieren image as sharp changes in image brightness. A uniform image brightness therefore means an even temperature distribution. It should be noted that the patterns in photographs taken represent the integrated refractive index variations within the entire depth of the liquid. The greatest temperature variations however, occur at the liquid-vapour or liquid-liquid interface.

Visualisation studies were performed on single-layer LIN columns, and two-layered LIN over LIN plus 2% ∪/∪ LAr systems. Photographic prints 1 to 4 show the liquid-vapour surface flow patterns for a typical single-layer LIN column experiment. The pool of liquid was about 120 mm deep. The diameter of the view shown in all photographs is 40 mm, real scale. Prints 5 to 8 show the liquid-vapour and liquid-liquid flow patterns for a two-layered experiment. Table 4.9. summarises the evaporative mass fluxes corresponding to prints 1 to 8. Print 5 shows the layer behaviour for very low surface flowrate conditions. Prints 6 to 8 reveal the behaviour of the liquid-vapour interface superimposed on the liquid-liquid interface pattern in each photograph.

Print 9 clearly shows the front of the boundary layer flow developed in the lower layer of a two-layered experiment, when the lower layer received a step input of heat. The boundary layer front is shown travelling parallel to the liquid-liquid interface. Print 10 shows an interesting surface instability associated with a subcooled LIN/LAr pool. The conditions leading up to this photograph were as follows:

Table 4.9. Evaporative Mass Fluxes Corresponding to Schlieren Prints.

Print Number	Time Minutes	Evaporative Mass Flux x 10^{-3} Kg m^{-2} s^{-1}	
1	0	0.39	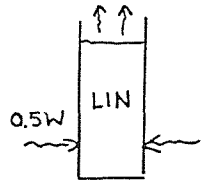
2	12	0.99	
3	20	1.88	
4	45	2.60	
5	0	< 0.15	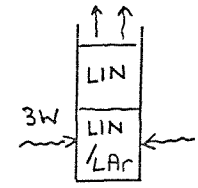
6	52	0.34	
7	150	2.03	
8	210	3.98	
10	40	1.99	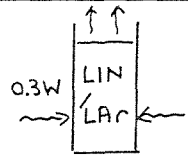

Print 1: Schlieren flow-visualisation print showing top view of LIN column. Surface evaporation mass flux = 0.39×10^{-3} Kg $m^{-2}s^{-1}$. No heat supplied, time = 0 minutes.

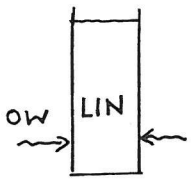

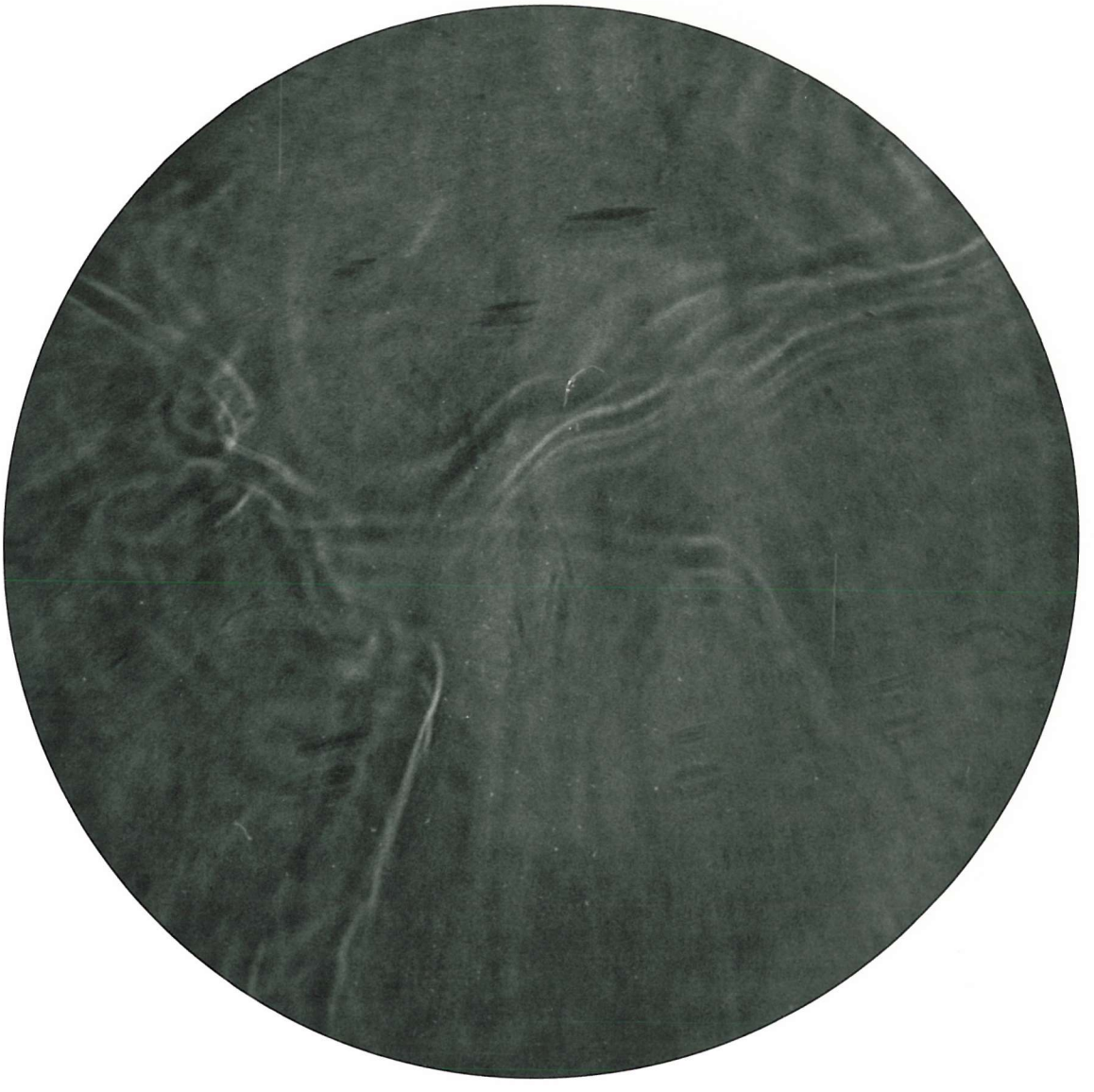

Print 2: Schlieren flow visualisation print showing top view of LIN column. Surface evaporation mass flux = 0.99×10^{-3} Kg $m^{-2}s^{-1}$ Time = 12 minutes after heat supplied.

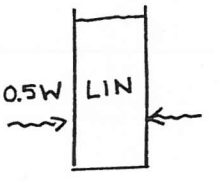

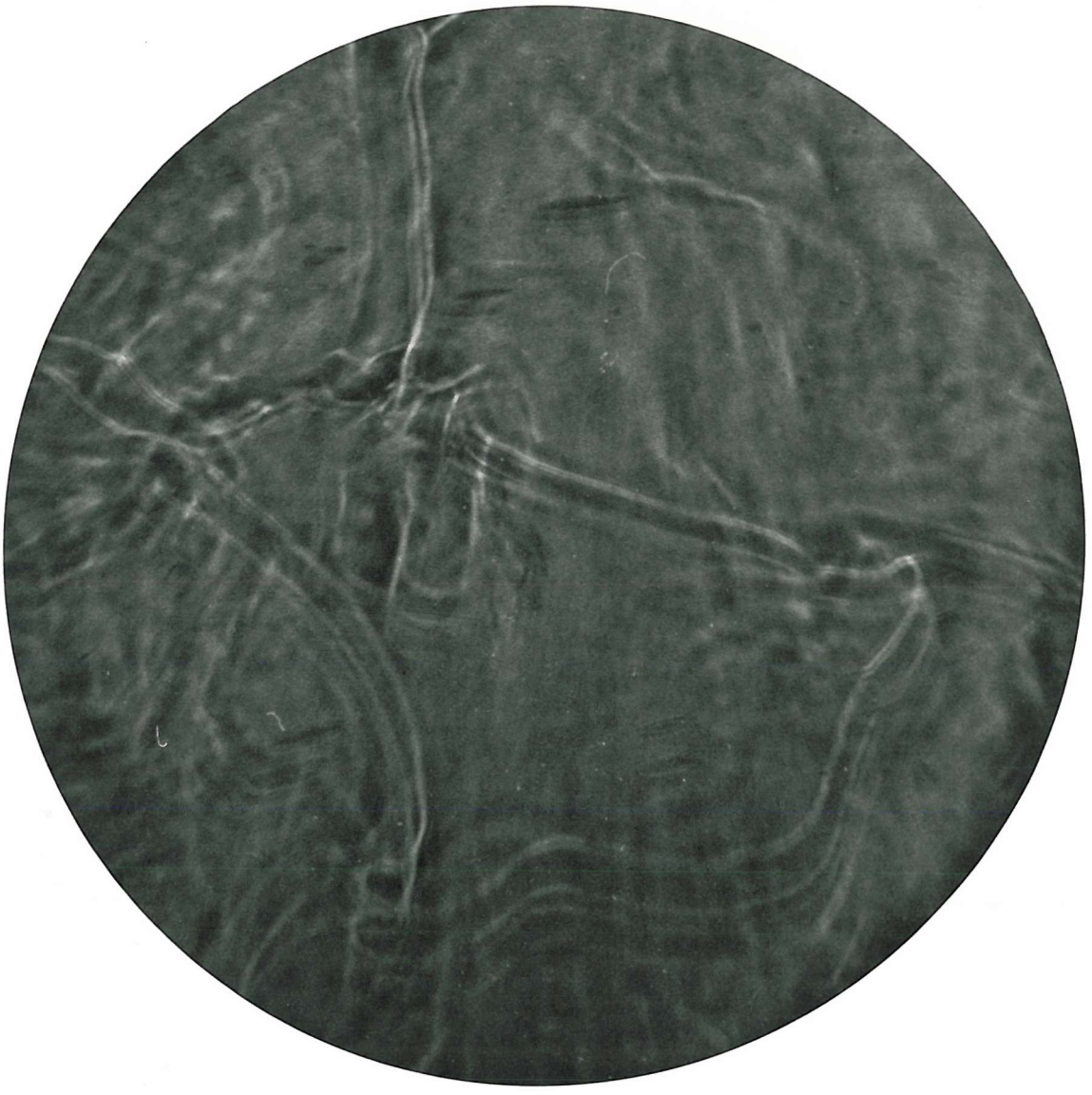

Print 3: Schlieren flow-visualisation print,
showing top view of LIN column.
Surface evaporation Mass flux =
1.88×10^{-3} Kg $m^{-2}s^{-1}$
Time = 20 minutes after heat supplied.

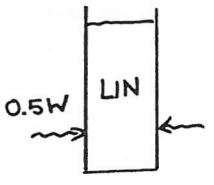

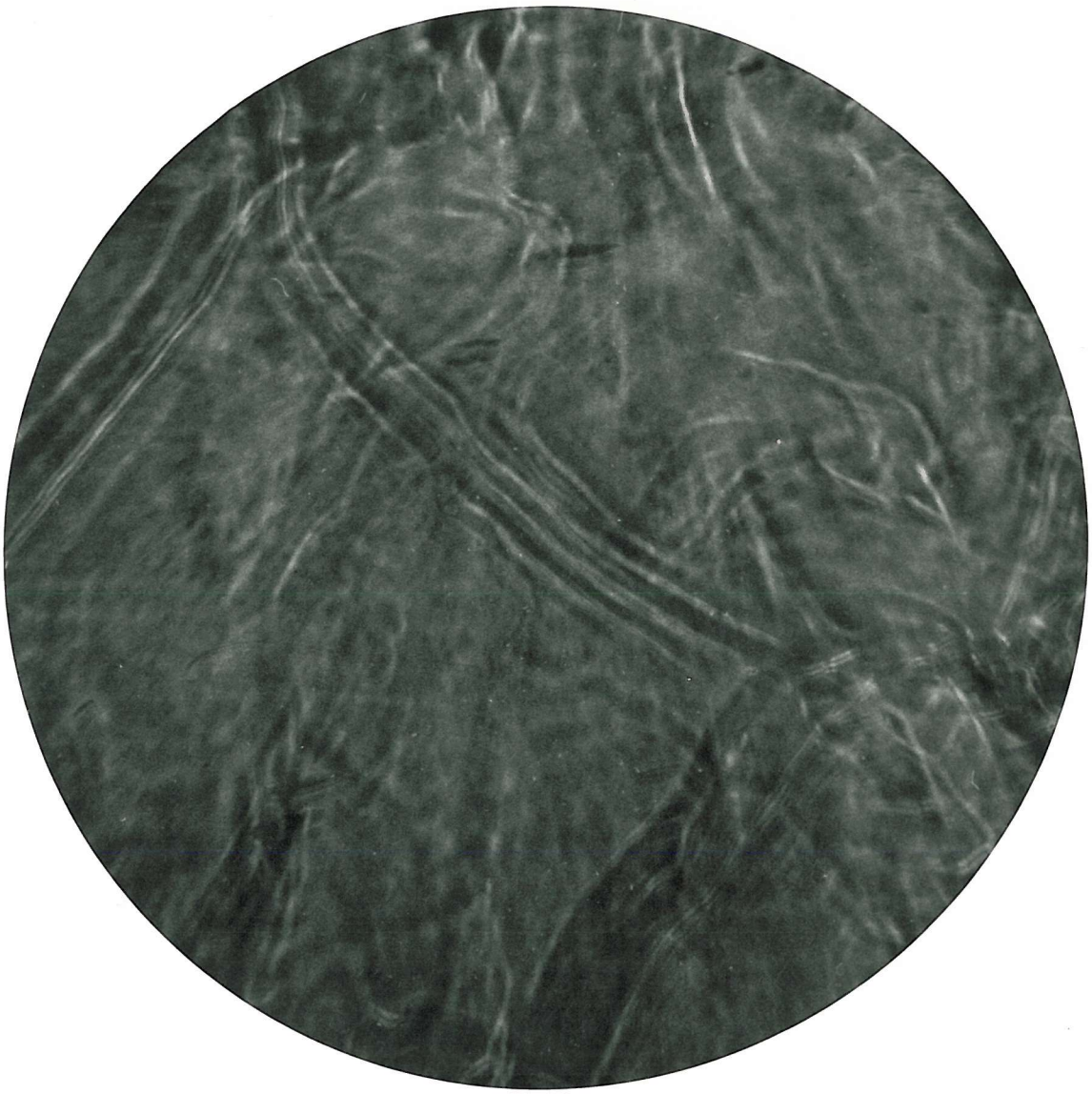

Print 4: Schlieren flow-visualisation print,
showing top view of LIN column.
Surface evaporation mass flux =
2.60×10^{-3} Kg $m^{-2}s^{-1}$
Time = 45 minutes after heat supplied.

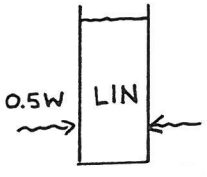

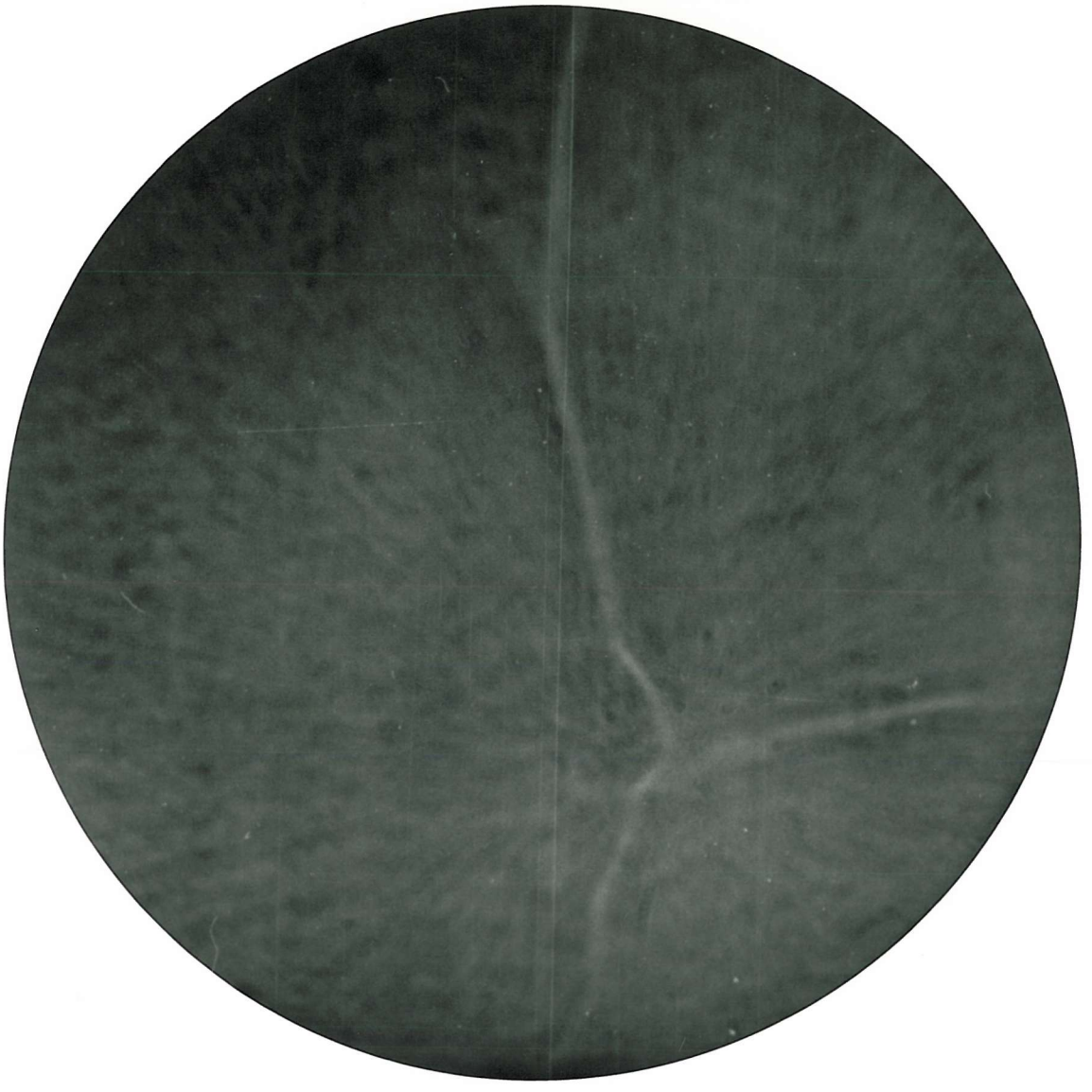

Print 5: Schlieren flow-visualisation print, showing top view of a two-layered LIN over LIN/LAr column. Surface evaporation mass flux = 0.15×10^{-3} Kg $m^{-2}s^{-1}$ No heat supplied. Time = 0 minutes.

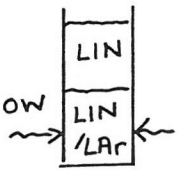

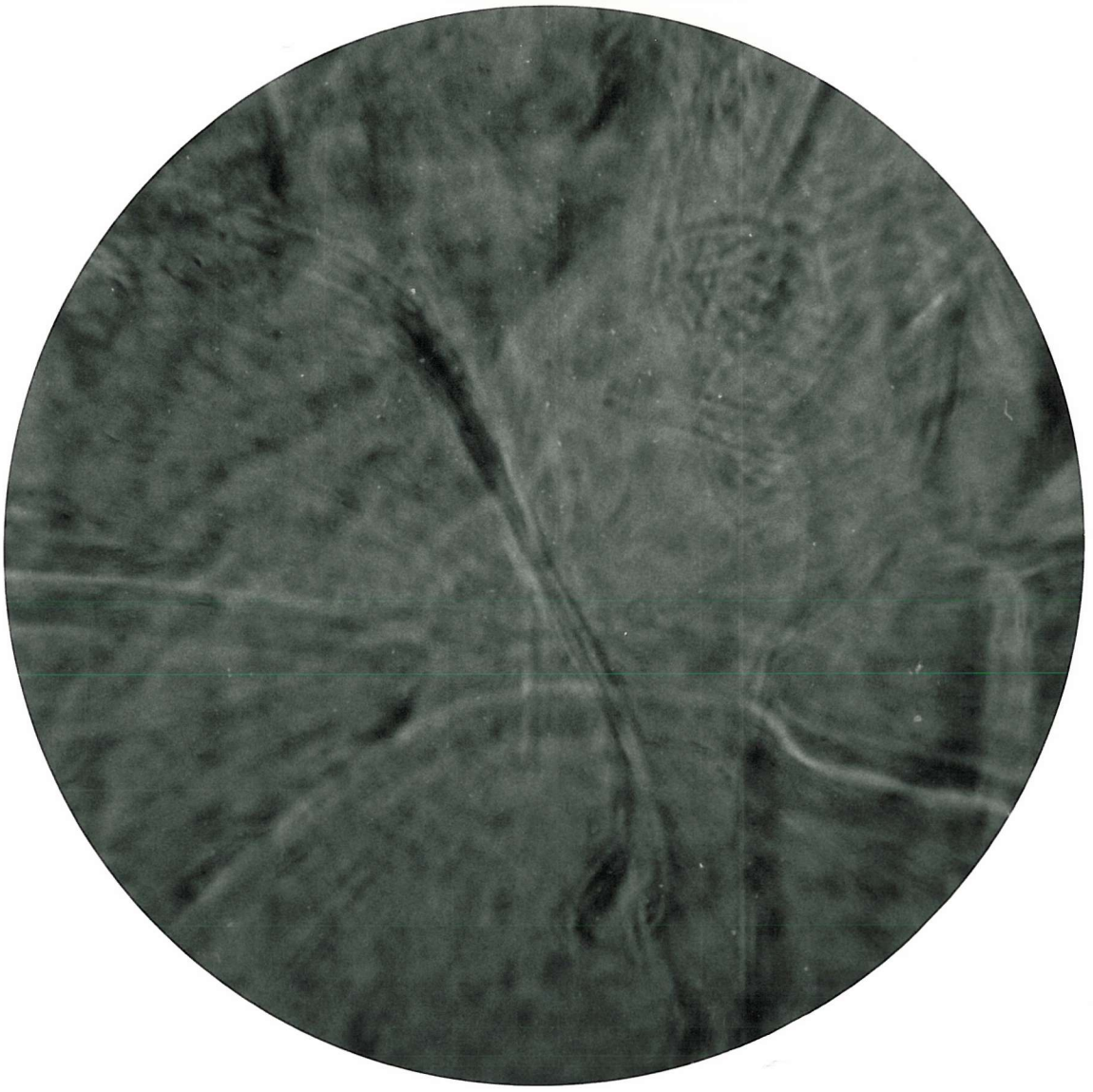

Print 6: Schlieren flow-visualisation print, showing top view of a two-layered LIN over LIN/LAr column. Surface evaporation mass flux = 0.34×10^{-3} Kg $m^{-2}s^{-1}$.
Time = 52 minutes after heat supplied.

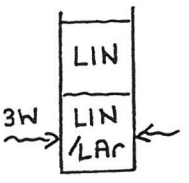

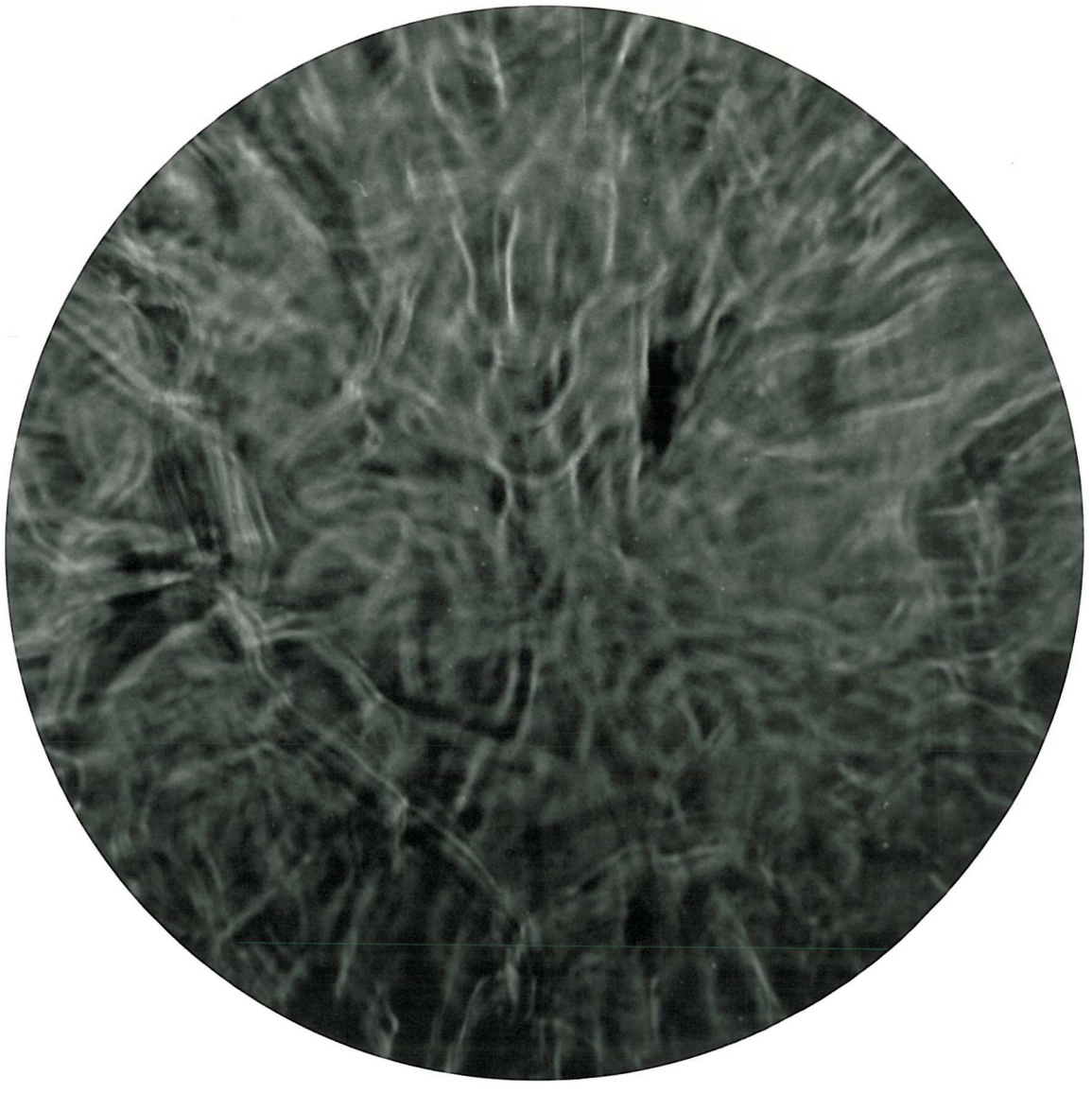

Print 7: Schlieren flow-visualisation print, showing top view of a two-layered LIN over LIN/LAr column. Surface evaporation mass flux = 2.03×10^{-3} Kg $m^{-2}s^{-1}$.
Time = 150 minutes after heat supplied.

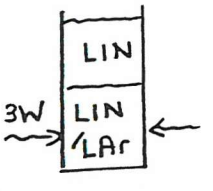

Print 8: Schlieren flow-visualisation print, showing top view of a two-layered LIN over LIN/LAr column during rollover. Surface evaporation mass flux = 3.98×10^{-3} Kg $m^{-2}s^{-1}$.
Time = 210 minutes after heat supplied.

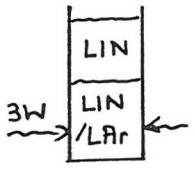

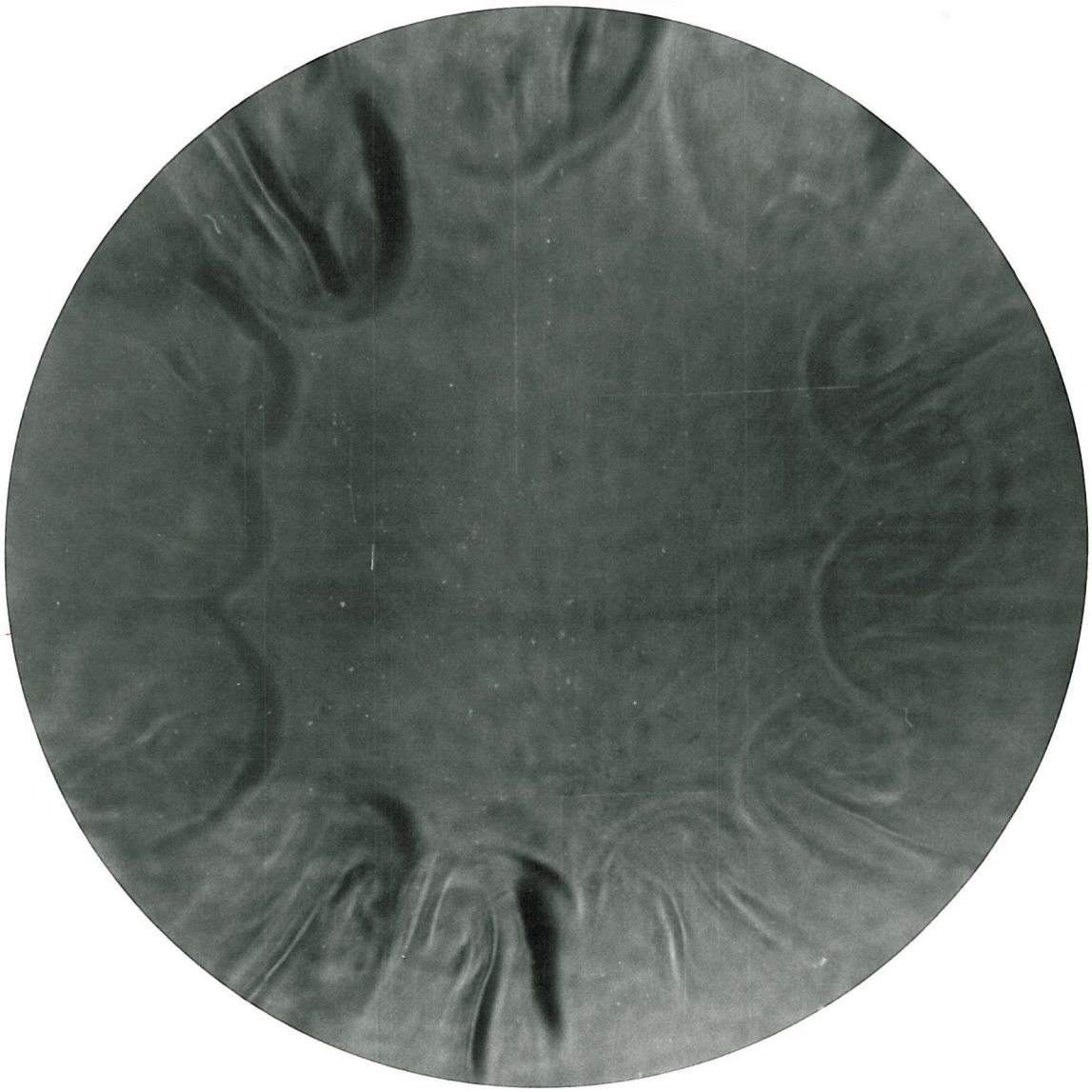

Print 9: Schlieren flow-visualisation print showing boundary layer movement after heat was suddently applied to the bottom layer. Boundary layer motion is at liquid-liquid interface of two-layered system. Before heating, evaporation mass flux = 0.15×10^{-3} Kg $m^{-2}s^{-1}$.

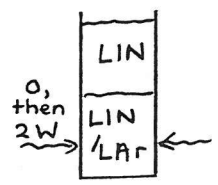

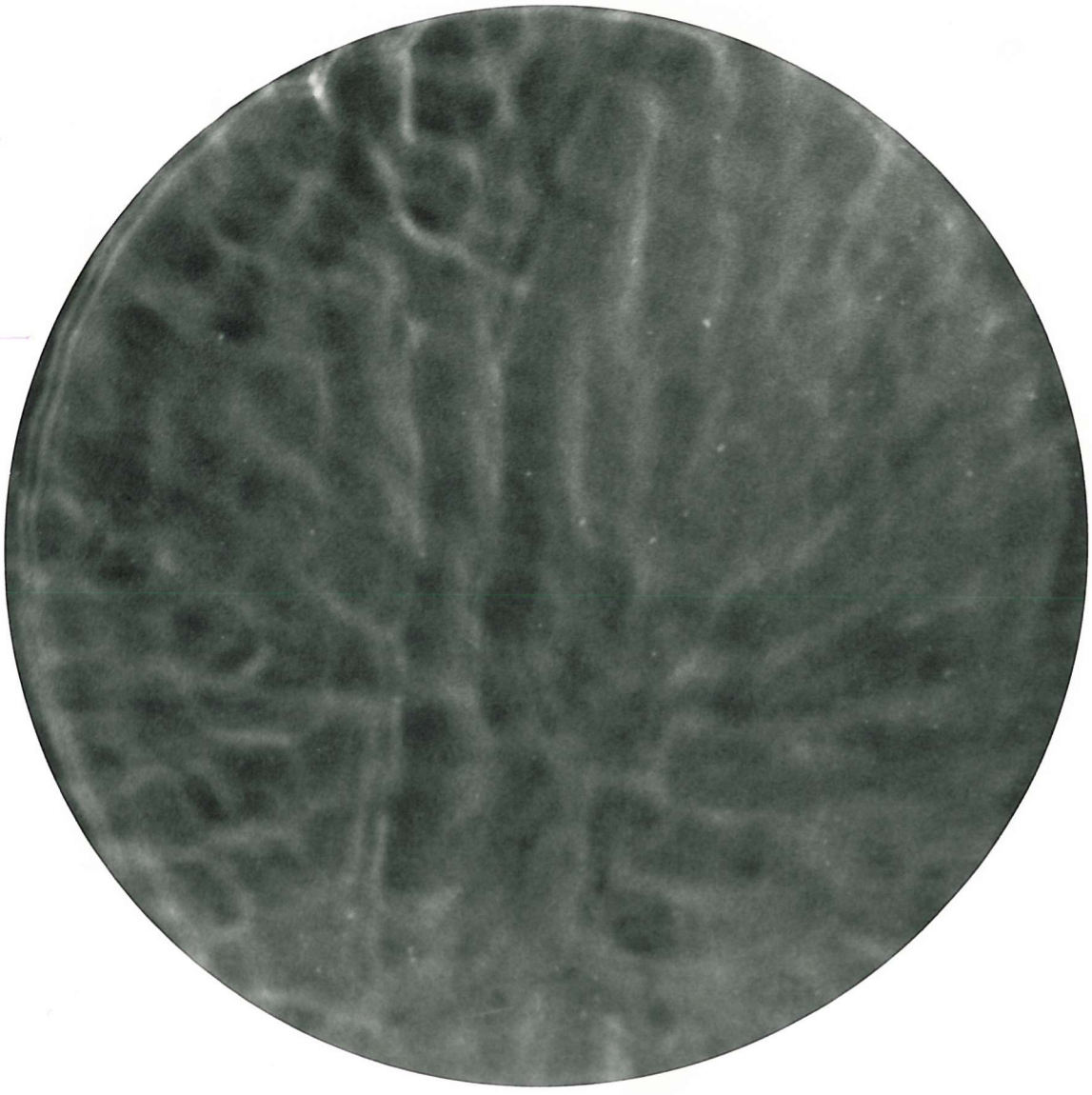

Print 10: Schlieren flow visualisation print showing surface instability after vapour space above fluid was well pumped and liquid heated for 40 minutes. Surface evaporation mass flux = 1.99×10^{-3} Kg $m^{-2}s^{-1}$.

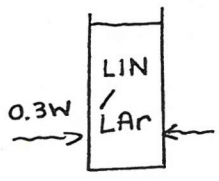

A two-layer experiment was in progress when bubbles were created in the dewar, so this particular experiment was abandoned. The vapour space above the liquid was then well pumped, and after 2 minutes, a low heat input (0.3W) was supplied to the liquid via the bottom side wall heater. Photograph 10 was taken after 40 minutes of heating.

4.6. Uncertainty of Data.

The results presented have various degrees of uncertainty due to the limitations in the experimental apparatus, and instrument display reading errors.

The uncertainty of calculated results were found using a method presented by Kline and McClintock (39). This approach assumes that a set of primary measurements are made with uncertainties expressed with 20 to 1 odds (95% confidence level). The result X is a function of the independent measurements, i.e.:

$$X = f(x_1, x_2, x_3, \ldots\ldots\ldots x_n) \qquad (4.15)$$

ω_x is the uncertainty of the result and ω_1, ω_2, ω_3 ..... ω_n are the uncertainties in the independent variables. If the uncertainty in the independent variables are all given with the same odds, then the uncertainty in the result ω_x is:

$$\omega_x = \left[\left(\frac{\partial X}{\partial x_1}\omega_1\right)^2 + \left(\frac{\partial X}{\partial x_2}\omega_2\right)^2 + \ldots\ldots\left(\frac{\partial X}{\partial x_n}\omega_n\right)^2\right]^{1/2} \qquad (4.16)$$

1) Concentration Uncertainty.

From observations made during experimental runs, the uncertainty of oxygen concentration measurements recorded at 2 minute intervals was $\pm$ 0.05 % σ/σ The manufacturers of the oxygen analysing system quote an instrument accuracy of $\pm$ 0.01% σ/σ oxygen, if the sensor head calibration and measurement temperatures differ by less than 5^{o}C.

2) Temperature Uncertainty.

The saturation temperature Ts for liquid mixtures was calculated using:

$$T_S = 7.111\ x_1 + 77.36 \qquad (4.17)$$

suppose $x_1 = 5 \pm 0.05\%$ LOX v/v, then:

$T_S = 77.72$ K = X. Hence:

$\frac{\partial X}{\partial x_1} = 7.111$ and $\omega_1 = \pm 0.0005$.

$$\omega_x = \left[(7.111 \times 0.0005)^2 \right]^{1/2} = \pm 0.0036 \text{ K}$$

For $T_S = 77.72$ K, this represents an uncertainty amounting to $\pm$ 0.05%.

The uncertainty of the thermocouple emf's was estimated to be $\pm$ 1.5 μV, accounting for reference junction temperature variations, and voltage reading errors. The fluid temperature T was calculated using the measured emf e and reference emf e_r corresponding to T_S, i.e:

$$T = \frac{e - e_r}{16} + T_S \qquad (4.18)$$

From equation (4.18),

$$\frac{\partial X}{\partial e} = \frac{1}{16\mu V}, \quad \frac{\partial X}{\partial e_r} = \frac{1}{16\mu V}, \quad \frac{\partial X}{\partial Ts} = 1$$

and $\omega_e = \pm 1.5\mu V$, $\omega_{e_r} = \pm 1.5\mu V$, $\omega_{T_S} = \pm 0.0036$ K

$$\therefore \omega_x = \left[\left(\frac{1.5}{16}\right)^2 + \left(\frac{1.5}{16}\right)^2 + (0.0036)^2 \right]^{\frac{1}{2}} = \pm 0.13 \text{ K}.$$

At a temperature of 77.4 K, the temperature uncertainty amounts to $\pm$ 0.2%

3) Flowrate Uncertainty.

The estimated uncertainty of flowmeter readings was $\pm$ 10% of the reading, based on the flowrate fluctuations during the various stages in an experiment. Fig. 4.32 shows flowrate values recorded using the Schell flowmeter,

compared with reference values obtained using the apparatus shown in Fig. 4.33. The Schell flowmeter specifications quote an accuracy (including linearity) of $\pm$ 0.5% of full scale.

The heat leak down the inner jacket of the visualisation dewar contributed to the net evaporation flowrate. One might ask how this heat leak value compared with the total heater input. If we assume that the major heat leak into the liquid was via conduction down the dewar wall, an expression defining the heat flow $\dot{Q}c$ down a tube of length L, and solid cross-sectional area A, is given by:

$$\dot{Q}c = \frac{\dot{m}_v C_p (T_h - T_c)}{\exp(\dot{m}_v C_p L / K_T A) - 1} \qquad (4.19)$$

where $\dot{m}_v$ = mass flow of vapour

C_p = specific heat of vapour

K_T = Thermal conductivity of wall (assumed to be temperature independent).

The vapour temperature is assumed to be the same as that of the wall. Typical initial flowrates were 20 cc min^{-1}. At 290K, the density of nitrogen vapour ρ_{N_2V} = 1.18 Kgm^{-3}, hence the vapour mass flowrate $\dot{m}_v$ is given by:

$$\dot{m}_v = \frac{20 \times 10^{-6} \times 1.18}{60} = 3.933 \times 10^{-7} \text{ Kg. } 5^{-1}$$

Using the following values to calculate $\dot{Q}c$;

C_p nitrogen vapour $\sim$ 1.05 KJ $Kg^{-1}K^{-1}$

$T_h - T_c$ = 290 - 77 = 213 K

L in dewar typically = 0.4 m.

K_T of glass = 0.4 Wm^{-1} K^{-1} (at 77K)

Thickness of inner jacket wall t = 2.5 mm.

Inner wall radius = 3.25 cm.

Wall cross-sectional area A = 5.105 x 10^{-4} m^2

$\therefore$ $\dot{Q}c$ = 0.071 W or 70 mW.

Fig. 4.32 Schell flowmeter linearity of reading.
(The broken line represents ideal behaviour).

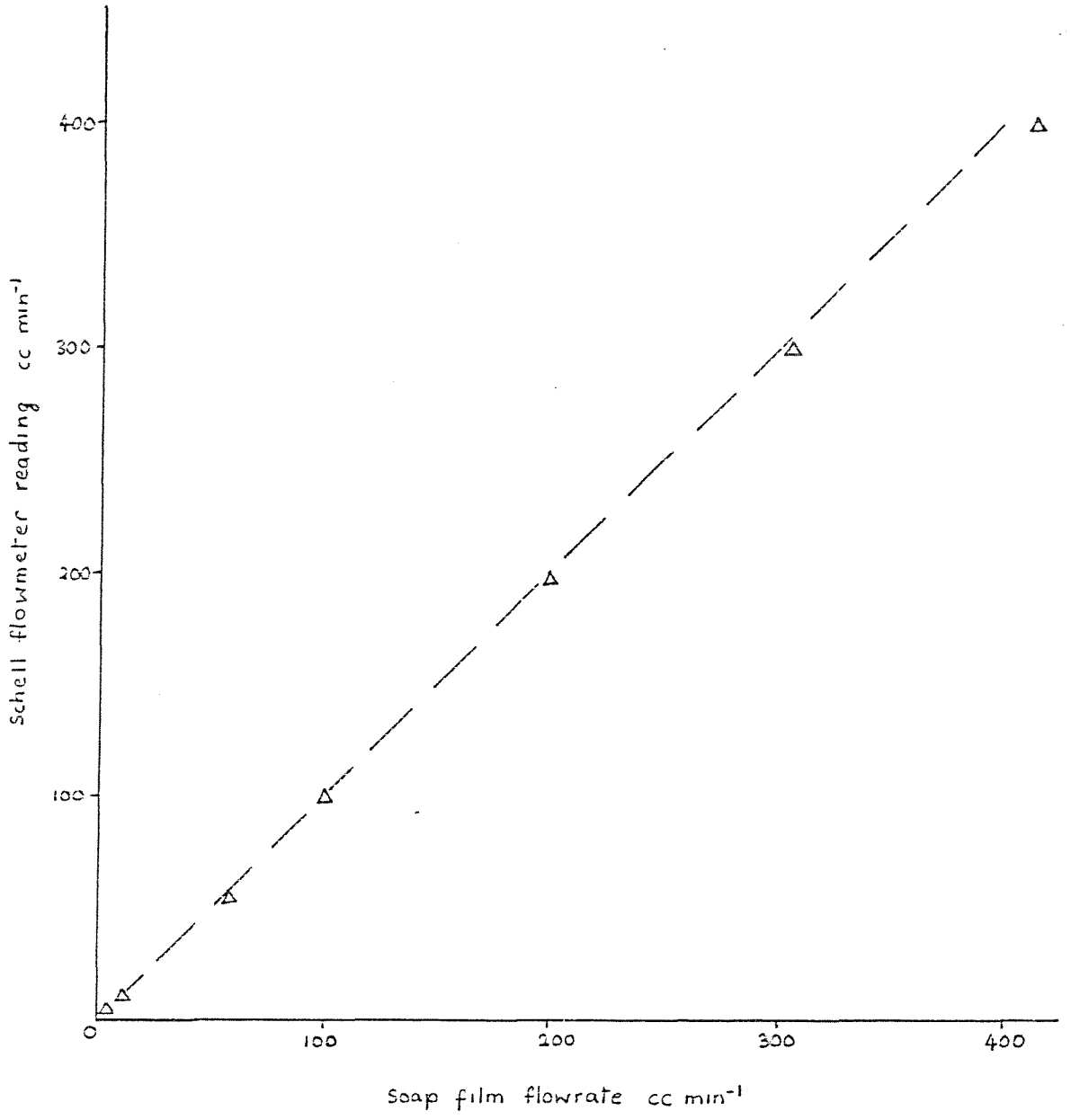

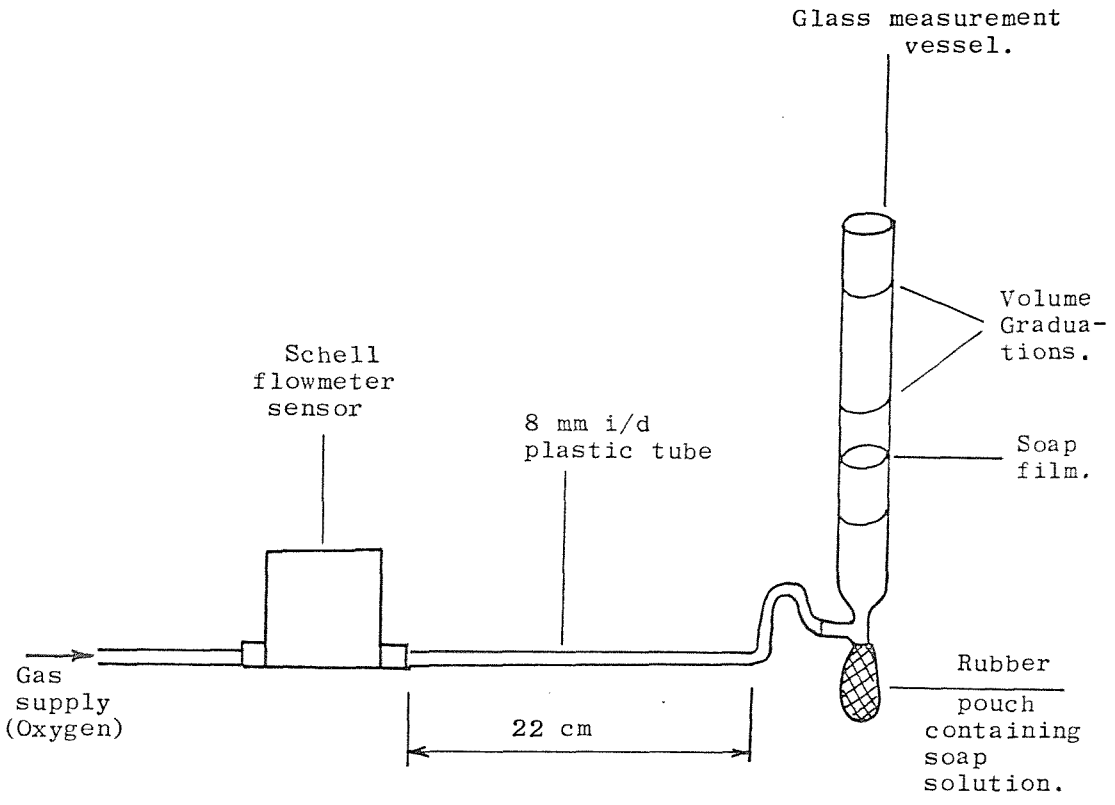

Fig. 4.33. Apparatus used to check Schell flowmeter readings.

For a 60 cc min^{-1} flow, $\dot{Q}c$ = 25 mw, and for a flowrate of 100 cc min^{-1}, $\dot{Q}c$ = 8 mw. In low heat input experiments with heat inputs $\dot{Q}$ typically 120 mw, and at low flowrate values, the heat inleak to a small layer of the top layer may have amounted to 50% of the heater input value. For higher heating experiments ($\dot{Q} \sim$ 1000 mw), Qc would only have been 7% of $\dot{Q}$, and even less at higher flowrate conditions.

The uncertainty of additional derived results are given in Table 4.10. The main contribution to the interface heat transfer uncertainty was due to the uncertainty in the heater input value. The uncertainty in the interface mass transfer would have been reduced by reducing the mass uncertainty and increasing the time period used in calculations. The interface heat and mass transfer uncertainties quoted in Table 4.10 correspond to values of the stability parameter $R < 2$. For $R > 2$, the uncertainties increase, and amount to $\pm$ 100% or more, which accounts for the scatter of data points shown in Figs. 4.22 and 4.23.

Table 4.10. Uncertainty in derived results.

Variable	Nominal Value	Uncertainty	% Uncertainty
Layer density	810 Kgm^{-3}	$\pm$ 0.1 Kgm^{-3}	$\pm$ 0.01%
Layer volume	332 cc	$\pm$ 26.3 cc	$\pm$ 6.6%
Layer Mass	0.27 Kg.	$\pm$ 0.02 Kg	$\pm$ 7%
Heater input	1.0 W.	$\pm$ 0.1 W.	$\pm$ 10%
Interface heat transfer.	600 mw.	$\pm$ 110 mw.	$\pm$ 18%
Interface Mass transfer.	0.10 gm S^{-1}	$\pm$ 0.047 gm S^{-1}	$\pm$ 50%

5.0. DISCUSSION

The rollover experiment results will be interpreted by discussion under the following headings:

1) Liquid-liquid interface behaviour.

2) Interface mass and heat transfer.

3) Vapour flowrate behaviour.

4) Schlieren flow-visualisation results.

Each discussion will take into account the inter-relation with the other headings. The interfacial heat and mass transfer for example, was dependent on the form of the liquid-liquid interface. The peak vapour flowrate depended on the thermal overfill of the system before rollover, and the variations in the surface flowrate had correspondingly different surface convective flow patterns.

5.1. Liquid-Liquid Interface.

The intermediate layer between the convecting layers remains at the same level throughout most experiments, before a rapid drop in level is observed, corresponding to the onset of enhanced mixing preceding the rollover peak. This observation, and the gradual thinning of the layer is in agreement with the results of Sugawara et al (12), for an LNG system. The fastest breakdown and descent of the intermediate layer corresponds to small initial layer density differences and high heat inputs.

The interface movement in predominantly top or bottom layer heated experiments (Figs. 4.17 and 4.18) shows the process of entrainment occurring in the intermediate layer. In bottom layer heated experiments, eddies produced by the well mixed convecting lower layer pierce the intermediate layer, trapping some of it between them, and hence raise the bottom layer interface boundary. The top layer interface boundary in this case remains at the same level because there is no convective loop in the top layer (see Fig. 5.1a). Motion occurs in the top

layer when the heat transfer from the bottom layer is sufficient to start a convective loop. These processes were clearly observed during layer flow visualisation experiments.

In predominantly top layer heated experiments, top layer convective rolls entrain elements of the intermediate layer into the convective layer, as shown in Fig. 5.1b. The process is similar to the bottom layer heated entrainment process, but not as effective, because the downward convective loops produce less turbulence at the intermediate layer, than the higher momentum boundary layer flows created by lower layer heating.

In combined top and bottom layer heated experiments, the total heat input to both layers was less than that supplied to one layer in predominantly top or bottom layer heated experiments. This explains why the intermediate layer didn't thin down so quickly, before the intermediate level dropped.

The drop in the intermediate layer can be explained by an observation made during flow-visualisation experiments. Near density equalisation (stability parameter $R \leq 2$), portions of liquid were seen to detach from bottom layer rolls entering the intermediate layer. These blobs of liquid were quickly mixed into the intermediate layer, due to the turbulent (i.e. wavy) motion of the layer as the layer densities equalised. The volume of the bottom layer therefore decreases due to the loss of these elements, so the lower layer interface boundary moves down. The top layer via enhanced entrainment of the intermediate layer, increases in volume, so the intermediate layer moves downwards.

Salt water entrainment experiments performed by Cromwell (40) using a mechanical stirrer in the top layer, showed that the well mixed layer bounded by a sharp interface, moved downwards, away from the stirrer.

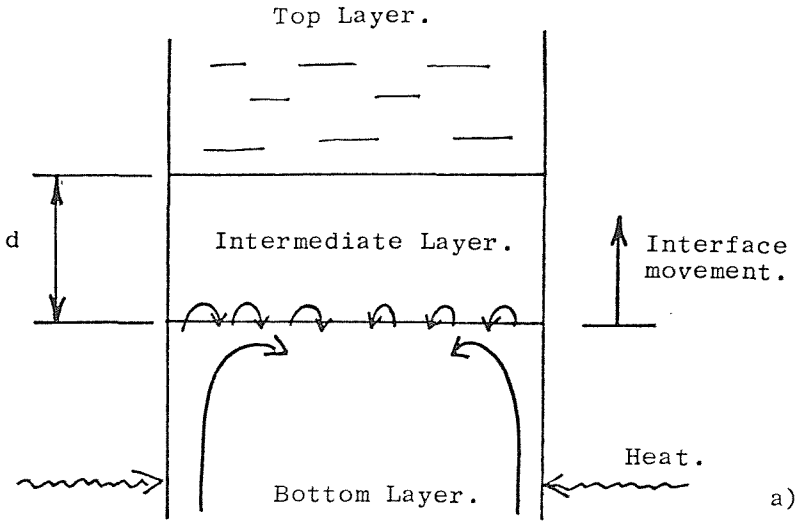

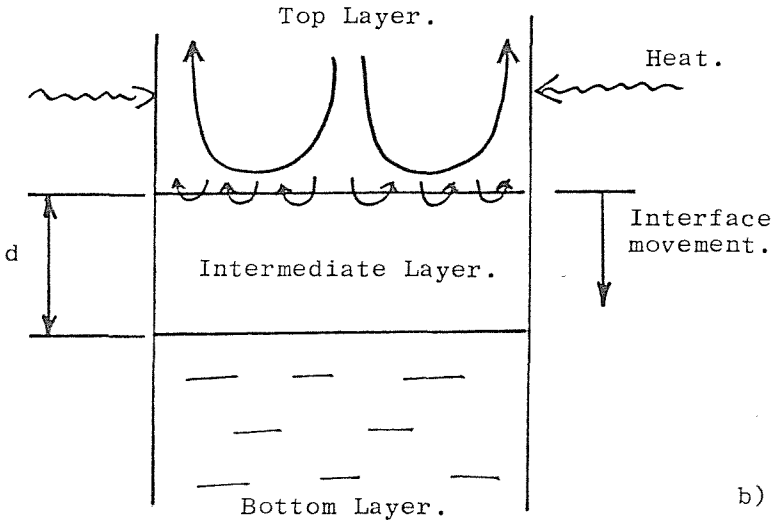

Fig. 5.1. Diagrams illustrating the thinning process of the intermediate layer of thickness d.

a) Bottom layer heating.

b) Top layer heating.

In other entrainment experiments reported by Turner (6), if both layers are stirred at the same rate, the interface bounding each layer remains at the same level. The entrainment rates and interface motion observed in these experiments, cannot however, be related to a Double-Diffusive system. The reason for this is that Double-Diffusive layers observed in this and other investigations, are separated by an intermediate layer, which controls the mixing rates between layers. Also, the turbulence created by a stirrer would not necessarily create the same turbulence as that produced by a heat induced convective flow.

The entrainment process observed in the experiments of this investigation are in contrast to the rapid mixing pattern reported by Nakano et al (16), in which the lower layer boundary layer flow penetrates up to the top layer surface. A boundary layer penetration up to the liquid-vapour interface was not possible in the experiments performed in this investigation, due to the small length scales involved. Consider the Grashof number of the bottom layer boundary layer flow in a "typical" experiment. If we assume the heater wall to be a vertical plane surface of length L = 9 cm, and a total heat input of 0.6 W. creating a wall-liquid temperature difference of 0.03 K., then using LIN properties, $Gr \sim 30 \times 10^6$. For Pr = 2.32 (LIN), this gives a Rayleigh number of 70×10^6, suggesting laminar flow. An LNG container may have a typical length scale of at least 10 metres. The boundary layer flow at the liquid-liquid interface would therefore be turbulent ($Ra > 10^9$), and have far greater momentum at the liquid-liquid interface.

The intermediate layer behaviour shows two general stages. The first stage involves the slight thinning of the intermediate layers by the convective flows bounding the layer. The second stage corresponds to the intermediate layer moving in a wavy motion, falling in level, and eventually breaking down. These two stages may be likened to the constant and variable regime described by Huppert (27). The variable regime in Huppert's analysis

corresponds to the density equalisation of the intermediate layer and one of the convecting layers.

5.2. Heat and Mass Transfer.

The form of the intermediate layer affected the rates of heat and mass transport between the convective layers, as observed by Sugawara et al (12). In the constant regime ($R > 2$), the heat flux between layers is lower than the theoretical heat flux based on the temperature difference between layers, so the convective layers are effectively independent systems. In the bottom layer heated experiments for example, convective motion occurred in the top layer when the intermediate layer entered the variable regime (see Fig. 4.19), corresponding to $R < 3$.

Referring to Fig. 4.19, three basic heat transfer stages can be seen, and are summarised as follows:

1) Low steady surface evaporation. The bottom layer convective cell is established. The maximum heat transfer to the top layer is via conduction through the intermediate layer. The temperature difference between layers steadily increases with time ($R > 2$ or 3).

2) Steadily increasing evaporation. Heat transfer between the top and bottom layer is sufficient for a convection loop to start in the top layer. The bottom layer interface boundary stops rising, and the intermediate layer moves in a wavy motion. The temperatures of the top and bottom layers increase at the same rate. ($2 < R < 3$).

3) Large scale mixing accompanies a rapid increase in evaporation flowrate. Eventually, top and bottom layers are thoroughly mixed, and a single convective flow loop is present. A peak flowrate is recorded, followed by an exponential decay in the flowrate, eventually reaching an equilibrium value. The intermediate layer rapidly drops in level during this process.

The processes in a top and bottom layer heated experiment (Fig.4.20) are similar to those described above, except that the initial steady evaporation flowrate is higher than that for bottom layer heating. Between 20 and 50 minutes the stability parameter drops rapidly from a value of $\sim$ 6 down to 2, due to the destabilising effect of the increase in temperature difference between layers. As heat and mass transfer are improved (i.e. after 50 minutes), the temperature difference between layers stops increasing and eventually decreases. The stability parameter still decreases slightly due to the decrease in concentration difference between layers. Fig. 4.20 clearly shows that when the two layer system enters the variable regime $R \lesssim 2$, heat and mass transfer between layers is enhanced due to the now unstable (i.e. wavy) intermediate layer.

Turner (14) attributed the increase in heat transfer observed in salt-water experiments, to the distortion of the interface by waves, which increases the interface surface area, and hence leads to higher heat transfer. A numerical analysis performed by Herring (41), (42), on three-dimensional convection between parallel plates, offers another explanation. Herring considered free boundaries (zero stress), and rigid boundaries (zero velocity). His calculations showed that the heat flux for free boundaries was 2.3 times larger than that possible for rigid boundaries (solid conduction case). The free boundary model allows fluid to flow along the boundaries and transfer heat better than the solid conduction case.

In the variable regime, when $Qi/Qs > 1$, heat transfer is enhanced by large penetrative rolls entraining fluid from the intermediate layer. One set of points (run a 1 to run a 4) in Fig.4.22. indicate a different trend at high density ratio R. This may be explained by the smaller intermediate layer thicknesses arising in these experiments, and the enhanced entrainment process in the layer due to the low concentration gradient existing across the intermediate layer.

The destabilising temperature gradient existing across the intermediate layer, was the driving force for the increased mass flux behaviour shown in Fig. 4.23. The high heat to mass diffusivity ratio (Lewis number = 18 for the LIN/LOX system), accounts for the sharp rise of the mass flux above the steady molecular diffusion value, due to the fluid being entrained from the intermediate layer.

Turners' heat-salt experiment data fit the LIN/LOX interface heat transfer results very well, for the range of values recorded. This fact, and the oscillating or wavy interface motion observed, suggests the LIN/LOX intermediate layer can be described by Double-Diffusive convection theory. The linear gradient of temperature and concentration both increasing with depth through the intermediate layer, gave rise to the diffusive (or oscillating element) instability as predicted by the theory for a Double-Diffusive system.

5.3. Vapour Flowrate.

The rollover intensity (i.e. peak flowrate) appears to be a function of the initial layer density difference, even when the flowrate uncertainty and slightly different initial mass conditions are taken into account. This result is not unexpected, because the higher initial density difference conditions meant the time for the layers to reach the same density was longer, and the bottom layer therefore built up a larger Thermal Overfill to be released through evaporation.

The thermal overfill and flowrate vs time plots show two general types of behaviour corresponding to different heating conditions. For the extreme case of very high heating to the lower layer (Fig. 4.29), the flowrate rises only after the heat transfer to the top layer is increased. The superheat lost by the bottom layer enthalpy, rapidly increases the surface evaporation flowrate.

In the other case of top and bottom layer heating (Fig.4.28), before the top layer reaches equilibrium (i.e. a steady evaporation flowrate), it begins receiving more heat from the lower layer. The flowrate rises accordingly, but the flowrate-time slope decreases, suggesting another "equilibrium flowrate" is being approached. This can be explained by assuming the interfacial heat transfer almost matches the equilibrium conditions necessary in the top layer which is increasing in mass, because of the fall in intermediate layer level. As the layer densities equalise, a final peak in flowrate is observed, due to the release of top layer energy caused by the rapid mixing of the hotter bottom layer into the top layer.

Only one of the flowrate plots obtained in this investigation (run b 8, Fig. 4.25), exhibits the very high peak to equilibrium flowrates experienced in some recorded rollover events (1), (2). It is certain, however, that bubbles created the very high flowrate recorded. The oxygen analyser capilliary was known to blow small bubbles into the test liquid when positioned in the top layer. These bubbles however momentarily changed the vapour flowrate by no more than 50 cc min^{-1}. A short period of boiling in the lower layer was the most probable cause of the sudden mixing observed. The bubble formation may have been triggered by quasi-homogenous nucleation, as described by Beduz et al (19). Nucleation in the lower layer could easily have been started by an ice particle in the liquid, or by movement of the experimental visualisation dewar. If this type of nucleation process occurred in a large LNG container, could the bubbles create a shock wave severe enough to mix the layers?

In the La Spezia incident (1), the bottom layer was originally 4K hotter than the top layer. The heat balance in the bottom layer was such that it cooled and became denser. The top layer evaporated off the more volatile lower density methane, and its density increased faster than that of the bottom layer. The layers reached equal density before the temperatures equalised, so the large Thermal Overfill accumulated by the bottom layer was released very quickly.

The experiments performed in this investigation were all gradual mixing processes (except run b 8). The thinning and eventual wavy form of the intermediate layer increases the mass and heat transport between layers. The conditions in the La Spezia case suggests that the intermediate layer (or layers) existing in the LNG mixture were the cause for two independent convecting systems to exist until density equalisation.

The equilibrium mass flux vs superheat temperature data (Fig.4.30) obtained from experiments, agree well with data obtained by Rebiai (38), but show a slightly different slope at low ΔT values. The temperature uncertainty of 0.13 K. could however account for this difference at low ΔT values. Fig. 4.31. shows that the mass flux correlation (equation (4.14)) didn't apply during the early heating stages. This can be explained by considering the wall boundary layer flow. As soon as heating is started, a boundary layer flow up the wall starts, carrying heat up to the liquid surface to raise the evaporation flowrate. The bulk fluid temperature cannot however change very much in the meantime, due to its high time constant (m Cp/LCA).

A higher initial heat input to the liquid would create an even hotter boundary layer flow, and hence higher flowrate. The transient mass flux behaviour is therefore dependent on the heat input $\dot{Q}b$ as well as T, i.e:

$$\dot{m} = f\ (\dot{Q}b,\ T) \qquad (5.1)$$

An extreme test for any mass flux correlation that may be used for rollover predictions, is to see if it can predict very high flowrates such as that which occurred in La Spezia case. The rollover account given by Sarsten (1) suggests that a peak to initial measured flowrate ratio (Vpeak/Vm) of 120 occurred.

A simple calculation using the mass flux correlation for liquid methane, obtained by Rebiai (38), shows that the

correlation given by:

$$\dot{m} = 1.45\,\Delta Ts^{0.94} \times 10^{-3}\ Kg\ m^{-2}s^{-1} \qquad (5.2),$$

could never predict such a high peak flowrate. For a ΔTs of 0.5 K, $\dot{m} = 0.76 \times 10^{-3}\ Kgm^{-2}s^{-1}$. For the mass flux $\dot{m}$ to be 120 times greater than this value, a ΔTs of 82 K would have to exist in the fluid to drive such a high evaporation rate. It appears that the constants c and n in the general relation:

$$\dot{m} = C\ \Delta T^{n} \qquad (5.3)$$

have to take into account a new effect in order to predict a La Spezia type behaviour. The only way very high peak flowrates can be produced, is to assume that the LNG system releases its thermal overfill through a flash evaporation. This means that the surface thermal resistance existing in the thin top layer of the evaporating liquid breaks down. The breakdown of the surface thermal resistance could occur if the layers in an LNG system instantaneously mix. The surface layer therefore doesn't have enough time to re-establish itself before all the superheat energy is released through sudden evaporation.

Another way in which hot fluid might break down the surface thermal resistance, is if the hot boundary layer created in the bottom layer, pierces through the intermediate layer, and reaches the liquid-vapour interface. This would require a turbulent boundary layer, with vertical length scales far greater than those occurring in this investigation.

5.4. Schlieren Flow-Visualisation.

Before discussing photographic points 1 to 10, it might be useful to summarise some convective patterns observed by Berg (43). Using Schlieren optics, and a variety of pure liquids (acetone, benzene, carbon tetrachloride, n-heptane, isopropyl alcohol and methyl alcohol), Berg obtained a variety of evaporative convection patterns. Four distinct convective structures were observed, and are as follows:

a) Convective cells similar to those recorded by Bénard.(44), were observed in liquids for depths of 2 mm or less.

b) When the liquid depth exceeded 7 or 8 mm, streamers were observed. These were "cold lines" in which cooled liquid would plunge in sheets into the fluid, as illustrated in Fig. 5.2a. The streamers moved slowly about the fluid, and closely resembled networks photographed by Spangenberg and Rowland (45).

c) The third convective pattern observed were ribs. These ribs moved rapidly, were able to travel perpendicular to each other, and could travel either perpendicular or parallel to streamers. Ribs represented lines where cold fluid would plunge from the surface into the interior liquid.

d) When a nonvolatile material was present in the surface region, vermiculated rolls were seen (Fig. 5.2b), instead of cellular convection.

Prints 1 to 4 show the progressive formation of streamers, and streamers plus ribs for increasing surface vapour mass fluxes. The low mass flux behaviour displayed in Print 1 shows no streamers or ribs, but close inspection reveals a "speckled" appearance in the photograph. The other low evaporation photograph (Print 5) also shows a similar pattern. Generally, in a pure evaporating fluid, the convective pattern occurs as a result of both a buoyancy and surface tension driving force. The fact that the conditions in Print 1 and 5 correspond to zero heat input, and the absence of ribs or streamers, suggests a surface tension effect may have been in operation. An illustration (Fig. 5.3) from the work of Beduz et al (15) on LIN can be used to explain the process. Studies showed that the top 5 mm of liquid above the bulk fluid contained a convection and thermal conducting layer as shown in the diagram.

Fig. 5.2. Two Evaporative convection forms (Berg. (43)).

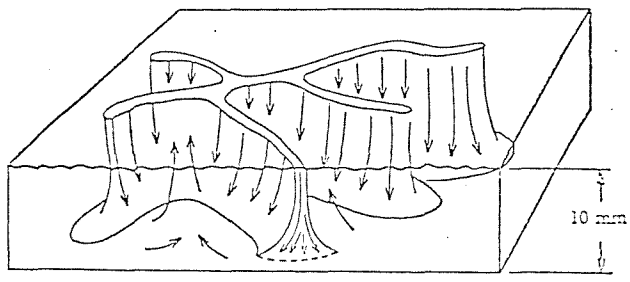

a) Evaporative convection in cold streamers. Cold fluid plunges along distinct lines in the surface, and warm fluid rises slowly in the area between the streamers.

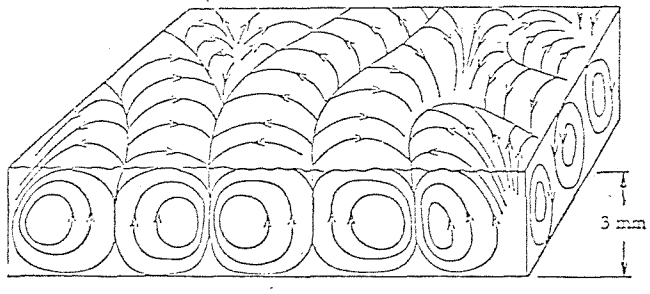

b) Evaporative convection in vermiculated rolls. Cold fluid flows down in a narrow region near the roll partition, and warm fluid rises over a wider, less distinct region.

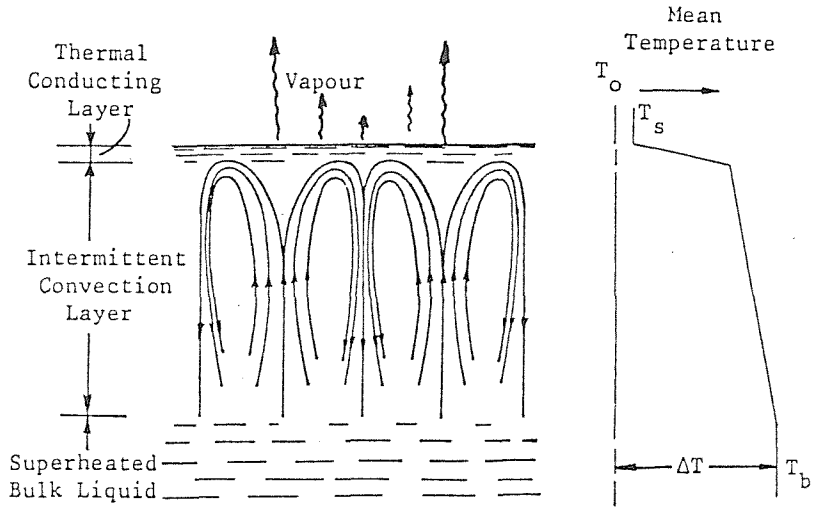

Fig. 5.3. Morphology of surface layers of liquid nitrogen. (Beduz et al (15)).

The surface tension of a liquid decreases with temperature, so if any liquid near the thermal conducting layer becomes hotter due to a small disturbance, fluid is drawn away from the region by the action of surface tension. Other fluid comes in from below to replace it. As this fluid has been closer to the hotter bulk liquid below, it will be hotter than the fluid at the surface. The original disturbance in the temperature distribution is thus amplified.

A steady state can exist with hot fluid moving up towards the conducting layer, losing heat as it travels parallel with it, and then falling down as cold fluid. In this way, a surface tension distribution can be maintained that drives the motion against the retarding action of viscous forces.

After 12 minutes of heating, Print 2 shows some slow moving streamers. Prints 3 and 4 show ribs moving haphazardly across the convective streamers. Both ribs and streamers occur just below the small surface convection layer shown in Fig. 5.3. Video recordings made during many other Schlieren studies performed in this investigation, show that the speed and number of the ribs increased with increasing evaporative mass flux, but existed for no more than a few seconds.

The Schlieren photograph sequence for a two-layered experiment is similar to that described for the single layer study, but is complicated by the fact that the image shows regions close to the liquid-vapour and liquid-liquid interfaces. Prints 7 and 8 reveal a "fish scale" pattern superimposed on the ribs and streamer formation. This pattern may be attributed to buoyancy driven convection in the small convection layer, as the heat transfer to the conduction layer is increased.

Print 8, which corresponds to conditions during rollover, shows a radial alignment superimposed on the surface cellular pattern. This is due to the strong radially directed flow resulting from the wall boundary

layer flow. Print 9 shows such a boundary layer flow that was deflected at the liquid-liquid interface (bottom boundary of intermediate layer), a few seconds after the bottom layer wall heater was switched on.

The surface instability displayed in Print 10 can be attributed to the effect of an impurity (a small amount of air), that entered the surface layer of the LIN. The pattern is similar to vermiculated rolls observed in melted wax covered with a film of Stearic acid by Avsec (46), whose result is shown in Fig. 5.4. for comparison with Print 10. An interesting feature of the instability was that the pattern changed very little in a period of 10 minutes, after which the pattern broke down, and streamers appeared.

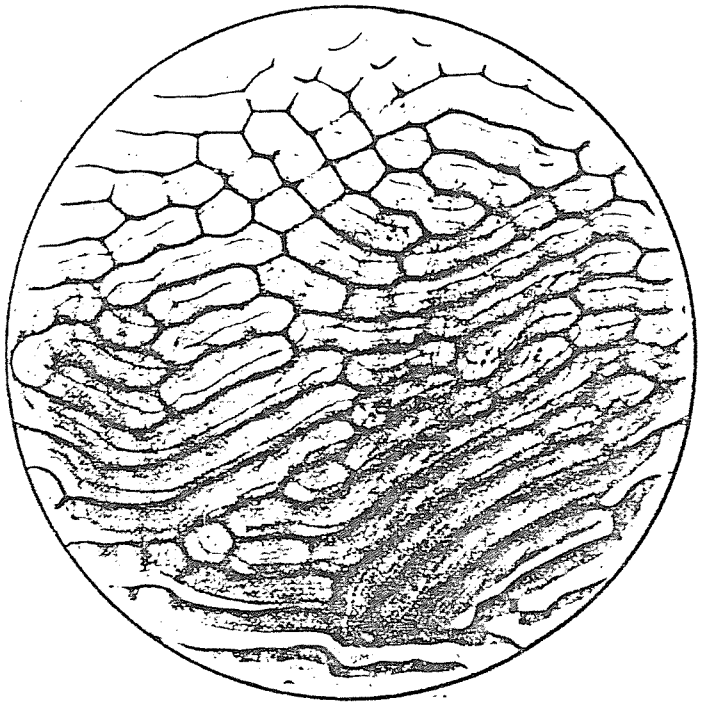

Fig. 5.4. Vermiculated rolls in melted wax covered with a film of stearic acid (Avsec (46)). Magnification about 2X.

6.0. CONCLUSIONS.

The description of an experimental investigation into LNG rollover using cryogenic liquids has been given. From the experimental results obtained, the following conclusions can be made;

1) The mixing of the two separate convective layers is primarily due to the entrainment of liquid from the intermediate layer separating the two layers. The complete penetration of the intermediate layer by boundary layer flow in the lower layer was not possible, due to the small length-scales associated with the experimental apparatus.

2) The intermediate layer can be described by Double-Diffusive convection theory. Two regimes predicted by previous theory correspond to when the ratio of density difference due to concentration to density difference due to temperature, (R), is greater than or less than 2.

3) The intermediate layer controls the transport of heat and mass between layers. For $R < 2$, enhanced interfacial transport accompanies the thinning and wavy motion of the intermediate layer.

4) For similar total heat inputs, the peak flowrate generated is a direct function of the initial density difference existing between layers.

5) Only one very high peak to equilibrium flowrate was recorded, because in the majority of experiments, convective motion in the simulated layers promoted good mixing between layers. The high flowrate recorded in one experiment is attributed to quasi-homogenous nucleation, which may be part of a rollover mechanism so far not studied.

6) A correlation between the evaporative mass flux ($\dot{m}$) and bulk fluid superheat (ΔTs) doesn't apply to transient flowrate behaviour. The transient flowrate is a function of the heat input to the vessel ($\dot{Q}b$) as well as ΔTs. The

mass flux correlation cannot predict a La Spezia - type peak flowrate based on a reasonable ΔTs value. The only way an extremely high flowrate can be produced, is to assume a flash evaporation, with the destruction of the surface thermal resistance layer. Another process that would destroy the surface thermal resistance (boundary layer penetration from the bottom to the top layer surface) was not observed in this investigation.

7) Schlieren flow-visualistion studies show the formation of streamers and increasing number of ribs accompanying an increase in evaporative mass flux. A clear radial convective cell network exists below the liquid surface during rollover.

6.1. Recommendations.

Further studies should be made using a large dewar in order to create a turbulent boundary layer up the side walls of the vessel. More video recordings of Schlieren visualisation experiments, capturing the transient behaviour during various flow regimes, would be useful. An investigation into the complete mechanism of a bubble-induced rollover process might also prove interesting.

ACKNOWLEDGEMENTS

I wish to thank Professor R.G.Scurlock for his advice and guidance given to me during the project.

I also wish to thank Dr. C. Beduz for his help and useful suggestions.

My thanks go to R. Welham, I.Mears, and all other staff of the department who have helped me, and to students past and present whose comments and discussions proved useful.

My final thanks go to Mrs. L. Puttock for typing this thesis, to the S.E.R.C. for awarding me a postgraduate student grant, and British Gas for providing me a CASE award.

REFERENCES

(1) Sarsten, J.A., "LNG stratification and rollover", Pipeline and gas journal, P.37, (September 1972).

(2) Bellus, Reveillard, Bonnawe, Chevalier "Essais au terminal de fos sur le comportment due GNL dans les grands reseroirs", LNG conference papers 5, (1977).

(3) Chatterjee, N. and Geist, J.M., "The Effects of Stratification on Boil-Off Rates in LNG tanks", Pipeline and gas journal, P.40, (September 1972).

(4) Germeles, A.E., "A model for LNG tank rollover", Advances in Crygenic Engineering, Vol. 21, P.326, (1975).

(5) Hashemi, H.T., and Wesson, H.R., "Cut LNG storage costs", Hydrocarbon Processing, P.117, (August 1971).

(6) Turner, J.S., Buoyancy effects in fluids, P. 251, Cambridge University Press, (1973).

(7) Chatterjee, N., and Geist, J.M., (Spontaneous Stratification in LNG tanks containing nitrogen", ASME Winter Annual meeting, Paper 76-WA/P.10-6, (December 1976).

(8) Schiesser, W.E., "LEANS version III for continuous systems simulation", Air Products and Chemicals Inc., (July 1970).

(9) Takao and Suzuki, "Prediction of LNG Rollover", Gastech, Paper 8, (1982).

(10) Takao and Narusawa, International Journal of Heat and Mass Transfer, Vol. 23, P.1283, (1980).

(11) Heestand, J., Shipman, C.W. and Meader, J.W., "A Predictive model for Rollover in stratified LNG tanks", AIChE Journal, Vol.29, No.2., P.199, (March 1983).

(12) Sugawara, Kubota and Muraki, "Rollover Test in LNG Storage tank and simulation model", Advances in Cryogenic Engineering, P.805, Colorado Springs, (1983).

(13) Muro, M., Yoshiwa, M., Yasuda, Y., Mujata, T., Iwata, V., Yamazaki, Y., "Experimental and Analytical study of rollover phenemenon using LNG", ICEC 11 papers, P.633, Berlin, (1986).

(14) Turner, J.S., "The coupled turbulent transports of salt and heat across a sharp density interface", International Journal of heat and mass transfer, Vol.8., P.759, (1965).

(15) Beduz, C., Rebiai, R., and Scurlock, R.G., "Thermal Overfill and the surface vaporisation of cryogenic liquids under storage conditions", Advances in cryogenic engineering, Vol.29, P.795, (1984).

(16) Nakano, R., Sugawara, Y., Yamagata, S., and Nakumara, J., "An Experimental study on the mixing of stratified layers using liquid freon", Gastech, Paper 7, (1982).

(17) Griffis, K.A., and Smith, K.A., "Convection patterns in stratified LNG tanks - cells due to lateral heating", Conference on natural gas research and technology, Session 6, Paper 4, Dallas, (1974).

(18) Maher, J.B., and Van Gelder, L.R., "Rollover and thermal overfill in flat bottom LNG tanks", Pipeline and gas journal, P.46, (September 1972).

(19) Beduz, C., Rebiai, R., and Scurlock, R.G., "Evaporation instabilities in cryogenic liquids, and the solution of water and carbon dioxide in liquid nutrogen", ICEC 9 papers, P.802 (1982).

(20) Stommel, H., Arons, A.D., and Blanchard, D., "An Oceanographical curiosity: the perpetual salt fountain", Deep sea research, Vol.3., P.252, (1956).

(21) Stern, M.E., "The Salt Fountain and thermohaline convection", Tellus, Vol.12, P.253, (1960).

(22) Veronis, C., "On Finite Amplitude Instability in thermohaline convection", Journal of marine research, Vol.23, P.1, (1965).

(23) Veronis, G., "Effect of Stabilising Gradient of solute on thermal convection", Journal of fluid mechanics, Vol.34., P.315, (1968).

(24) Nield, D.A., "The Thermohaline Rayleigh - Jeffreys problem", Journal of fluid mechanics, Vol.29, P.545, (1967).

(25) Baines, P.G., and Gill, A.E., "On Thermohaline convection with linear gradients", Journal of fluid mechanics, Vol.37, P.289, (1969).

(26) Chandrasekhar, S., Hydrodynamic and Hydromagnetic stability, Clarendon Press, Oxford, (1961).

(27) Huppert, H.E., "On the stability of a series of double-diffusive layers", Deep Sea Research, Vol.18, P.1005, (1971).

(28) Agbabi, T., Beduz, C., and Scurlock, R.G., "Convection Processes during heat and mass transfer across liquid/vapour and liquid/liquid interfaces in cryogenic systems", ICEC II papers, P.627, Berlin (1986).

(29) Lewis, G.N., and Randall, M., Thermodynamics and the free energy of chemical substances, P.226, (1923).

(30) Krichevsky, J., and Torocheshnikov, N., Zeitschr, f, phys.Chemie (A), 176, P.338, (1936).

(31) Steward, R.B., Phd.Thesis, University of Iowa, Iowa City, (June 1966).

(32) National Bureau of Standards, Technical note No.129, (January 1962).

(33) A compendium of the properties of materials at low temperatures, Phases I and II WADD Technical report, 60-56, (1960).

(34) de Groot, S.R. Thermodynamics of irreversible processes, North-Holland, Amsterdam, (1951).

(35) Wilke, C.R., and Chang, P., AlChe Journal, Vol.1, P.264, (1955).

(36) Scheibel, E.G., Ind.Eng. Chem, Vol.46, P.2007, (1954).

(37) Le Bas, G., The Molecular volume of liquid chemical compounds, Longmans, Green and Company Ltd., London, (1915).

(38) Rebiai, R., Phd. Thesis, University of Southampton, (September 1985).

(39) Kline, S.J., and McClintock, F.A., "Describing uncertainties in single-sample experiments", Mechanical Engineering, P.3, (January 1953).

(40) Cromwell, T., "Pycnoclines created by mixing in an aquarium tank", Journal of marine research, Vol.18, P.289, (1960).

(41) Herring, J.R., "Investigation of problems in thermal convection", Journal of Meteorology, Vol.20, P.325, (1963).

(42) Herring, J.R., "Investigation of problems in thermal convection: rigid boundaries", Journal of meteorology, Vol.21, P.277, (1964).

(43) Berg, J.C., Phd. Thesis, University of California, Berkeley, California, (1964).

(44) Benard, H., Ann. Chim.Phys., Vol.23, P.62, (1901).

(45) Spangenberg, W.B., and Rowland, W.R., Physics of Fluids, Vol.18., P.513, (1964).

(46) Avsec, D., Publ.Sci.Tech.Min.Air (France), 155 (1939).

APPENDIX A.

Oxygen Concentration Conversion.

Vapour to Liquid Oxygen Concentration Conversion.

Assuming the analyser head to be at 290 K, the corresponding nitrogen and oxygen gas densities are:

$$\rho_{N_2V} = 1.184 \text{ Kg m}^{-3}$$

and $$\rho_{O_2V} = 1.353 \text{ Kg m}^{-3}$$

respectively. But what is the liquid temperature? Table A1 shows the change in expansion ratios at various liquid mixture temperatures. The gaseous state corresponds to 290 K, 1 atmosphere. The change in expansion ratios for the temperature range given, amounts to less than 1% of their total values. Taking this into account, and using the fact that the temperature range envisaged for the majority of experiments was 77.5 to 78.5 K, values corresponding to 78 K were chosen. Hence:

$$\left(\frac{V_{N_2}}{V_{LIN}}\right) = 679, \qquad \left(\frac{V_{O_2}}{V_{LOX}}\right) = 886.$$

Between 78 K and 290 K.

Let the total volume of liquid V_L, expand to a gas volume of V_g. Using the expansion ratios;

$$V_{LOX}\ 886 + V_{LIN}\ 679 = V_g \qquad \text{(A1)}.$$

As $x_{O_2L} = V_{LOX}/V_L$ and $x_{N_2L} = V_{LIN}/V_L$, dividing (A1) by V_L gives:

$$x_{O_2L}886 + x_{N_2L}679 = V_g/V_L \qquad \text{(A2)}$$

As $x_{O_2L} + x_{N_2L} = 1$,

$$x_{O_2L}886 + (1 - x_{O_2L})\ 679 = V_g/V_L$$

$$207\ x_{O_2L} + 679 = V_g/V_L \qquad \text{(A3)}$$

The oxygen vapour concentration is given by:

$$x_{O_2 g} = \frac{V_{O_2 g}}{V_g} \qquad \text{(A4)}$$

But as $V_{O_2 g} = 886\ V_{LOx}$, (A4) becomes:

$$x_{O_2 g} = \frac{886\ V_{LOx}}{V_g}$$

$$\therefore\ V_g = \frac{886}{x_{O_2 g}}\ x_{O_2 L} \qquad \text{(A5)}$$

Substituting this expression for Vg into (A3) gives:

$$207\ x_{O_2 L} + 679 = \frac{886}{x_{O_2 g}}\ x_{O_2 L} \qquad \text{(A6)}$$

Rearrangement of (A6) gives:

$$x_{O_2 L} = \frac{679\ x_{O_2 g}}{886 - 207\ x_{O_2 g}} \qquad \text{(4.3)}$$

Table A2 shows some values of $x_{O_2 L}$ converted from $x_{O_2 g}$.

Table A.1. Liquid to gas expansion ratios for oxygen and nitrogen.

Liquid mixture temperature K	LOX density Kg m^{-3}	LIN density Kg m^{-3}	Expansion Ratio. N_2	O_2
77.36	1201.31	807.36	681.9	887.9
78	1198.4	804.45	679.4	885.7
79	1193.8	799.81	675.5	882.3

Table A.2. Liquid to vapour concentration conversion. % ע / ע

x_{N_2L}	x_{O_2L}	x_{N_2g}	x_{O_2g}
90.00	10.00	87.34	12.66
91.00	9.00	88.57	11.43
92.00	8.00	89.81	10.19
93.00	7.00	91.06	8.94
94.00	6.00	92.31	7.69
95.00	5.00	93.57	6.43
96.00	4.00	94.84	5.16
97.00	3.00	96.12	3.88
98.00	2.00	97.41	2.59
99.00	1.00	98.70	1.30
100.00	0	100.00	0

APPENDIX B

Original data: Temperature and concentration profile measurements.

Run a 1. Concentration Profiles.

Time	0	80	95	110	125
(± 5 minutes)	a	b	c	d	e

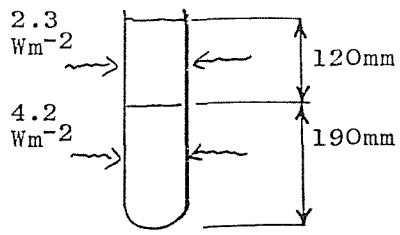

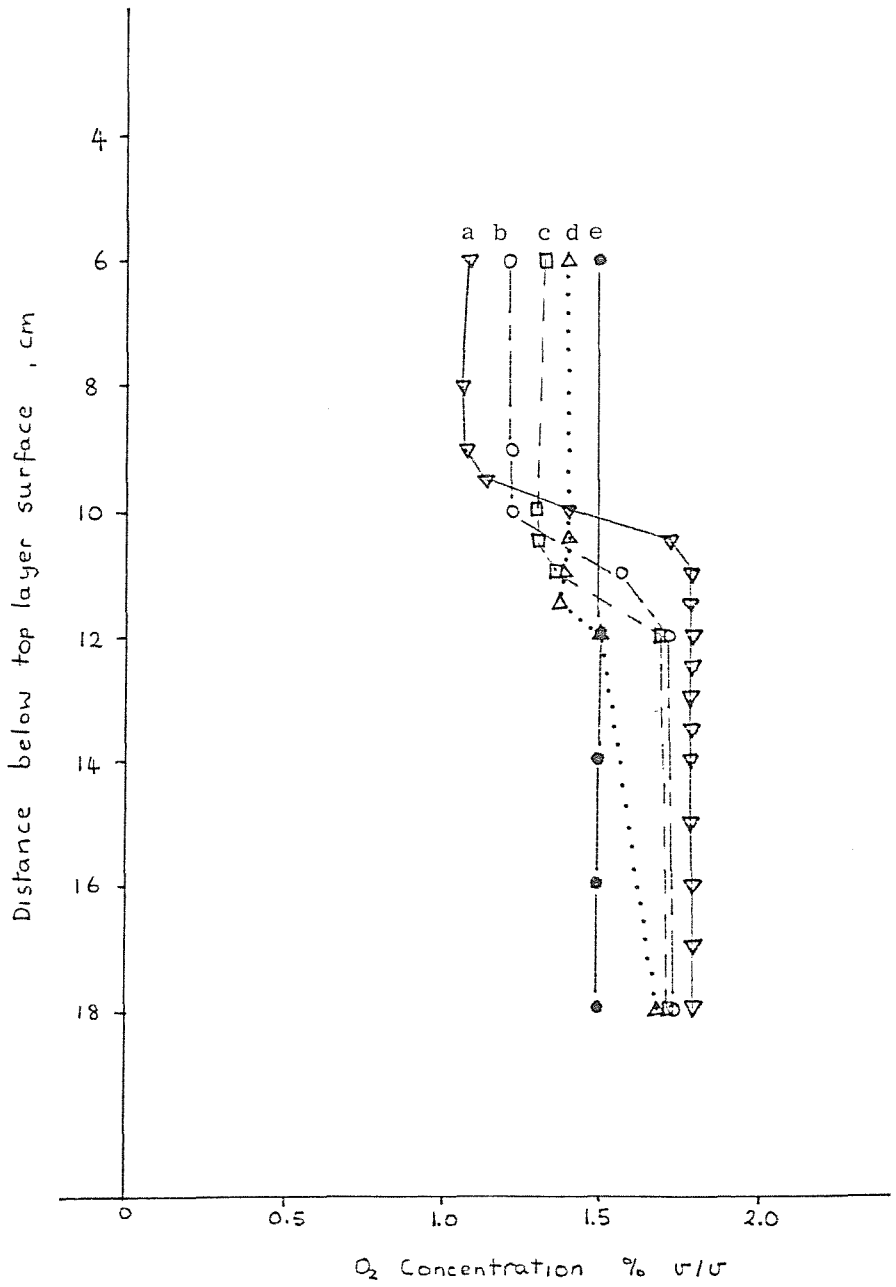

Run a 1. Temperature Profiles.

Data point symbols refer to the same times as shown in the concentration plot.

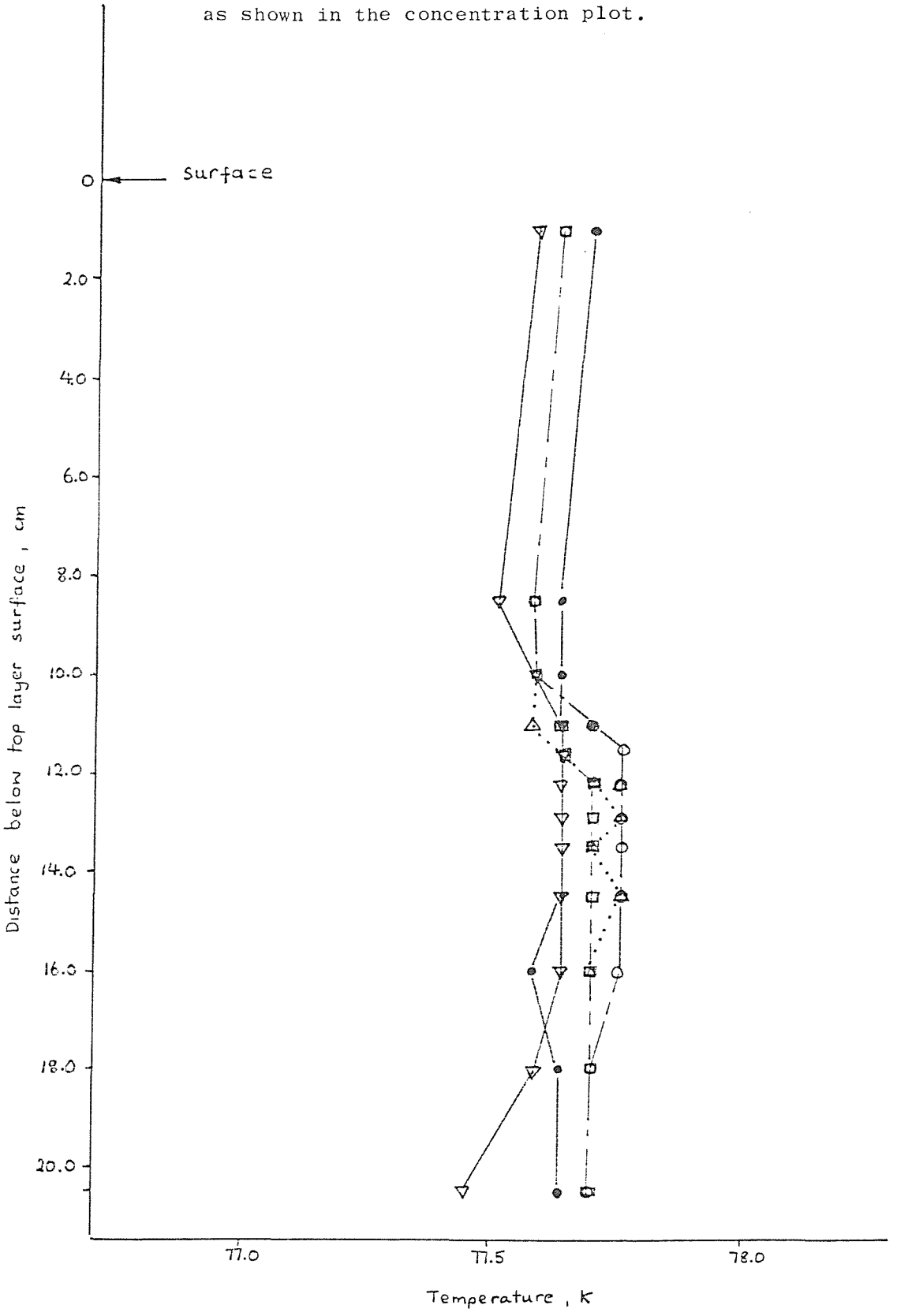

Run a 2. Concentration Profiles.

Time	0	20	50	65	80
(± 5 minutes)	a	b	c	d	e

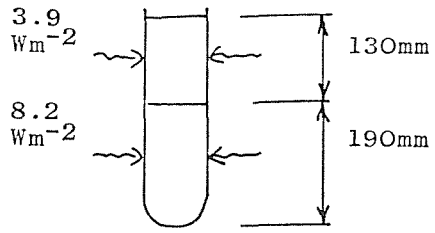

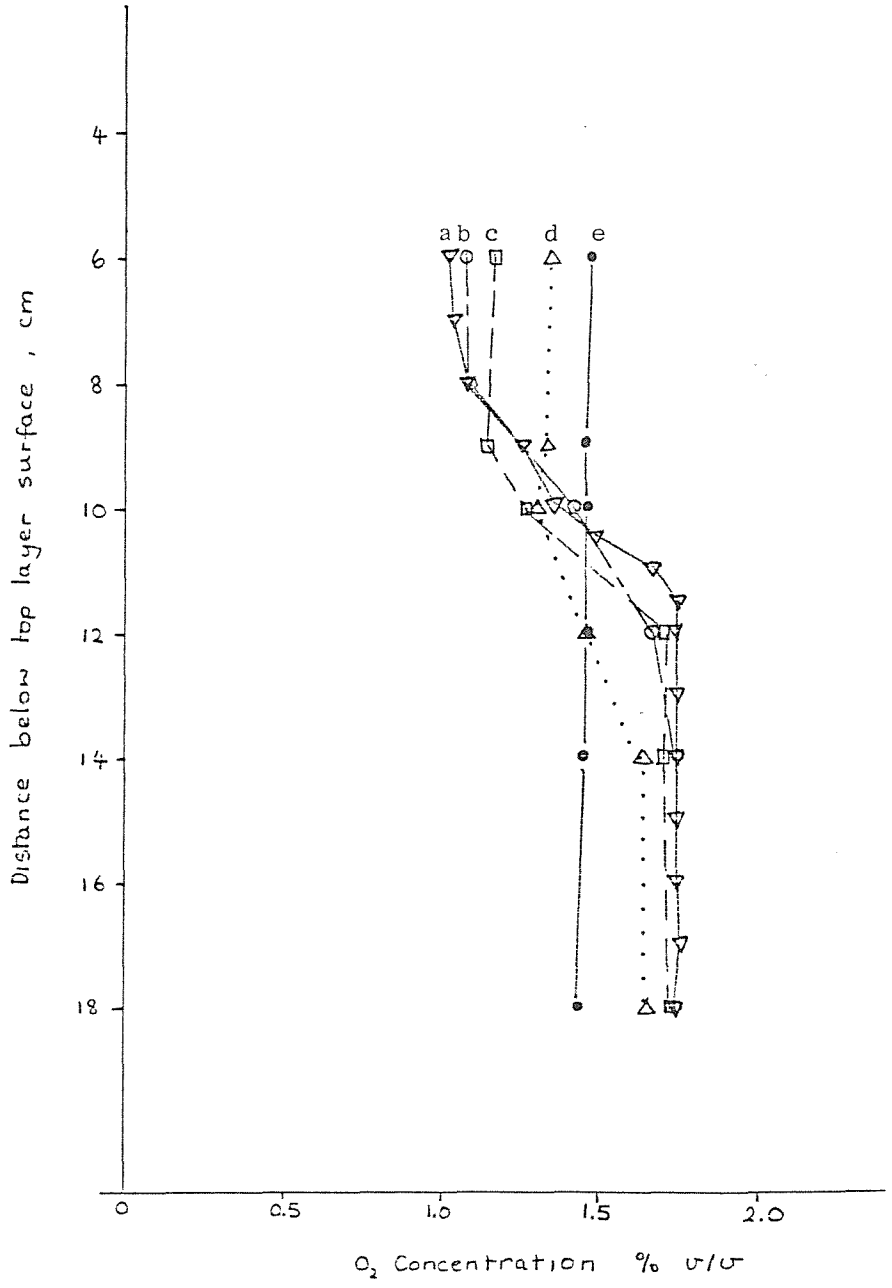

Run a 2. Temperature Profiles.

Data point symbols refer to the same times as shown in the concentration plot.

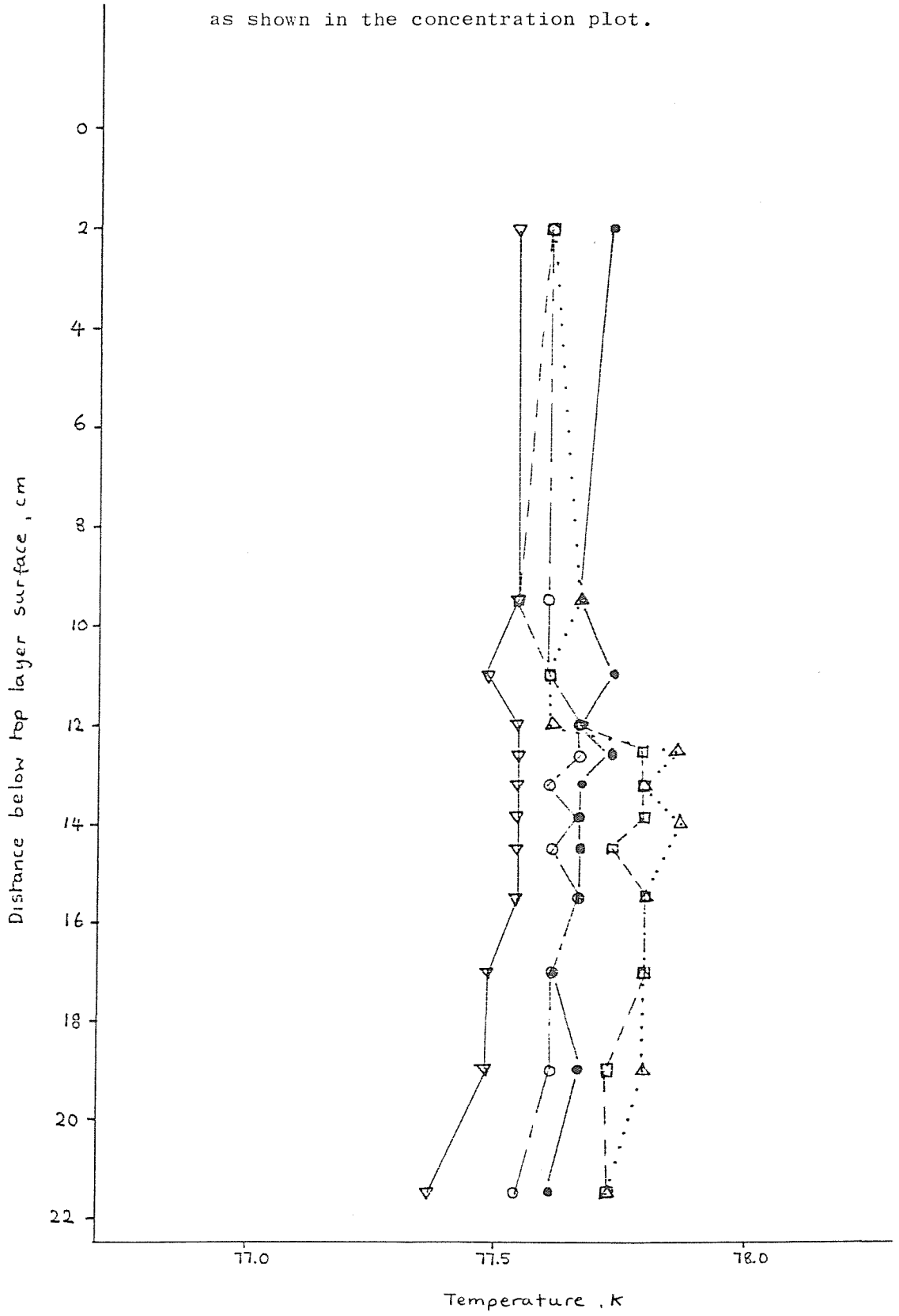

Run a 3. Concentration Profiles.

Time	0	20	35	47
(± 5 minutes)	a	b	c	d

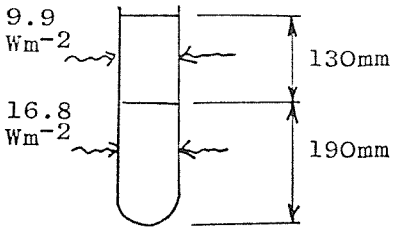

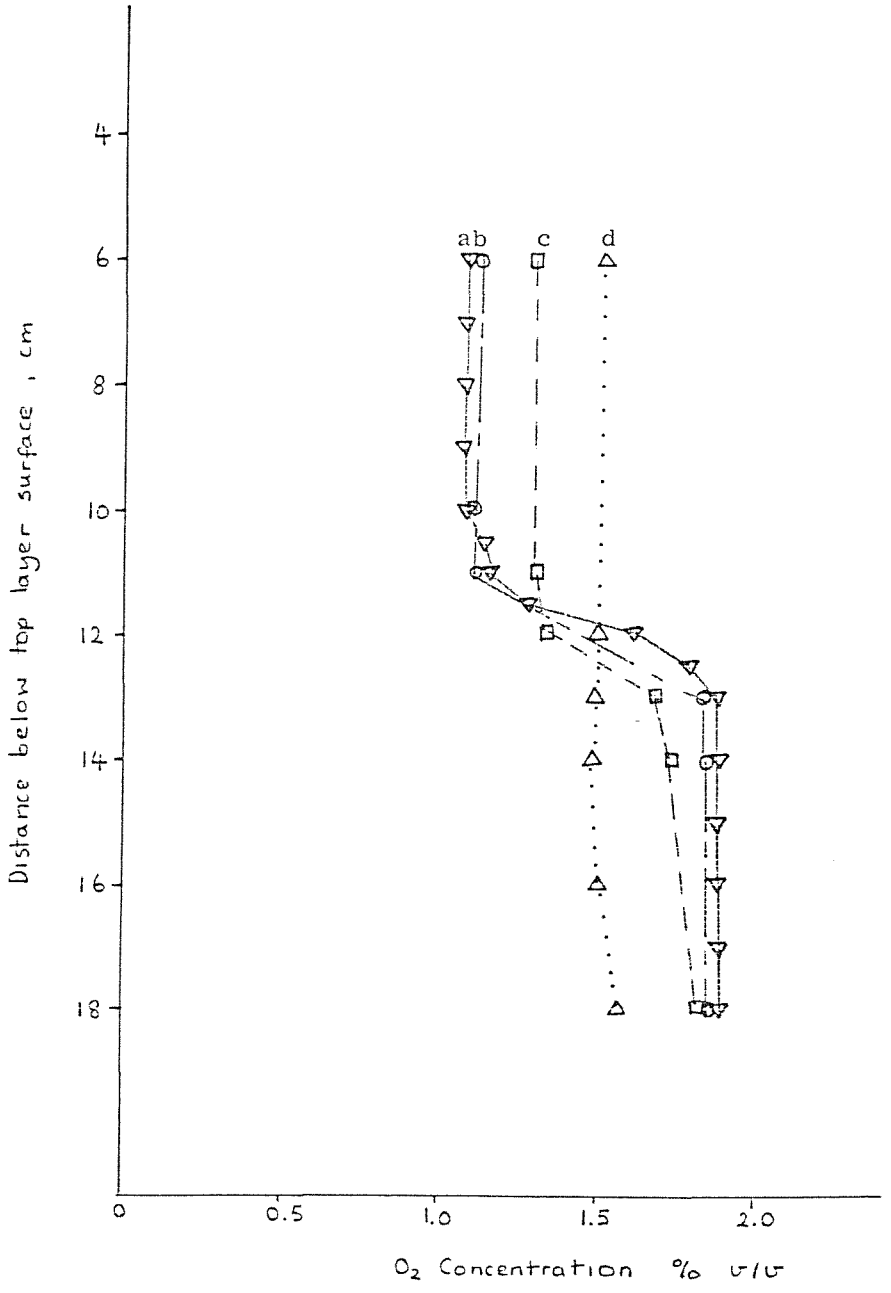

Run a 3. Temperature Profiles.

Time	0	20	35	47
(± 1 minute)	a	b	c	d

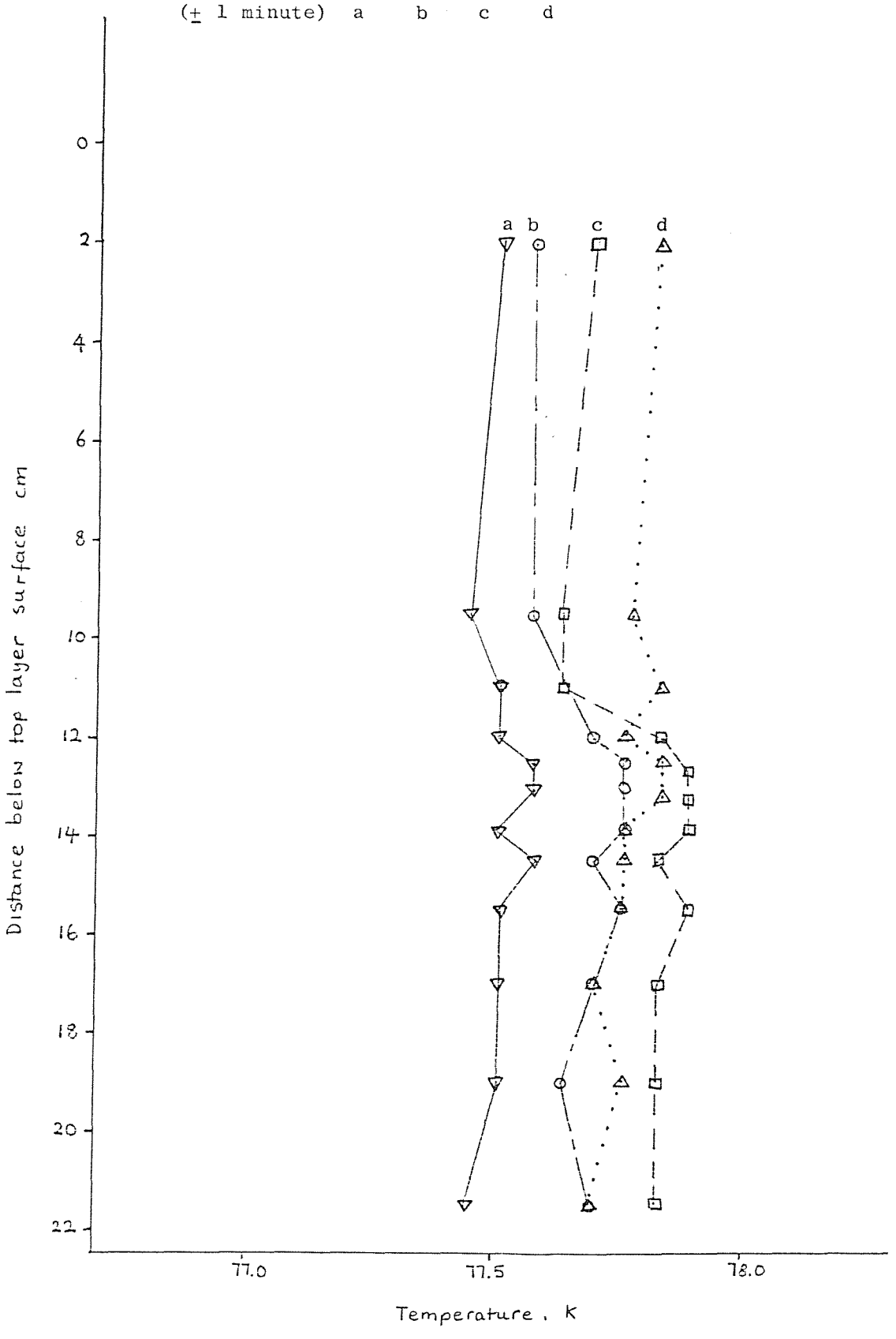

Run a 4. Concentration Profiles.

Time	0	5	17	29
(± 5 minutes)	a	b	c	d

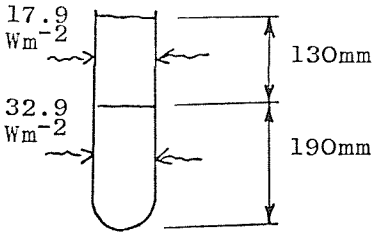

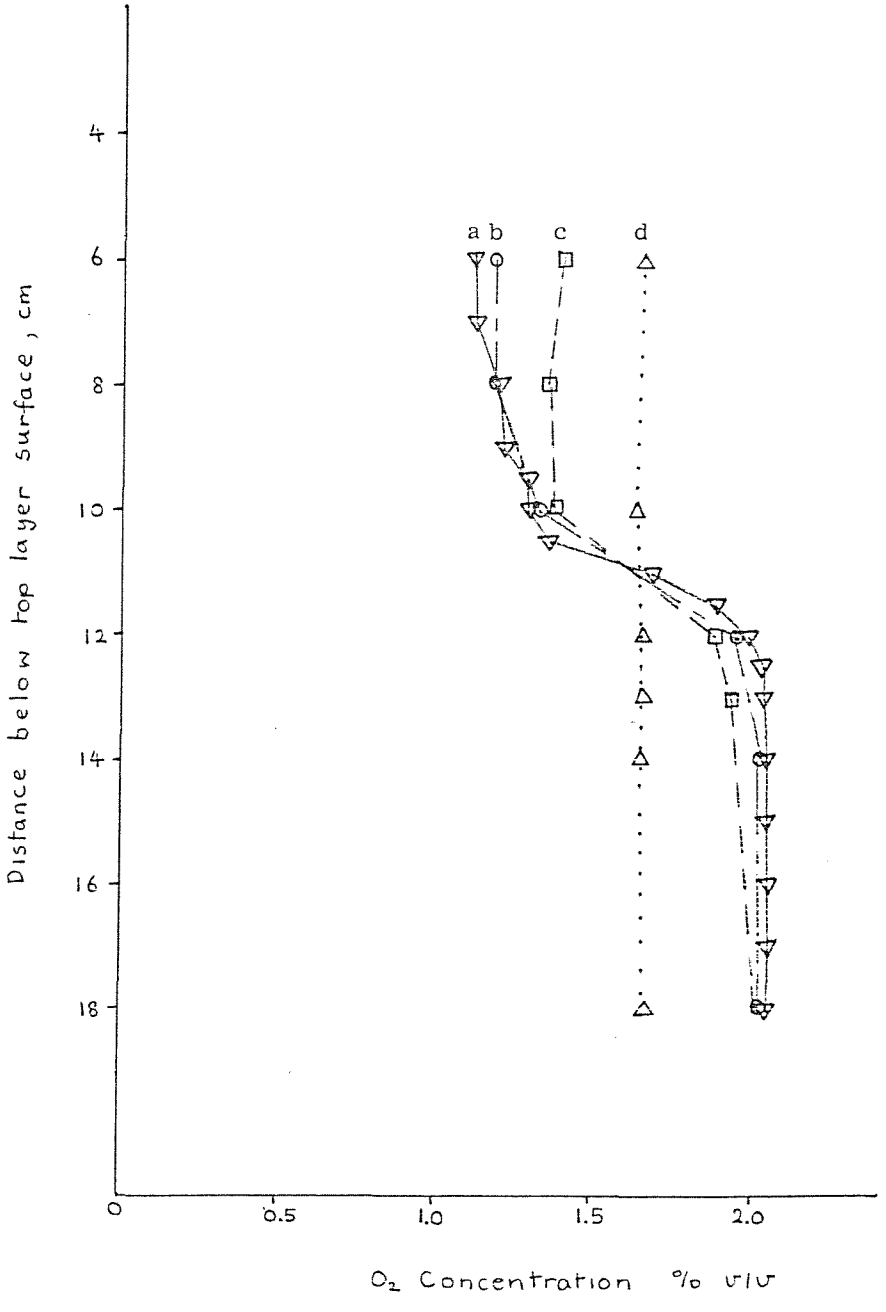

Run a 4. Temperature Profiles.

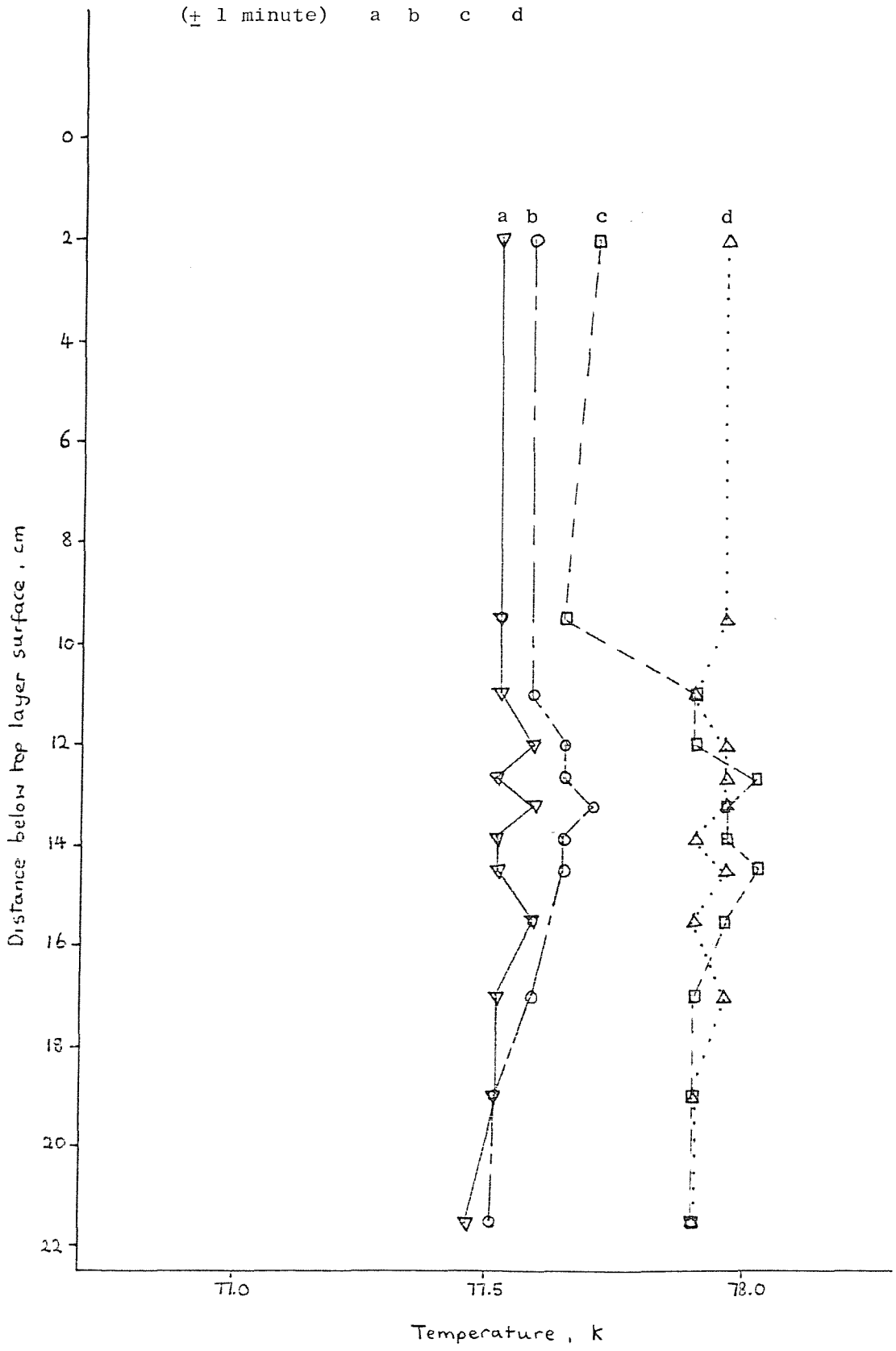

Run a 5. Concentration Profiles.

Time	0	5	20	30
(± 5 minutes)	a	b	c	d

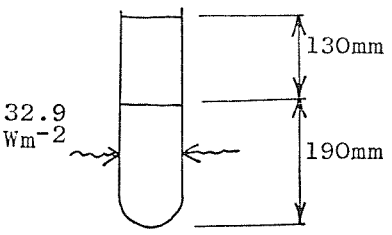

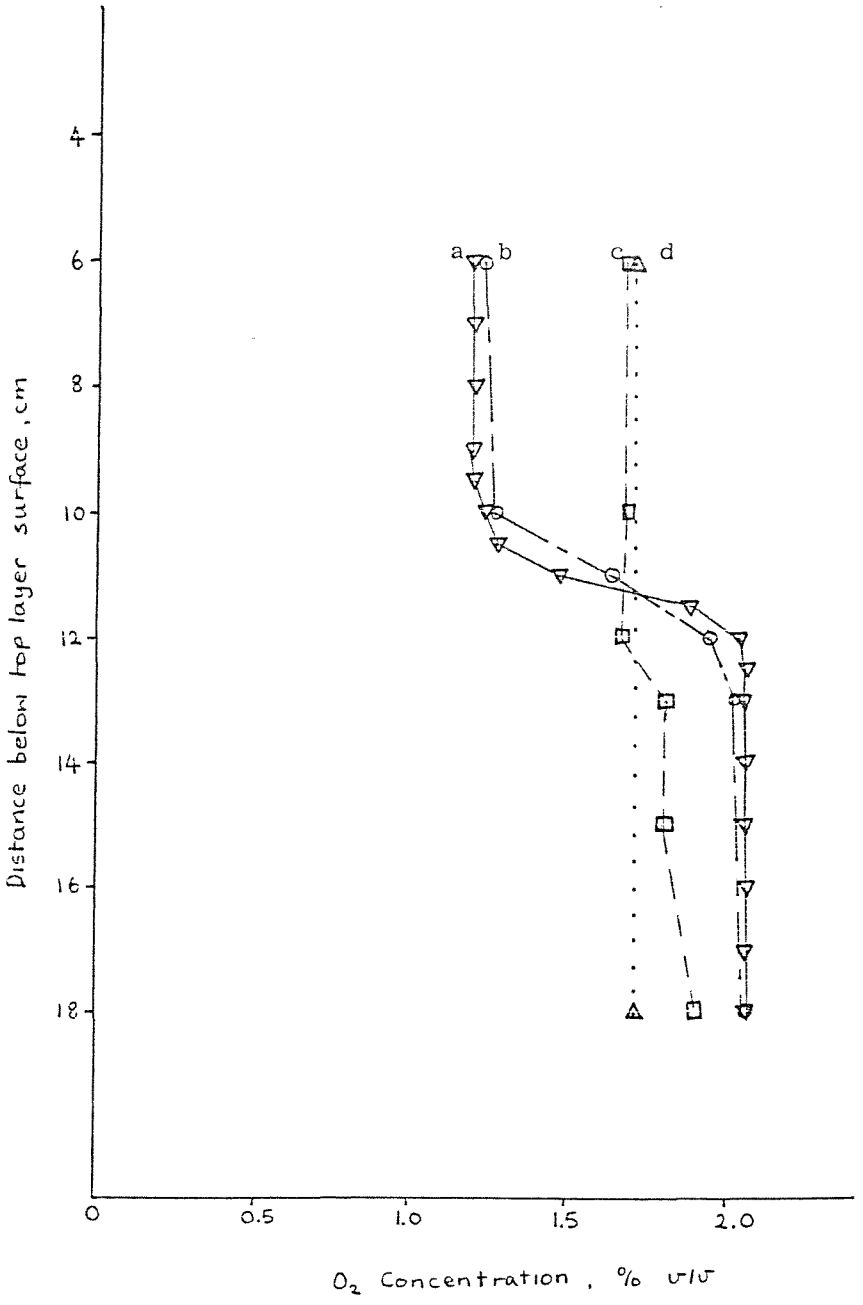

Run a 5. Temperature Profiles.

Data point symbols refer to the same times as shown in the concentration plot.

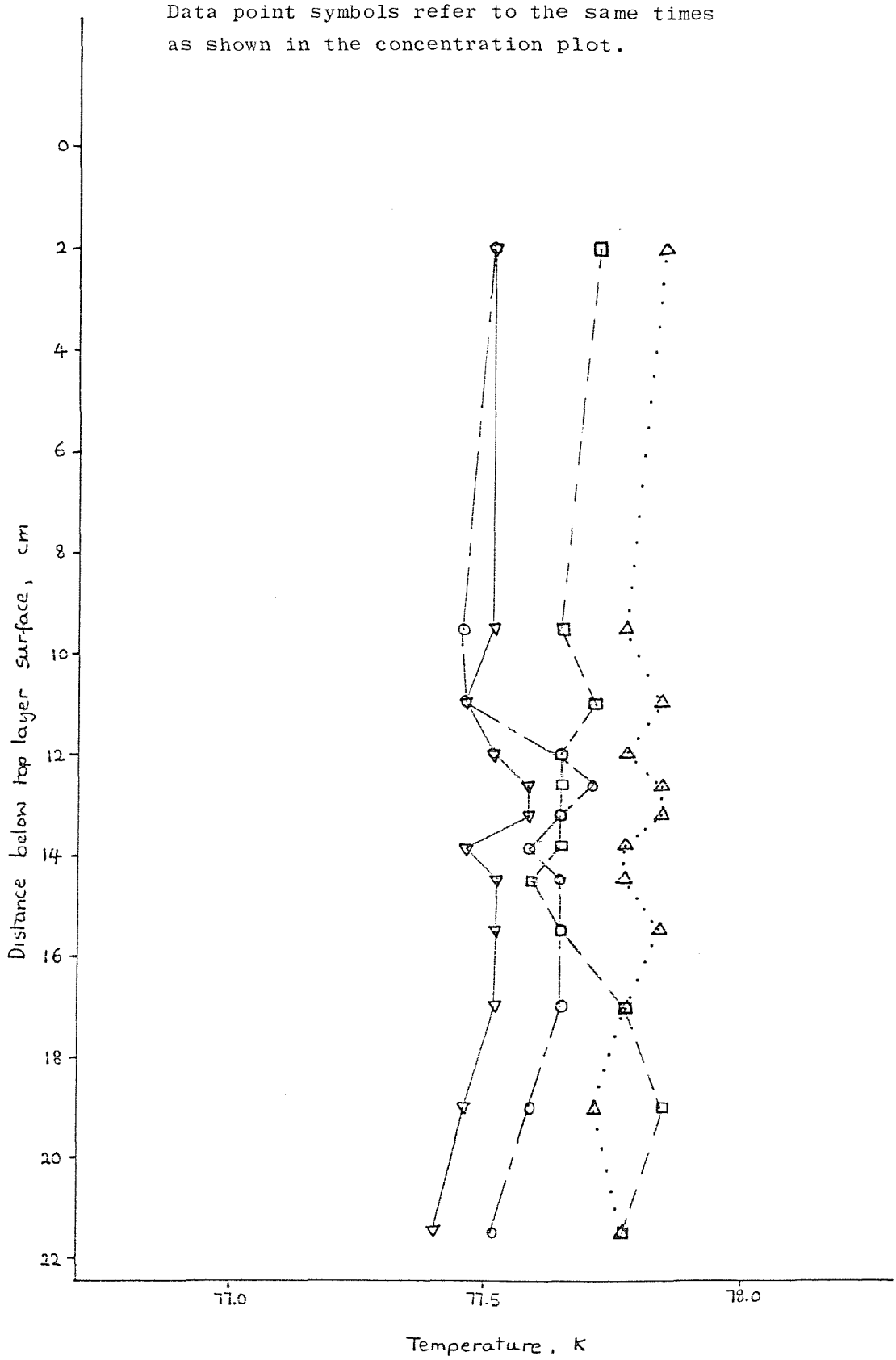

Run a 6. Concentration Profiles.

Time	0	50	95	140	185
(± 5 minutes)	a	b	c	d	e

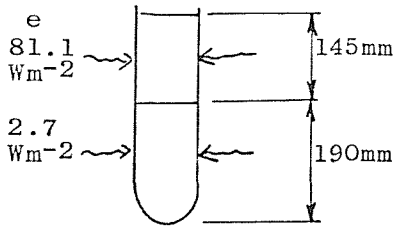

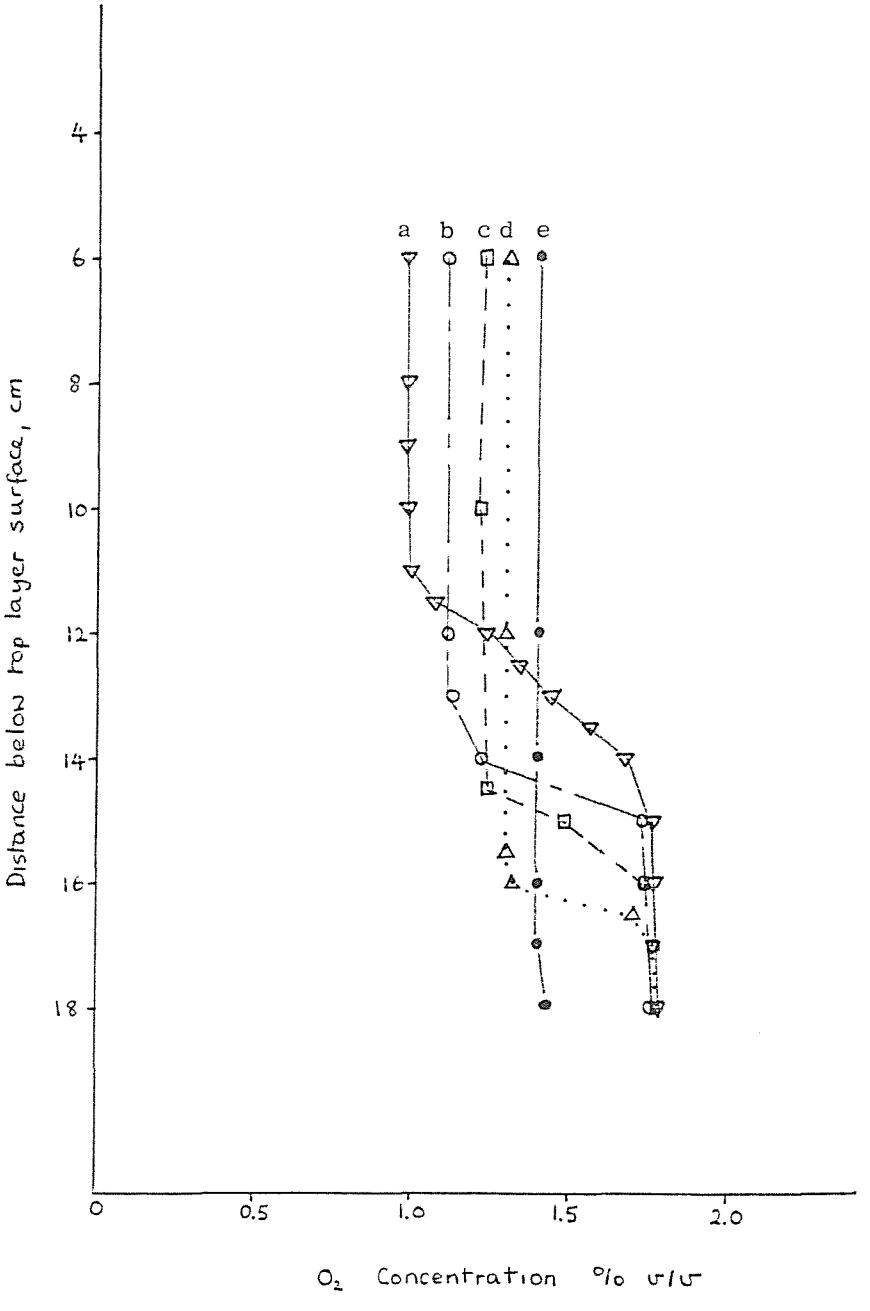

Run a 6. Temperature Profiles.

Data point symbols refer to the same time as shown in the concentration plot.

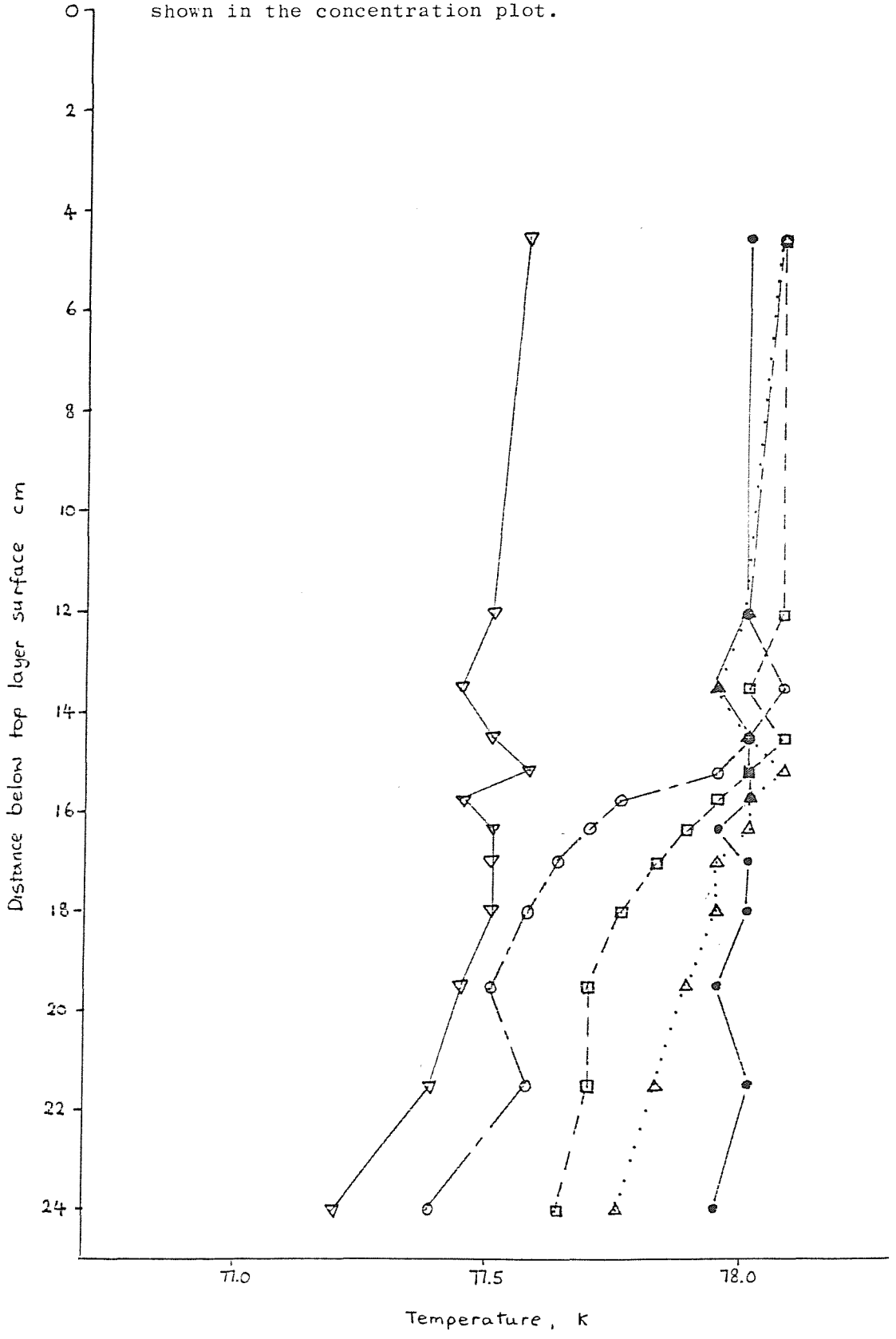

Run b 1. Concentration Profiles.

Time	0	121	241	357	477
(± 7 minutes)	a	b	c	d	e

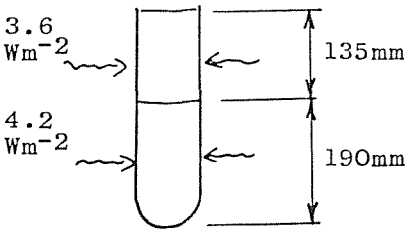

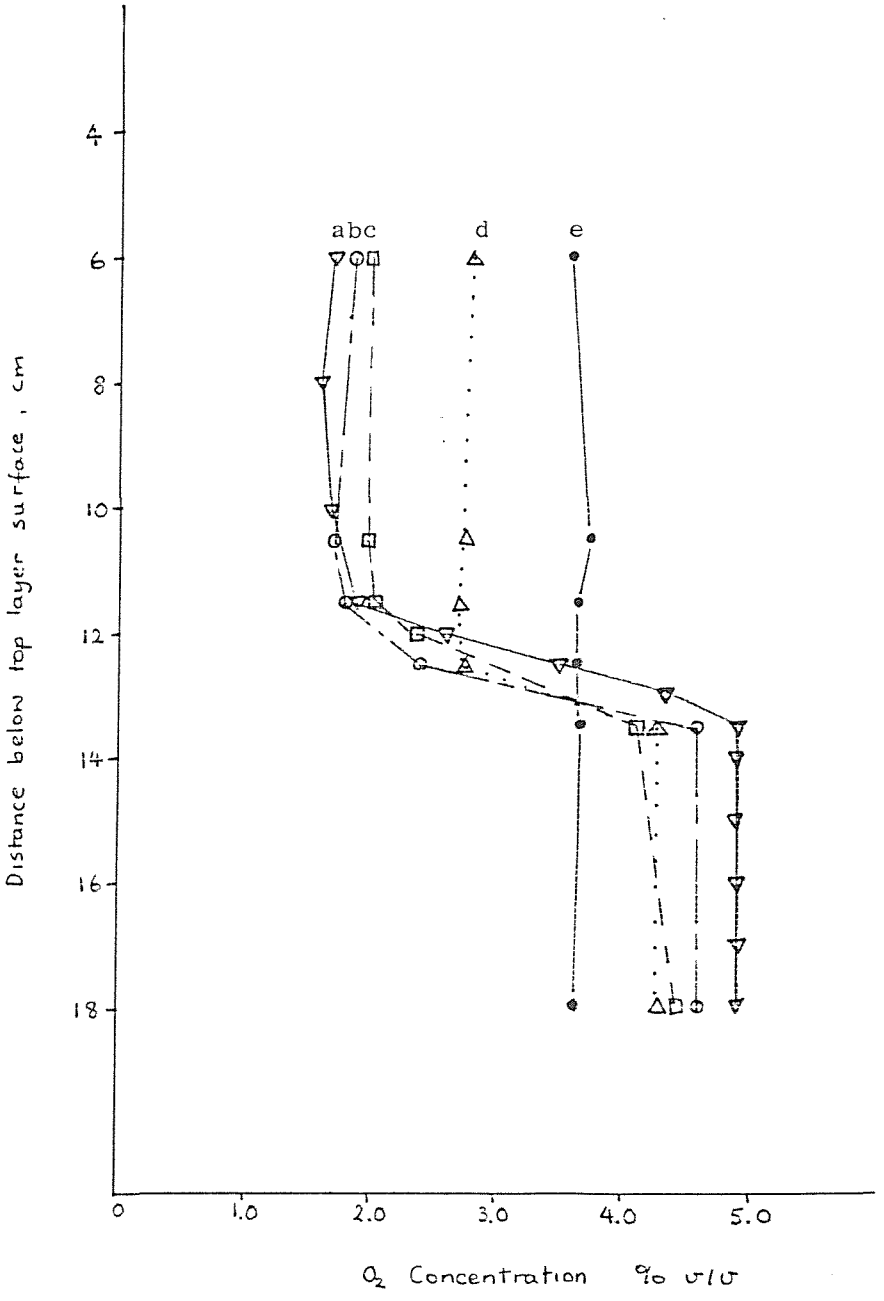

Run b 1. Temperature Profiles.

Data point symbols refer to the same times as shown in the concentration plot.

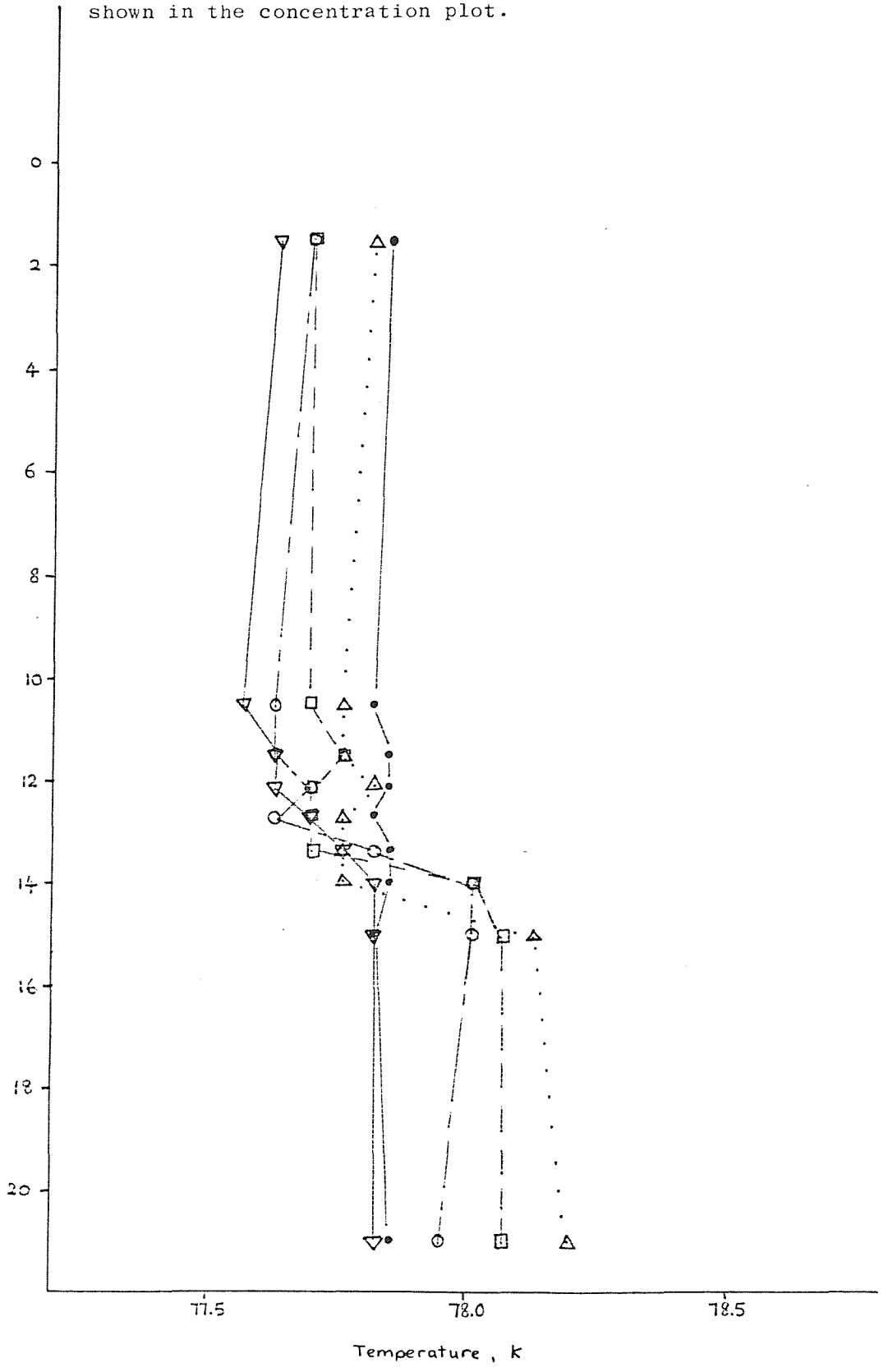

Run b 2. Concentration Profiles.

Time	0	81	126	141	164
(± 5 minutes)	a	b	c	d	e

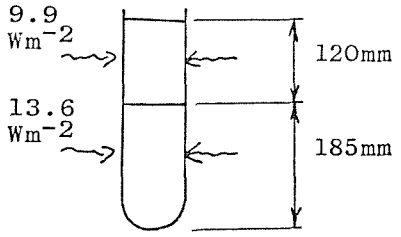

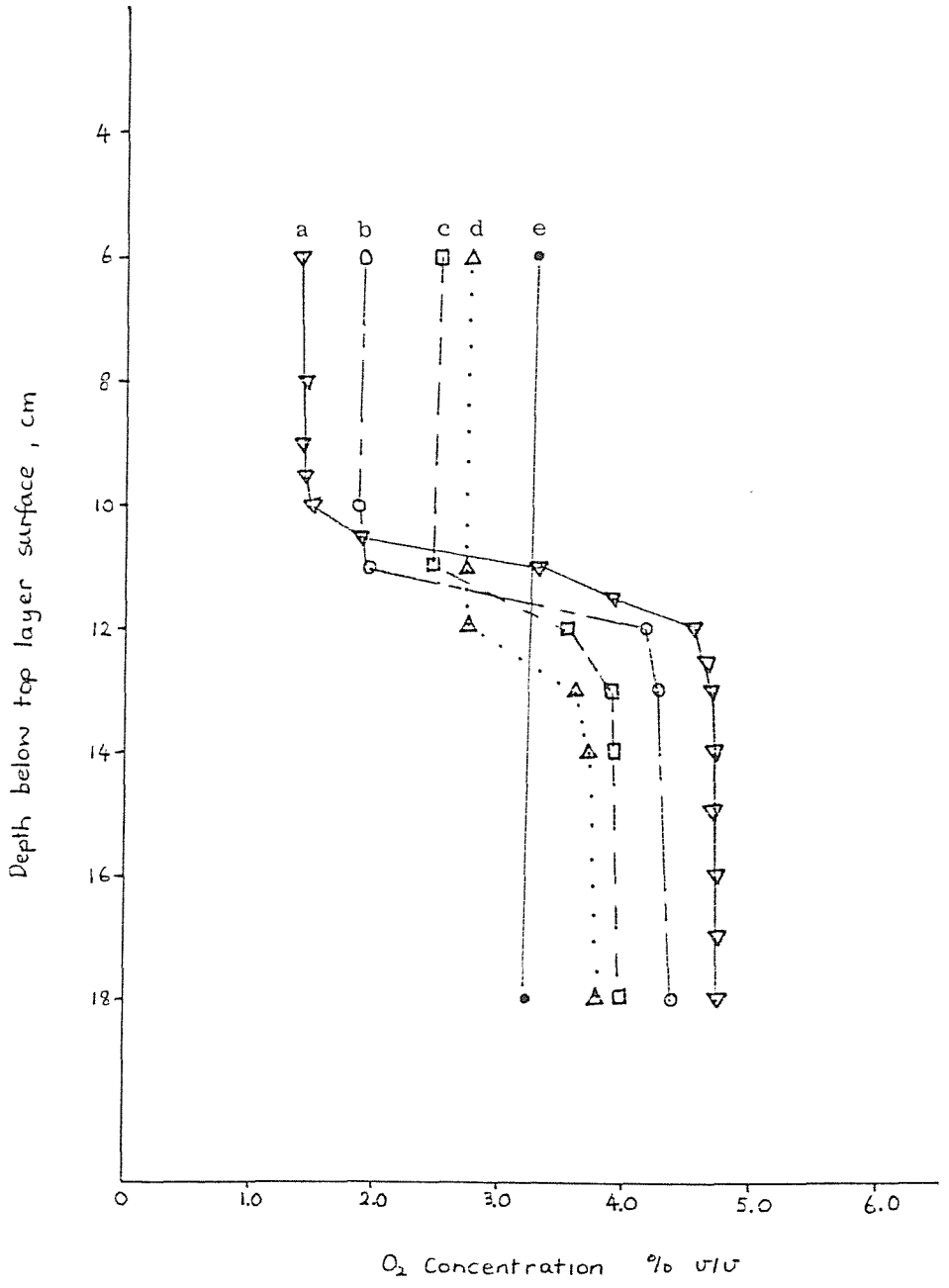

Run b 2. Temperature Profiles.

Time 0 81 126 141 164

(± 1 minute) a b c d e

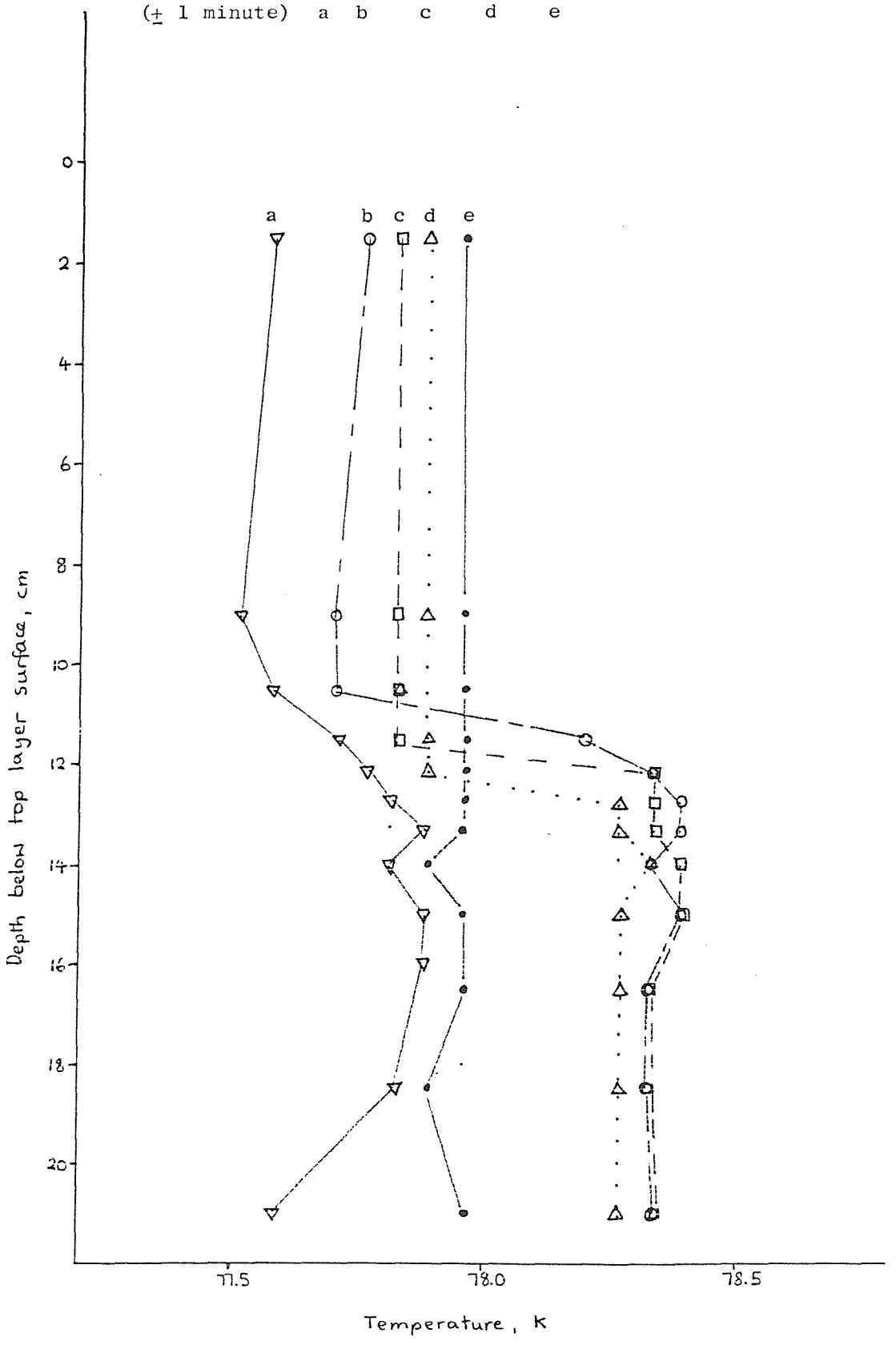

Run b 3. Concentration Profiles.

Time	0	18	82	94	106
(± 4 minutes)	a	b	c	d	e

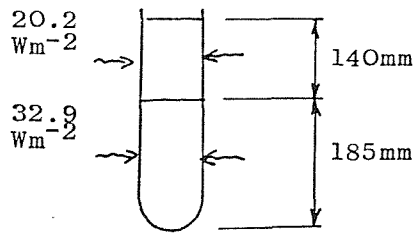

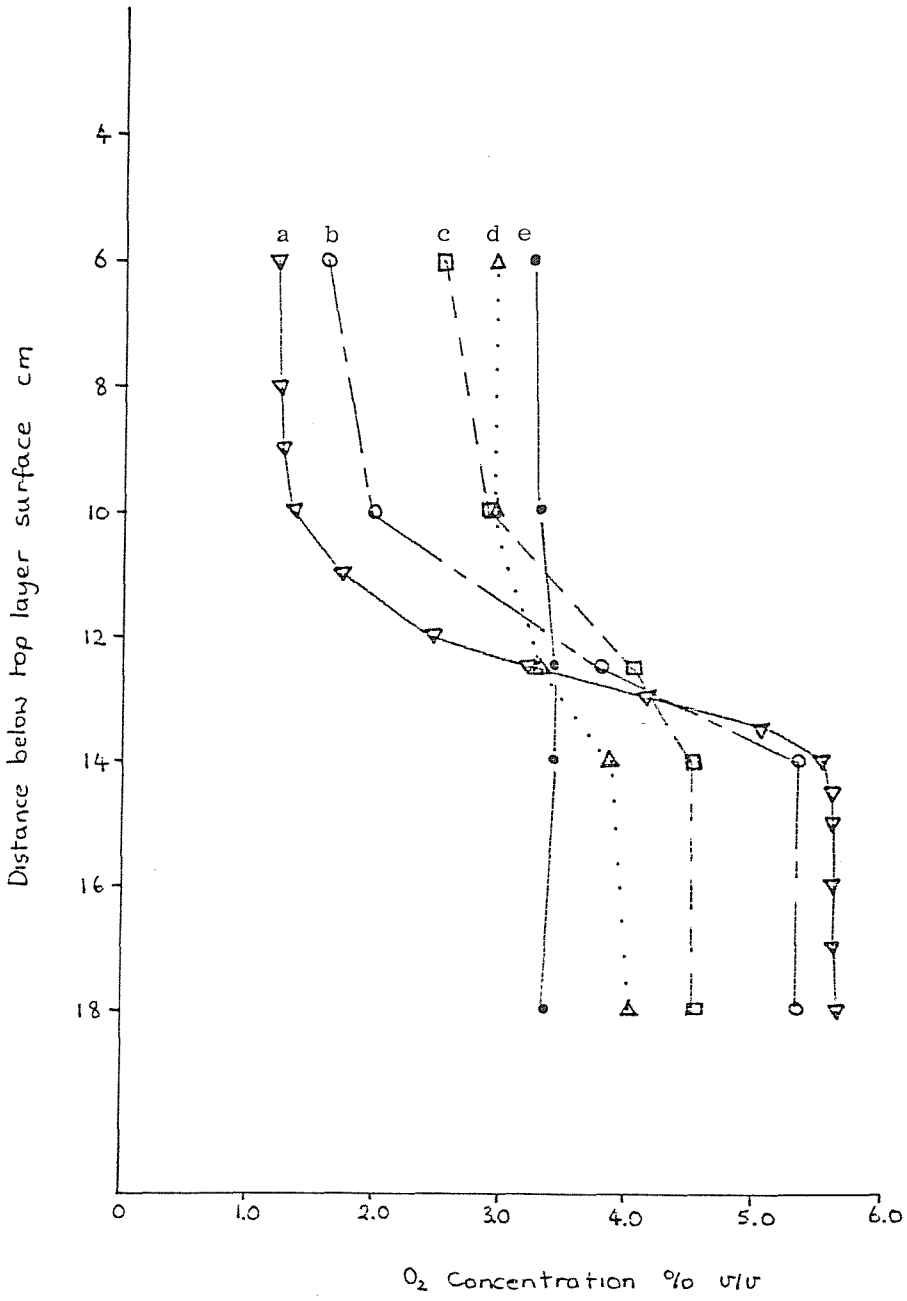

Run b 3. Temperature Profiles.

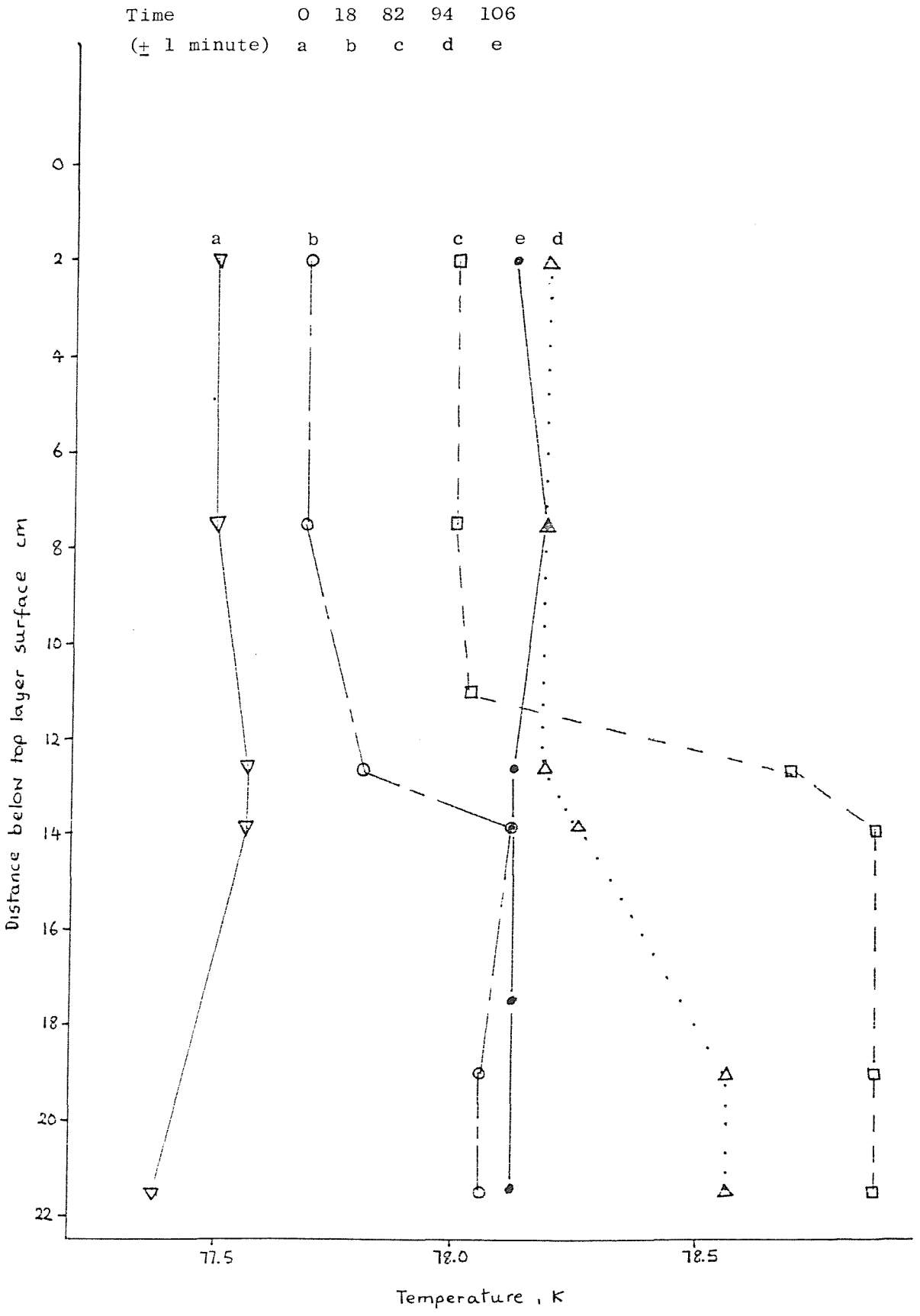

Run b 4. Concentration Profile,
Prior to Heating.

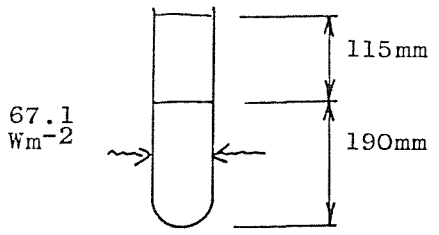

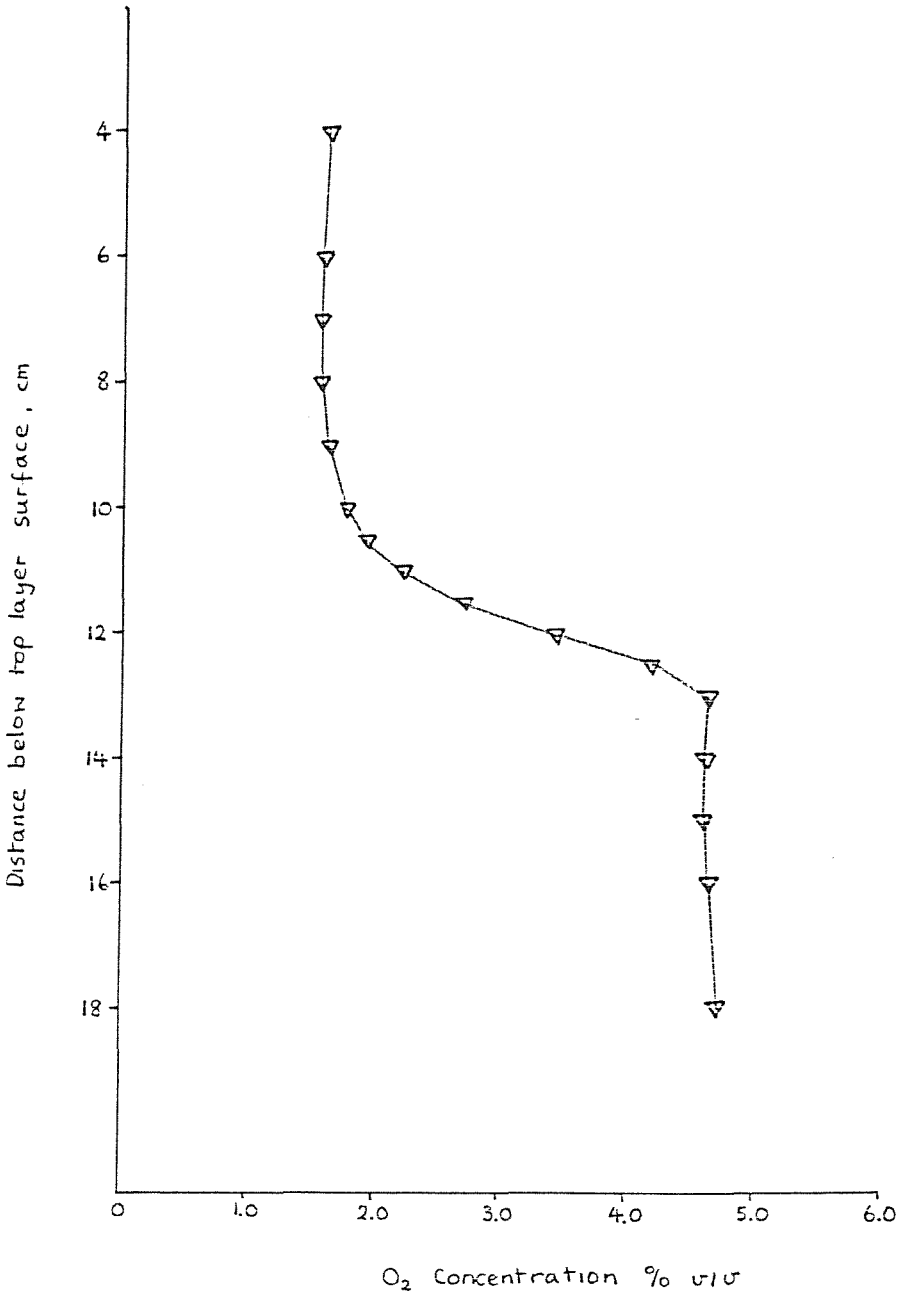

Run b 4. Temperature Profiles.

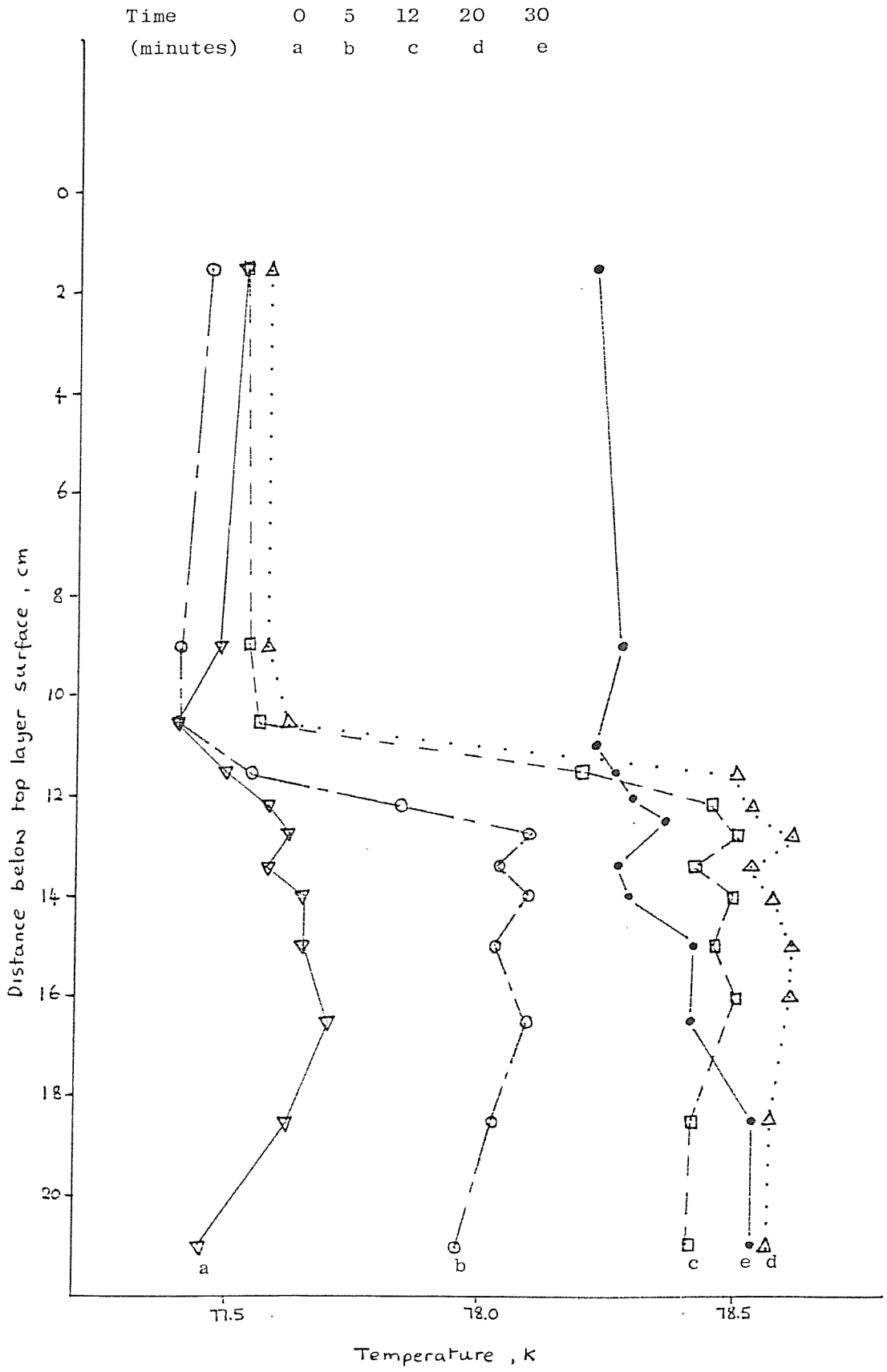

Run b 5. Concentration Profiles.

Time	0	57	117	157	217
(minutes)	a	b	c	d	e

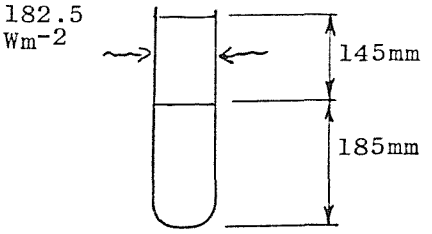

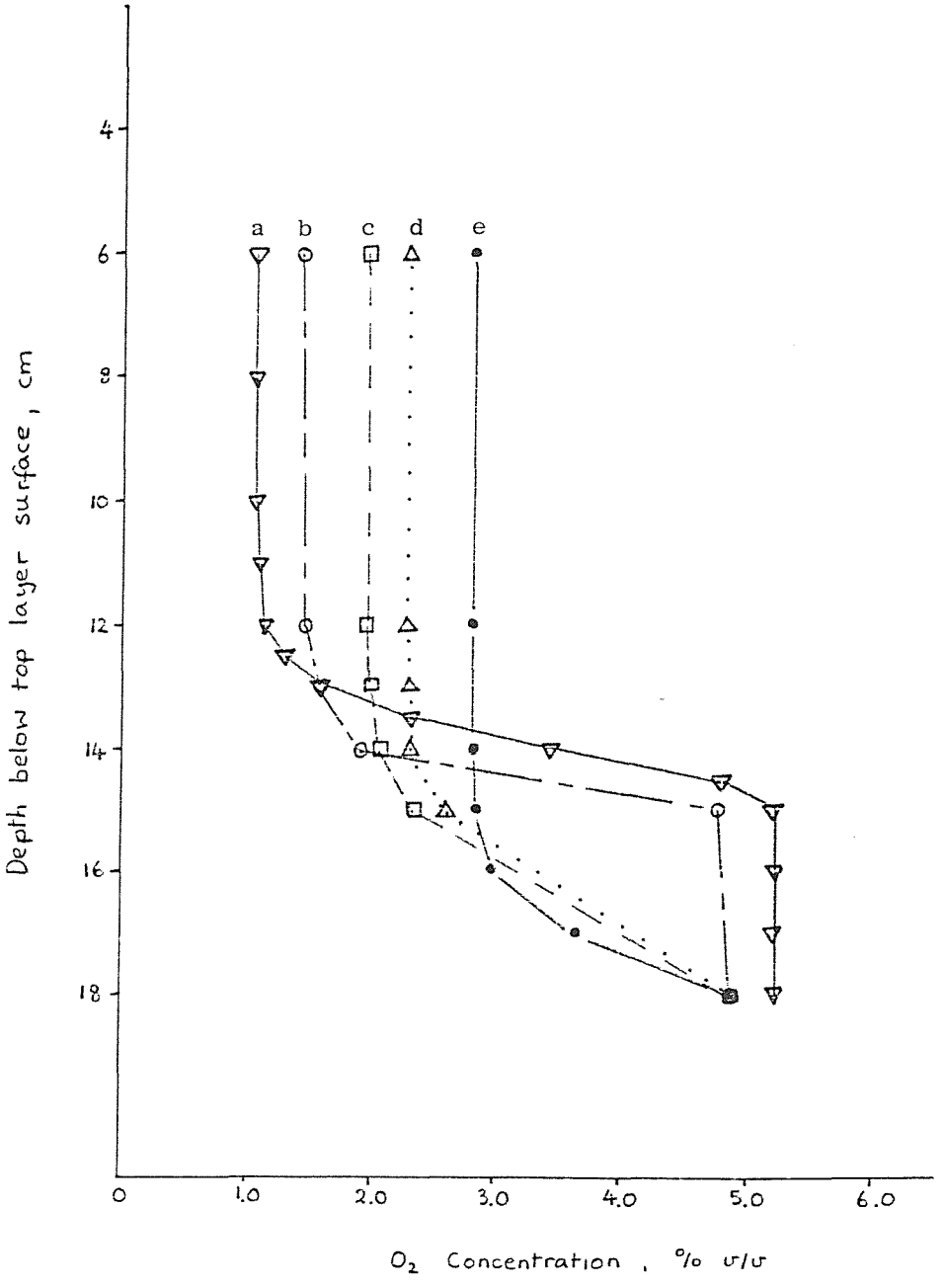

Run b 5. Temperature Profiles.

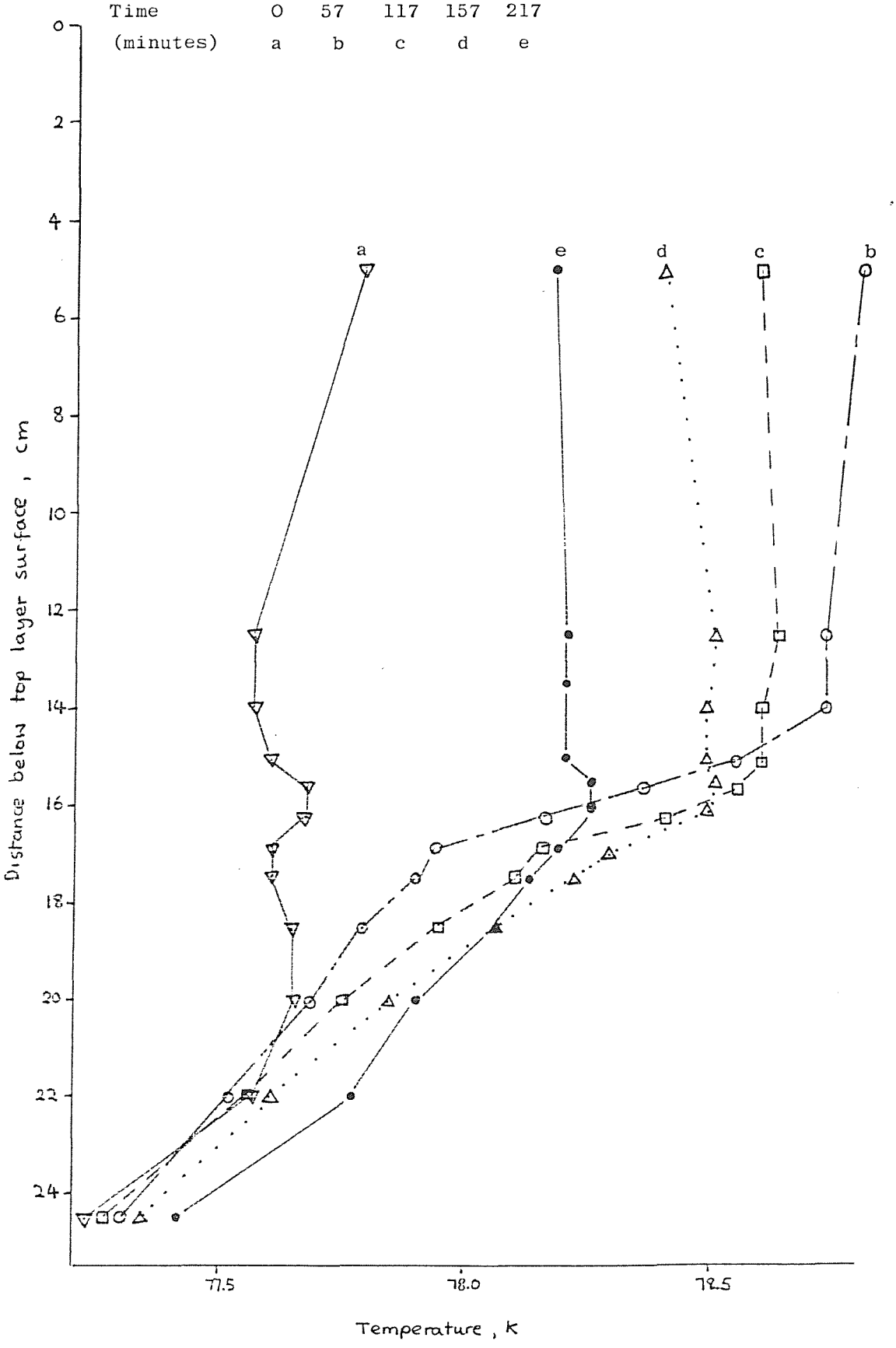

Run c 1. Concentration Profiles.

Time	0	50	80	110	150
(± 5 minutes)	a	b	c	d	e

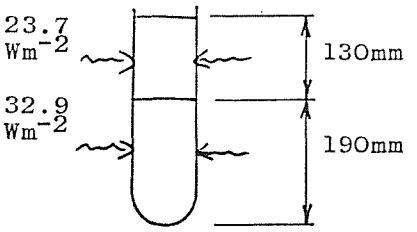

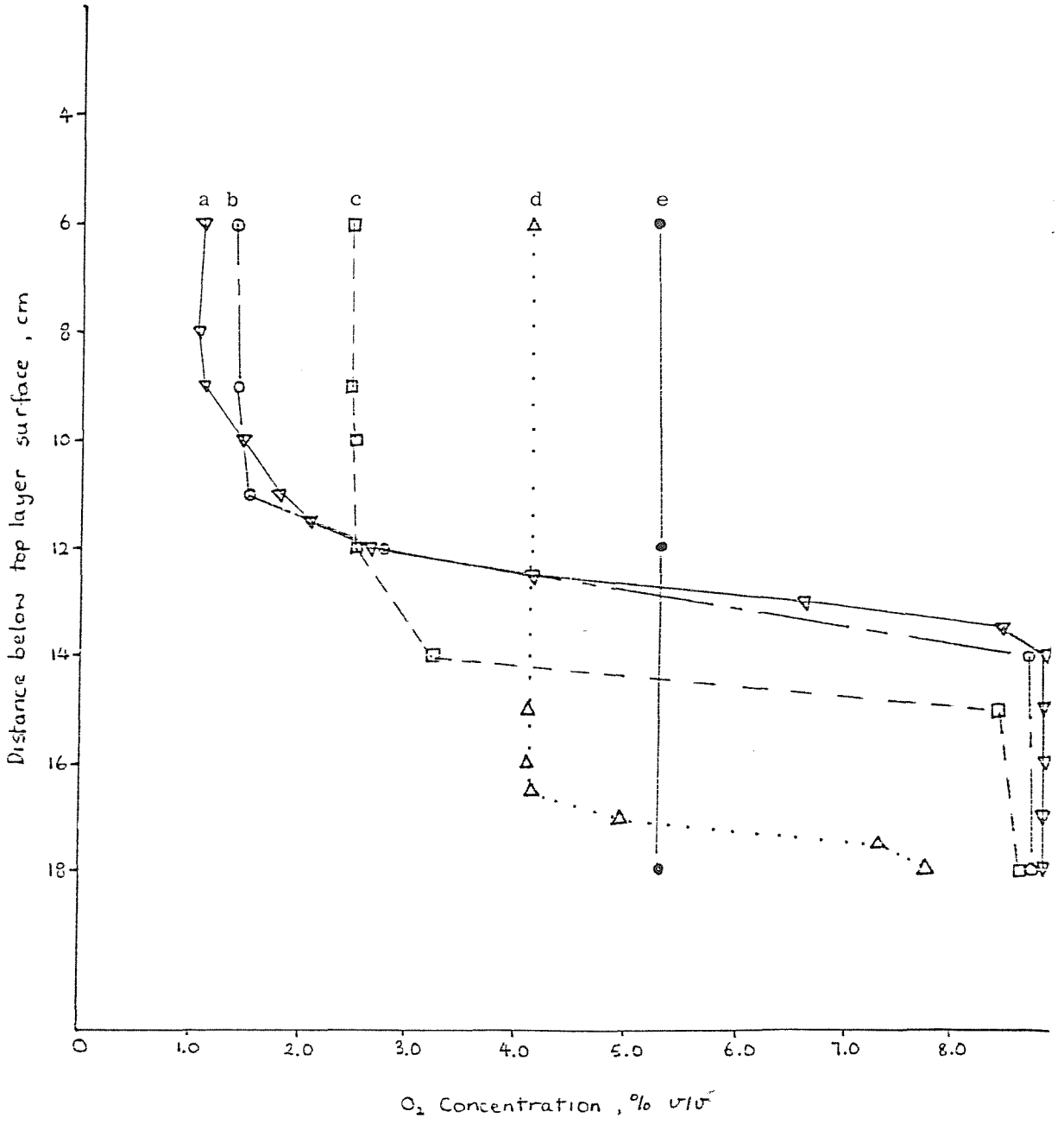

Run c 1. Temperature Profiles.

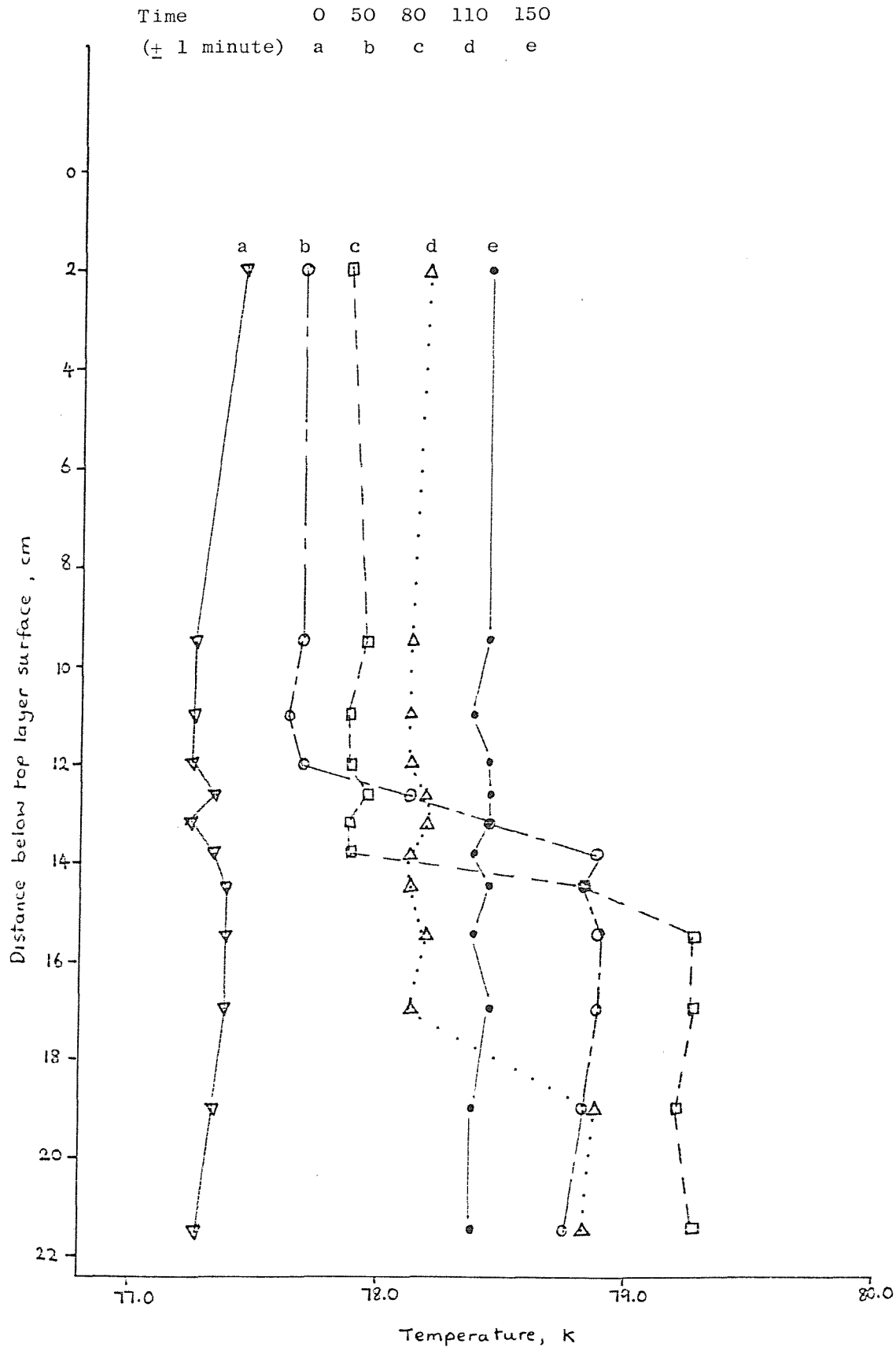

Run C.2. Concentration Profiles.

Time	0	20	35	55
(± 5 minutes)	a	b	c	d

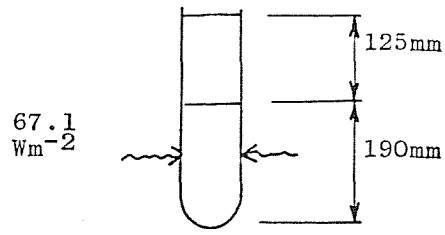

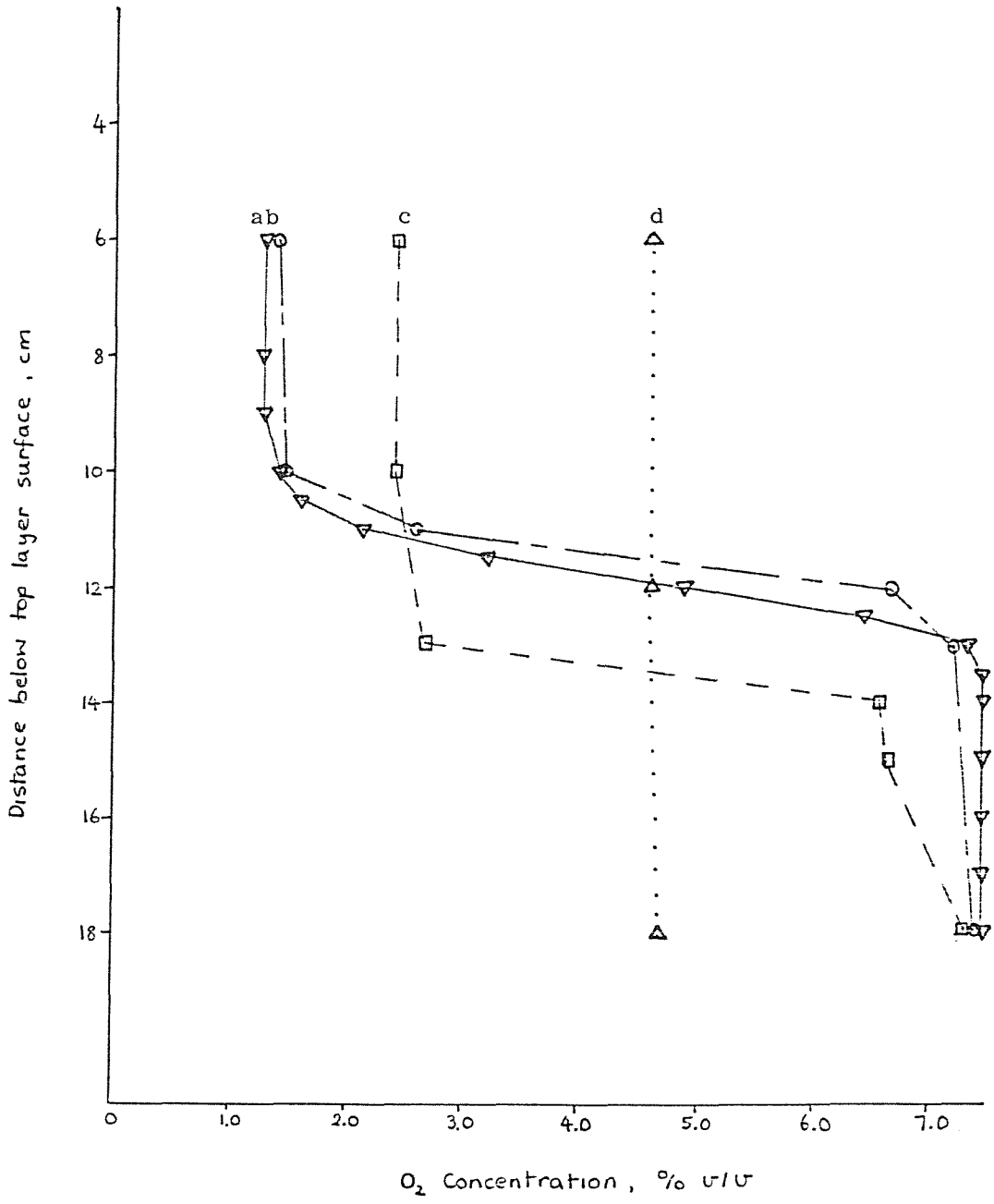

Run c 2. Temperature Profiles.

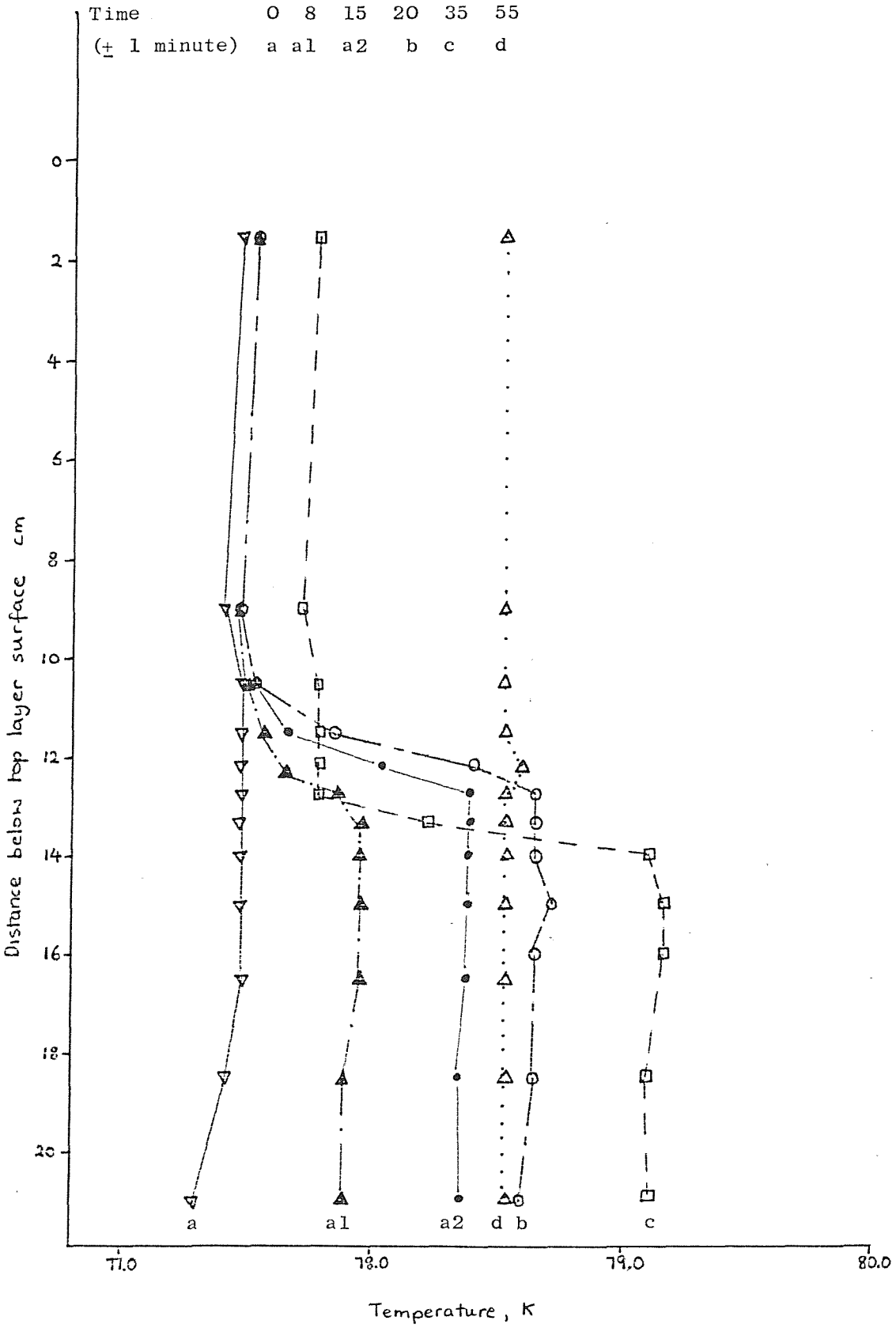

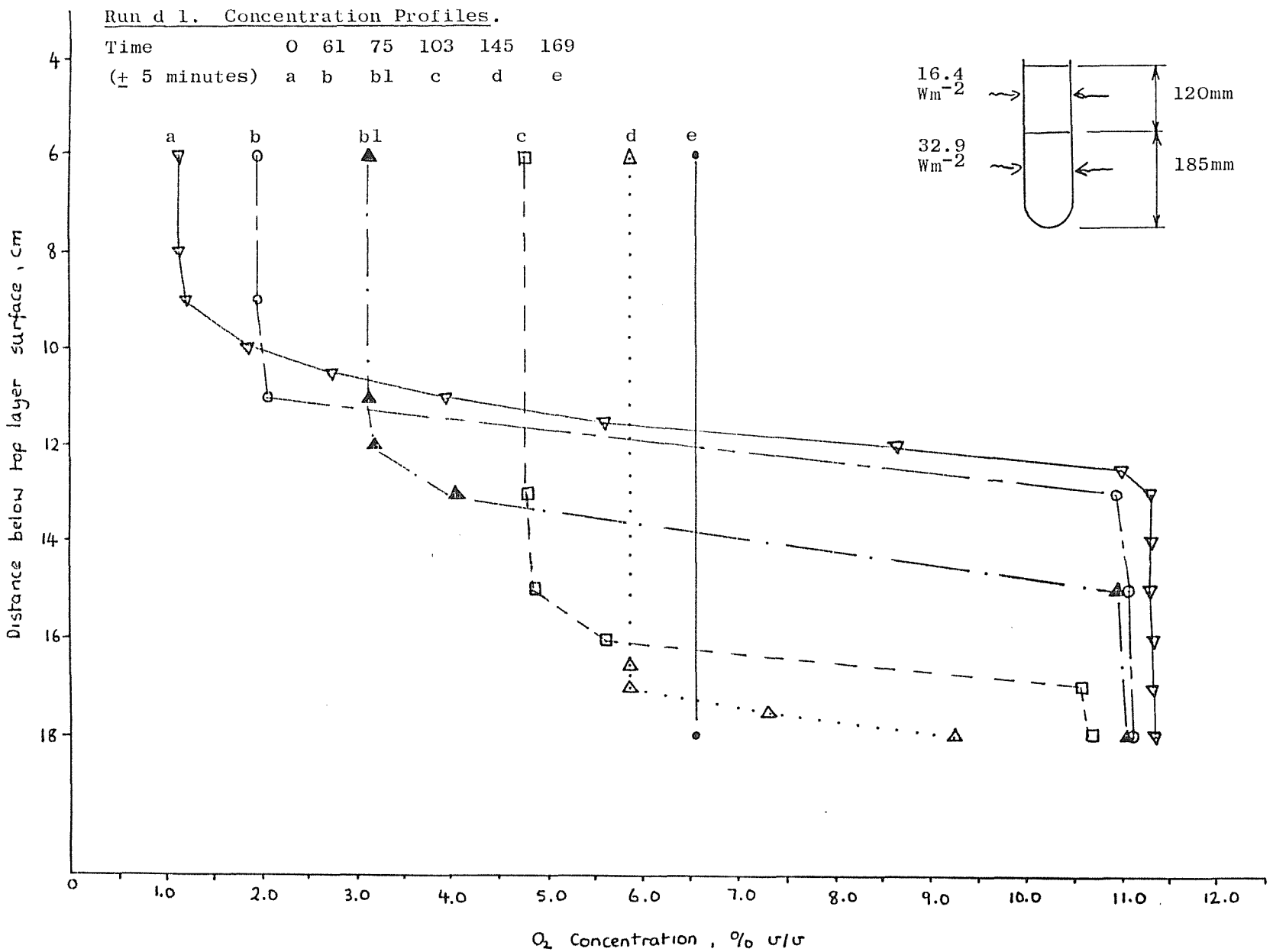
Run d 1. Concentration Profiles.
Time 0 61 75 103 145 169
(± 5 minutes) a b bl c d e
a
b
bl
c
d
e
16.4 Wm-2
32.9 Wm-2
120mm
185mm
Distance below top layer surface, cm
4
6
8
10
12
14
16
18
0
1.0
2.0
3.0
4.0
5.0
6.0
7.0
8.0
9.0
10.0
11.0
12.0
O2 Concentration, % v/v

Run d 1. Temperature Profiles.

Time	0	61	75	103	145	169
(± 5 minutes)	a	b	b1	c	d	e

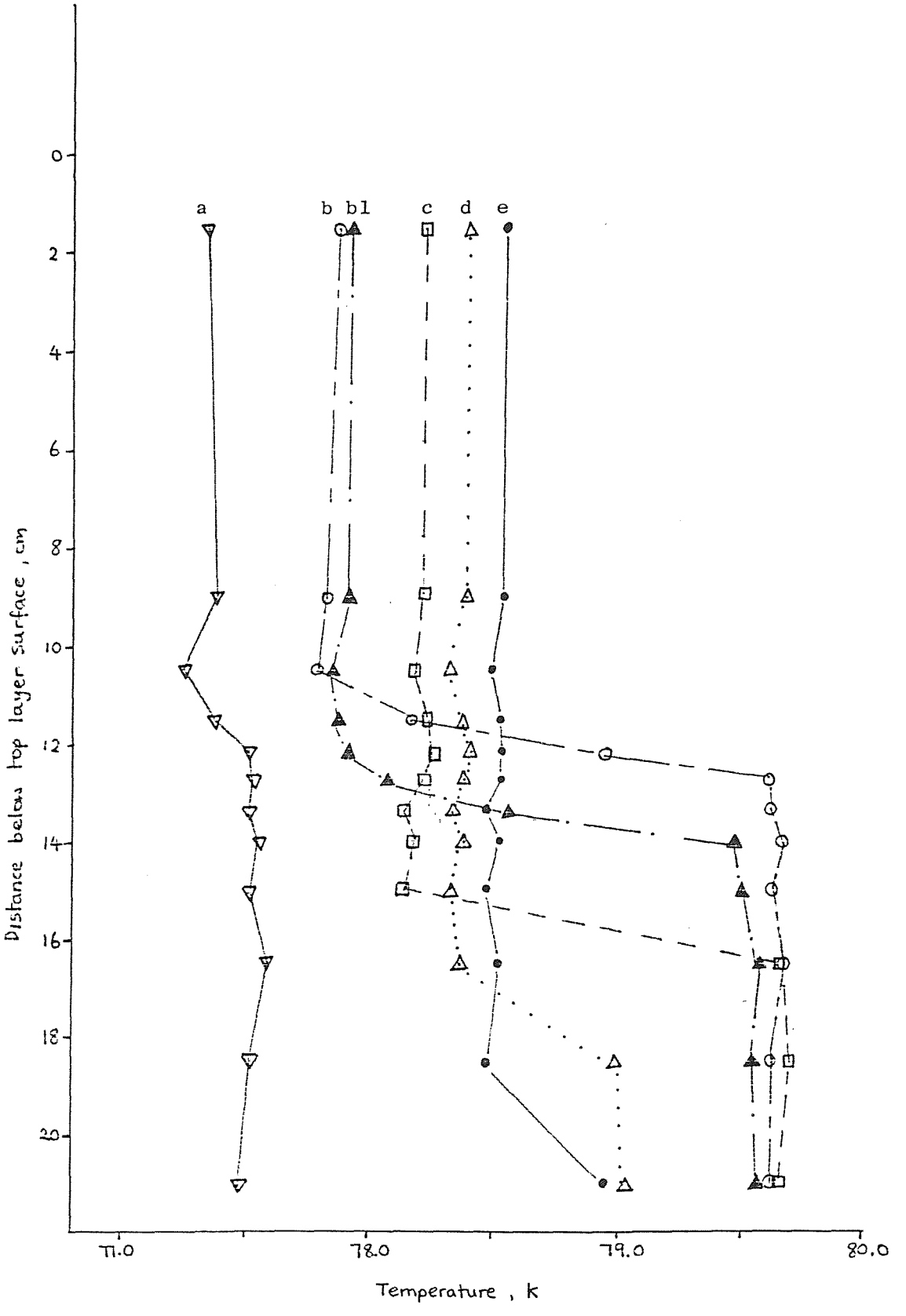

APPENDIX C.

Paper presented at International Cryogenic Engineering Conference, Berlin, April 1986.

CONVECTION PROCESSES DURING HEAT AND MASS TRANSFER ACROSS LIQUID/VAPOUR AND LIQUID/LIQUID INTERFACES IN CRYOGENIC SYSTEMS

T.Agbabi, M.C.M.Atkinson, C.Beduz and R.G.Scurlock

Institute of Cryogenics, University of Southampton, Southampton SO9 5NH, England

Video-Schlieren photography has been used to study the structure of convective streamers in the liquid/liquid interface between LIN and LIN/LA mixtures heated from below to simulate rollover. Detailed measurements of laboratory scale "rollover" using the above liquid layers have revealed that mixing takes place via entrainment extended across the whole area of the interface rather than by penetrative convection or solely boundary layer induced penetration. There was no "rollover" as such between the layers. However, the peak evaporative mass fluxes were considerably smaller than in some real rollover events.

INTRODUCTION

As part of an ongoing study of interfacial phenomena in cryogenic liquids, this paper describes preliminary observations on the understanding of rollover in large storage tanks.

Initial results using Schlieren visualization reveal that convection at the liquid/liquid interface is characterized by convective streamers similar to those observed in the liquid/vapour interface (1).

In our experiments the upper layer is liquid nitrogen (LIN) while the lower denser layer is a mixture of LIN and 0.5 - 3 vol % of Liquid Argon. A typical rollover experiment is described in which the evaporation rate, vertical temperature profile and heat transfer coefficient are displayed as function of time. Rollover occurred 45 minutes after wall heating of the bottom layer was commenced.

EXPERIMENTAL APPARATUS

A double wall transparent vacuum insulated dewar 50 mm diameter was used to perform the experiments. In order to reduce the heat inleak a second dewar containing LIN was placed around the 50mm dewar. A heater was wound on the inner wall (in the vacuum space) to control the heat dissipated into the pool without nucleate boiling.

A vertical array of 16 copper-constantan thermocouples spaced at 10 mm intervals was used to obtain the temperature profile in the two layers. For flow visualization, a thin diametral plane of the liquids was illuminated in the standard way.

The forward light scattering by small particles occurring naturally with different number densities in the 2 layers enabled convection loops in the 2 layers and convection phenomena at the liquid/liquid interface to be observed. Some additional optics enabled a shadowgraph visualization of fluid motion at the interface to be observed.

The Schlieren visualization was performed using a 45 mm diameter dewar, shown in Fig.1. A parallel beam of light is directed vertically through a window in the top flange. At the bottom of the dewar a circular stainless steel mirror reflects the light back to the usual Schlieren optics. The intensity of illumination at a point of the image produced is related to the integrated horizontal refractive index gradient along the optical path. One heater at the bottom and two on the side wall allow heating of the bottom and of the two layers to be controlled independently.

Schlieren visualization of liquid/liquid interface

Previous Schlieren visualization of surface convection during evaporation has shown a radial cellular structure when a boundary layer is produced at the walls of a cylindrical container (1).

With an improved dewar we have been able to observe convective patterns on the whole liquid/liquid interface. If convection is present at both liquid/liquid and liquid/vapour interfaces the Schlieren image is a superposition of two patterns. However during the first stage of the experiment with bottom layer heating only, the upper layer has no convective motion and the image should correspond only to liquid/liquid interface convection. This has been validated by introducing a perspex light pipe through the liquid/vapour interface but covering only part of the surface.

Some representative Schlieren images are shown in Figs 2-5. Fig. 2 shows the boundary layer front moving towards the centre after being deflected at the liquid/liquid interface a few seconds after the bottom layer wall heater was switched on. The pattern presents the expected cylindrical geometry and radial convective streamers are evident behind the boundary layer front.

Figs 3 and 4 show the formation of convective cells at the liquid/liquid interface for very low heat and intermediate heat inputs respectively. In Fig.3 the underlying fluid velocity is small and no preferred orientation is evident for the slowly moving convection boundaries.

Fig.5 shows the image obtained during a rollover event. In this case the image is the superposition of the liquid/liquid and liquid/vapour interfacial convection. Although it is difficult to separate the two patterns, the video recording shows intermittent areas of high activity which are probably associated with large scale entrainment at the liquid/liquid interface during the mixing process.

ROLLOVER BETWEEN LIN AND LIN/LA MIXTURES

We report here on a typical rollover experiment using LIN for the top layer and LIN/LA for the bottom layer, the concentration of Argon being 1 vol %. The unsilvered dewar enabled good observation of the mixing event to be achieved and it was easy to check that no nucleation occurred. The initial depths of the bottom and top layers were 85 mm and 170 mm respectively. The addition of the top layer without mixing was achieved by using a vacuum insulated stainless steel tube with a diffuser at the bottom. In this experiment 0.36 W was applied to the side wall heater into the bottom layer only.

Fig.6 shows the development of the temperature profiles with time.

At t = o the temperature of the two layers is approximately homogeneous with the lower part of the top layer slightly subcooled. Fig.6a shows that, during the first 15-20 minutes, all the heat is being absorbed by the bottom layer with negligible heat transfer to the top layer. Visualization of the layers in this time

interval showed a strong convective cell in the lower layer and no convective motion in the upper LIN layer.

Fig.6a		Fig.6b	
curve	time (min)	curve	time (min)
1	1	1	40
2	5	2	44
3	9	3	45
4	15	4	46
5	25	5	58
6	35	6	95

Between t = 15 and 25 minutes, heat transfer commences between the layers Thereafter, the temperature of the 2 layers increase with the temperature difference remaining constant. The thickness of the interfacial region, containing the temperature gradient, appears to decrease with time. However, the mid-point of this region appears to move up about 15 mm during the first 15-20 minutes, and then remains stationary until it disappears at rollover.

At t = 44 minutes, the previously stable temperature profiles start to contain oscillations. At t = 45 minutes, large scale mixing (the rollover) takes place. At t = 46 minutes the interface has disappeared and the temperature is homogeneous over the whole depth of the liquid pool. The evaporative mass flux as a function of time is shown in Fig.7a, where for clarity the evaporation produced by the small natural heat inleak has been subtracted. The temperature difference between the two layers and the heat transfer coefficient across the liquid/liquid interface are shown in Fig 7b and 7c.

The time dependence of these parameters and the temperature profiles suggest the following sequence of events:

A. Initially there is very little heat transfer between the two layers and the heat dissipated in the lower layer increases its temperature linearly with time (t = 0-20 min). The evaporation rate is zero because the top layer is very near saturation. The absence of convective motion in the top layer and the turbulence of the bottom convection loop causes the interface to move upward with entrainment into the bottom layer (2). The stability parameter $R = \frac{\beta\Delta S}{\alpha\Delta T}$ decreases gradually and at t = 20 min heat transfer commences betwen the lower and upper layers.

B. At the same time, a convective loop commences in the upper layer. In this phase (t = 20 - 44 min) the mean temperature difference remains constant and the evaporation rate increases with the superheat of the top layer.

Two factors contribute to the increase in the heat transfer coefficient with time: (a) the mass flux through the interface reduces the value of R by decreasing ΔS, the concentration difference (b) the thinning of the interfacial region by the increased intensity of turbulence on both sides of the region (3).

C. At t_4 = 45 min the mixing takes place and a peak evaporative mass flux of 3.0×10^{-4} g cm^{-2} s^{-1} is observed. The bulk superheat and evaporation rate decay exponentially to the equilibrium value of 1.4×10^{-4} g.cm^{-2} s^{-1} at t ≈ 80 min.

DISCUSSION

This experiment indicates how a complete picture of rollover events can be studied. Further studies are planned which will incorporate the measurement of the layer compositions with time.

From the continuous flow visualization, no (laminar) boundary layer penetration

was observed during the whole mixing event, and mixing was observed to be produced entirely by entrainment. This may not be the case for turbulent boundary layers.

At all times, the experimentally observed evaporative mass flux was related to the bulk superheat ΔT_s of the upper layer according to our correlation for LIN (4).

$$\dot{m} = 3.32\ \Delta T^{1.17} \times 10^{-4}\ g\ cm^{-2}\ s^{-1}$$

This conclusion leaves a puzzle. Some of the real rollover events have much higher evaporative mass fluxes than predicted by this correlation. Our laboratory experiments do not simulate these very high peak evaporation rates.

ACKNOWLEDGEMENTS

We are grateful to SERC for a research grant to develop visualization techniques. TA and MCMA acknowledge SERC and British Gas Corporation for the award of CASE research studentships.

REFERENCES

1 Atkinson, M.C.M., Beduz, C., Rebiai, R. and Scurlock, R.G., Proc. 10th Int. Cryogenic Eng. Conf, Helsinki, (1984) p.95

2 Turner, J.S. 'Buoynacy Effects in Fluids', Cambridge Univ.Press (1979)

3 Kamiya, A., Tashida, M. and Sugawara, Y., ASME Winter Annual Meeting (1985)

4 Beduz, C., Rebiai, R. and Scurlock, R.G., Adv. Cryo. Eng. 29. (1983) p.795

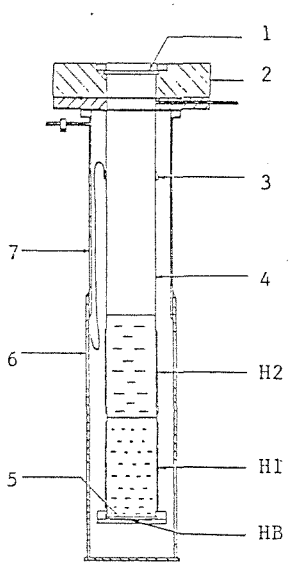

Fig 1. Dewar used for schlieren visualisation. 1: window; 2: top flange heater; 3: thermal anchor; 4: stainless steel tube; 5: mirror; 6: outer copper casing; 7: stainless steel tube; H1: side wall heater for the bottom layer; H2: side wall heater for the top layer; H3:bottom heater

Fig.2 Schlieren image of the boundary layer moving radially inwards at the liquid/liquid interface

Fig.3 Schlieren image of the liquid/liquid interface for low heat flux

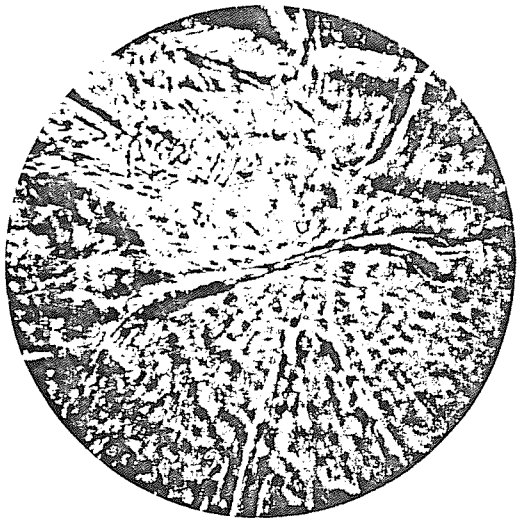

Fig.4 Schlieren image of the liquid/liquid interface for moderate heat flux

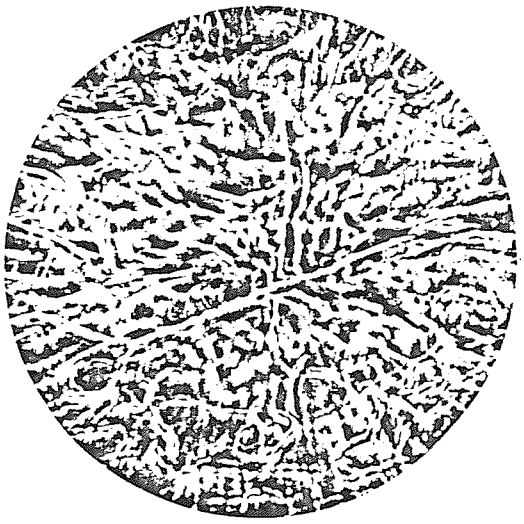

Fig.5 Schlieren image of the liquid/liquid interface during rollover

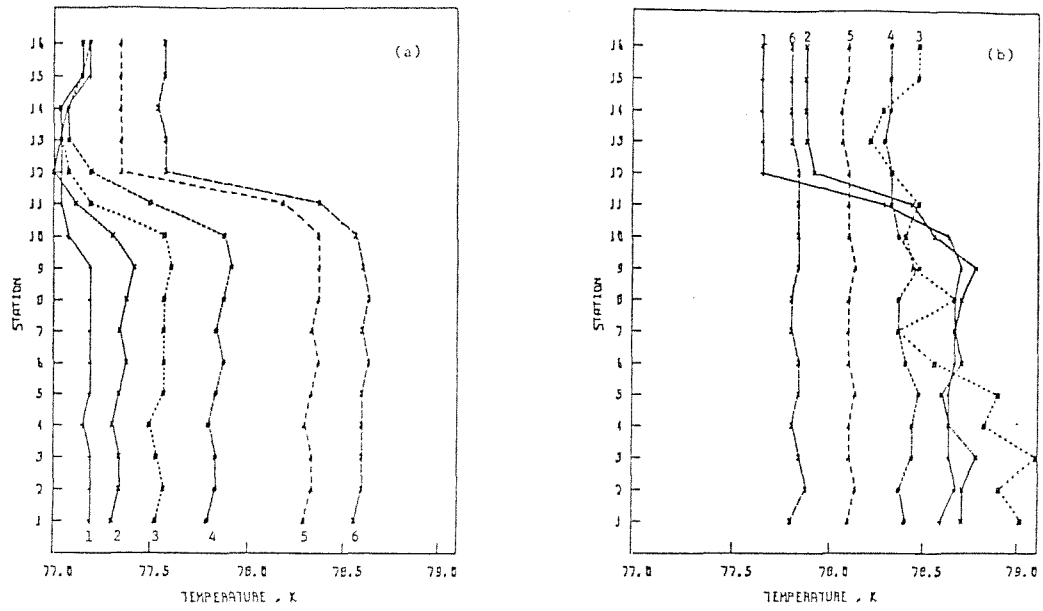

Fig.6 Vertical temperature profiles as function of time during rollover event

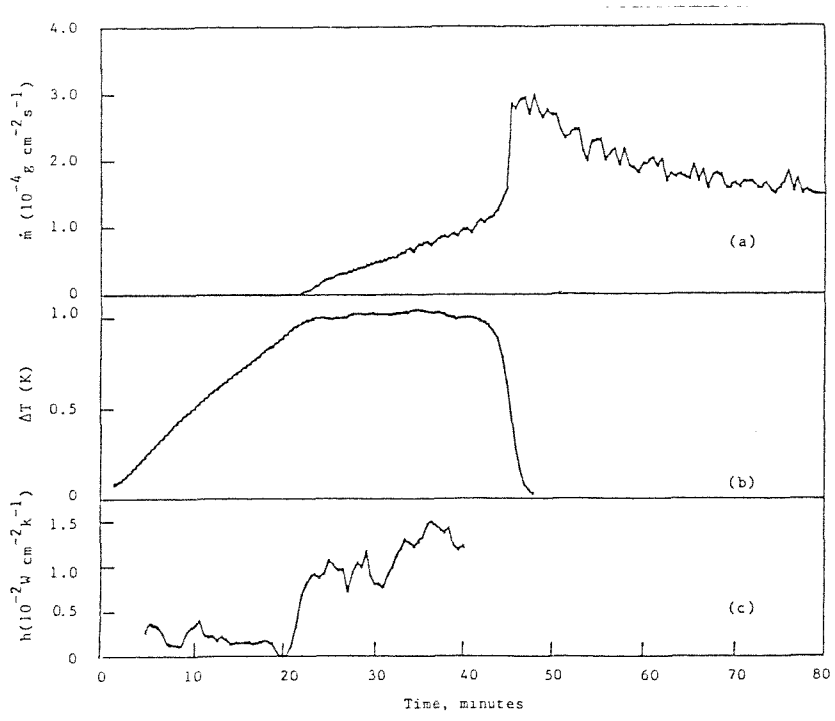

Fig.7 (a) Evaporative mass flux. (b) Mean temperature difference between layers and (c) Heat transfer coefficient across liquid/liquid interface, all as a function of time